



ELECTROMAGNETIC WAVE PROPAGATION IN PHOTONIC CRYSTALS AND METAMATERIALS

by

Charalampos Mavidis

A dissertation submitted
in partial fulfillment of the requirements for the degree of

Doctor of Philosophy

Supervisor: Prof. Maria Kafesaki

Co-supervisor: Prof. Willem L. Vos

Department of Materials Science and Technology

University of Crete

Heraklion, April 2022

Copyright © Charalampos Mavidis 2022

All Rights Reserved

ABSTRACT

The great advancements in nanotechnology during the 20th century unveiled numerous, previously unattainable, applications involving electromagnetic wave propagation and control. This led to the emergence of man-made composite structures with engineerable properties through proper structuring, allowing the exploration of previously unexplored light-matter interaction aspects. Characteristic examples are Photonic Crystals and Metamaterials/Metasurfaces. In this thesis, three different photonic systems are investigated: (i) The position dependence of Local Density of States inside a finite 3D photonic crystal is calculated, for different trajectories inside the crystal, and a model was derived to obtain a physical understanding of the calculated response. (ii) The conditions for perfect absorption for planar structures comprised of a dielectric between a thin resistive film and a metallic back-reflector are derived, based on a proper extension of the Transfer Matrix Method. Three distinct cases are investigated, where the resistive thin film is a: (a) uniform metal film; (b) graphene layer; (c) metasurface showing both electric and magnetic surface conductivities. (iii) The scattering properties of multilayered infinitely-long cylinders are calculated, based on Mie theory combined with a Transfer Matrix Method formulation, for cylinders incorporating metasurfaces at their interfaces, and a previously established effective medium model is extended for systems/metamaterials of such cylinders. Three relevant systems are investigated: (a) single-layered polaritonic cylinders; (b) multi-layered graphene-based nanotubes; and (c) metasurface-based cylinders. We found the parameters required for different electromagnetic phases in those systems, including hyperbolic dispersion, double negative response, epsilon near zero response, etc.

To my family and friends
who always believed in me

“ I was like a boy playing on
the sea-shore, and diverting
myself now and then
finding a smoother pebble
or a prettier shell than
ordinary, whilst the great
ocean of truth lay all
undiscovered before me. ”

—Isaac Newton

CONTENTS

ABSTRACT	iii
LIST OF FIGURES	vii
LIST OF TABLES	xiv
ACKNOWLEDGEMENTS	xvii
CHAPTERS	
1 Introduction	1
1.1 Outline of this thesis	3
1.2 Publications in the context of this thesis	3
2 Transfer Matrix Method for Planar layered structures	5
2.1 Introduction	5
2.2 Transfer Matrix for p polarization	6
2.3 Transfer Matrix for s polarization	7
2.4 Reflection and transmission coefficients	9
2.5 Specific cases	10
2.5.1 Interface between two semi-infinite media	10
2.5.2 Electric surface current at the interface between two semi-infinite media ..	11
2.5.3 Electric and magnetic current sheet in a homogeneous medium	12
2.6 The pyTransferMatrix package	12
2.6.1 Example: One-dimensional photonic crystal cavity	13
3 Metal-Insulator-Metal based Perfect Absorbers	15
3.1 Introduction	15
3.2 Structure and theoretical model	15
3.3 Results and discussion	17
3.4 Conclusions	19
4 Perfect absorption conditions in metasurface-based perfect absorbers	21
4.1 Introduction	21
4.2 Transfer matrix and conditions for perfect absorption	22
4.3 Uniform graphene perfect absorber	24
4.4 Metasurface-based perfect absorber	27
4.5 Conclusions	29
5 Polaritonic cylinders as multifunctional metamaterials: Single scattering and effective medium description	31

5.1	Introduction	31
5.2	Methods	34
5.2.1	Single Scattering	34
5.2.2	Effective medium	37
5.3	Results and Discussion	39
5.3.1	Single scattering	39
5.3.2	Effective Medium	41
5.4	Conclusions	47
5.5	Appendices	47
5.5.1	Effective Medium Derivation	47
5.5.2	Scattering/absorption	52
5.5.3	Effective parameters	52
6	Single scattering and effective medium description for graphene- and for metasurface-coated and multicoated cylinders	53
6.1	Introduction	53
6.2	Methods	55
6.2.1	2D Conductivities	56
6.2.2	Single Scattering	57
6.2.3	Effective Medium Theory	60
6.3	Results and Discussion	61
6.3.1	Single scattering	61
6.3.2	Effective medium theory and alternating optical phases	64
6.4	Conclusions	70
6.5	Appendices	71
6.5.1	Transfer Matrix Method	71
6.5.2	Effective Medium Theory	72
6.5.3	Extinction efficiencies for $N = 2$ and $\sigma_e = 0$ or $\sigma_m = 0$	73
7	Local Density of States for Inverse Woodpile Structures	75
7.1	Introduction	75
7.2	Methods	76
7.2.1	The structure of the finite crystal	76
7.2.2	Computation of the local density of states	77
7.3	Results and discussion	79
7.3.1	Local density of states versus emitter position	79
7.3.2	Model parameters and far-field and near-field	81
7.3.3	Comparison between LDOS decay length and Bragg length	84
7.3.4	LDOS along different trajectories	84
7.3.5	Practical consequences	85
7.4	Conclusions	87
7.5	Appendices	87
7.5.1	Numerical calculation of the LDOS	87
	BIBLIOGRAPHY	89

LIST OF FIGURES

1.1	Types of photonic systems studied in this thesis: (a) A dielectric sandwiched between a thin resistive film (e.g. metal, graphene, metasurface) and a metallic back-reflector, (b) an array of infinitely-long cylinders and (c) an three-dimensional finite inverse woodpile photonic crystal.	3
2.1	(a) Interface with surface conductivities σ_e and σ_m between two media i and j with electrical permittivities $\varepsilon_i, \varepsilon_j$, magnetic permeabilities μ_i, μ_j . (b) Layered structure consisting of N layers. We assume that a plane wave is incident from the left of the structure.	6
2.2	(a) A defect of thickness $4a_1$ between two photonic crystals with N unit cells each. (b) Reflection and transmission spectra for $N = 10$ unit cells of a photonic crystal of unit cell consisting of a slab with thickness $a_1 = 86$ nm and refractive index $n_1 = \sqrt{\varepsilon_1} = 2.9$ and a slab with thickness $a_2 = 70$ nm and refractive index $n_2 = \sqrt{\varepsilon_2} = 3.57$	14
3.1	The Metal-Insulator-Metal (MIM)-based absorber structure under investigation. A lossy dielectric layer of thickness d_{TiO_2} is sandwiched between a thin metallic film with thickness d_{Au} and an optically thick metallic substrate.	16
3.2	(a) Experimental (dashed red line) and theoretical (black solid line) absorption spectra for normal incidence on our Metal-Insulator-Metal Structure with a $d_{\text{TiO}_2} = 120$ nm TiO_2 dielectric layer between two metallic gold films and $d_{\text{Au}} = 20$ nm and 120 nm respectively. (b), (c) Electric field amplitudes at the absorption maxima: (b) 537 nm and (c) 952 nm. The colors indicate the extent of the different materials (Au: yellow, TiO_2 : gray: Air: white).	17
3.3	Simulations indicating the desirable thickness of TiO_2 dielectric layer as a function of the wavelength that absorption occurs, corresponding to absorption higher than 90% (a), and FWHM of the absorption peaks with intensity higher than 90%, between 10 and 100 nm (b), respectively. The color codes (in connection with the right vertical bars) indicate the intensity (a), or the FWHM (b) of the absorption peaks of the proposed structure, respectively.	18
3.4	Absorption spectra for (a) s-polarization and (b) p polarization for different angles of incidence, varying from 0 to 75 degrees, for the Metal-Insulator-Metal Structure with a 120 nm TiO_2 dielectric layer between two metallic gold films.	18
3.5	Absorption spectra under normal incidence for a MIM structure comprising of (a) 2 and (b) 5 Au- TiO_2 layers. The thickness of the TiO_2 layers is set to 150 nm and the thicknesses of the Au films to 15 nm except from the top metallic film which has thickness 20 nm. The absorption of a single MIM stack (blue dashed line) is also plotted for comparison.	19

4.1	(a) Setup for the derivation of the transfer matrix equation for s and p polarizations. An interface with surface conductivities σ_e and σ_m between two semi-infinite (along x and y directions) media 1, 2 and Perfect Electric Conductor (PEC) substrate. (b) Schematic of a metasurface with surface conductivities σ_e, σ_m on top of a grounded dielectric of thickness d with permittivity ε_2 and permeability μ_2 .	23
4.2	(a) Real and (b) imaginary part of normalized conductivity of graphene for Fermi energies $E_F = 0.2$ eV, $E_F = 0.4$ eV, $E_F = 0.8$ eV and $E_F = 1.2$ eV. The relaxation time of the electrons in graphene is $\tau = 0.1$ ps.	24
4.3	Absorption spectra under normal incidence for a graphene on a grounded dielectric substrate of relative permittivity $\varepsilon_{2r} = 3.9$ as function of the thickness of the dielectric and for Fermi energies (a) $E_F = 0.2$ eV, (b) $E_F = 0.4$ eV, (c) $E_F = 0.8$ eV and (d) $E_F = 1$ eV. The relaxation time of the electrons in graphene is $\tau = 0.1$ ps.	25
4.4	(a) Absorption spectrum under normal incidence for a graphene on a grounded dielectric substrate of thickness $d = 20 \mu\text{m}$ and relative permittivity $\varepsilon_{2r} = 3.9$, for different Fermi levels, $E_F = [0.2 - 1.2]$ eV. (b)-(c) Perfect absorption conditions based on (b) Eq. (4.8) and (c) Eq. (4.9). The relaxation time of electrons in graphene is $\tau = 0.1$ ps.	26
4.5	Contour plots of absorption under normal incidence for a uniform graphene Salisbury screen as a function of the dielectric substrate thickness and the graphene's Fermi energy, for frequency of operation: (a) $f = 2$ THz and (b) $f = 2.7$ THz. The relative permittivity of the dielectric is $\varepsilon_{2r} = 3.9$.	27
4.6	Real (solid lines) and imaginary (dashed lines) parts of normalized sheet conductivities as a function of frequency (top row) and corresponding absorption spectra as function of the thickness of the dielectric and frequency (bottom row) for four different metasurfaces: A: $s_m = 0$ (first column); B: $\omega_m/2\pi = 17$ THz (second column); C: $\omega_m = \omega_e, \kappa_m = \kappa_e/10$ (third column) and D: $s_e = s_m$ (fourth column). For all cases the parameters of the electric sheet conductivity are $\omega_e/2\pi = 15$ THz, $\kappa_e/2\pi = 2$ THz and $\Gamma_e/2\pi = \Gamma_m/2\pi = 1$ THz. For the definition of the parameters see main text.	28
4.7	Absorption under normal incidence (left column) and conditions α (Eq. (4.8)) (right column - solid lines) and β (Eq. (4.9)) (right column - dashed lines) for: (a)-(b) a metasurface (metasurface B) with $\omega_e \neq \omega_m/2\pi = 17$ THz ($\kappa_e = \kappa_m$) and (c)-(d) a metasurface (metasurface C) with $\omega_m = \omega_e, \kappa_m = \kappa_e/10$, for two different dielectric thicknesses (note that α is thickness independent). For all cases the parameters of the electric sheet conductivity are $\omega_e/2\pi = 15$ THz, $\kappa_e/2\pi = 2$ THz and $\Gamma_e/2\pi = \Gamma_m/2\pi = 1$ THz. The definition of the parameters is given in the main text.	29
5.1	Real and imaginary parts of the relative dielectric function for (a) LiF and (b) SiC calculated from Eq. (5.1) and using the data from Table 5.1. The gray areas indicate the frequency regions where the real part of the corresponding dielectric function is negative, between approximately ω_T and ω_L .	32

5.2	(a) An assembly of cylinders in a host medium (our system of interest) and definitions of the TE and TM polarization and the normal to the cylinders axes plane of incidence. (b) The unit cell of the system of (a), along with its relevant geometry and material parameters, i.e. electrical permittivity, ε , and magnetic permeability μ . The subscripts h , c stand for the host and cylinder material respectively. (c) Geometry for the derivation of the effective electric permittivity, ε_{eff} , and effective magnetic permeability, μ_{eff} : A single cylinder of radius $R_1 = R$ coated by a coating of thickness $R_2 - R_1$ made of the host material of the original system, embedded in the effective medium. R_2 is such as $f = R_1^2/R_2^2$, where f is the cylinder filling ratio in the original system.	35
5.3	Extinction efficiency of a LiF cylinder in air [(a),(b)] and in a dielectric with $\varepsilon_h = 2$ [(c),(d) for TM (left column) and TE (right column) polarizations. The legend shows the cylinder radius. The shaded areas correspond to the frequency region where the dielectric function of LiF is negative. (e) Electric (green color) and magnetic (blue color) field distributions for the TM_0 , TM_1 , TE_0 and TE_1 modes.	40
5.4	Extinction efficiency of a SiC cylinder (of radius 0.1, 0.5 and 0.8 μm) in air for (a) TM and (b) TE polarizations. The shaded areas correspond to the frequency region where the dielectric function of SiC is negative.	41
5.5	Top panels: Resonance frequencies and absorption over scattering efficiency $Q_{\text{abs}}/Q_{\text{sc}}$ (color) at the resonance frequency of the TM_0 (rotated triangles), TE_0/TM_1 (circles) and the TE_1 (upright triangles) modes as function of the radius for a (a) LiF and a (b) SiC cylinder in air ($\varepsilon_h = 1$). The dashed line shows the quasi-static resonance condition for the TE_1 $\varepsilon_c(\omega) = -\varepsilon_h$, and the shaded area corresponds to the frequency region where the dielectric functions of LiF and SiC are negative. Bottom panels: Quality factor $-\text{Re}(\omega_{\text{res}})/(2\text{Im}(\omega_{\text{res}}))$ for the modes of a (c) LiF and (d) SiC cylinder in air.	42
5.6	Real (upper row) and imaginary (lower row) parts of the parallel and perpendicular components of the relative effective permittivity, ε_{eff} (first and second columns), and permeability, μ_{eff} (third and fourth columns), for LiF cylinders with filling ratio 30% in air, for different radii, R , (mentioned in the legends) using the CPA (lines) and the Maxwell-Garnett approximation (circles). The shaded areas correspond to the frequency region where the dielectric function of LiF is negative.	43
5.7	Normal incidence, TM reflection spectra for a slab of LiF cylinders with radius $R = 1.3\mu\text{m}$ and filling ratio $f = 6.95\%$ in KCl host in a square arrangement. The reflection is calculated by the commercial finite element method electromagnetic solver Comsol Multiphysics, considering a computational system of 7 unit cell thickness (along propagation direction). The full wave reflection results (black line and dots) are compared with results for a homogeneous effective medium of the same thickness as the actual system and effective parameters obtained through CPA (red line) and Maxwell-Garnett approximation (green line). KCl was modelled using Eq. (5.1) with parameters $\varepsilon_\infty = 2.045$, $\omega_T/2\pi = 4.21\text{THz}$, $\omega_L/2\pi = 6.196\text{THz}$ and $\Gamma/2\pi = 0.156\text{THz}$ [105].	44
5.8	Real (upper row) and imaginary (lower row) parts of the parallel and perpendicular components of the relative effective permittivity ε (first and second columns), and permeability, μ (third and fourth columns), for SiC cylinders with filling ratio 30% in air, for different radii, R (mentioned in the legends), using the CPA (lines) and the Maxwell-Garnett approximation (circles). The shaded areas correspond to the frequency region where the dielectric function of SiC is negative.	45

5.9	Optical phase diagrams for the TM modes for LiF (top row) and SiC (bottom row) cylinders in air for different radii, R , of the cylinders. The color marks the different attainable metamaterial-related responses of the systems: Dielectric (White color): Both $\varepsilon_{\text{eff}}^{\parallel} > 0$, $\varepsilon_{\text{eff}}^{\perp} > 0$, $\mu_{\text{eff}}^{\parallel} > 0$, $\mu_{\text{eff}}^{\perp} > 0$, HMM Type I (red): $\varepsilon_{\text{eff}}^{\parallel} < 0$, $\varepsilon_{\text{eff}}^{\perp} > 0$, HMM Type II (green): $\varepsilon_{\text{eff}}^{\parallel} > 0$, $\varepsilon_{\text{eff}}^{\perp} < 0$, Metallic (blue): $\varepsilon_{\text{eff}}^{\parallel} < 0$, $\varepsilon_{\text{eff}}^{\perp} < 0$, DNG (yellow): $\varepsilon_{\text{eff}}^{\parallel} < 0$, $\mu_{\text{eff}}^{\perp} < 0$	46
5.10	Scattering (solid lines) and absorption (dashed lines) efficiencies of a LiF cylinder (of radius 0.3 and 1.5 μm) in air for (a) TM and (b) TE polarization. The shaded areas correspond to the frequency region where the dielectric function of LiF is negative.	48
5.11	Scattering (solid lines) and absorption (dashed lines) efficiencies of a SiC cylinder (of radius 0.1 and 0.5 μm) in air for (a) TM and (b) TE polarization. The shaded areas correspond to the frequency region where the dielectric function of SiC is negative.	49
5.12	Imaginary (solid lines) and real (dashed lines) parts of the parallel (a) and the perpendicular (b) components of the relative effective permittivity for LiF cylinders with filling ratio 30% in air, for different radii, R (mentioned in the legends), using the CPA. The shaded areas correspond to the frequency region where the dielectric function of LiF is negative.	50
5.13	Imaginary (solid lines) and real (dashed lines) parts of parallel ((a),(d)) and perpendicular ((b), (c)) components of the relative effective permittivity (upper row) and permeability (lower row) for SiC cylinders with filling ratio 30% in air, for different radii, R (mentioned in the legends) using the CPA. The shaded areas correspond to the frequency region where the dielectric function of SiC is negative.	51
6.1	(a) Top view schematic of N co-centric cylinders and polarization definition. We assume normal incidence. Each cylinder layer is characterized by electric permittivity ε_{ℓ} and magnetic permeability μ_{ℓ} . The interface between the ℓ -th and the $(\ell + 1)$ -th layer is coated, in the most general case, with a metasurface with arbitrary electric conductivity $\sigma_{e(\ell)}$ and magnetic conductivity $\sigma_{m(\ell)}$. The coated cylinder is embedded in a host with electric permittivity ε_h and magnetic permeability μ_h . (b) Schematic of the setup for the effective medium derivation for a system of infinite parallel cylinders as the one of (a) -see panel (c). In the effective medium setup the original coated cylinder is coated with an additional cylindrical layer made of the host material of the original system, with radius $R_{N+1} = R_N/\sqrt{f}$, where f is the cylinders filling ratio in the original system; the augmented cylinder is embedded in the homogeneous effective medium to be evaluated, with permittivity ε_{eff} and permeability μ_{eff} . (c) Three-dimensional view of a metamaterial formed as an array of coated cylinders as the one of (a).	55
6.2	(a) Real part (times 100) (left axis, blue line) and imaginary part (right axis, red line) of the sheet conductivity of a uniform graphene sheet modelled by RPA and Eq. (6.1), assuming Fermi level $E_F = 0.2$ eV and relaxation time $\tau = 1$ ps. (b) Normalized real (solid lines) and imaginary (dashed lines) parts of electric (s_e) and magnetic (s_m) sheet conductivities calculated using Eqs. (6.4)-(6.5), assuming parameters $\omega_e/2\pi = 21$ THz, $\Gamma_e/2\pi = \Gamma_m/2\pi = 2$ THz, $\kappa_e/2\pi = \kappa_m/2\pi = 1$ THz and $\omega_m/2\pi = 18$ THz; for the definition of those parameters see main text.	56

6.3	Extinction efficiencies, Q_{ext} , in (a) a single-layer graphene cylindrical tube in air with varying radius, R , and (b) a double-layered graphene cylinder in air with inner radius $R_1 = 45$ nm, and variable outer layer radii R_2 for TE polarization. All layers exhibit surface conductivity σ_g with Fermi level $E_F = 0.2$ eV and relaxation time $\tau = 1$ ps. All cylinder bulk (inter-surface) layers are made of air.	62
6.4	Resonance frequencies of first two modes, $\nu = 0$ and $\nu = 1$, per polarization, TE and TM, for: (a) a single-layered graphene cylinder versus its radius, R ; (b) a double-layered graphene cylinder for different outer-layer radii, R_2 and constant core radius $R_1 = 45$ nm; (c) a single-layered metasurface-formed cylinder of different radii, R ; (d) a double-layered metasurface cylinder with core radius $R_1 = 100$ nm and variable interlayer radii R_2 . The characteristic field distributions of the z component of the electric (magnetic) field for TM (TE) polarization for the $\nu = 0$ and $\nu = 1$ modes are shown in the insets of (c).	63
6.5	Extinction efficiencies, Q_{ext} , for: (a) and (b), a single-layered ($N = 1$) metasurface-formed cylinder of variable radius, R , for TE (a) and TM (b) polarization; (c) and (d), a double-layered ($N = 2$) metasurface cylinder with constant core radius $R_1 = 100$ nm and variable outer-layer radius, R_2 , for TE (c) and TM (d) polarization. The vertical dashed grey lines in the panels indicate the resonant frequencies of the metasurface magnetic and the electric conductivities at $f_m = 18$ THz and $f_e = 21$ THz, respectively. The symbols associated with each resonance are explained in the main text.	64
6.6	Zeroth-order scattering coefficients, a_0 , as a function of the magnetic surface conductivity resonance frequency f_m for (a) TE and (b) TM polarizations for a double-layered metasurface cylinder ($N = 2$) with core radius $R_1 = 100$ nm, inter-layer distance $R_2 = 150$ nm and constant electric surface conductivity resonance frequency $f_e = 21$ THz (dashed vertical line).	65
6.7	Real (top row) and imaginary (bottom row) parts of the parallel $\varepsilon_{\text{eff}}^{\parallel}$ (dashed curves) and perpendicular $\varepsilon_{\text{eff}}^{\perp}$ (solid curves) components of the relative effective permittivity ε_{eff} for: (a) and (c) a system made of single-layered ($N = 1$) graphene cylinders of variable radius, $R = 45$ nm (blue curves) and $R = 55$ nm (red curves) in air; (b) and (d) a system of double-layered ($N = 2$) graphene cylinders in air, with constant core radius $R_1 = 45$ nm, and for outer layer radii $R_2 = 70$ nm (green curves) and $R_2 = 90$ nm (purple curves); the cylinders filling ratio is in all cases equal to $f = 20\%$	66
6.8	(a) Extinction efficiency for TE polarization for a single-layered graphene cylinder with radius $R = 45$ nm in air, for different Fermi energies, E_F . (b) Real part of the in-plane component of effective electric permittivity $\varepsilon_{\text{eff}}^{\perp}$ for a system of single-layered graphene cylinders as the one of panel (a), in air, with cylinder filling ratio $f = 20\%$	67
6.9	Normal incidence, TE transmission spectra for a slab of triple-layered graphene cylinders with radii $R_1 = 45$ nm, $R_2 = 90$ nm and $R_3 = 135$ nm and filling ratio $f = 20\%$ in air, in a square arrangement. The transmission is calculated by the commercial finite element method electromagnetic solver Comsol Multiphysics, considering a computational system of 7 unit cell thickness (along the propagation direction). The full wave transmission results (red circles) are compared with results for a homogeneous effective medium of the same thickness as the actual system and effective parameters obtained through our CPA-based effective medium approach (black line).	68

6.10	Real (top row) and imaginary (bottom) parts of the tensor components of effective permittivity ε_{eff} (first column $\varepsilon_{\text{eff}}^{\parallel}$ and second column $\varepsilon_{\text{eff}}^{\perp}$) and effective permeability μ_{eff} (third column $\mu_{\text{eff}}^{\parallel}$ and fourth column μ_{eff}^{\perp}) for a system/metamaterial of single-layered ($N = 1$) metasurface-formed cylinders in air, for different radii, $R = 100$ nm (blue lines) and $R = 200$ nm (red lines), and filling ratio $f = 20\%$. The vertical dashed lines indicate the resonance frequencies of the magnetic ($f_m = 18$ THz) and electric sheet conductivity ($f_e = 21$ THz).	69
6.11	Real (top row) and imaginary (bottom) parts of the tensor components of effective permittivity ε_{eff} (first column $\varepsilon_{\text{eff}}^{\parallel}$, second column $\varepsilon_{\text{eff}}^{\perp}$) and effective permeability μ_{eff} (third column $\mu_{\text{eff}}^{\parallel}$, fourth column μ_{eff}^{\perp}) for a system/metamaterial of double-layered ($N = 2$) metasurface-formed cylinders in air, with core radius $R_1 = 100$ nm and for different outer-layer radii, $R_2 = 150$ nm (blue lines) and $R_2 = 250$ nm (red lines), and filling ratio $f = 20\%$. The vertical dashed lines indicate the resonance frequencies of the magnetic ($f_m = 18$ THz) and electric sheet conductivity ($f_e = 21$ THz).	70
6.12	TE (solid lines) and TM (dashed lines) extinction efficiencies for a double-layered metasurface-coated cylinder ($N=2$) with core radius $R_1 = 100$ nm and variable outer layer radii R_2 for metasurfaces with (a) magnetic surface conductivity σ_m with $f_m = 18$ THz and $\sigma_e = 0$, and (b) electric surface conductivity σ_e with $f_e = 21$ THz and $\sigma_m = 0$. The vertical dashed grey lines indicate the resonances of the sheet conductivities.	73
7.1	Unit cell of the inverse woodpile structure. (a) Bird's eye view of the tetragonal unit cell with two cylinders per lattice point, with lattice parameters c in the x -direction, a in the y -direction, and c in the z -direction. (b) View of the xy face of the unit cell, (c) of the yz face, and (d) of the xz face.	77
7.2	Band structures for an infinite inverse woodpile crystal made of silicon ($\varepsilon_b = 12.1$) with cylindrical pores filled with (a) air ($\varepsilon_p = 1.0$) and (b) toluene ($\varepsilon_p = 2.25$). The letters on the x -axes stand for the high symmetry points of the Brillouin zone shown in the inset. The blue and pink shaded bars indicate the 3D photonic band gap, from 0.511 to 0.658 in (a) and from 0.475 to 0.507 in (b).	78
7.3	(a) Schematic of the $V = N^3 = 3^3$ crystal (N : unit cells number per direction) from two different perspectives; left: (001) view, right: (100) view. The green line ($x = 0$, $y = 0$, z) connects the positions where the LDOS is probed. (b, c) Normalized LDOS as a function of position along the z -axis at the mid-gap frequency for a (b) silicon-air crystal ($\tilde{\omega}_{\text{mid}} = 0.58$) and (c) a toluene-air crystal ($\tilde{\omega}_{\text{mid}} = 0.49$) with size $N^3 = 3^3$. Blue circles are for x -dipoles, p_x , red up-pointing triangles for y -dipoles, p_y , and green right-pointing triangles for z -dipoles, p_z . The drawn curves are exponential models of the data [Eq. (7.3)], with colors matching the relevant dipole orientation. The extent of the crystal is indicated by vertical dashed lines.	80
7.4	Schematic of a dipole (green) and its radiation pattern inside a finite photonic crystal. (a) The far-field components are maximal in the equatorial plane, where stop bands affect the local density of states. (b) For a dipole at the center of a pore, the near-field component is enhanced by the nearby high-index medium when the dipole is orientated toward this medium. The near-field component is hardly enhanced when the dipole is oriented along the pore axis (x or z).	82

7.5	Schematic representation of the position vector $\mathbf{r}=(r_x, r_y, r_z)$ and the complex wavevector $\mathbf{k} = (k'_x + ik''_x, k'_y + ik''_y, k'_z + ik''_z)$ in the crystal under study, comprising of $N = 3$ unit cells. Inside the band gap where we calculate the LDOS the imaginary part of \mathbf{k} is nonzero. The position vector lies along the axis defined in each of the position dependence case studies in Fig. 7.3, Fig. 7.6 and Fig. 7.7.	83
7.6	(a) Schematic of the $V = N^3 = 3^3$ crystal (N : unit cells number per direction) from two different perspectives; left: (001) view, right: (100) view. The blue line ($x, y = 0, z = 0$) connecting the positions where the LDOS is probed seen from two different perspectives. (b) Normalized LDOS as a function of position along the x -axis at the mid-gap frequency ($\tilde{\omega}_{\text{mid}} = 0.58$) for a silicon-air crystal with size $N^3 = 3^3$. Blue circles are for x -dipoles, p_x , red triangles are for y -dipoles, p_y , blue-green right-pointing triangles are for z -dipoles, p_z . The lines passing through the data points are guides to the eye. The shaded areas are the silicon backbone. .	85
7.7	(a) Schematic of the $V = N^3 = 3^3$ crystal (N : unit cells number per direction) from two different perspectives, left: (001) view, right: (0 $\bar{1}$ 0) view. The black line ($x, y = 0, z = x$) connecting the positions where the LDOS is probed. (b) Normalized LDOS as a function of position along the xz -diagonal ($y = 0$) at the mid-gap frequency ($\tilde{\omega}_{\text{mid}} = 0.58$) for a silicon-air crystal with size $N^3 = 3^3$. Blue circles are for x -dipoles p_x , red triangles are for y -dipoles p_y , blue-green right-pointing triangles are for z -dipoles p_z . The lines passing through the data points are guides to the eye and the shaded areas are the silicon backbone.	86
7.8	(a) LDOS at the center of a sphere for three different resolutions (10 (blue-green squares), 20 (blue triangles), and 30 points per radius (red circles)) of the FDTD grid versus the analytical solution (black curve). (b) Difference between the FDTD calculated results and the analytical solution for three different resolutions: 10 grid points per radius (blue-green squares), 20 grid points per radius (blue triangles), and 30 grid points per radius (red circles)).	87

LIST OF TABLES

5.1	Lorentz model material parameters for LiF and SiC.	33
7.1	Parameters of Eq. (7.3) to model the normalized LDOS versus position along the z -direction shown in Fig. 7.3(b) and (c) for crystals with $N = 3$. Here, $\ell_\rho^{(i)}$ is the LDOS decay length and A_i is the amplitude prefactor. Parameters are given for silicon-air and for silicon-toluene crystals, and the rows are for dipoles oriented in the x , y , and z directions.	81
7.2	Table summarizing the discussion of the near and far field effects on the LDOS decay lengths $\ell_\rho^{(i)}$ and the prefactor A_i . The LDOS decay lengths are mainly affected by the far field and the band gaps in the directions of the radiation. The prefactors A_i are mainly affected by near field effects and by polarization effects due to presence of nearby high-index material.	83

ACKNOWLEDGEMENTS

This dissertation is the result of years of work that would not be possible without the support and encouragement from so many people.

First, I would like to express my deepest and sincerest my advisor, Prof. Maria Kafesaki. for her support, patience, inspiration and knowledge throughout all the years of my undergraduate and graduate studies. I really appreciate the opportunity to carry out my graduate studies under her guidance.

I would also like to thank Prof. Willem Vos for the incredible collaboration that we established and his patience the countless online meetings during most of my PhD.

Next I would like to thank all the members of the Photonic-, Phononic- and Metamaterials (PPM) group for their support and for the pleasant atmosphere that I experienced in the office during all the years of my studies. Especially, I would like to thank Dr. Anna Tasolamprou for the amazing collaboration, endless discussions, daily support and patience.

I would also want to express my gratitude to all the people, both from University of Crete, Foundation for Research and Technology -Hellas (FORTH) and abroad that I collaborated during my studies. I would like to thank the FORTH and the University of Crete and for the financial support throughout my studies.

Additionally, I would like to thank Prof. Stelios Tzortakis, Prof. Dimitris Papazoglou, Dr. George Kenanakis, Prof. Eleftherios Lidorikis and Prof. Ioannis Remediakis for their presence in my Ph.D. and the evaluation of this work.

Finally, my heartfelt gratitude goes to my beloved friends Despoina and Alexios, my sisters Sophia and Petroula and my parents Maria and Panagiotis. Without their presence, love, constant support, understanding and encouragement in tough and happy times, the completion of this thesis would not be possible.

CHAPTER 1

INTRODUCTION

Since ancient times people were fascinated by the interaction of matter and light. The first-known studies of optics date back to ancient Greece and Egypt, with characteristic examples being the studies by Euclid and Hero of Alexandria [1]. A famous example of practical application of light-matter interaction from the Roman period is the Lyncurgus' cup, which exhibits different colors when it is illuminated from outside with respect to its colors when it is illuminated from the inside. However, the physical mechanism behind this effect was not known before the seminal work by Michael Faraday, in the mid-19th century, who studied the optical response of colloidal solutions of small metallic particles [2].

In 1865, James Clerk Maxwell unified the work by Gauss, Faraday, Ampère and others into a unified framework, by demonstrating that light is an electromagnetic wave travelling with speed $c = 1/\sqrt{\epsilon_0\mu_0}$ in free space, where $\epsilon_0 = 8.854 \times 10^{-12} \text{ m}^{-3} \text{ kg}^{-1} \text{ s}^4 \text{ A}^2$ is the permittivity of free space and $\mu_0 = 1.257 \times 10^{-6} \text{ m kg s}^{-2} \text{ A}^{-2}$ is the magnetic permeability of free space (in SI units) [3]. Maxwell's work established the basis of classical electrodynamics that we know today, summarized in the following equations (known as *Maxwell equations*):

$$\nabla \cdot \mathbf{D} = \rho_e \quad (1.1)$$

$$\nabla \cdot \mathbf{B} = 0 \quad (1.2)$$

$$\nabla \times \mathbf{E} = -\frac{\partial \mathbf{B}}{\partial t} \quad (1.3)$$

$$\nabla \times \mathbf{H} = \mathbf{J}_e + \frac{\partial \mathbf{D}}{\partial t} \quad (1.4)$$

In the above equations ρ_e is the electric charge density of free charges, \mathbf{J}_e is the electric current density, \mathbf{E} is the total electric field and \mathbf{B} is the total magnetic field (known as magnetic induction), respectively. The fields \mathbf{D} and \mathbf{H} are auxiliary fields, with the \mathbf{D} known as displacement field and \mathbf{H} as magnetic field. Throughout this thesis we will assume linear response, that is, constitutive relations of the form $\mathbf{B} = \mu\mathbf{H}$ and $\mathbf{D} = \epsilon\mathbf{E}$, with ϵ and μ denoting the electric permittivity and magnetic permeability of the material, respectively. In general, to solve every problem in classical electrodynamics we need to solve Maxwell Equations [Eqs. (1.1)-(1.4)] in conjunction with models for the representation of the materials¹ (through ϵ and μ) and with appropriate boundary conditions.

The great advancements in the fabrication processes and nanotechnology during the 20th century led to the implementation of numerous, previously unattainable, applications involving electromagnetic wave propagation and control, e.g. in telecommunications, sensing, photovoltaics and others. This made a critical contribution to the emergence of *man-made* composite

¹Note that in the representation of the Maxwell's equations given by Eqs. (1.1)-(1.4), the free and the bound charges are separated; the free charges are represented by the current density $\mathbf{J}_e = \sigma\mathbf{E}$, with σ being the conductivity of the medium, while the permittivity is connected only with the bound charges. In a different representation \mathbf{J}_e, ρ_e are zero (if there are not any external to the system charges and currents) and the permittivity and conductivity represent both bound and free charges (which behave practically in the same way in high frequencies); in this case permittivity and conductivity are connected through the relation $\epsilon = \epsilon_0 + i\sigma/\omega$, with i being the imaginary unit and ω the angular frequency. In this work we use both the above mentioned representations of the Maxwell's equations, depending on the system studied.

structures which allow engineering of their properties through proper structuring, allowing thus the exploration of previously unexplored regimes and/or aspects of light-matter interaction. Characteristic examples of such structures are *Photonic Crystals*, *Metamaterials* and *Metasurfaces* (i.e. ultrathin metamaterial layers), which are the main systems investigated in the current work.

Photonic Crystals (PCs) are periodic structures with unit cell size comparable to the operation wavelength of light, which can offer frequency ranges where no electromagnetic states are allowed, in a similar manner to band gaps of electrons in semiconducting and dielectric materials [4]. These frequency ranges are called *photonic band gaps* [5]. Photonic crystals can be used, among others, as platforms for quantum optics and cavity quantum electrodynamics (cQED) applications like emission rate engineering [6], [7].

In contrast to photonic crystals, *metamaterials* and *metasurfaces* are comprised of units (commonly called *meta-atoms*) with characteristic size much smaller than their operation wavelength. By exploiting this fact, one can treat these structures as homogeneous media characterized by effective electric permittivity, effective magnetic permeability and, for the case of metasurfaces, with effective electric and magnetic sheet conductivities. Metamaterials and metasurfaces can allow, through proper structuring, permittivity and/or permeability values unachievable by natural materials; for example engineerable negative permittivity and/or permeability, negative refractive index, permittivity and permeability near zero, etc, offering thus very rich physics and unprecedented possibilities in a large variety of applications related with light-matter interaction (telecommunications, imaging, sensing, etc). The calculation of the effective materials parameters in such systems, which is crucial for the assessment of their response, can be done in the framework of *Effective Medium Theories*, which are simplified models that offer a simple physical description of the metamaterial response.

The large potential and the scientific and technological impact of photonic crystals and metamaterials/metasurfaces make the importance of development of analytical and computational tools for the solution and understanding of the wave interaction with such complex photonic structures even greater. For numerical analysis, depending on the application and the computational cost, one can choose one of the appropriate numerical methods for solving Maxwell equations for the exact system. Such numerical methods include Finite Difference Time Domain (FDTD) method, Finite Element Method (FEM), Boundary Element Method (BEM), Plane Wave Expansion (PWE) and others.

There are however structures which allow analytical or semi-analytical solutions, which greatly facilitates their understanding and their optimization towards specific properties or applications. The most straightforward solutions can be obtained for planar structures which are finite only in one direction. For two- or three-dimensional symmetrical structures, like cylinders and spheres, it is possible to find semi-analytical solutions of Maxwell equations by expanding the electromagnetic fields in different structure areas into elemental solutions of the wave equation, namely the cylindrical and spherical harmonics respectively. This approach is called *Mie theory* [8], [9] and it is the starting point for our calculations in Chapters 5 and 6. A method for the calculation of the fields in the above types of structures, if composed of multiple layers, is called *Transfer Matrix Method* [10] (TMM). Since, in principle, we can obtain semi-analytical expressions for all the quantities of interest, Mie theory in combination with the transfer matrix method can offer invaluable physical insight into, otherwise, complex structures comprising of many layers and different materials. We derive and employ the Transfer Matrix Method in Chapters 2, 3, 4 and 6 for the calculation of the scattering properties of planar and cylinders-based structures, including two-dimensional metamaterials and metasurfaces. In Fig. 1.1 we show schematics of the types of the systems that are studied in this thesis.

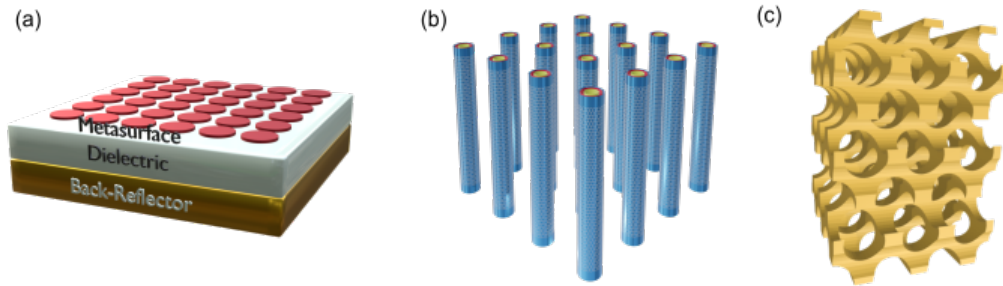


Figure 1.1: Types of photonic systems studied in this thesis: (a) A dielectric sandwiched between a thin resistive film (e.g. metal, graphene, metasurface) and a metallic back-reflector, (b) an array of infinitely-long cylinders and (c) an three-dimensional finite inverse woodpile photonic crystal.

1.1 Outline of this thesis

This thesis is organized as follows: In the first part (Chapters 2, 3 and 4) we study planar absorbers made of a dielectric sandwiched between a thin resistive film and a metallic back-reflector. This type of structure is referred also as a Salisbury screen. In Chapter 2 we derive the transfer matrix method for planar multi-layered structures incorporating two-dimensional (2D) materials (e.g. graphene) and/or metasurfaces at each of the interfaces; this is applied in the studies of the next two chapters. In Chapter 3 we consider structures for the optical part of the spectrum with the top resistive film being a thin metal film. On the other hand, in Chapter 4 the top resistive sheet is (a) a graphene layer and (b) a metasurface layer showing both electric and magnetic response.

In the second part of the thesis, Chapters 5 and 6, we turn our attention to the scattering response of cylindrical particles in the THz part of the spectrum. In Chapter 5 we employ Mie theory [8], [9] to derive analytical expressions for the scattering properties of single infinitely-long cylindrical particles and an effective medium model based on the well-known in the solid-state-physics community Coherent Potential Approximation [11]. Then, we apply our derivations to cylindrical particles made of polaritonic materials (i.e. materials with phonon-polariton resonances) in the THz part of the spectrum. In Chapter 6 we extend the formalism for the scattering properties and effective medium model used in Chapter 5 to multi-layer co-centric cylinders with arbitrary number of layers and with 2D materials or metasurfaces at each interface (between layers).

Last, but not least, in the third part of the thesis, Chapter 7, we turn our attention to photonic crystals. Specifically, we study the position dependence of the local density of states for emitters placed inside three-dimensional (3D) *finite* inverse woodpile photonic crystals. The study is done by employing the Finite Difference Time Domain (FDTD) method.

1.2 Publications in the context of this thesis

1. G. Kenanakis, C. P. Mavidis, E. Vasilaki, N. Katsarakis, M. Kafesaki, E. N. Economou, C. M. Soukoulis, *Perfect absorbers based on metal-insulator-metal structures in the visible region: a simple approach for practical applications*, Appl. Phys. A **123**, 77 (2017).
2. A. C. Tasolamprou, A. D. Koulouklidis, C. Daskalaki, C. P. Mavidis, G. Kenanakis, G. Deligeorgis, Z. Viskadourakis, P. Kuzhir, S. Tzortzakis, M. Kafesaki, E. N. Economou, and C. M. Soukoulis, *Experimental Demonstration of Ultrafast THz Modulation in a Graphene-Based Thin Film Absorber through Negative Photoinduced Conductivity*, ACS Photonics **6**, 720 (2019).

3. C. P. Mavdis, A. C. Tasolamprou, S. B. Hasan, T. Koschny, E. N. Economou, M. Kafesaki, C. M. Soukoulis, and W. L. Vos, *Local density of optical states in the three-dimensional band gap of a finite photonic crystal*, Phys. Rev. B **101**, 235309 (2020).
4. C. P. Mavdis, A. C. Tasolamprou, E. N. Economou, C. M. Soukoulis, and M. Kafesaki *Polaritonic cylinders as multifunctional metamaterials: Single scattering and effective medium description* Phys. Review B **102**, 155310 (2020).
5. C. P. Mavdis, A. C. Tasolamprou, E. N. Economou, C. M. Soukoulis, and M. Kafesaki *Single scattering and effective medium description for multi-coated and metasurface-coated cylinders* (in preparation).
6. C. P. Mavdis, A. C. Tasolamprou, E. N. Economou, C. M. Soukoulis, and M. Kafesaki *Perfect absorption conditions in metasurface-based perfect absorbers: A transfer matrix approach* (in preparation).

CHAPTER 2

TRANSFER MATRIX METHOD FOR PLANAR LAYERED STRUCTURES

2.1 Introduction

The transfer matrix method is one of the most convenient approaches to evaluate the fields and the scattering properties of layered systems [10], [12]. It relates the fields at one side of a layered system with the fields at the opposite side. In this chapter we derive the transfer matrix for planar layered structures, as the example system of Fig. 2.1(a). This derivation is the basis for the majority of our calculations in Chapters 3 and 4, where we will study planar perfect absorbers. We assume that each medium extends to infinity in two directions and it is only finite in the direction transverse to the media interfaces.

First we will find the transfer matrix for an interface between two media, i and j , with electric permittivities and magnetic permeabilities ε_i , μ_i and ε_j and μ_j . The geometry is shown in Fig. 2.1(b). We have chosen the z -axis to be perpendicular to the interface (and to all interfaces of the layered system). We also take into account electric and magnetic surface currents \mathbf{j}_e and \mathbf{j}_m at the interface of the two media. The surface currents offer us the possibility to effectively include 2D materials and/or metasurfaces in our calculations. Throughout this chapter we will assume a linear relation between the surface electric and magnetic currents and the corresponding electric and magnetic fields:

$$\mathbf{j}_e = \sigma_e \mathbf{E}_{av}|_{\text{surface}} \quad (2.1)$$

$$\mathbf{j}_m = \sigma_m \mathbf{H}_{av}|_{\text{surface}} \quad (2.2)$$

where \mathbf{E} and \mathbf{H} stand for the electric and magnetic field respectively, and σ_e and σ_m are the surface electric and magnetic conductivity, respectively. The surface currents are defined through the corresponding average fields at the interface in order to account for the discontinuities. We assume that at each medium there are forward-propagating electromagnetic fields ($\mathbf{E}^{(+)}$, $\mathbf{H}^{(+)}$) and backward-propagating fields ($\mathbf{E}^{(-)}$, $\mathbf{H}^{(-)}$), travelling towards the positive and negative z -axis respectively. At each medium the fields will have a planewave-form with frequency ω and wavevector $\mathbf{k} = k_x \hat{x} + k_z \hat{z}$:

$$\mathbf{E} = \mathbf{E}_0 e^{i(\mathbf{k} \cdot \mathbf{r} - \omega t)} \quad (2.3)$$

$$\mathbf{H} = \mathbf{H}_0 e^{i(\mathbf{k} \cdot \mathbf{r} - \omega t)} \quad (2.4)$$

At each interface we apply the appropriate boundary conditions for the electric and magnetic fields [13], [14]:

$$\hat{z} \times [\mathbf{E}_j - \mathbf{E}_i] = -\mathbf{j}_{m,j} = -\sigma_{m(j)} \frac{\mathbf{H}_i + \mathbf{H}_j}{2} \quad (2.5)$$

$$\hat{z} \times [\mathbf{H}_j - \mathbf{H}_i] = \mathbf{j}_{e,j} = \sigma_{e(j)} \frac{\mathbf{E}_i + \mathbf{E}_j}{2} \quad (2.6)$$

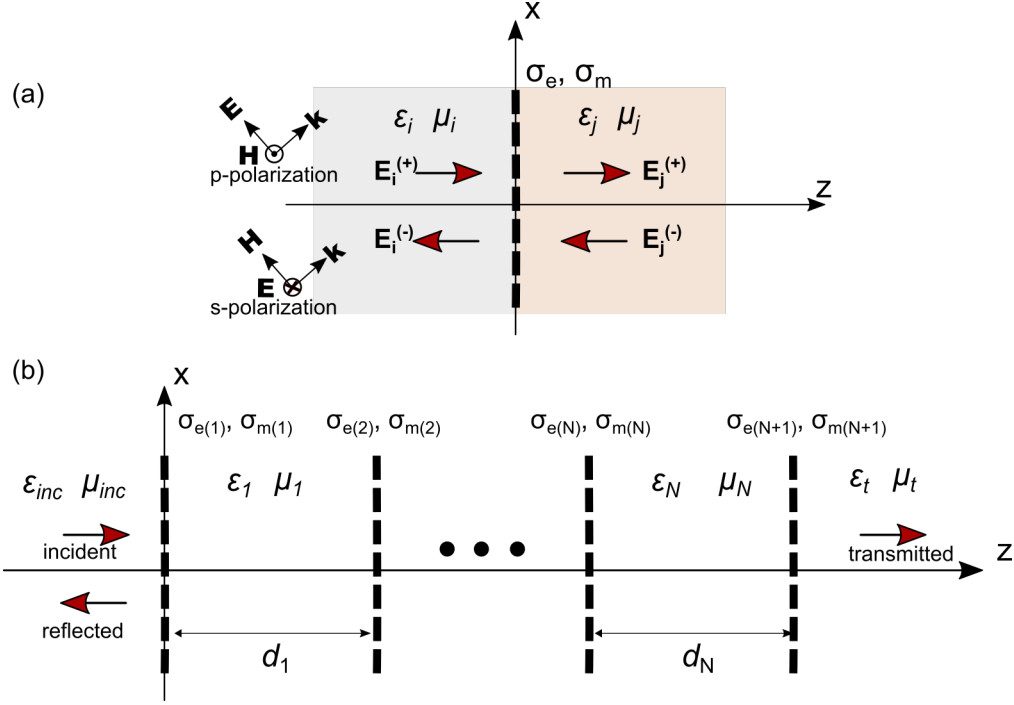


Figure 2.1: (a) Interface with surface conductivities σ_e and σ_m between two media i and j with electrical permittivities ϵ_i, ϵ_j , magnetic permeabilities μ_i, μ_j . (b) Layered structure consisting of N layers. We assume that a plane wave is incident from the left of the structure.

Due to the symmetry of the problem we splitted it into two problems: For (a) p -polarization, with fields $\mathbf{E} = E_x \hat{x} + E_z \hat{z}$, $\mathbf{H} = H_y \hat{y}$, and (b) s -polarization, with fields $\mathbf{E} = E_y \hat{y}$, $\mathbf{H} = H_x \hat{x} + H_z \hat{z}$, where \hat{x}, \hat{y} and \hat{z} are the unit vectors along the x, y and z axes respectively.

2.2 Transfer Matrix for p polarization

For p polarization the electric and magnetic fields have the form

$$\mathbf{E} = E_x \hat{x} + E_z \hat{z} \quad (2.7)$$

$$\mathbf{H} = H_y \hat{y} \quad (2.8)$$

Using these relations in the boundary conditions (2.5)-(2.6) we can write for the fields at the interface

$$\hat{z} \times [\mathbf{E}_j^{(+)} + \mathbf{E}_j^{(-)} - \mathbf{E}_i^{(+)} - \mathbf{E}_i^{(-)}] = -\frac{\sigma_{m(j)}}{2} [\mathbf{H}_j^{(+)} + \mathbf{H}_j^{(-)} + \mathbf{H}_i^{(+)} + \mathbf{H}_i^{(-)}] \quad (2.9)$$

$$\hat{z} \times [\mathbf{H}_j^{(+)} + \mathbf{H}_j^{(-)} - \mathbf{H}_i^{(+)} - \mathbf{H}_i^{(-)}] = \frac{\sigma_{e(j)}}{2} [\mathbf{E}_j^{(+)} + \mathbf{E}_j^{(-)} + \mathbf{E}_i^{(+)} + \mathbf{E}_i^{(-)}] \quad (2.10)$$

The relation between electric and magnetic fields in a semi-infinite medium with permittivity ϵ can be obtained from Ampere's law as

$$\nabla \times \mathbf{H} = -\frac{\partial \mathbf{D}}{\partial t} = -i\omega \epsilon \mathbf{E} \quad (2.11)$$

or

$$\mathbf{k} \times \mathbf{H} = \omega \epsilon \mathbf{E} \quad (2.12)$$

For a wave propagating towards the $\pm z$ axis with $\mathbf{k} = k_x \hat{x} \pm k_z \hat{z}$:

$$E_x^{(\pm)} = \pm \frac{k_z}{\omega \epsilon} H^{(\pm)} \quad (2.13)$$

Inserting Eq. (2.13) to Eq. (2.9) we get

$$\left[-\frac{k_{iz}}{\omega\varepsilon_i} + \frac{\sigma_{m(j)}}{2} \right] H_i^{(+)} + \left[\frac{k_{iz}}{\omega\varepsilon_i} + \frac{\sigma_{m(j)}}{2} \right] H_i^{(-)} = \left[-\frac{k_{jz}}{\omega\varepsilon_j} - \frac{\sigma_{m(j)}}{2} \right] H_j^{(+)} + \left[\frac{k_{jz}}{\omega\varepsilon_j} - \frac{\sigma_{m(j)}}{2} \right] H_j^{(-)} \quad (2.14)$$

Next, we insert Eq. (2.13) to Eq. (2.10):

$$\left[1 - \frac{k_{iz}\sigma_{e(j)}}{2\omega\varepsilon_i} \right] H_i^{(+)} + \left[1 + \frac{k_{iz}\sigma_{e(j)}}{2\omega\varepsilon_i} \right] H_i^{(-)} = \left[1 + \frac{k_{jz}\sigma_{e(j)}}{2\omega\varepsilon_j} \right] H_j^{(+)} + \left[1 - \frac{k_{jz}\sigma_{e(j)}}{2\omega\varepsilon_j} \right] H_j^{(-)} \quad (2.15)$$

Now we can write Eqs. (2.14) and (2.15) in matrix form as:

$$\begin{pmatrix} 1 - \frac{k_{iz}\sigma_{e(j)}}{2\omega\varepsilon_i} & 1 + \frac{k_{iz}\sigma_{e(j)}}{2\omega\varepsilon_i} \\ \frac{k_{iz}}{\omega\varepsilon_i} - \frac{\sigma_{m(j)}}{2} & -\frac{k_{iz}}{\omega\varepsilon_i} - \frac{\sigma_{m(j)}}{2} \end{pmatrix} \begin{pmatrix} H_i^{(+)} \\ H_i^{(-)} \end{pmatrix} = \begin{pmatrix} 1 + \frac{k_{jz}\sigma_{e(j)}}{\omega\varepsilon_j} & 1 - \frac{k_{jz}\sigma_{e(j)}}{2\omega\varepsilon_j} \\ \frac{k_{jz}}{\omega\varepsilon_j} + \frac{\sigma_{m(j)}}{2} & -\frac{k_{jz}}{2\omega\varepsilon_j} + \frac{\sigma_{m(j)}}{2} \end{pmatrix} \begin{pmatrix} H_j^{(+)} \\ H_j^{(-)} \end{pmatrix} \quad (2.16)$$

By multiplying with the inverse of the 2×2 matrix in the left-hand side of the equation above we will end up with the final relation for the transfer matrix:

$$\begin{pmatrix} H_i^{(+)} \\ H_i^{(-)} \end{pmatrix} = \mathbb{L}_{ij}^{(p)} \begin{pmatrix} H_j^{(+)} \\ H_j^{(-)} \end{pmatrix} \quad (2.17)$$

with the transfer matrix $\mathbb{L}_{ij}^{(p)}$ having the following elements:

$$\mathbb{L}_{ij}^{(p)(11)} = -\frac{(\zeta_{ji} + s_{m(ji)}) (s_{e(ji)} + 1) + (s_{m(ji)} + 1) (\zeta_{ji}s_{e(ji)} + 1)}{2 (s_{e(ji)}s_{m(ji)} - 1)} \quad (2.18)$$

$$\mathbb{L}_{ij}^{(p)(12)} = \frac{(\zeta_{ji} - s_{m(ji)}) (s_{e(ji)} + 1) + (s_{m(ji)} + 1) (\zeta_{ji}s_{e(ji)} - 1)}{2 (s_{e(ji)}s_{m(ji)} - 1)} \quad (2.19)$$

$$\mathbb{L}_{ij}^{(p)(21)} = \frac{-(\zeta_{ji} + s_{m(ji)}) (s_{e(ji)} - 1) + (s_{m(ji)} - 1) (\zeta_{ji}s_{e(ji)} + 1)}{2 (s_{e(ji)}s_{m(ji)} - 1)} \quad (2.20)$$

$$\mathbb{L}_{ij}^{(p)(22)} = \frac{(\zeta_{ji} - s_{m(ji)}) (s_{e(ji)} - 1) - (s_{m(ji)} - 1) (\zeta_{ji}s_{e(ji)} - 1)}{2 (s_{e(ji)}s_{m(ji)} - 1)} \quad (2.21)$$

where $\zeta_{ji} = \eta_j/\eta_i$ and $\eta_j = \eta_j^{(p)} = k_{jz}/\omega\varepsilon_j$, and normalized sheet conductivities as $s_{e(ji)} = \sigma_e\eta_i/2$, $s_{m(ji)} = \sigma_m(j)/2\eta_i$.

For a structure consisting of $N + 1$ interfaces separated by distances $\{d_1, d_2, \dots, d_N\}$, the total transfer matrix can be written as

$$\mathbb{L}_{\text{tot}} = \mathbb{L}_{01}\mathbb{P}_1(d_1)\mathbb{L}_{12}\mathbb{P}_2(d_2) \dots \mathbb{P}_N(d_N)\mathbb{L}_{N,N+1} \quad (2.22)$$

The subscripts 0 and $N + 1$ in Eq. (2.22) stand for the semi-infinite "superstrate" (left-layer of Fig. 2.1(b)) and the "substrate" (right-medium of Fig. 2.1(b)) of the structure. With $\mathbb{P}_i(d_i)$ we denote the propagation matrix which accounts for the propagation in the space between two interfaces and can be written as

$$\mathbb{P}_i(z) = \begin{pmatrix} e^{-ik_{iz}z} & 0 \\ 0 & e^{+ik_{iz}z} \end{pmatrix} \quad (2.23)$$

2.3 Transfer Matrix for s polarization

For s polarization the electric and magnetic fields will be

$$\mathbf{E} = E\hat{y} \quad (2.24)$$

$$\mathbf{H} = H_x\hat{x} + H_z\hat{z} \quad (2.25)$$

Starting from the boundary conditions given by Eqs. (2.9) and (2.10), we get for the fields at the interface (since $\hat{z} \times \hat{y} = -\hat{x}$):

$$E_j^{(+)} + E_j^{(-)} - E_i^{(+)} - E_i^{(-)} = \frac{\sigma_m(j)}{2} \left(H_{jx}^{(+)} + H_{jx}^{(-)} + H_{ix}^{(+)} + H_{ix}^{(-)} \right) \quad (2.26)$$

$$H_{jx}^{(+)} + H_{jx}^{(-)} - H_{ix}^{(+)} - H_{ix}^{(-)} = \frac{\sigma_e(j)}{2} \left(E_j^{(+)} + E_j^{(-)} + E_i^{(+)} + E_i^{(-)} \right) \quad (2.27)$$

From Faraday's law we can write:

$$\nabla \times \mathbf{E} = -\frac{\partial \mathbf{B}}{\partial t} = i\omega\mu\mathbf{H} \quad (2.28)$$

or

$$\mathbf{k} \times \mathbf{E} = \omega\mu\mathbf{H} \quad (2.29)$$

For a wave propagating towards the $\pm z$ axis with $\mathbf{k} = k_x \hat{x} \pm k_z \hat{z}$:

$$H_x^{(\pm)} = \mp \frac{k_z E^{(\pm)}}{\omega\mu} \quad (2.30)$$

Now we insert Eq. (2.30) into Eq. (2.26):

$$E_j^{(+)} - E_j^{(-)} - E_i^{(+)} - E_i^{(-)} = \frac{\sigma_m(j)}{2} \left[-\frac{k_{jz}}{\omega\mu_j} E_j^{(+)} + \frac{k_{jz}}{\omega\mu_j} E_j^{(-)} - \frac{k_{iz}}{\omega\mu_i} E_i^{(+)} + \frac{k_{iz}}{\omega\mu_i} E_i^{(-)} \right] \quad (2.31)$$

or

$$\left[1 - \frac{k_{iz}\sigma_m(j)}{2\omega\mu_i} \right] E_i^{(+)} + \left[1 + \frac{k_{iz}\sigma_m(j)}{2\omega\mu_i} \right] E_i^{(-)} = \left[1 + \frac{k_{jz}\sigma_m(j)}{2\omega\mu_j} \right] E_j^{(+)} + \left[1 - \frac{k_{jz}\sigma_m(j)}{2\omega\mu_j} \right] E_j^{(-)} \quad (2.32)$$

And finally from Eq. (2.27):

$$\left[\frac{k_{iz}}{\omega\mu_i} - \frac{\sigma_e(j)}{2} \right] E_i^{(+)} + \left[-\frac{k_{iz}}{\omega\mu_i} - \frac{\sigma_e(j)}{2} \right] E_i^{(-)} = \left[\frac{\sigma_e(j)}{2} + \frac{k_{jz}}{\omega\mu_j} \right] E_j^{(+)} + \left[\frac{\sigma_e(j)}{2} - \frac{k_{jz}}{\omega\mu_j} \right] E_j^{(-)} \quad (2.33)$$

We can now combine Eqs. (2.32)-(2.33) in matrix form as:

$$\begin{pmatrix} 1 - \frac{k_{iz}\sigma_m(j)}{\omega\mu_i} & 1 + \frac{k_{iz}\sigma_m(j)}{\omega\mu_i} \\ \frac{k_{iz}}{\omega\mu_i} - \frac{\sigma_e(j)}{2} & -\frac{k_{iz}}{\omega\mu_i} - \frac{\sigma_e(j)}{2} \end{pmatrix} \begin{pmatrix} E_i^{(+)} \\ E_i^{(-)} \end{pmatrix} = \begin{pmatrix} 1 + \frac{k_{jz}\sigma_m(j)}{2\omega\mu_j} & 1 - \frac{k_{jz}\sigma_m(j)}{2\omega\mu_j} \\ \frac{k_{jz}}{\omega\mu_j} + \frac{\sigma_e(j)}{2} & -\frac{k_{jz}}{\omega\mu_j} + \frac{\sigma_e(j)}{2} \end{pmatrix} \begin{pmatrix} E_j^{(+)} \\ E_j^{(-)} \end{pmatrix} \quad (2.34)$$

By multiplying with the inverse of the 2×2 matrix in the left-hand side of the equation above we will end up with the final relation for the transfer matrix:

$$\begin{pmatrix} E_i^{(+)} \\ E_i^{(-)} \end{pmatrix} = \mathbb{L}_{ij}^{(s)} \begin{pmatrix} E_j^{(+)} \\ E_j^{(-)} \end{pmatrix} \quad (2.35)$$

with

$$\mathbb{L}_{ij}^{(s)(11)} = -\frac{(\zeta_{ji} + s_{m(j)}) (s_{e(ji)} + 1) + (s_{m(ji)} + 1) (\zeta_{ji}s_{e(ji)} + 1)}{2\zeta_{ji} (s_{e(ji)}s_{m(ji)} - 1)} \quad (2.36)$$

$$\mathbb{L}_{ij}^{(s)(12)} = -\frac{(\zeta_{ji} - s_{m(j)}) (s_{e(ji)} + 1) + (s_{m(ji)} + 1) (\zeta_{ji}s_{e(ji)} - 1)}{2\zeta_{ji} (s_{e(ji)}s_{m(ji)} - 1)} \quad (2.37)$$

$$\mathbb{L}_{ij}^{(s)(21)} = \frac{(\zeta_{ji} + s_{m(j)}) (s_{e(ji)} - 1) - (s_{m(ji)} - 1) (\zeta_{ji}s_{e(ji)} + 1)}{2\zeta_{ji} (s_{e(ji)}s_{m(ji)} - 1)} \quad (2.38)$$

$$\mathbb{L}_{ij}^{(s)(22)} = \frac{(\zeta_{ji} - s_{m(j)}) (s_{e(ji)} - 1) - (s_{m(ji)} - 1) (\zeta_{ji}s_{e(ji)} - 1)}{2\zeta_{ji} (s_{e(ji)}s_{m(ji)} - 1)} \quad (2.39)$$

with $\eta_j^{(s)} = \omega\mu_j/k_{jz}$, $\zeta_{ji} = \eta_j/\eta_i$ and normalized sheet conductivities as $s_{e(ji)} = \sigma_e\eta_i/2$, $s_{m(ji)} = \sigma_m(j)/2\eta_i$.

2.4 Reflection and transmission coefficients

In this section we will derive the reflection and transmission coefficients, r and t , as well as the transmission efficiencies, R and T , for a multilayer planar structure (see Fig. 2.1(b)). Let us consider a structure with total transfer matrix \mathbb{L} connecting the fields at the left (incident and reflected) with the fields at the right structure side (transmitted). We assume that $F_{\text{inc}} + F_R = e^{ik_{iz}z} + re^{-ik_{iz}z}$ is the total field at the left and $F_T = te^{ik_{Tz}(z-\Delta)}$ is the field at the right side ($F = E$ for s polarization, $F = H$ for p polarization and Δ is the total thickness of the structure under consideration; we assume here that there is no incident wave coming from the right side of the structure). Using the transfer matrix formulation we can write

$$\begin{pmatrix} 1 \\ r \end{pmatrix} = \begin{pmatrix} \mathbb{L}^{(11)} & \mathbb{L}^{(12)} \\ \mathbb{L}^{(21)} & \mathbb{L}^{(22)} \end{pmatrix} \begin{pmatrix} t \\ 0 \end{pmatrix} \quad (2.40)$$

From Eq. (2.40) we can find the reflection and transmission coefficients as

$$r = \frac{\mathbb{L}^{(21)}}{\mathbb{L}^{(11)}} \quad (2.41)$$

$$t = \frac{1}{\mathbb{L}^{(11)}} \quad (2.42)$$

We can calculate the reflection and transmission efficiencies from the time-averaged Poynting vectors, \mathbf{S} in the direction of propagation as [15]

$$R = \frac{|\mathbf{S}_R \cdot \hat{z}|}{|\mathbf{S}_{\text{inc}} \cdot \hat{z}|} \quad (2.43)$$

$$T = \frac{|\mathbf{S}_T \cdot \hat{z}|}{|\mathbf{S}_{\text{inc}} \cdot \hat{z}|} \quad (2.44)$$

$$(2.45)$$

where

$$\mathbf{S}_{\text{inc}} = \frac{1}{2} \text{Re} [\mathbf{E}_{\text{inc}} \times \mathbf{H}_{\text{inc}}^*] \quad (2.46)$$

$$\mathbf{S}_R = \frac{1}{2} \text{Re} [\mathbf{E}_R \times \mathbf{H}_R^*] \quad (2.47)$$

$$\mathbf{S}_T = \frac{1}{2} \text{Re} [\mathbf{E}_T \times \mathbf{H}_T^*] \quad (2.48)$$

and the subscripts inc (or i), R , T indicate the incident, reflected and transmitted waves respectively. For s-polarization and using Eq. (2.30) we get

$$\mathbf{S}_{\text{inc}} \cdot \hat{z} = \frac{1}{2} \text{Re} \left[\frac{k_{iz}}{\omega \mu_i} \right] \quad (2.49)$$

$$\mathbf{S}_R \cdot \hat{z} = -\frac{1}{2} \text{Re} \left[\frac{k_{iz}}{\omega \mu_i} \right] |r^{(s)}|^2 \quad (2.50)$$

$$\mathbf{S}_T \cdot \hat{z} = \frac{1}{2} \text{Re} \left[\frac{k_{Tz}}{\omega \mu_T} \right] |t^{(s)}|^2 \quad (2.51)$$

Therefore,

$$T^{(s)} = \frac{\text{Re} \left[\frac{k_{Tz}}{\mu_T} \right]}{\text{Re} \left[\frac{k_{iz}}{\mu_i} \right]} |t^{(s)}|^2 \quad (2.52)$$

$$R^{(s)} = |r^{(s)}|^2 \quad (2.53)$$

In a similar fashion, for p-polarization we will have

$$T^{(p)} = \frac{\operatorname{Re} \left[\frac{k_{Tz}}{\varepsilon_T} \right]}{\operatorname{Re} \left[\frac{k_{iz}}{\varepsilon_i} \right]} |t^{(p)}|^2 \quad (2.54)$$

$$R^{(p)} = |r^{(p)}|^2 \quad (2.55)$$

2.5 Specific cases

Here we apply the formulas of the previous sections to particular cases/interfaces of interest in the study of photonic systems.

2.5.1 Interface between two semi-infinite media

We start from the simple case of an interface between two semi-infinite media with permittivities $\varepsilon_i, \varepsilon_j$ and permeabilities μ_i, μ_j . Also, there is no surface current at the interface, i.e., $\sigma_e = 0, \sigma_m = 0$. We assume an incident plane wave that is travelling from the left of the structure. In this case the transfer matrix for p polarization will be:

$$\mathbb{L}_{ij}^{(p)(11)} = \frac{\eta_i^{(p)} + \eta_j^{(p)}}{2\eta_i^{(p)}} \quad (2.56)$$

$$\mathbb{L}_{ij}^{(p)(12)} = \frac{\eta_i^{(p)} - \eta_j^{(p)}}{2\eta_i^{(p)}} \quad (2.57)$$

$$\mathbb{L}_{ij}^{(p)(21)} = \frac{\eta_i^{(p)} - \eta_j^{(p)}}{2\eta_i^{(p)}} \quad (2.58)$$

$$\mathbb{L}_{ij}^{(p)(22)} = \frac{\eta_i^{(p)} + \eta_j^{(p)}}{2\eta_i^{(p)}} \quad (2.59)$$

Therefore, the transmission and reflection coefficients will be:

$$t^{(p)} = \frac{2\eta_i^{(p)}}{\eta_i^{(p)} + \eta_j^{(p)}} \quad (2.60)$$

$$r^{(p)} = \frac{\eta_i^{(p)} - \eta_j^{(p)}}{\eta_i^{(p)} + \eta_j^{(p)}} \quad (2.61)$$

For s polarization:

$$\mathbb{L}_{ij}^{(s)(11)} = \frac{\eta_i^{(s)} + \eta_j^{(s)}}{2\eta_j^{(s)}} \quad (2.62)$$

$$\mathbb{L}_{ij}^{(s)(12)} = \frac{-\eta_i^{(s)} + \eta_j^{(s)}}{2\eta_j^{(s)}} \quad (2.63)$$

$$\mathbb{L}_{ij}^{(s)(21)} = \frac{-\eta_i^{(s)} + \eta_j^{(s)}}{2\eta_j^{(s)}} \quad (2.64)$$

$$\mathbb{L}_{ij}^{(s)(22)} = \frac{\eta_i^{(s)} + \eta_j^{(s)}}{2\eta_j^{(s)}} \quad (2.65)$$

And the transmission and reflection coefficients:

$$t^{(s)} = \frac{2\eta_j^{(s)}}{\eta_i + \eta_j} \quad (2.66)$$

$$r^{(s)} = \frac{-\eta_i^{(s)} + \eta_j^{(s)}}{\eta_i^{(s)} + \eta_j^{(s)}} \quad (2.67)$$

2.5.2 Electric surface current at the interface between two semi-infinite media

Here we consider an interface with electric sheet conductivity σ_e between two semi-infinite media i and j . We obtain

$$\mathbb{L}_{ij}^{(p)(11)} = \frac{\eta_i^{(p)} \eta_j^{(p)} \sigma_e + \eta_i^{(p)} + \eta_j^{(p)}}{2\eta_i^{(p)}} \quad (2.68)$$

$$\mathbb{L}_{ij}^{(p)(12)} = \frac{-\eta_i^{(p)} \eta_j^{(p)} \sigma_e + \eta_i^{(p)} - \eta_j^{(p)}}{2\eta_i^{(p)}} \quad (2.69)$$

$$\mathbb{L}_{ij}^{(p)(21)} = \frac{\eta_i^{(p)} \eta_j^{(p)} \sigma_e + \eta_i^{(p)} - \eta_j^{(p)}}{2\eta_i^{(p)}} \quad (2.70)$$

$$\mathbb{L}_{ij}^{(p)(22)} = \frac{-\eta_i^{(p)} \eta_j^{(p)} \sigma_e + \eta_i^{(p)} + \eta_j^{(p)}}{2\eta_i^{(p)}} \quad (2.71)$$

If the conductive sheet is in a homogeneous medium ($\varepsilon_i = \varepsilon_j$ and $\mu_i = \mu_j$) the transmission and reflection coefficients will be:

$$t^{(p)} = \frac{2}{\eta_i^{(p)} \sigma_e + 2} \quad (2.72)$$

$$r^{(p)} = \left(1 + \frac{2}{\eta_i^{(p)} \sigma_e} \right)^{-1} \quad (2.73)$$

And for s polarization:

$$t^{(s)} = \frac{2}{\eta_i^{(s)} \sigma_e + 2} \quad (2.74)$$

$$r^{(s)} = - \left(1 + \frac{2}{\eta_i^{(s)} \sigma_e} \right)^{-1} \quad (2.75)$$

2.5.3 Electric and magnetic current sheet in a homogeneous medium

Finally we write here the reflection and transmission coefficients of a sheet with both electric and magnetic surface currents in a homogeneous medium ($\varepsilon_i = \varepsilon_j$ and $\mu_i = \mu_j$). The transfer matrix elements will be:

$$\mathbb{L}_{ij}^{(p)(11)} = \frac{-2\eta_i^{(p)2}\sigma_e - \eta_i^{(p)}\sigma_e\sigma_m - 4\eta_i^{(p)} - 2\sigma_m}{\eta_i^{(p)}(\sigma_e\sigma_m - 4)} \quad (2.76)$$

$$\mathbb{L}_{ij}^{(p)(12)} = \frac{2\eta_i^{(p)2}\sigma_e - 2\sigma_m}{\eta_i^{(p)}(\sigma_e\sigma_m - 4)} \quad (2.77)$$

$$\mathbb{L}_{ij}^{(p)(21)} = \frac{-2\eta_i^{(p)}\sigma_e + 2\sigma_m}{\eta_i^{(p)}(\sigma_e\sigma_m - 4)} \quad (2.78)$$

$$\mathbb{L}_{ij}^{(p)(22)} = \frac{2\eta_i^{(p)2}\sigma_e - \eta_i^{(p)}\sigma_e\sigma_m - 4\eta_i^{(p)} + 2\sigma_m}{\eta_i^{(p)}(\sigma_e\sigma_m - 4)} \quad (2.79)$$

And the transmission and reflection coefficients will be:

$$t^{(p)} = \frac{4 - \sigma_e\sigma_m}{4 + 2\eta_i^{(p)}\sigma_e + \sigma_e\sigma_m + 2[\eta_i^{(p)}]^{-1}\sigma_m} \quad (2.80)$$

$$r^{(p)} = \frac{2\left(\eta_i^{(p)}\sigma_e - [\eta_i^{(p)}]^{-1}\sigma_m\right)}{4 + 2\eta_i^{(p)}\sigma_e + \sigma_e\sigma_m + 2[\eta_i^{(p)}]^{-1}\sigma_m} \quad (2.81)$$

These results are consistent with the derivations in Ref. [14], [16], [17]. Also, for s polarization, the transfer matrix elements are:

$$\mathbb{L}_{ij}^{(s)(11)} = \frac{-2\left(\eta_i^{(s)}\right)^2\sigma_e - \eta_i^{(s)}\sigma_e\sigma_m - 4\eta_i^{(s)} - 2\sigma_m}{\eta_i^{(s)}(\sigma_e\sigma_m - 4)} \quad (2.82)$$

$$\mathbb{L}_{ij}^{(p)(12)} = \frac{-2\left(\eta_i^{(s)}\right)^2\sigma_e + 2\sigma_m}{\eta_i^{(s)}(\sigma_e\sigma_m - 4)} \quad (2.83)$$

$$\mathbb{L}_{ij}^{(p)(21)} = \frac{2\left(\eta_i^{(s)}\right)^2\sigma_e - 2\sigma_m}{\eta_i^{(s)}(\sigma_e\sigma_m - 4)} \quad (2.84)$$

$$\mathbb{L}_{ij}^{(p)(22)} = \frac{2\left(\eta_i^{(s)}\right)^2\sigma_e - \eta_i^{(s)}\sigma_e\sigma_m - 4\eta_i^{(s)} + 2\sigma_m}{\eta_i^{(s)}(\sigma_e\sigma_m - 4)} \quad (2.85)$$

and the transmission and reflection coefficients:

$$t^{(s)} = \frac{4 - \sigma_e\sigma_m}{2\eta_i^{(s)}\sigma_e + \sigma_e\sigma_m + 4 + 2\sigma_m\left[\eta_i^{(s)}\right]^{-1}} \quad (2.86)$$

$$r^{(s)} = \frac{-2\eta_i^{(s)}\sigma_e + 2\left[\eta_i^{(s)}\right]^{-1}\sigma_m}{2\eta_i^{(s)}\sigma_e + \sigma_e\sigma_m + 4 + 2\left[\eta_i^{(s)}\right]^{-1}\sigma_m} \quad (2.87)$$

2.6 The pyTransferMatrix package

In this Section we introduce the basic functionality of our transfer matrix package in Python which is based on the formalism developed in the previous sections of this chapter. The

package is under an open-source license and can be found on <https://github.com/mahar/pyTransferMatrix>. The core class of the Transfer Matrix package is called `TransferMatrix` and takes as arguments a list of the layers that comprise the layered structure.

```
system = tma.TransferMatrix(structure, frequency)
```

A layer is defined by calling the `Layer` class.

```
layer = tma.Layer(eps, mu, sigma_e, sigma_m, thickness, kz, frequency, name="")
```

where `eps` is the relative electrical permittivity, `mu` is the relative magnetic permeability and `sigmae`, `sigmam` are the electric and magnetic conductivities at the interface. Also, `thickness` is the layer thickness in meters, `kz` is the transverse component of the wavevector (see Fig. 2.1) and `frequency` is the angular frequency. Below we provide an example of application of our code for the calculation of reflection and transmission spectra for a one-dimensional photonic crystal cavity [18].

2.6.1 Example: One-dimensional photonic crystal cavity

As a demonstration of the transfer matrix code we will calculate the reflection and transmission of a one-dimensional Bragg stack cavity, consisting of a defect between two identical Bragg mirrors (1D-photonic-crystals) of 10 unit cells each. The unit cell of the photonic crystals considered is composed of a slab with thickness $a_1 = 86$ nm and refractive index $n_1 = \sqrt{\epsilon_1} = 2.9$ and a slab with thickness $a_2 = 70$ nm and refractive index $n_2 = \sqrt{\epsilon_2} = 3.57$. These values of refractive indices correspond to AlAs and GaAs around $\lambda = 1000$ nm. In the absence of any defects this structure will exhibit a stop-gap, not allowing any electromagnetic wave to pass through the structure. If we introduce a defect to the structure, a state will be created inside the photonic band-gap. In this example we consider a defect with thickness $d = 4a_1$ sandwiched between 10 unit cells of the photonic crystal on each side. We assume that the whole structure is placed in air ($n_0 = 1$). The total transfer matrix can be written as:

$$\mathbb{L}_{\text{total}} = \mathbb{L}_{\text{air},1} \mathbb{P}_1(a_1) \mathbb{L}_{12} \mathbb{P}_2(a_2) \mathbb{L}_{21} \dots \mathbb{L}_{21} \cdot \mathbb{P}_1(4a_1) \mathbb{L}_{21} \mathbb{P}_1(a_1) \dots \mathbb{L}_{1,\text{air}} \quad (2.88)$$

The reflection and transmission spectra for normal incidence and $N = 10$ (on each side of the cavity) are plotted in Fig. 2.2 along with a schematic of the structure. As one can see there is a peak at normalized frequency $a/\lambda = 0.156$ where $a = a_1 + a_2$ is the lattice constant of the photonic crystal.

```
1 import numpy as np
2 from scipy import constants
3 import transfermatrix as tma
4
5 # Materials and Lattice constants
6 eps1 = 2.9**2 # AlAs
7 mu1 = 1.0
8 eps2 = 3.57**2 # GaAs
9 mu2 = 1.0
10 a1 = 86e-9
11 a2 = 70e-9
12 N = 10 # Number of Unit cells at each side of the defect
13
14 # 1000 values of Wavelength from 600nm to 1000nm
15 wls = np.linspace(600,1400,1000)*1e-9 # wavelength
16 rad_freqs = 2*np.pi*constants.c/wls # angular frequency
17
18 # Initialize Arrays for reflection R and transmission T
19 # zeros_like(A) creates an array of zeros with the same shape as array A
20 R = np.zeros_like(rad_freqs)
21 T = np.zeros_like(rad_freqs)
```

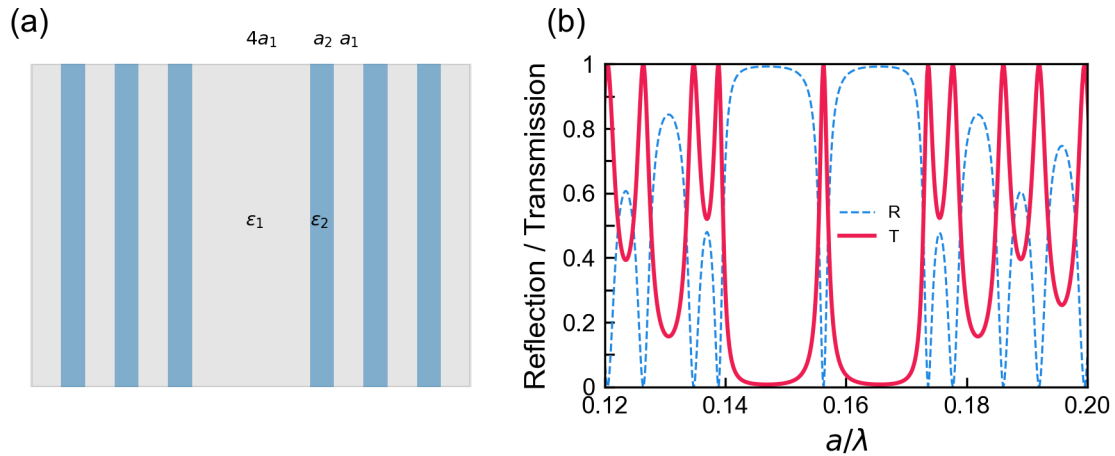


Figure 2.2: (a) A defect of thickness $4a_1$ between two photonic crystals with N unit cells each. (b) Reflection and transmission spectra for $N = 10$ unit cells of a photonic crystal of unit cell consisting of a slab with thickness $a_1 = 86$ nm and refractive index $n_1 = \sqrt{\epsilon_1} = 2.9$ and a slab with thickness $a_2 = 70$ nm and refractive index $n_2 = \sqrt{\epsilon_2} = 3.57$.

```

22
23 for wi, w in enumerate(rad_freqs):
24     kinc = w/constants.c
25     kz_air = kinc
26     kz1 = kinc*np.sqrt(eps1*mu1)
27     kz2 = kinc*np.sqrt(eps2*mu2)
28
29     air_superstrate = tma.SeminfiniteLayer(1,kz_air,w,name="Air superstrate")
30     air_substrate = tma.SeminfiniteLayer(1,kz_air,w,name="Air substrate")
31
32     top_pc = []
33     bottom_pc = []
34
35     for i in range(N):
36         top_pc.append(tma.Layer(eps1,mu1,0,0,a1,kz1,w, name=""))
37         top_pc.append(tma.Layer(eps2,mu2,0,0,a2,kz2,w, name=""))
38
39         bottom_pc.append(tma.Layer(eps2,mu2,0,0,a2,kz2,w, name=""))
40         bottom_pc.append(tma.Layer(eps1,mu1,0,0,a1,kz1,w, name=""))
41     # -----
42     # cavity layer
43     d_cavity = 4*a1
44     cavity_layer = tma.Layer(eps1,mu1,0,0,d_cavity,kz1,w, name="")
45
46     # Concatenate the lists
47     structure = [air_superstrate]+top_pc+[cavity_layer]+ bottom_pc+[
48         air_substrate]
49
50     # Setup the calculation
51     system = tma.TransferMatrix(structure,freqs=[w])
52     system.calculate()
53
54     R[wi] = np.abs(system.rs)**2
55     T[wi] = np.abs(system.ts)**2

```

Listing 2.1: Reflection and transmission calculation for one dimensional photonic crystal cavity.

CHAPTER 3

METAL-INSULATOR-METAL BASED PERFECT ABSORBERS

3.1 Introduction

During the last decades, perfect absorbers have been widely investigated for many applications [19]–[21], including photovoltaics [22], [23], thermal imaging [24] and electromagnetic shielding [21]. Also, perfect absorbers can be designed for either narrowband or broadband applications in the wavelength range of interest. Mechanisms that can be utilized for the design of perfect absorbers include destructive interference of the scattered electromagnetic waves with the incident wave [20], [25], [26] by the device and impedance matching between free space and a lossy medium [27], [28]. One of the simplest realizations of a perfect absorber is a planar structure consisting of a lossy dielectric layer between a thin metallic film and a optically thick metallic substrate which acts as a back-reflector. This type of structures is often referred in the literature as a *Metal-Insulator-Metal* (MIM) absorber [26], [29]. The MIM absorber can be viewed as an asymmetric Fabry-Pérot cavity with the incident wave being coupled to the modes of this structure, which originate from the multiple reflections of the electromagnetic waves trapped into the dielectric and between the two metallic layers. Assuming that there is loss present in the structure, perfect absorption in this case is a result of the destructive interference of the reflected and the incident electromagnetic waves. We will examine this mechanism further in Section 3.2). The main advantages of the simple MIM-based structures over more complicated structures, which may include patterned layers, is the simplicity and the low cost of fabrication, since it does not require any lithography (such as electron-beam lithography or nanoimprint lithography) steps, and that they can be readily fabricated over large areas.

In this chapter we discuss the design of a simple MIM absorber operating in the visible range, and we demonstrate and analyze the absorber performance and its extensions towards broadband response. Our absorber was also fabricated and characterized experimentally (by experimental colleagues), and its electromagnetic characterization results are in very good agreement with our theoretical data, verifying the validity of our study and results.

The chapter is organized as follows: In Section 3.2 we introduce the proposed MIM structure and derive the conditions for perfect absorption, and in Section 3.3 we present our results for MIM absorbers consisting of a single-, double- and five stacks of metal-dielectric layers on top of the metallic substrate. Finally, in Section 3.4 we summarize our results.

3.2 Structure and theoretical model

The basic Metal-Insulator-Metal (MIM) structure that we study here consists of two metallic gold layers, with permittivity ϵ_{Au} , separated by a TiO_2 dielectric slab, of permittivity ϵ_{TiO_2} and thickness d_{TiO_2} , with the bottom metallic layer being electrically thick in order to not allow transmission through the structure at the wavelengths of interest. The top metallic film has thickness d_{Au} . The structure is shown in Fig. 3.1.

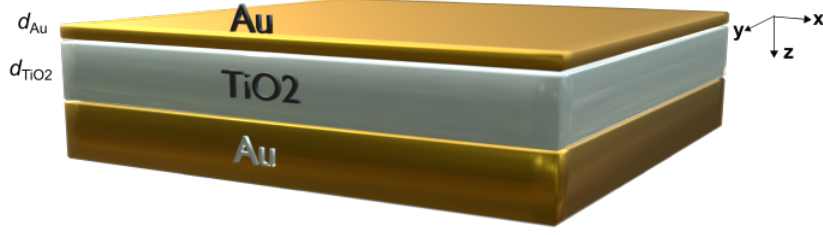


Figure 3.1: The Metal-Insulator-Metal (MIM)-based absorber structure under investigation. A lossy dielectric layer of thickness d_{TiO_2} is sandwiched between a thin metallic film with thickness d_{Au} and an optically thick metallic substrate.

To calculate the absorption of this structure we employ the transfer matrix method that we introduced in Chapter 2. To simplify our analysis we assume that the metallic substrate is semi-infinite. This is justified by the requirement of zero transmission through the structure. The same result can be obtained if we take a thick-enough metallic substrate, considering the fact that the skin depth of metals like gold is smaller than $0.1\lambda_0$ at the visible part of the spectrum [30], where λ_0 is the free-space wavelength.

The total transfer matrix of this structure is given as matrix product of the transfer matrices at each interface, \mathbb{L}_{ij} , and the propagation matrices $\mathbb{P}_j(d_j)$ as defined in Chapter 2. To simplify and generalize our notation we will use the following convention for the subscripts of different areas in our structure: {1: air, 2: thin-metallic film, 3: dielectric, 4: metallic substrate}.

$$\mathbb{L}_{\text{tot}} = \mathbb{L}_{12} \cdot \mathbb{P}_2(d_2) \cdot \mathbb{L}_{23} \cdot \mathbb{P}_3(d_3) \cdot \mathbb{L}_{34} \quad (3.1)$$

Since the transmission coefficient is zero, $t = 0$, the absorption is equal to $A = 1 - |r|^2$ with r being the reflection coefficient $r = \mathbb{L}_{\text{tot}}^{(21)} / \mathbb{L}_{\text{tot}}^{(11)}$. From this expression we can derive a condition for perfect absorption by requiring the reflection coefficient to vanish, $r = 0$ [26], or

$$\mathbb{L}_{\text{tot}}^{(21)} = 0 \quad (3.2)$$

or

$$i \tan(k_{2z}d_2) = \frac{iF_+ \tan(k_{3z}d_3) + G_+}{iF_- \tan(k_{3z}d_3) + G_-} \quad (3.3)$$

where

$$F_{\pm} = \mathbb{L}_{12}^{(21)} \left[\mathbb{L}_{23}^{(11)} \mathbb{L}_{34}^{(12)} + \mathbb{L}_{23}^{(12)} \mathbb{L}_{34}^{(22)} \right] \pm \mathbb{L}_{12}^{(22)} \left[\mathbb{L}_{23}^{(21)} \mathbb{L}_{34}^{(12)} + \mathbb{L}_{23}^{(22)} \mathbb{L}_{34}^{(22)} \right] \quad (3.4)$$

$$G_{\pm} = \mathbb{L}_{12}^{(21)} \left[-\mathbb{L}_{23}^{(11)} \mathbb{L}_{34}^{(12)} + \mathbb{L}_{23}^{(12)} \mathbb{L}_{34}^{(22)} \right] \pm \mathbb{L}_{12}^{(22)} \left[\mathbb{L}_{23}^{(22)} \mathbb{L}_{34}^{(22)} - \mathbb{L}_{23}^{(21)} \mathbb{L}_{34}^{(12)} \right] \quad (3.5)$$

Eq. (3.3) is general and can be applied for any materials, surface conductivities and angles of incidence for the geometry shown in Fig. 3.1. In the case of the MIM absorber that we study here we have $\varepsilon_2 = \varepsilon_4 = \varepsilon_{\text{Au}}$ and $\varepsilon_3 = \varepsilon_{\text{TiO}_2}$, $\mu = \mu_0$ and $\sigma_e = 0$, $\sigma_m = 0$. Eq. (3.3) can be further simplified [26]

$$\tanh(|k_2|d_2) = \frac{1}{2} \frac{\sqrt{\frac{|\varepsilon_2|}{\varepsilon_3}} \tan(k_3d_3) + 1}{\sqrt{\frac{\varepsilon_3}{|\varepsilon_2|}} \tan(k_3d_3) - 1} \quad (3.6)$$

The thickness of the top metallic layer has been set to $d_2 = d_{\text{Au}} = 20$ nm. For our calculations we used experimental data for the permittivities of Au (Johnson and Christy [31])

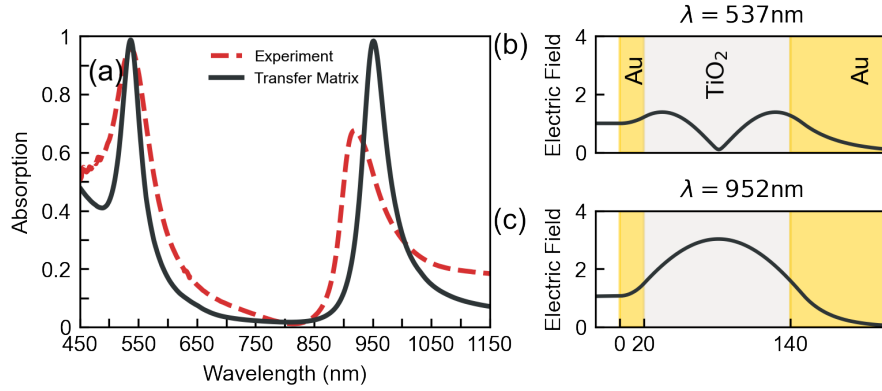


Figure 3.2: (a) Experimental (dashed red line) and theoretical (black solid line) absorption spectra for normal incidence on our Metal-Insulator-Metal Structure with a $d_{\text{TiO}_2} = 120\text{ nm}$ TiO₂ dielectric layer between two metallic gold films and $d_{\text{Au}} = 20\text{ nm}$ and 120 nm respectively. (b), (c) Electric field amplitudes at the absorption maxima: (b) 537 nm and (c) 952 nm. The colors indicate the extent of the different materials (Au: yellow, TiO₂: gray, Air: white).

and TiO₂ (with relative permittivity between 10 and 7 in the wavelength range 450 nm-1250 nm) (Palik [32]). As mentioned already, one of the main advantages of these type of structures is their ease of fabrication using lithography-free approaches like sol-gel/spin coating for the dielectric layer and thermal evaporation for the metallic layer [33].

3.3 Results and discussion

The absorption for normal incidence of the MIM structure shown in Fig. 3.1, calculated with the transfer matrix method, is shown in Fig. 3.2(a). Here, the thickness of the top Au layer was chosen to be 20 nm while thickness of the TiO₂ layer is 120 nm. Since there is no transmission from the structure, the Au substrate is treated as a semi-infinite layer in our calculations. As one can see, there are two peaks in the absorption spectrum, at wavelengths 537 nm and 956 nm, originating from the Fabry-Pérot resonances on the MIM structure. The field profiles are shown in Figs. 3.2(b)-(c) for the two absorption peaks. We also plot an experimental measurement of the absorption for the proposed MIM structure, in Fig. 3.2(a) (red dashed line). There is a very good agreement between the theoretical and experimental calculations and any differences can be attributed to imperfections of the fabricated structure (e.g. non uniform metal and/or dielectric layer thickness throughout the structure).

The main advantage of the proposed MIM structure is that one can tune the absorption peaks by changing the thickness of the TiO₂ dielectric spacer. For example, Fig. 3.3(a) illustrates the thickness of the dielectric spacer needed in order to get absorption peaks higher than 90%. One can notice the shift of the absorption peaks to longer wavelengths, as the TiO₂ spacer increases [26]. However, the two peaks behave differently as the thickness of the TiO₂ spacer increases. The peak at smaller wavelengths has a maximum in absorption at a wavelength around $\lambda = 550\text{ nm}$, and the absorption has not monotonic change with the thickness, while for the second peak (larger wavelengths) the absorption increases with increasing thickness. Finally, the Full Width at Half Maximum (FWHM) of the absorption peaks can be tuned by changing the dielectric thickness, and adapted to the desired application. Fig. 3.3(b) illustrates the FWHM of the absorption peaks (with absorption higher than 90%), varying from 10 to 100 nm. For example, one can notice from Fig. 3.3(b) that the absorption peak centered at 537 nm

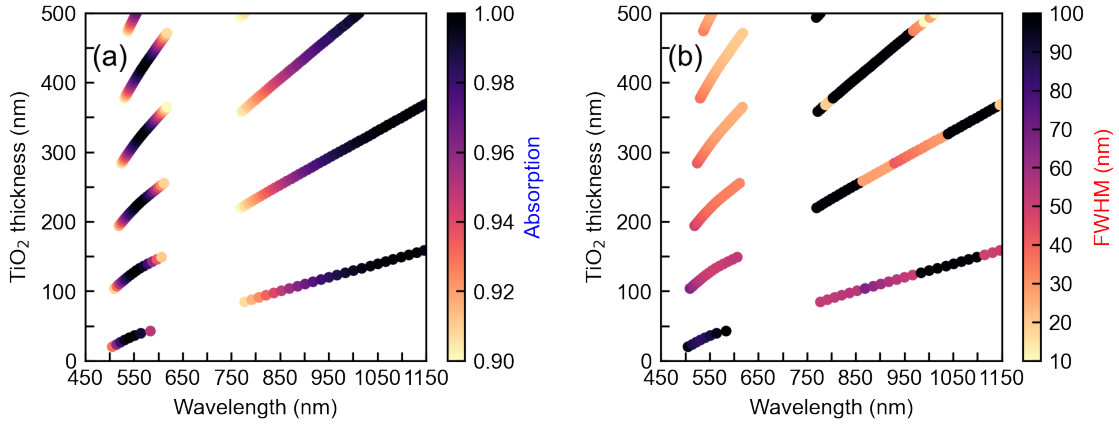


Figure 3.3: Simulations indicating the desirable thickness of TiO_2 dielectric layer as a function of the wavelength that absorption occurs, corresponding to absorption higher than 90% (a), and FWHM of the absorption peaks with intensity higher than 90%, between 10 and 100 nm (b), respectively. The color codes (in connection with the right vertical bars) indicate the intensity (a), or the FWHM (b) of the absorption peaks of the proposed structure, respectively.

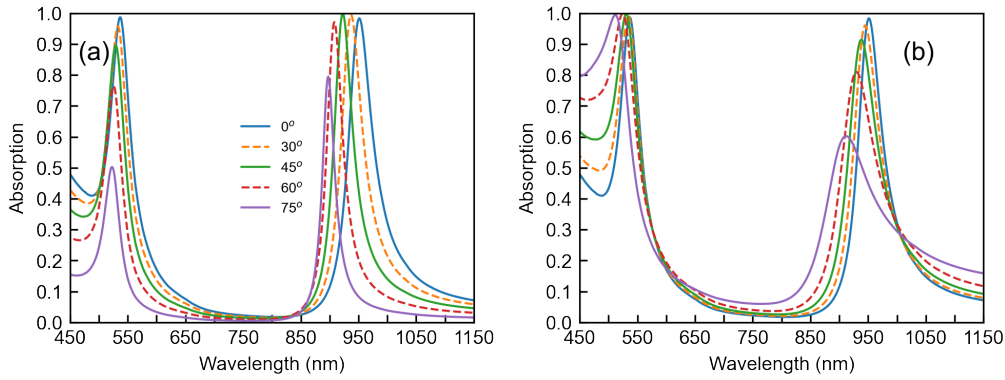


Figure 3.4: Absorption spectra for (a) s-polarization and (b) p polarization for different angles of incidence, varying from 0 to 75 degrees, for the Metal-Insulator-Metal Structure with a 120 nm TiO_2 dielectric layer between two metallic gold films.

can be quite sharp (FWHM 10 nm), or relatively broad (FWHM 100nm), by simply changing the thickness of the TiO_2 layer from 175-475 nm to 25-50 nm, respectively. Again, one can see that the FWHM of the smaller- and the larger-wavelength peaks is different. For instance, for an absorption peak at a wavelength around 550 nm, the FWHM decreases with the thickness of the dielectric space. On the other hand, for the larger wavelength peak the dependence of the FWHM on the TiO_2 thickness is much more complicated.

Since, as already stated, the structures of Fig. 3.1 are essentially proposed as broadband perfect absorbers, their high absorption should be maintained for off-normal incidence and for any incident wave polarization. In Fig. 3.4 we plot the absorption spectra for different angles of incidence for s (electric field parallel to the surface) [Fig. 3.4(a)] and p- (magnetic field parallel to the surface) [Fig. 3.4(b)] polarized incident waves, for the structure of Fig. 3.1. As the incident angle increases the absorption peak displays a shift towards smaller wavelengths but still has near perfect absorption efficiency for both polarizations. We note here that perfect absorption is maintained up to incident angle of 30° for both polarization and for both peaks. Also, high

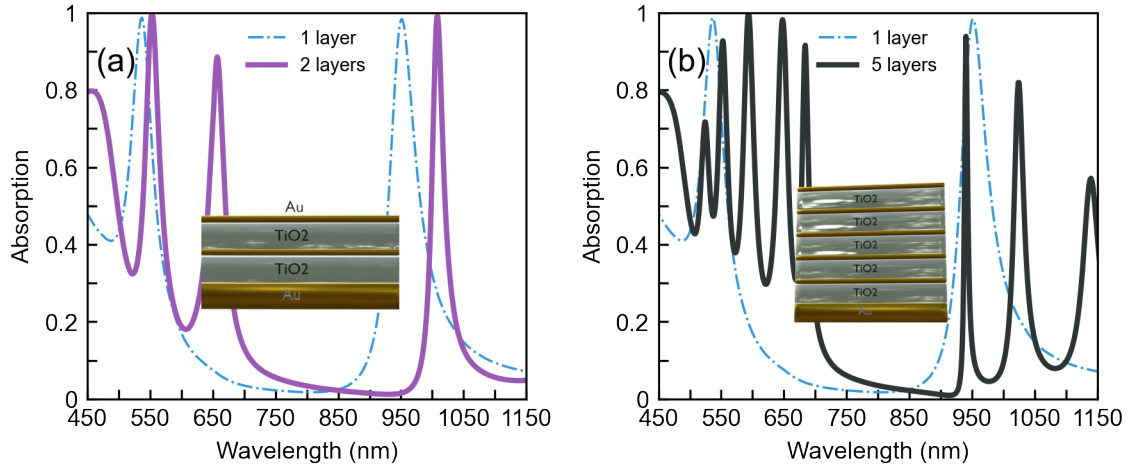


Figure 3.5: Absorption spectra under normal incidence for a MIM structure comprising of (a) 2 and (b) 5 Au-TiO₂ layers. The thickness of the TiO₂ layers is set to 150 nm and the thicknesses of the Au films to 15 nm except from the top metallic film which has thickness 20 nm. The absorption of a single MIM stack (blue dashed line) is also plotted for comparison.

values of absorption are maintained for a large range of incidence angles, greater than 30°, as shown in Fig. 3.4.

Using this type of MIM structure as building blocks, one can design a multiband or even a broadband perfect absorber by cascading multiple MIM stacks [26], [29]. In Fig. 3.5 we plot the absorption spectra under normal incidence for two [Fig. 3.5(a)] and five stacks of Au-TiO₂ layers on top of a metallic optically thick substrate. The thickness of the TiO₂ dielectric layers is 150 nm and the thickness of the Au layers is 15 nm except for the top Au layer, which is set to 20 nm. As one can see, for the case of two metal-dielectric stacks there are two peaks of high absorption in the 500-700 nm wavelength range. If we further increase the number of stacks to five, more absorption peaks appear closer to each other with maximum absorption equal to unity and quite high minimum absorption, indicating broader band high absorption. To illustrate this effect, we also plot the absorption of the single MIM structure in Fig. 3.5.

3.4 Conclusions

We have demonstrated a perfect absorber in the visible region based on a MIM structure of proper geometric dimensions, for both s and p incident polarization, and for angles of incidence up to 75 degrees. The absorber was fabricated and characterized experimentally (by experimental colleagues), with characterization results in very good agreement with our simulations. Moreover, We have provided evidence that our simple and narrowband absorber can be transformed to a substantially broader one, by simply building several layers of the proposed MIM structure, while no nanofabrication steps are required; thus, the absorber can easily be made to cover a large area. The highly efficient absorption characteristics of the proposed structures can be potentially deployed for solar cells, optical filter elements and others.

CHAPTER 4

PERFECT ABSORPTION CONDITIONS IN METASURFACE-BASED PERFECT ABSORBERS

4.1 Introduction

Metasurfaces are artificial, electromagnetically ultrathin structures with exotic functionalities that can be engineered through engineering of their periodic architecture and the geometry and materials of their constituent elementary units, known as the meta-atoms, which are in fact subwavelength resonant elements. An electromagnetic wave impinging on a metasurface induces the excitation of local currents whose distribution is defined by the details of the electromagnetic wave, i.e. frequency, incidence angle and polarization, and by the shape, size and materials of the meta-atoms. The meta-atom-enabled manipulation of these currents leads to a controllable electromagnetic response [34], [35] and thus, by properly designing the meta-atoms, advanced wave control is possible. Indeed a plethora of exotic electromagnetic metasurface-based functionalities has been demonstrated, from steering, imaging, cloaking and polarization control to sensing and energy harvesting [36]–[41].

Depending on the frequency of operation, the targeted functionality, the available materials and the fabrication techniques, metasurfaces can have many different forms. In microwaves they usually consist of metallic meta-atoms, of the form of rings or wires or patches [42]–[44]; in IR and optical region, where the losses of metals are high, the more common scheme is metasurfaces of high-index dielectric meta-atoms, of the form of rods, disks or spheres [45]–[47]. A particularly interesting frequency regime is the THz regime, as it bridges electronics and photonics, attracting also growing interest in connection with its 6G applications [48], [49]. In that regime a plethora of metasurface structures has been proposed or demonstrated, based on the common metallic schemes, but also on more exotic materials like polaritonic materials [50], [51] and graphene. Graphene is an ideal material for the realization of THz metasurfaces as it exhibits unique mechanical, thermal, electrical and optical properties that stem from the linear dispersion of the 2D Dirac Fermions, and allows for a wide tunability. THz graphene-based plasmonic metasurfaces attract growing attention and have unveiled interesting features for a large number of applications [52]–[61].

One of the most desired metasurface functionalities is that of enhanced or perfect absorption by ultrathin metasurface-based structures; there, the properly designed electromagnetic metasurfaces act as impedance matched sheets, creating also waves that cancel the incident wave. This impedance-match may be achieved by two resonators that couple separately to electric and magnetic fields so as to absorb all incident radiation or more bulky approaches such as multilayer Salisbury absorbers [19], [53], [56], [62]–[67]. A scheme that has attracted great attention involves the combination of the Salisbury approach with ultrathin resistive metasurfaces, i.e. a thin metasurface-insulator-metal reflective configuration (i.e. the back-metal plate is fully reflective). This kind of configuration provides an additional design freedom coming from the cavity (i.e. the dielectric between metasurface and back-metal) and enhances the

effect of the metasurface, leading to enhanced absorption, broader bandwidths and increased robustness [68]–[71].

The perfect absorption mechanisms in dielectric-metal structures that incorporate metasurfaces have been analytically explained with various techniques, for example in terms of multipole scattering [72], transmission line [70], equivalent circuit approach [73], and others. In this chapter we derive the transfer matrix formulation for metasurfaces supporting both electric and magnetic responses, for both s and p polarization, and we derive the conditions in order to achieve perfect absorption in metasurface-insulator-metal structures, i.e., metasurfaces placed on top of a dielectric substrate back-plated by a metallic, fully reflective layer. For the overlying metasurface we assume cases of variable effective surface electric and magnetic conductivities. In particular we examine the case of a uniform graphene layer/metasurface that exhibits only electric (and tunable) surface conductivity and four different metasurfaces with unmatched (i.e. overlapping), matched or partially matched surface electric and magnetic conductivity resonances. For the case of graphene-based absorber we show that by properly choosing the thickness of the dielectric and the Fermi level of graphene the structure can absorb 100% of the impinging electromagnetic radiation; the absorption levels also present high tunability. For the case of the arbitrary metasurfaces we show that the proper design of the electric and magnetic surface conductivity response provides control over both the absorption level and the bandwidth of operation. Moreover we show that when we pair (match) the electric and magnetic surface conductivity of the metasurface, perfect absorption is achieved independently of the thickness of the dielectric substrate standing between the metasurface and the back reflector. The chapter is organized as follows: in Section 4.2 we present the analytical formulation of the transfer matrix that leads to the derivation of the perfect absorption conditions; in Section 4.3 we present the results of the uniform graphene metasurface investigation; in Section 4.4 we present the analysis of the metasurfaces with both electric and magnetic conductivity, and unveil the case of the substrate thickness independent absorber; finally we present the conclusions of our work.

4.2 Transfer matrix and conditions for perfect absorption

We analyse the scattering properties of the metasurface-based structures under investigation by employing the transfer matrix formalism [10], [12], a powerful tool for analysing the wave propagation in complex media. By considering an electromagnetic wave incident from the left side of the structure at angle θ as schematically depicted in Fig. 4.1(a), we can write the transfer matrix equation as follows:

$$\begin{pmatrix} F_1^+ \\ F_1^- \end{pmatrix} = \mathbb{L}_{\text{total}} \begin{pmatrix} F_3^+ \\ 0 \end{pmatrix} \quad (4.1)$$

where F_1^+ , F_1^- and F_3^+ stand for the incident, reflected and transmitted field, respectively, $F = \{E, H\}$ is either the electric (for s polarization) or the magnetic (for p polarization) field, and $\mathbb{L}_{\text{total}}$ is the total transfer matrix of the structure.

As discussed already, in this chapter we are interested in the absorption of the structure shown in Fig. 4.1(b): a dielectric layer (medium 2) standing between a resistive sheet with surface electric conductivity σ_e and surface magnetic conductivity σ_m and an optically thick metallic back reflector (medium 3); the total structure is placed in air (medium 1). The transfer matrix for this structure reads:

$$\mathbb{L}_{\text{total}} = \mathbb{L}_{12} \mathbb{P}_2(d) \mathbb{L}_{23} \quad (4.2)$$

where \mathbb{L}_{ij} denotes the transfer matrix for the interface between media i and j and

$$\mathbb{P}_m(d) = \begin{pmatrix} e^{-ik_m z d} & 0 \\ 0 & e^{ik_m z d} \end{pmatrix}$$

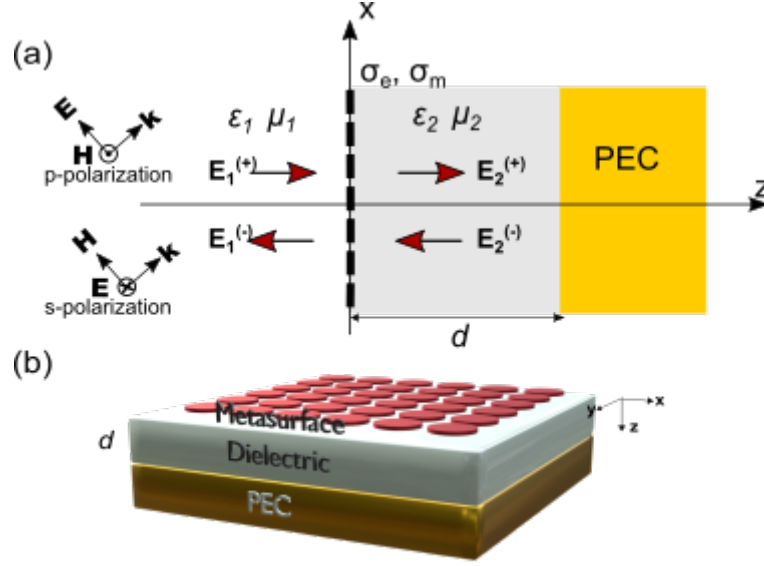


Figure 4.1: (a) Setup for the derivation of the transfer matrix equation for s and p polarizations. An interface with surface conductivities σ_e and σ_m between two semi-infinite (along x and y directions) media 1, 2 and Perfect Electric Conductor (PEC) substrate. (b) Schematic of a metasurface with surface conductivities σ_e , σ_m on top of a grounded dielectric of thickness d with permittivity ϵ_2 and permeability μ_2 .

stands for the propagation matrix in the medium with permittivity ϵ_m , and $k_{mz} = \sqrt{k_m^2 - k_x^2}$ is the z component of the wavevector in medium m . The interface matrices \mathbb{L}_{ij} are polarization-dependent and can be derived from the boundary conditions between media i and j

$$\hat{\mathbf{n}} \times \mathbf{E}|_{\text{interface}} = -\mathbf{J}_m = -\sigma_m \mathbf{H}_{\text{av}}|_{\text{interface}} \quad (4.3)$$

$$\hat{\mathbf{n}} \times \mathbf{H}|_{\text{interface}} = \mathbf{J}_e = \sigma_e \mathbf{E}_{\text{av}}|_{\text{interface}}, \quad (4.4)$$

where $\hat{\mathbf{n}}$ is the unit vector normal to the interface ($\hat{\mathbf{n}} = \hat{\mathbf{z}}$) and the subscript av refers to the averaged fields at the interface between the two media (see Chapter 2 for more detail). For p polarization the magnetic and electric fields are $\mathbf{H} = H_y \hat{\mathbf{y}}$ and $\mathbf{E} = E_x \hat{\mathbf{x}} + E_z \hat{\mathbf{z}}$ respectively. For s polarization $\mathbf{H} = H_x \hat{\mathbf{x}} + H_z \hat{\mathbf{z}}$ and $\mathbf{E} = E_y \hat{\mathbf{y}}$. By imposing the boundary conditions (4.3)-(4.4) at the interface between the two media we can obtain the elements of the transfer matrix for an interface, as given by Eqs. (2.18)-(2.21) and Eqs. (2.36)-(2.39) of Chapter 2, for p and s polarizations respectively.

Having calculated the total transfer matrix of the structure, we can proceed to the derivation of perfect absorption conditions. Since the transmission vanishes due to the presence of the back reflector, the absorption of the structure can be calculated only from the reflectivity, as $A = 1 - |r|^2$, where $r = F_1^+ / F_1^- = \mathbb{L}_{\text{total}}^{(21)} / \mathbb{L}_{\text{total}}^{(11)}$. Therefore, perfect absorption by our structure is obtained for $r = 0$:

$$r = 0 \Rightarrow \mathbb{L}_{\text{total}}^{(21)} = 0 \quad (4.5)$$

or

$$i \tan(k_{2z}d) = \frac{\mathbb{L}_{12}^{(22)} \mathbb{L}_{23}^{(21)} + \mathbb{L}_{12}^{(21)} \mathbb{L}_{23}^{(11)}}{\mathbb{L}_{12}^{(22)} \mathbb{L}_{23}^{(21)} - \mathbb{L}_{12}^{(21)} \mathbb{L}_{23}^{(11)}} \quad (4.6)$$

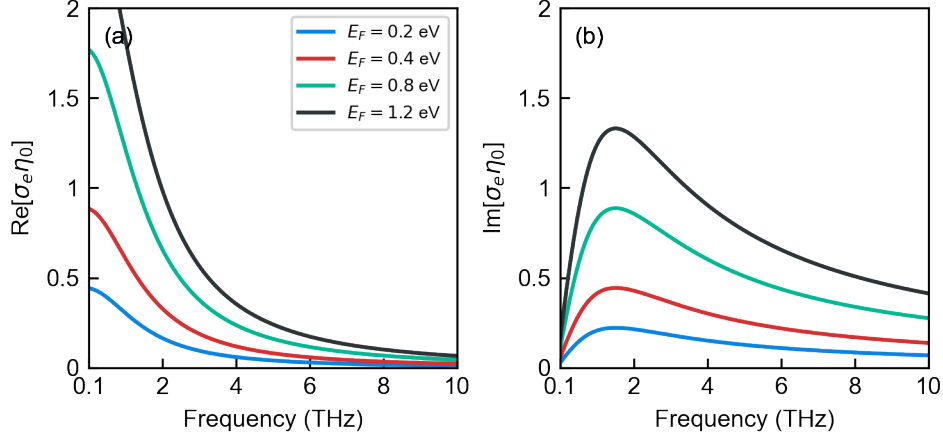


Figure 4.2: (a) Real and (b) imaginary part of normalized conductivity of graphene for Fermi energies $E_F = 0.2$ eV, $E_F = 0.4$ eV, $E_F = 0.8$ eV and $E_F = 1.2$ eV. The relaxation time of the electrons in graphene is $\tau = 0.1$ ps.

If the back-reflector is a Perfect Electric Conductor (PEC) we can write

$$\frac{\eta_2}{\eta_1} i \tan(k_{2z}d) = \frac{-s_e s_m + 2s_m - 1}{s_e s_m - 2s_e + 1} = G(s_e, s_m) \quad (4.7)$$

where $G(s_e, s_m)$ is a function of the normalized sheet conductivities $s_e = \sigma_e \eta_1 / 2$ and $s_m = \sigma_m / 2\eta_1$, $\eta_j^{(p)} = k_{jz} / \omega \varepsilon_j$ and $\eta_j^{(s)} = \omega \mu_j / k_{jz}$. For the rest of this chapter we will assume that the dielectric is lossless. In this case the total absorption condition (4.7) can be written as:

$$\alpha = \text{Re}G(s_e, s_m) = 0 \quad (4.8)$$

$$\beta = \frac{\eta_2}{\eta_1} \tan(k_{2z}d) - \text{Im}G(s_e, s_m) = 0 \quad (4.9)$$

4.3 Uniform graphene perfect absorber

We first investigate the case of a Salisbury absorber structures with a uniform sheet of graphene placed on top of a grounded lossless dielectric. The superstrate medium is considered to be vacuum ($\varepsilon_1 = \varepsilon_0$, $\mu_1 = \mu_0$). In this case there is no magnetic sheet conductivity, $s_m = 0$, and therefore the conditions for perfect absorption from Eq. (4.7) are reduced to

$$\text{Re}[\sigma_e(\omega)\eta_0] = 1 \quad (4.10)$$

$$\text{Im}[\sigma_e(\omega)\eta_0] = -\frac{1}{\sqrt{\varepsilon_{2r}}} \cot\left(\sqrt{\varepsilon_{2r}} \frac{\omega}{c} d\right), \quad (4.11)$$

where $\eta_0 = c\mu_0 = 376.73 \Omega$ is the impedance of free space and $\varepsilon_{2r} = \varepsilon_2 / \varepsilon_0$ stands for the relative permittivity.

In this section we are using an unpatterned graphene sheet and the surface conductivity is a function of Fermi energy, E_F , the temperature, T , and the relaxation time of the electrons, τ . For the calculation of the conductivity we use the Kubo formula, derived in the context of Rapid Phase Approximation [74], as

$$\begin{aligned} \sigma_e(\omega) = & \frac{2e^2 k_B T}{\pi \hbar^2} \frac{i}{\omega + i\tau^{-1}} \ln \left[2 \cosh \left(\frac{E_F}{2k_B T} \right) \right] \\ & + \frac{e^2}{4\hbar} \left[\mathcal{H}(\omega/2) + \frac{4i\omega}{\pi} \int_0^\infty d\varepsilon \frac{\mathcal{H}(\varepsilon) - \mathcal{H}(\omega/2)}{\omega^2 - 4\varepsilon^2} \right], \end{aligned} \quad (4.12)$$

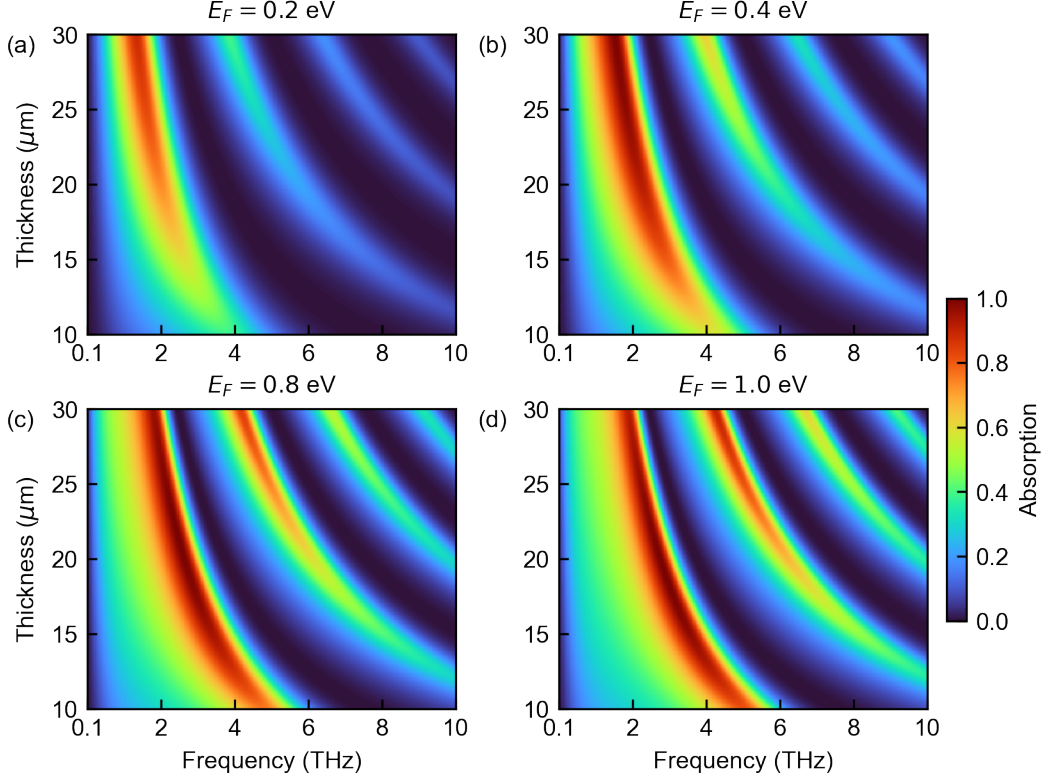


Figure 4.3: Absorption spectra under normal incidence for a graphene on a grounded dielectric substrate of relative permittivity $\varepsilon_{2r} = 3.9$ as function of the thickness of the dielectric and for Fermi energies (a) $E_F = 0.2$ eV, (b) $E_F = 0.4$ eV, (c) $E_F = 0.8$ eV and (d) $E_F = 1$ eV. The relaxation time of the electrons in graphene is $\tau = 0.1$ ps.

where

$$\mathcal{H}(\omega) = \frac{\sinh(\hbar\omega/k_B T)}{\cosh(E_F/k_B T) + \cosh(\hbar\omega/k_B T)}, \quad (4.13)$$

where ω is the angular frequency, $\hbar = 1.055 \times 10^{-34}$ J·s the reduced Planck constant, $k_B = 1.38 \times 10^{-23}$ m² · kg · s⁻² · K⁻¹ the Boltzmann constant, $e = 1.602 \times 10^{-19}$ C the electron charge and τ the electrons relaxation time (τ is assumed here equal to 0.1 ps). The first term of Eq. (4.12) accounts for the contribution of intraband transitions, which are more relevant in low frequencies (GHz, THz), while the second term accounts for interband transitions in graphene, which are more prominent in the optical part of the electromagnetic spectrum. We plot the real and imaginary parts of conductivity of graphene for different Fermi levels in Fig. 4.2.

As a reference case study we choose the dielectric substrate relative permittivity to be equal to $\varepsilon_{2r} = 3.9$ (zero imaginary part), a value typical for many polymers in the THz part of the spectrum. We choose to study the lossless dielectric case so as to ensure that the obtained absorption will come exclusively from the monolayer graphene sheet. The absorption spectra under normal incidence as a function of frequency and dielectric thickness are shown in Fig. 4.3 for Fermi energies $E_F = 0.2$ eV, 0.4 eV, 0.8 eV and 1.2 eV. As one can see, for all cases there is a series of maxima and minima in the absorption spectra originating from multiple reflections inside the dielectric. The maxima of absorption follow Eq. (4.11) and perfect absorption is achieved when Eq. (4.10) is satisfied as well. As the Fermi energy grows, the absorption in the higher order Fabry-Pérot resonances grow as well. We should note here that as the thickness of the dielectric layer decreases, the Fermi level required for perfect absorption is increased. Also, the resonance frequency increases with larger Fermi level. This is expected since a thickness of

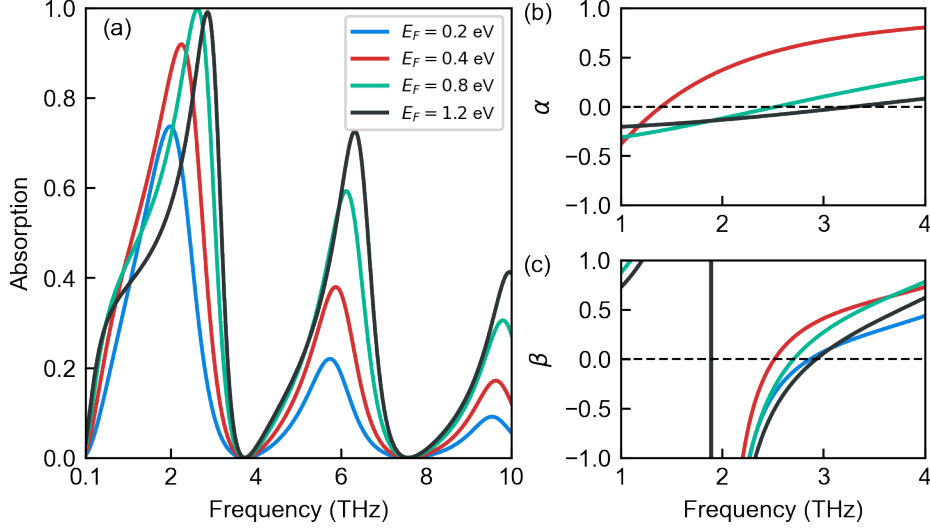


Figure 4.4: (a) Absorption spectrum under normal incidence for a graphene on a grounded dielectric substrate of thickness $d = 20 \mu\text{m}$ and relative permittivity $\epsilon_{2r} = 3.9$, for different Fermi levels, $E_F = [0.2 - 1.2] \text{ eV}$. (b)-(c) Perfect absorption conditions based on (b) Eq. (4.8) and (c) Eq. (4.9). The relaxation time of electrons in graphene is $\tau = 0.1 \text{ ps}$.

$d \approx \lambda/4$ (where λ is the wavelength inside the dielectric) is required for perfect absorption in a Salisbury screen-type perfect absorber [67].

We also plot in Fig. 4.4(a) the absorption spectra in frequency [0.1-10] THz for a structure with the dielectric substrate thickness equal to $d = 20 \mu\text{m}$, assuming that the graphene Fermi levels range in $E_F = [0.2 - 1.2] \text{ eV}$. Along with the absorption spectra we plot in the frequencies [1-4] THz the perfect absorption conditions, $\alpha = 0$ and $\beta = 0$, obtained from Eqs. (4.8)-(4.9) - see Fig. 4.4(b) and Fig. 4.4(c), respectively. In Fig. 4.4(a) a fast increase in absorption as a function of the Fermi level is observed, especially in the lowest part of the frequency spectrum. The first absorption peak occurs at $f = 2 \text{ THz}$ for $E_F = 0.2 \text{ eV}$ and it increases in intensity quite quickly with increased Fermi level. In fact, absorption becomes greater than 90% for Fermi levels larger than $E_F = 0.4 \text{ eV}$, which is a Fermi energy value easily achievable experimentally. For $E_F = 0.8 \text{ eV}$ perfect absorption is achieved at $f = 2.7 \text{ THz}$ which is also the frequency where the conditions $\alpha = 0$ and $\beta = 0$ are satisfied. Due to the ability to tune the conductive properties of graphene, which makes it valuable for modulation applications, it is useful to evaluate the relative change of absorption with respect to the changing Fermi level for different dielectric thickness values. In Fig. 4.5 we plot the absorption contours as a function of Fermi level and dielectric thickness for 2 THz and 2.7 THz. For illustration purposes we have chosen to depict absorption levels greater than 40%. As can be observed, the equi-absorption curves are ellipsoidal-like in the Fermi energy-thickness plane. The main difference between the two frequencies of operation is that the equi-absorption curves become narrower along the thickness axis for the 2.7 THz case; we can find thicknesses that maximize the relative change of absorption with respect to Fermi energy change, $\Delta A / \Delta E_F$, a feature very important for modulators. For instance, for dielectric thickness $d = 20 \mu\text{m}$ and frequency $f = 2.7 \text{ THz}$ the absorption moves from 32% for $E_F = 0.2 \text{ eV}$ to 67% for $E_F = 0.4 \text{ eV}$ and 99% for $E_F = 0.75 \text{ eV}$.

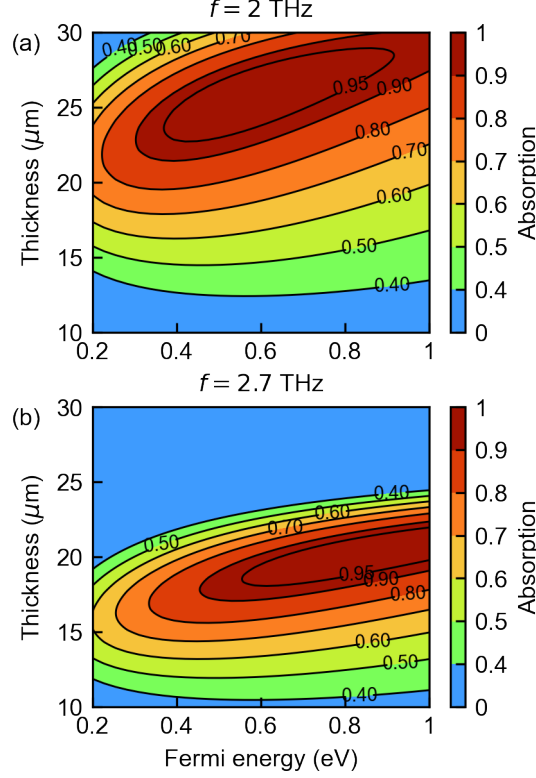


Figure 4.5: Contour plots of absorption under normal incidence for a uniform graphene Salisbury screen as a function of the dielectric substrate thickness and the graphene's Fermi energy, for frequency of operation: (a) $f = 2$ THz and (b) $f = 2.7$ THz. The relative permittivity of the dielectric is $\varepsilon_{2r} = 3.9$.

4.4 Metasurface-based perfect absorber

In this section we investigate the properties of a Salisbury-typed absorber where the resistive sheet has both electric and magnetic dipolar response. Similar to the case of the graphene absorber in the previous section, the dielectric substrate material is considered lossless with $\varepsilon_{2r} = 3.9$. Assuming that the elements comprising the metasurface are subwavelength and there is only one electric resonance at frequency ω_e and one magnetic resonance at frequency ω_m , the normalized sheet conductivities can be written as [14], [16], [17]:

$$s_e = \frac{\sigma_e \eta_1}{2} = \frac{i\kappa_e \omega}{\omega^2 - \omega_e^2 + i\omega\Gamma_e} \quad (4.14)$$

$$s_m = \frac{\sigma_m}{2\eta_1} = \frac{i\kappa_m \omega}{\omega^2 - \omega_m^2 + i\omega\Gamma_m}, \quad (4.15)$$

where κ_e, κ_m stand for the resonance strengths and Γ_e, Γ_m are the relaxation rates. We examine four distinct cases: A) a metasurface with only electric response, i.e. $s_m = 0$; B) a metasurface where the electric and magnetic sheet conductivities have different resonance frequencies, i.e., $\omega_m \neq \omega_e$ (with $\omega_m/2\pi = 17$ THz, $\kappa_e = \kappa_m$, $\Gamma_e = \Gamma_m$); C) a metasurface with matching resonance frequencies, $\omega_e = \omega_m$, but different resonance strengths ($\kappa_m = \kappa_e/10$); and D) a metasurface with matching normalized sheet conductivities, i.e. $s_e = s_m$. For all cases we have chosen parameters $\kappa_e/2\pi = 2$ THz, $\omega_e/2\pi = 15$ THz and $\Gamma_e/2\pi = 1$ THz. The normalized sheet conductivities along with the corresponding absorption spectra as a function of frequency for all four cases (A-D) are shown in Fig. 4.6 (the absorption spectra are plotted also with respect to the dielectric thickness).

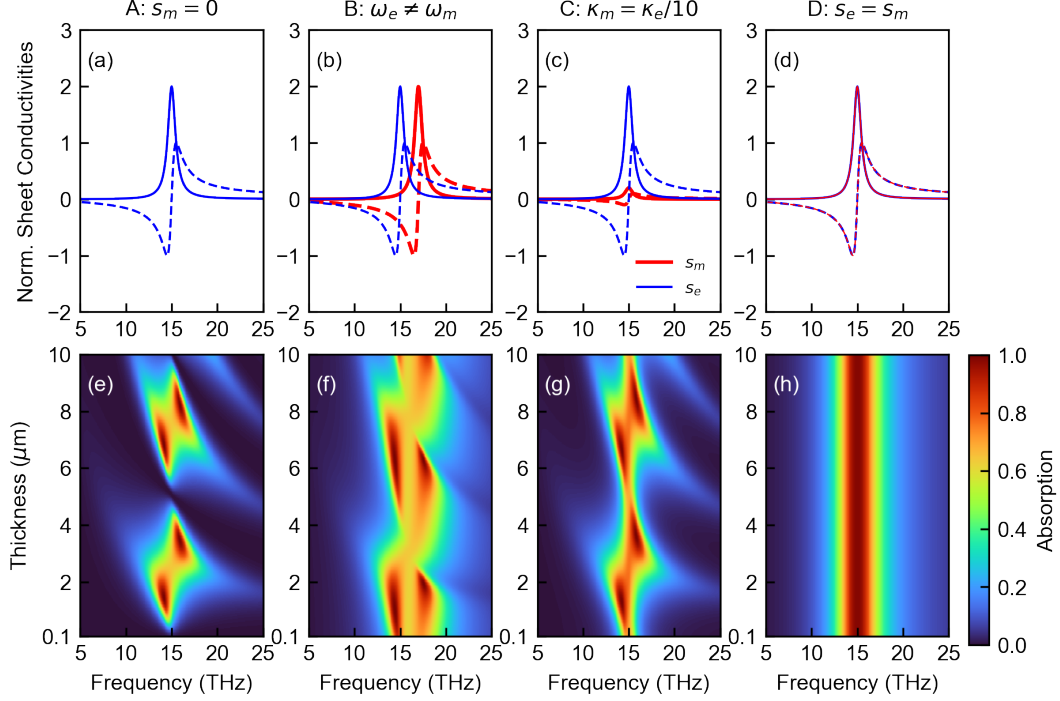


Figure 4.6: Real (solid lines) and imaginary (dashed lines) parts of normalized sheet conductivities as a function of frequency (top row) and corresponding absorption spectra as function of the thickness of the dielectric and frequency (bottom row) for four different metasurfaces: A: $s_m = 0$ (first column); B: $\omega_m/2\pi = 17$ THz (second column); C: $\omega_m = \omega_e$, $\kappa_m = \kappa_e/10$ (third column) and D: $s_e = s_m$ (fourth column). For all cases the parameters of the electric sheet conductivity are $\omega_e/2\pi = 15$ THz, $\kappa_e/2\pi = 2$ THz and $\Gamma_e/2\pi = \Gamma_m/2\pi = 1$ THz. For the definition of the parameters see main text.

Starting from the case of metasurface A where there is no magnetic response, $s_m = 0$, in Fig. 4.6(a) and Fig. 4.6(e) we observe that there are values of the dielectric substrate thickness that give 100% absorption and zero absorption similar to the case of the graphene absorber studied in Section 4.3. The introduction of magnetic response in the metasurface (cases B and C) allows for the lifting-of the absorption zeros in the frequency range around the resonances in sheet conductivities. For the metasurface B where we have conductivities with unmatched resonance frequencies and matched amplitudes ($\omega_e \neq \omega_m$ and $\kappa_e = \kappa_m$) we find absorption consistently above 50% in the frequency region around $\omega_e/2\pi = 15$ THz and $\omega_m/2\pi = 17$ THz (and in-between the two frequencies). On the other hand, for the metasurface C where we have conductivities with matched resonance frequencies and unmatched amplitudes ($\omega_e = \omega_m$ and $\kappa_e \neq \kappa_m$; the magnetic response is weaker but in the same frequency as the electric response), we get very high absorption for all thicknesses. However, the frequency of maximum absorption as well as the bandwidth where the absorption is large are highly dependent on the dielectric thickness. To illustrate this effect, we plot in Fig. 4.7 the absorption spectra and the functions α and β for metasurfaces B and C, for two different thicknesses, $d = 2.5 \mu\text{m}$ and $d = 6.3 \mu\text{m}$.

Last but not least, we present the case of the metasurface D with matching electric and magnetic resonances, $s_e = s_m$, in Fig. 4.6(d) (sheet conductivities) and Fig. 4.6(h) (absorption spectra). It is observed that absorption is independent of the thickness of the dielectric and it reaches 100% around $\omega_e = \omega_m$. The independence of absorption on the dielectric thickness originates from the fact that this type of metasurface completely matches the impedance of the surrounding medium, resulting in the cancellation of the reflected radiation, i.e. it satisfies the

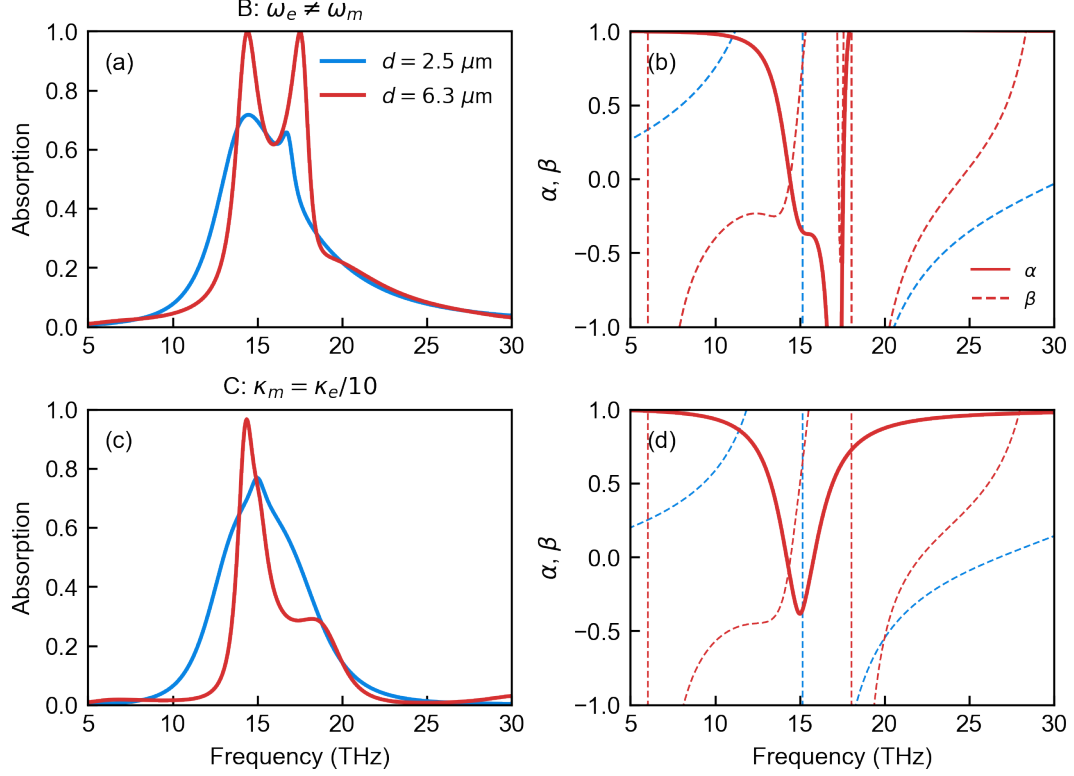


Figure 4.7: Absorption under normal incidence (left column) and conditions α (Eq. (4.8)) (right column - solid lines) and β (Eq. (4.9)) (right column - dashed lines) for: (a)-(b) a metasurface (metasurface B) with $\omega_e \neq \omega_m/2\pi = 17$ THz ($\kappa_e = \kappa_m$) and (c)-(d) a metasurface (metasurface C) with $\omega_m = \omega_e$, $\kappa_m = \kappa_e/10$, for two different dielectric thicknesses (note that α is thickness independent). For all cases the parameters of the electric sheet conductivity are $\omega_e/2\pi = 15$ THz, $\kappa_e/2\pi = 2$ THz and $\Gamma_e/2\pi = \Gamma_m/2\pi = 1$ THz. The definition of the parameters is given in the main text.

Kerker condition [75]. From Eq. (4.7), we can see that, on resonance, $G(s_e, s_e) = -1$ leading to $\beta = \tan(k_{2z}d)/\sqrt{\varepsilon_{2r}}$ and $\alpha = -1$. Therefore, the condition (4.8) ($\alpha = 0$) cannot be fulfilled in this case. More investigation is needed to clarify this result.

We should note here that although metasurface D ($s_e = s_m$) provides the best absorption results among all the cases considered, it is not always possible to design metasurfaces with exact matching of the electric and magnetic response over a given frequency band. Such matching is sensitive to both theoretical/fundamental and practical limitations; e.g. magnetic resonances are usually weaker and more narrow-band than the electric ones; it is important though to be able to quickly identify the effect of the deviations from the optimum metasurface D on the achievable absorption. The theoretical/analytical framework developed in this chapter can constitute a valuable tool towards this direction, and more generally, a valuable tool in the design of metasurface-assisted dielectric-metal structures suitable for absorption or other desired applications.

4.5 Conclusions

We have derived the transfer matrix formulation for metasurfaces supporting both electric and magnetic responses for both s and p polarization. Using the transfer matrix framework

we derived conditions for perfect absorption in structures comprised of a metasurface on top of a grounded dielectric substrate of variable thickness, and we applied our method for the cases of a uniform graphene sheet/metasurface and four different metasurfaces. For the case of graphene-assisted absorber we have shown that by properly choosing the thickness of the dielectric and the Fermi level of graphene the structure can absorb 100% of the impinging electromagnetic radiation. Additionally, the high tunability of the conductivity of graphene allows considerable modulation of the absorption amplitude of the structure. Regarding the metasurface-assisted absorbers, i.e. metasurface-dielectric-metal structures, we calculated the absorption spectra as a function of frequency and thickness of the dielectric for metasurfaces exhibiting both electric and magnetic resonant responses, which are fully matched, partially matched or unmatched. We found that by properly designing the electric and magnetic response of the metasurface it is possible to control both the absorption level and the bandwidth of operation; a particularly interesting case was the one of the fully matched electric and magnetic resonances, where we found perfect absorption independently of the thickness of the dielectric. Our formulation and results provide analytical guidelines for the design and optimization of metasurface-assisted absorbers with narrowband or broadband operation, valuable in a variety of applications, including electromagnetic shielding, harvesting, detection/sensing, etc.

CHAPTER 5

POLARITONIC CYLINDERS AS MULTIFUNCTIONAL METAMATERIALS: SINGLE SCATTERING AND EFFECTIVE MEDIUM DESCRIPTION

5.1 Introduction

The emergence of electromagnetic (EM) metamaterials (MM), i.e. engineerable structured materials made of sub-wavelength resonant building blocks (meta-atoms) with novel and unique EM properties and response, made possible the demonstration of novel and unconventional EM wave phenomena, entailing possibilities to advance or even revolutionize a great variety of applications related with EM wave control, from telecommunications, to imaging, sensing etc. Particularly interesting categories of metamaterials that have been designed and demonstrated so far include: (a) Negative effective permeability (μ -negative, MNG) and negative refractive index metamaterials (NIMs, usually achievable by combining negative effective permittivity and permeability) [76], [77]. NIMs are associated with many counter intuitive phenomena, such as opposite phase and energy velocity, negative refraction etc., and unique potential in imaging and telecommunications applications. The first realizations of MNG and NIM structures were obtained employing and properly structuring metals [78], while, later, it was shown that the same response can be achieved also by metamaterials made of high-index dielectrics [79], [80], where the strong displacement current undertakes the role that conduction current plays in metals. (b) Hyperbolic metamaterials (HMMs) [81], [82], i.e. anisotropic metamaterials showing hyperbolic dispersion relation, own to the mixed positive and negative values of their effective permittivity or permeability tensor components [83]. Such metamaterials, which are usually realized by properly alternating metallic and dielectric layers or by employing metallic rod systems, show great potential in imaging applications [84]–[86], as they can offer almost perfect imaging, even with magnification (they can transform evanescent waves to propagating), and in spontaneous emission enhancement [87], [88] (as they can offer very high density of EM states). (c) Metamaterials with permittivity near zero (ENZ) [89]–[91]; such metamaterials, which can be realized by properly engineering electrical permittivity resonances (e.g. by proper structuring), are associated with peculiar phenomena and possibilities, e.g. squeezing of EM waves in very narrow channels, easy wavefront engineering, etc. Moreover, the huge wavelength in such metamaterials makes them ideal hosts for demonstration of subwavelength phenomena, as it makes all the wave propagation and scattering features in to them to fall in the extreme sub-wavelength region, almost for any type of embedded scatterers. As we aim to show in this chapter, all the above metamaterial categories and their related novel phenomena are achievable with properly engineered systems of phonon-polariton materials (polaritonic systems) [30], in particular in systems made of polaritonic cylinders in a dielectric host.

Phonon-polariton (polaritonic) materials [30], [92], [93] is a particularly interesting category of materials, combining both metallic and dielectric response. They are polar crystals (e.g. NaCl) where the EM radiation excites lattice vibrations, resonant in the region from THz to far- and

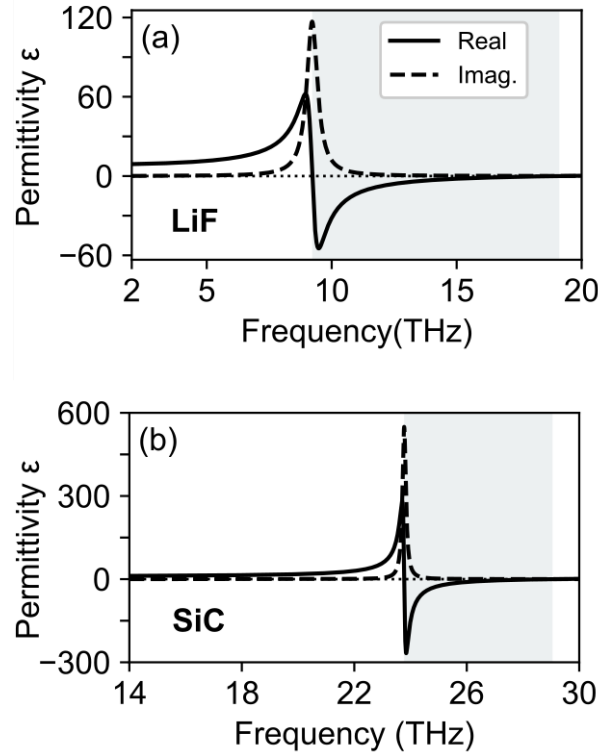


Figure 5.1: Real and imaginary parts of the relative dielectric function for (a) LiF and (b) SiC calculated from Eq. (5.1) and using the data from Table 5.1. The gray areas indicate the frequency regions where the real part of the corresponding dielectric function is negative, between approximately ω_T and ω_L .

mid-IR. The coupling of the EM radiation with the lattice vibrations in that region results to a resonant permittivity response of Lorentz-type, i.e.

$$\varepsilon(\omega) = \varepsilon_\infty \frac{\omega^2 - \omega_L^2 + i\omega\Gamma}{\omega^2 - \omega_T^2 + i\omega\Gamma} \quad (5.1)$$

where $\varepsilon(\omega)$ is the relative permittivity, the resonance frequency ω_T is the transverse optical phonon frequency, Γ is the collision frequency, ω_L is the longitudinal optical phonon frequency, at which the dielectric function practically vanishes (ω_L is the analogue of the bulk plasmon frequency of the metallic case) and ε_∞ stands for the asymptotic value of the relative permittivity at high frequencies (much higher than ω_L and lower than the frequencies of the inter-band electronic excitations). (Note that in this chapter, to keep a simplicity in the formalism, the symbols ε and μ stand for the *relative* permittivity and permeability, respectively, and not for absolute permittivity and permeability - unlike the previous chapters.)

The relative permittivity for two characteristic polaritonic materials, namely LiF and SiC, is plotted in Fig. 5.1. Examining the permittivity forms of Fig. 5.1, one can easily realize the great potential of the polaritonic materials in MM-related phenomena and applications. Polaritonic materials offer regions of (a) high positive permittivity and thus they can be used for designing and demonstration of any kind of dielectric metamaterials [94] and metasurfaces; (b) negative permittivity, similar to that of metals in the optical region (with smaller loss-tangent); thus they can provide all the properties and possibilities that metallic metamaterials offer in optics, e.g. plasmonic effects, hyperbolic metamaterial response; (c) permittivity near zero, offering a convenient alternative to complex metamaterial structures that are usually designed to achieve

epsilon-near-zero (ENZ) response; besides, they can act as bulk ENZ hosts for demonstration of uncommon scattering and propagation effects [95].

An additional merit of the polaritonic materials is that the above mentioned rich response is exhibited in the THz and far-IR region of the electromagnetic spectrum, a region particularly interesting for sensing, security, biological and medical imaging, and thermal management, and also a region where there is considerable lack of advanced optical components (e.g. the THz gap). Finally, since many of the polaritonic materials are semiconducting, their properties and response can be highly tunable, e.g. by photoexcitation [30].

The potential of the polaritonic materials in MMs-related applications makes important the development or adaptation of not only advanced computational tools suitable for the study of such materials, but also of simplified models able to explore, identify, explain and even predict the rich variety of phenomena and possibilities allowed by those materials. Such a category of simplified models are the well known effective medium models, describing metamaterials as homogeneous (effective) media. Such models can offer a simple physical description of the response of the structures, revealing the dominant factors determining this response and their dependence on the structure parameters. Therefore they constitute an invaluable tool not only for the physical understanding and optimization of a given system but also, and more importantly, for the design of systems with desired response. The most well established today analytic effective medium model is the Maxwell-Garnett (MG) [96] model, suitable for the designing and description of structures in the quasistatic region. The MG model has been extensively applied for either the prediction or the analysis of the metamaterial response of many different structures, especially of structures composed of metallic scatterers of spherical or cylindrical shape, in the low-frequency limit, and specifically when $k_h R \ll 1$, $k_s R \ll 1$, with k_h , k_s , the wavenumber in the host and scattering material, respectively, and R the scatterers radius. In the case of systems though made of polaritonic scatterers, as well as in systems of high permittivity dielectric scatterers [97], [98], the high permittivity of the scatterers (resulting to small associated wavelength) leads to scattering resonances also in the long-wavelength region (i.e. resonances in the region $k_h R \ll 1$) the influence of which, although crucial for the wave propagation, can not be described by the simple quasistatic MG model. As a result, important features of polaritonic or high-index dielectric systems, such as magnetic response by non-magnetic scatterers, cannot be reproduced. To overcome this problem extended MG models have been developed (valid in the region $k_h R \ll 1$, $k_s R \approx 1$) in the three-dimensional case and have been applied with great success in systems made of spherical scatterers, either polaritonic or high-index dielectric [99], [100]. For the case of cylindrical scatterers (2D) [101]–[103], though, the most well-known suitable effective medium description is a description based on field homogenization [101], which is not straightforward to apply, while extended Maxwell-Garnett approaches, to our knowledge, have not been developed and applied in detail up now. In this chapter, we show that a homogenization approach based on the well known in the Solid State Physics community Coherent Potential Approximation (CPA) method [11], [104] can be applied with great success in the case of polaritonic rod systems, demonstrating a variety of novel and unconventional metamaterial phenomena in such systems. We have to note here that various systems of polaritonic rods in a host have been already studied, not only theoretically but also experimentally, and interesting phenomena and possibilities have been predicted or demonstrated: It has been shown that by properly designing the radii, heights and

Table 5.1: Lorentz model material parameters for LiF and SiC.

Material	ε_∞	$\omega_T/2\pi$ (THz)	$\omega_L/2\pi$ (THz)	$\Gamma/2\pi$ (THz)
LiF [105]	2.027	9.22	19.11	0.527
SiC [106]	6.7	23.79	29.05	0.143

distances of the rods, one can achieve both negative permeability and negative refractive index response [102]; moreover, hyperbolic response has been already theoretically demonstrated [93], [105], [107], as well as exotic phenomena such as toroidal dipolar response [108], [109], epsilon-near-zero originated waveguiding [110], and others. Finally, the possibility to relatively easily obtain such systems by, e.g. eutectics self-organization [105], [111], laser micromachining [112], etc., makes their study even more appealing and indispensable.

The aim of this chapter is to analyze in detail the wave propagation in systems of circular polaritonic rods (of infinite height) in a dielectric host and to identify the different interesting propagation regions and their associated characteristics. Of particular interest is the investigation and analysis of the effect of the combination of the material resonances (such as those shown in Fig. 5.1) with the structure resonances, dependent on the shape and size of the rods. To that extent, the approaches and many of the results presented here are not applicable only in the case of phonon-polariton systems but they can be applied in any system made of scatterers from a resonant material (e.g. exciton-polariton systems, macroscopic MMs forming cylindrical scatterers, etc.); moreover, the results can be transferred easily in the case of high-index dielectric scatterers [113]–[117].

To analyze the response of the polaritonic rod systems and to understand the effect of the interplay of material and structure resonances, we start from calculation and analysis of the single rod extinction and scattering cross section; then we use the single rod results in the application of the CPA approach [104], [118], [119], which is employed for the investigation and analysis of the multirod systems. As model systems we employ two different polaritonic rod systems: systems made of LiF rods and systems made of SiC rods (see Fig. 5.1 for the materials permittivity). Specifically, the chapter is organized as follows: In Sec. 5.2 we introduce the methods used for the calculation of the single rod extinction efficiencies and the relations for the effective medium determination. In Sec. 5.3 we present the results of single rod scattering (subsection 5.3.1) and of the effective medium (subsection 5.3.2) for our particular systems and we identify the different attainable interesting MM properties and capabilities. Comparison of our results with full-wave simulations demonstrate and verify the validity and merit of our approach in the study of polaritonic and high-index dielectric MMs, validating also further the feasibility of the interesting attainable effects predicted.

5.2 Methods

Although the systems of interest in this work are systems of polaritonic rods in air or in a dielectric host, the methods discussed in this section are derived for a general system of (identical) rods in a host, allowing any permittivity and permeability for both the rod and the host material. This is in order to achieve the widest possible applicability regime of the derived formulas, allowing their use for prediction or understanding of the properties of other potentially interesting MM systems or categories.

5.2.1 Single Scattering

We consider a single infinitely-long cylinder [9], [120] with radius R , composed of a material with relative electrical permittivity ε_c and magnetic permeability μ_c embedded in a host material with material parameters ε_h and μ_h . Along the rest of the chapter the subscripts h and c in any quantity would refer to host and cylinder respectively. Moreover we consider propagation in a plane perpendicular to the cylinder axis. Since the cylinder is infinitely-long and there is no propagation component parallel to its axis, the problem is two dimensional and, due to symmetry, it can be decoupled into two separate polarizations, the Transverse Electric (TE) polarization, with the electric field normal to the cylinder axis, and the Transverse

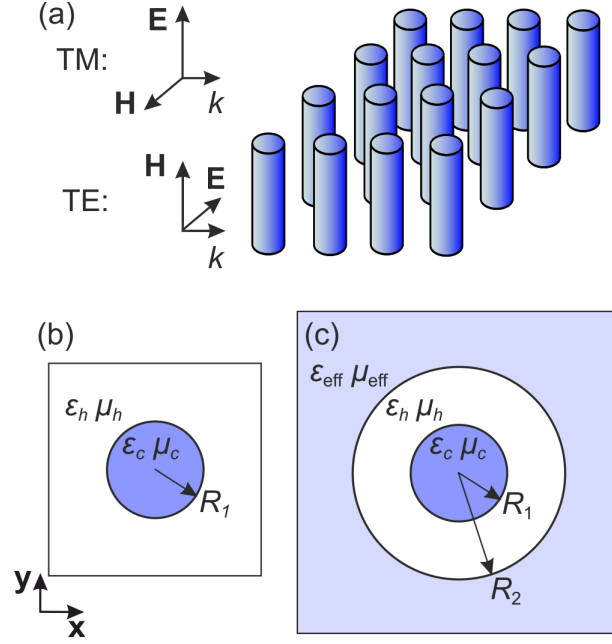


Figure 5.2: (a) An assembly of cylinders in a host medium (our system of interest) and definitions of the TE and TM polarization and the normal to the cylinders axes plane of incidence. (b) The unit cell of the system of (a), along with its relevant geometry and material parameters, i.e. electrical permittivity, ϵ , and magnetic permeability μ . The subscripts h, c stand for the host and cylinder material respectively. (c) Geometry for the derivation of the effective electric permittivity, ϵ_{eff} , and effective magnetic permeability, μ_{eff} : A single cylinder of radius $R_1 = R$ coated by a coating of thickness $R_2 - R_1$ made of the host material of the original system, embedded in the effective medium. R_2 is such as $f = R_1^2/R_2^2$, where f is the cylinder filling ratio in the original system.

Magnetic (TM) polarization, with the magnetic field normal to the cylinder axis, as seen in Fig. 5.2(a). The fields can be expanded on the basis of cylindrical harmonics inside and outside of the cylinder and the expansion coefficients can be found by imposing the appropriate boundary conditions on the cylinder's surface [15]. Specifically, the parallel to the cylinder axis component of the scattered magnetic/electric field is proportional to $\sum_{m=-\infty}^{\infty} a_m^{\text{P}} \mathbf{N}_{em,k_h}$ where $\mathbf{N}_{em,k_h} = k_h H_m(k_h \rho) \cos(m\varphi) \hat{\mathbf{z}}$ denotes the m -th order cylindrical harmonic and the coefficient a_m^{P} denotes the Mie scattering coefficient of the m -th mode for polarization $\text{P} = \{\text{TE}, \text{TM}\}$, which is given [9], [120] by

$$a_m^{\text{TE}} = \frac{\eta_h J_m(k_c R) J'_m(k_h R) - \eta_c J_m(k_h R) J'_m(k_c R)}{\eta_c J'_m(k_c R) H_m(k_h R) - \eta_h H'_m(k_h R) J_m(k_c R)} \quad (5.2)$$

$$a_m^{\text{TM}} = \frac{\eta_h J'_m(k_c R) J_m(k_h R) - \eta_c J'_m(k_h R) J_m(k_c R)}{\eta_c J_m(k_c R) H'_m(k_h R) - \eta_h H_m(k_h R) J'_m(k_c R)} \quad (5.3)$$

where $k_h = \sqrt{\epsilon_h \mu_h} \omega / c$ is the wavenumber in the host material, $k_c = \sqrt{\epsilon_c \mu_c} \omega / c$ is the wavenumber in the cylinder and $\eta_c = \sqrt{\mu_c / \epsilon_c}$, $\eta_h = \sqrt{\mu_h / \epsilon_h}$ denote the impedances of the cylinder and the host material respectively. J_m and H_m stand for the Bessel and Hankel function (respectively) of the first kind and order m , and J'_m and H'_m are their derivatives in respect to their argument.

The dominant modes for each case can be identified from the extinction efficiency, Q_{ext} , which is defined as the sum of the electromagnetic field energy scattered and absorbed by the cylinder, normalized to the incident energy and the geometric cross section of the cylinder, $2R$.

In terms of the scattering coefficients it can be written as¹

$$Q_{\text{ext}}^{\text{P}} = -\frac{2}{|k_h R|} \text{Re} \left[a_0^{\text{P}} + 2 \sum_{m=1}^{\infty} a_m^{\text{P}} \right] \quad (5.4)$$

and it can be decomposed into scattering efficiency, Q_{sc} , and absorption efficiency, Q_{abs} , given by

$$Q_{\text{sc}}^{\text{P}} = \frac{2}{|k_h R|} \left[|a_0^{\text{P}}|^2 + 2 \sum_{m=1}^{\infty} |a_m^{\text{P}}|^2 \right] \quad (5.5)$$

$$Q_{\text{abs}}^{\text{P}} = Q_{\text{ext}}^{\text{P}} - Q_{\text{sc}}^{\text{P}} \quad (5.6)$$

The resonances in the extinction spectra of the cylinders (also known as Mie resonances [8]) can be classified by their polarization P and an integer m associated with the corresponding cylindrical harmonic. The resonance frequencies or eigenfrequencies of the system can be calculated by setting the denominators of the scattering coefficients for each polarization, Eq. (5.2) for TE and Eq. (5.3) for TM, equal to zero:

$$\frac{1}{\eta_c} \frac{J_m(k_c R)}{J'_m(k_c R)} = \frac{1}{\eta_h} \frac{H_m(k_h R)}{H'_m(k_h R)} \quad (5.7)$$

$$\eta_c \frac{J_m(k_c R)}{J'_m(k_c R)} = \eta_h \frac{H_m(k_h R)}{H'_m(k_h R)} \quad (5.8)$$

In the limit $k_h R \ll 1$ (where a system of cylinders behaves as a metamaterial) it is sufficient to consider only the first two fundamental modes, i.e. $m = 0$ and $m = 1$, since the contribution of higher order modes is insignificant. In the discussion below, these modes are identified as TE₀, TE₁, TM₀ and TM₁ (for the fields distribution of those modes see Fig. 5.3). Using recurrence and other relations of Bessel functions [121] (e.g. $J'_0(x) = -J_1(x)$ and $H'_0(x) = -H_1(x)$) we see that for $\mu_h = \mu_c$ the eigenfrequency relations of the TE₀ and the TM₁ modes are identical; therefore, TE₀ and the TM₁ modes are degenerate.

To explore the eigenfrequency relations of the above modes in the limits of small size parameters $k_h R$ and $k_c R$, we use the limiting expressions of Bessel functions [121] listed in Appendix 5.5.1. For the TM₁ mode, in the limit of $k_h R \ll 1$ we have

$$\eta_c \frac{J_1(k_c R)}{J'_1(k_c R)} = -\eta_h k_h R = -\mu_h \frac{\omega}{c} R \quad (5.9)$$

In the quasistatic limit of both $k_h R \ll 1$ and $k_c R \ll 1$ the TM₁ resonance condition becomes

$$\mu_c = -\mu_h \quad (5.10)$$

Thus, the TM₁ mode does not present resonances in the quasistatic limit, except in the case of a magnetic host or cylinder. For the TE₀ in the limit of $k_h R \ll 1$ we have

$$\frac{1}{\eta_c} \frac{J_0(k_c R)}{J'_0(k_c R)} = \varepsilon_h \left[\ln \left(\frac{k_h R}{2} \right) + \gamma - i \frac{\pi}{2} \right] \frac{\omega}{c} R \quad (5.11)$$

where γ is Euler's constant. In the quasistatic limit of both $k_h R \ll 1$ and $k_c R \ll 1$, the resonance condition has solutions only if $1/\mu_c \rightarrow 0$ in this limit.

In an analogous way one can obtain limiting expressions also for the TM₀ mode; in the limit of $k_h R \ll 1$

$$\eta_c \frac{J_0(k_c R)}{J'_0(k_c R)} = \mu_h \left[\ln \left(\frac{k_h R}{2} \right) + \gamma - i \frac{\pi}{2} \right] \frac{\omega}{c} R \quad (5.12)$$

¹In literature [9], [97] there is no minus sign in the extinction efficiency; it is due to the definition of the coefficients a_m with an extra minus sign (see Appendix 5.5.1).

In the quasistatic limit, of both $k_h R \ll 1$ and $k_c R \ll 1$, we can have resonance in the case that $1/\varepsilon_c \rightarrow 0$, a condition that can be fulfilled in the case of a polaritonic cylinder, with the resonance frequency to coincide with the phonon polariton resonance frequency of the cylinder material.

Finally, for the TE_1 mode in the limit of $k_h R \ll 1$ we obtain

$$\frac{1}{\eta_c} \frac{J_1(k_c R)}{J'_1(k_c R)} = -\frac{1}{\eta_h} k_h R = -\varepsilon_h \frac{\omega}{c} R \quad (5.13)$$

In the limit $k_h R \ll 1$ and $k_c R \ll 1$ the resonance condition becomes

$$\varepsilon_c = -\varepsilon_h. \quad (5.14)$$

Equation (5.14), which can be fulfilled in the case of a polaritonic cylinder (owing to its metal-like behavior in frequencies above the phonon-polariton resonance frequency), is identical to the resonance condition of a Surface Plasmon Polariton (SPP) mode in a dielectric-metal planar interface [122].

5.2.2 Effective medium

We now calculate the components of the effective medium permittivity and permeability tensors for a uniaxial anisotropic system of infinitely long parallel circular cylinders employing a Coherent Potential Approximation (CPA) based approach as developed by Wu *et al.* [104]. As was already mentioned, unlike the quasistatic Maxwell-Garnett approximation [96], which is valid only when all $k_h R$, $k_c R$ and $k_{\text{eff}} R$ are much less than unity, the CPA approach allows application in higher frequency regions, where particle resonances occur (and thus interesting metamaterial effects), allowing treatment of metamaterials made of high-index dielectric or polaritonic scatterers. A considerable advantage of CPA over other suitable effective medium approaches (like the field-averaging method [101], [107]) is that the effective parameters are given in a closed form as we will see below. Moreover, the effective parameters do not depend on the specific lattice-type of the system to be described, as it would be in the case of extended Maxwell-Garnett approaches [123] applied in two-dimensional systems [124].

Regarding our systems, as an implication of symmetry, for a proper choice of axes, that is the cylinders are oriented along the z axis, the effective electric permittivity and magnetic permeability must be uniaxial, i.e. diagonal tensors with only two free parameters. In dyadic form they can be written as $\varepsilon_{\text{eff}} = \varepsilon_{\text{eff}}^{\perp}(\hat{x}\hat{x} + \hat{y}\hat{y}) + \varepsilon_{\text{eff}}^{\parallel}\hat{z}\hat{z}$ and $\mu_{\text{eff}} = \mu_{\text{eff}}^{\perp}(\hat{x}\hat{x} + \hat{y}\hat{y}) + \mu_{\text{eff}}^{\parallel}\hat{z}\hat{z}$ respectively, where \hat{x} , \hat{y} and \hat{z} are the unit vectors along the axes, and the symbols \parallel and \perp denote that the corresponding field (electric for ε and magnetic for μ) is parallel and perpendicular (respectively) to the cylinders axis.

In order to derive semi-analytical expressions for the components of the effective parameters in the framework of CPA we should require vanishing of the scattering between effective and actual medium. To apply this requirement we consider the scattering configuration shown in Fig. 5.2(c), where the actual medium is represented by a coated cylindrical inclusion (of infinite height) with core of radius $R_1 = R$ and material the same as the original cylinders, and coating of thickness $R_2 - R_1$ made of the host material of the original system; the coated inclusion is embedded in the homogeneous effective medium with relative electric permittivity ε_{eff} and magnetic permeability μ_{eff} . The radius R_2 of the coated inclusion is defined by the filling ratio, f , of the cylinders in the original system, as $f = R_1^2/R_2^2$. In order for the effective medium of Fig. 5.2(c) to be the one accurately describing our inhomogeneous system CPA requires the scattering cross section from the embedded into the effective medium coated cylinder to be identically zero. Hence, all the scattering coefficients of the coated inclusion must be set equal to zero, which, after some algebraic manipulations (see Appendix 5.5.1), leads to the following

condition:

$$a_m^P(R_1; c, h) = a_m^P(R_2; \text{eff}, h) \quad (5.15)$$

In Eq. (5.15) $a_m^P(R; A, B)$ stands for the m -th order scattering coefficient for a cylinder with radius R made of a material A immersed in a host made of material B for polarization P . Equation (5.15) defines an infinite system of nonlinear equations which has to be solved self-consistently for the components ε_{eff} and μ_{eff} to be obtained. However, in the region of $k_h R < 1$, which is the region of interest for metamaterials, we can limit ourselves only to the first two modes per polarization, $m = 0$ and $m = 1$; then, assuming also that $k_{\text{eff}} R_2 \ll 1$ (k_{eff} is the wavevector norm in the effective medium), we can derive semi-analytical relations for all the components of the effective material tensors (see Appendix 5.5.1), which read as

$$\varepsilon_{\text{eff}}^{\parallel} = -\frac{2\varepsilon_h}{k_h R_2} \left[\frac{J'_0(k_h R_2) + H'_0(k_h R_2)a_0^{\text{TM}}}{J_0(k_h R_2) + H_0(k_h R_2)a_0^{\text{TM}}} \right] \quad (5.16)$$

$$\mu_{\text{eff}}^{\perp} = \frac{\mu_h}{k_h R_2} \left[\frac{J_1(k_h R_2) + H_1(k_h R_2)a_1^{\text{TM}}}{J'_1(k_h R_2) + H'_1(k_h R_2)a_1^{\text{TM}}} \right] \quad (5.17)$$

$$\mu_{\text{eff}}^{\parallel} = -\frac{2\mu_h}{k_h R_2} \left[\frac{J'_0(k_h R_2) + H'_0(k_h R_2)a_0^{\text{TE}}}{J_0(k_h R_2) + H_0(k_h R_2)a_0^{\text{TE}}} \right] \quad (5.18)$$

$$\varepsilon_{\text{eff}}^{\perp} = \frac{\varepsilon_h}{k_h R_2} \left[\frac{J_1(k_h R_2) + H_1(k_h R_2)a_1^{\text{TE}}}{J'_1(k_h R_2) + H'_1(k_h R_2)a_1^{\text{TE}}} \right] \quad (5.19)$$

where $a_m^P = a_m^P(R_1; c, h)$. As can be seen in Eqs. (5.16)-(5.19), each one of the effective parameters is related with a particular mode in the single scattering cross section. This connection, justifying the characterization of the modes as electric and magnetic, can be understood also physically by observing the field distribution corresponding to those modes - see Fig. 5.5 and Section 5.3.1.

Equations (5.16)-(5.19) under certain conditions can lead to resonances in the effective parameters, associated with interesting propagating and scattering effects for the composite structure as we will discuss in the next section. For $k_h R_2 \ll 1$ (thus also $k_h R_1 \ll 1$) the resonance conditions/frequencies (obtained by setting the denominators equal to zero and employing limiting expressions for the Bessel functions - see Appendix 5.5.1) are approximated as follows.

For $\varepsilon_{\text{eff}}^{\parallel}$ (related to TM_0 mode):

$$\eta_c \frac{J_0(k_c R_1)}{J'_0(k_c R_1)} = \mu_h \ln(R_2/R_1) \frac{\omega}{c} R_1 = -\frac{1}{2} \mu_h \ln(f) \frac{\omega}{c} R_1 \quad (5.20)$$

For μ_{eff}^{\perp} (related to TM_1 mode):

$$\eta_c \frac{J_1(k_c R_1)}{J'_1(k_c R_1)} = \frac{f+1}{f-1} \mu_h \frac{\omega}{c} R_1 \quad (5.21)$$

For $\mu_{\text{eff}}^{\parallel}$ (related to TE_0 mode):

$$\frac{1}{\eta_c} \frac{J_0(k_c R_1)}{J'_0(k_c R_1)} = \varepsilon_h \ln(R_2/R_1) \frac{\omega}{c} R_1 = -\frac{1}{2} \varepsilon_h \ln(f) \frac{\omega}{c} R_1 \quad (5.22)$$

For $\varepsilon_{\text{eff}}^{\perp}$ (related to TE_1 mode):

$$\frac{1}{\eta_c} \frac{J_1(k_c R_1)}{J'_1(k_c R_1)} = \frac{f+1}{f-1} \varepsilon_h \frac{\omega}{c} R_1 \quad (5.23)$$

One can see that the above relations (5.20)-(5.23) are very similar with the corresponding conditions for single scattering resonances discussed in the previous subsection. In particular,

Eqs. (5.21) and (5.23) for low cylinder filling ratio f lead to resonance frequencies very close to those of the corresponding TM_1 and TE_1 , respectively, single cylinder resonances - see Eqs. (5.9) and (5.13) respectively.

Finally, in the quasistatic limit (i.e. for a $k_h R_2 \ll 1$, $k_h R_1 \ll 1$ and $k_c R_1 \ll 1$), Equations (5.16)-(5.19) reduce to the well-known MG formulae:

$$\varepsilon_{\text{eff}}^{\parallel} = f\varepsilon_c + (1 - f)\varepsilon_h \quad (5.24)$$

$$\mu_{\text{eff}}^{\parallel} = f\mu_c + (1 - f)\mu_h \quad (5.25)$$

$$\varepsilon_{\text{eff}}^{\perp} = \varepsilon_h \frac{(1 + f)\varepsilon_c + (1 - f)\varepsilon_h}{(1 - f)\varepsilon_c + (1 + f)\varepsilon_h} \quad (5.26)$$

$$\mu_{\text{eff}}^{\perp} = \mu_h \frac{(1 + f)\mu_c + (1 - f)\mu_h}{(1 - f)\mu_c + (1 + f)\mu_h} \quad (5.27)$$

5.3 Results and Discussion

5.3.1 Single scattering

We begin our analysis by calculating the extinction efficiency of a LiF cylinder in air ($\varepsilon_h = 1$, $\mu_h = 1$) and in a host with $\varepsilon_h = 2$, $\mu_h = 1$, and for a SiC cylinder in air, for both TM and TE polarizations and various radii. The dielectric functions of both LiF and SiC, which are shown in Fig. 5.1, are calculated using Eq. (5.1) with parameters tabulated in Table 5.1. The extinction efficiency results for the LiF and the SiC cylinders are shown in Figs. 5.3 and 5.4, respectively. It is apparent that for each polarization there are two dominant resonances in the low-frequency extinction spectra which originate from the $m = 0$ and $m = 1$ modes. Using the notation defined in Sec. 5.2.1 we have the TE_0 , TE_1 , TM_0 and TM_1 modes, where the TE_0 and TM_1 modes resonate at the same frequency, as was also discussed in Section 5.2.1. Illustrations of the fields for each of these four modes are shown in Fig. 5.3(e). From the field illustrations one can characterize the modes as electric in nature (i.e. associated with strong induced electric field in the direction of the incoming field), as TM_0 and TE_1 , and magnetic in nature (i.e. with strong induced magnetic field in the direction of the incoming magnetic field), as TE_0 and TM_1 .

As can be observed in both Figs. 5.3 and 5.4, only the TE_1 mode falls in the negative permittivity region of the polaritonic materials (shaded region in the plots) and is similar in nature to the Localized Surface Plasmon Resonance (LSPR) [125] sustained by metallic particles in the visible part of the spectrum. For very small radii the mode frequency approaches the quasi-static limit ($k_h R \ll 1$ and $k_c R \ll 1$) value, where $\varepsilon_h = -\varepsilon_c(\omega_{\text{res}})$. This relation suggests that the resonance frequency of the TE_1 mode is affected greatly by the environment of the cylindrical particle. To the contrary, there is no significant dependence of the resonance frequencies of the TE_0 , TM_1 and TM_0 modes on the host parameters (only the values of Q_{ext} change). This result can be partially explained by the fact that we are in the high-index dielectric regime for the cylinder and that the electric fields for these modes are concentrated in or at the surface of the cylinder as related field simulations show. On the other hand this is not true for the TE_1 mode, where the electric field is dipole-like and highly extends into the dielectric.

We turn now our focus on the dependence of resonances on the radius of the polaritonic cylinder. In Fig. 5.5 we plot the resonance frequencies for a LiF (panel (a)) and a SiC (panel (b)) cylinder in air as a function of cylinder radius, indicating also the ratio of absorption over scattering $Q_{\text{abs}}/Q_{\text{sc}}$ of each mode (the resonance frequencies were obtained by solving Eqs. (5.7) and (5.8) numerically for $m = 0$ and $m = 1$). For small radii only the modes of electric nature appear; i.e. TM_0 and TE_1 . For TM polarization, where the incident electric field (parallel to the cylinder) does not experience any "boundaries", the only factor affecting the induced polarization is the polarizability of the bulk material; the resulting mode is the

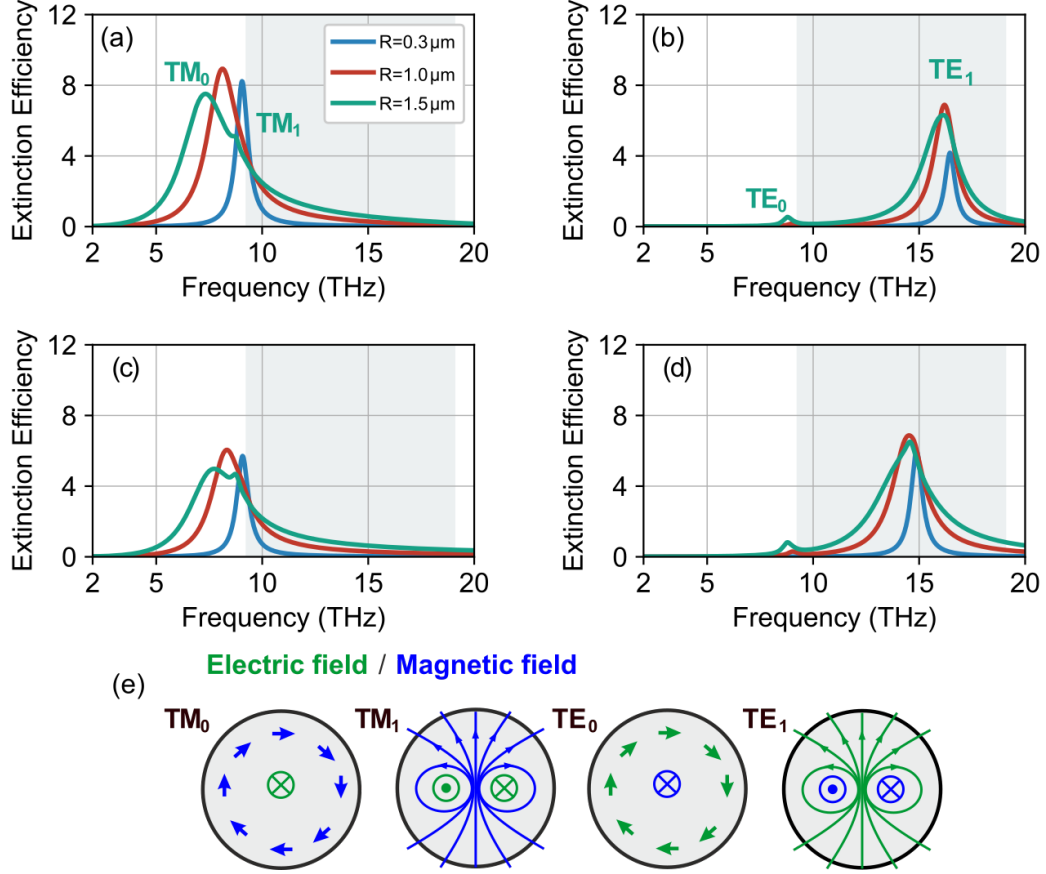


Figure 5.3: Extinction efficiency of a LiF cylinder in air [(a),(b)] and in a dielectric with $\epsilon_h = 2$ [(c),(d)] for TM (left column) and TE (right column) polarizations. The legend shows the cylinder radius. The shaded areas correspond to the frequency region where the dielectric function of LiF is negative. (e) Electric (green color) and magnetic (blue color) field distributions for the TM_0 , TM_1 , TE_0 and TE_1 modes.

spherically symmetric TM_0 mode, with resonance for small radius values almost at the bulk material resonance frequency, ω_T . The resonance frequency moves to lower values as the radius of the cylinder increases and the wavelength inside the cylinder becomes comparable to the radius. This departure of TM_0 resonance frequency from ω_T is faster for the SiC cylinder due to the higher permittivity values and the associated smaller wavelength inside the cylinder. In both TE_1 and TM_0 modes absorption dominates extinction for small radii, as can be concluded from Fig. 5.5(a), but for larger radii scattering takes over, as happens also in the case of a metallic cylinder. In the SiC case (Fig. 5.5(b)) though, the dominance of the scattering over absorption for the TM_0 mode occurs in very small radius values (even smaller than $0.1\mu\text{m}$, which is the threshold value of Fig. 5.5(b)), and the absorption cross-section for R larger than $0.2\mu\text{m}$ is practically negligible. This can be explained by the quicker departure of the TM_0 mode from ω_T resonance where the losses of SiC are quite high, combined with the much higher quality factor of SiC compared to LiF (note that for SiC $\Gamma/\omega_T \approx 0.006$ while for LiF $\Gamma/\omega_T \approx 0.057$).

The TE_0 and TM_1 modes, appearing for radius values larger than $0.5\mu\text{m}$ for LiF and $0.4\mu\text{m}$ for SiC, appear also just below optical phonon frequency ω_T . Their resonance frequency changes only slightly with the increase of the radius. Moreover, absorption dominates over scattering for small radii and as the radius increases scattering starts to take over. For the case of LiF this happens for radii much larger than those studied here. This is probably not-surprising taking into account the weak extinction cross-section of the TE_0 and TM_1 modes and the fact

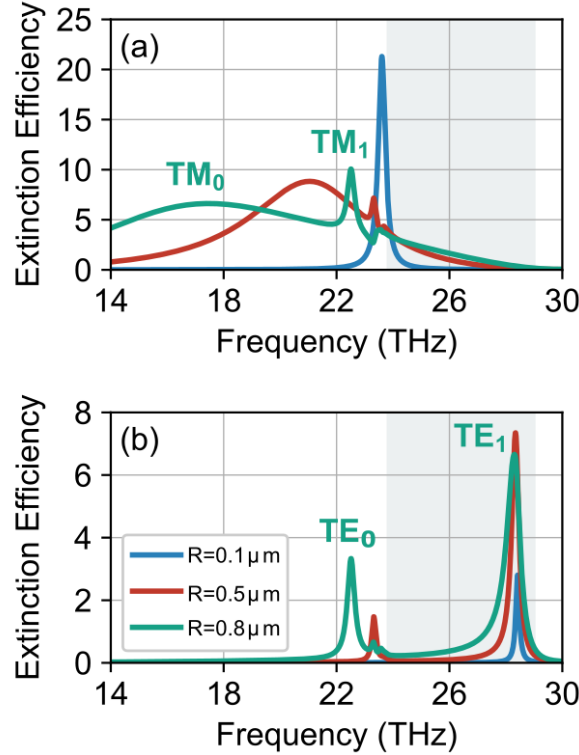


Figure 5.4: Extinction efficiency of a SiC cylinder (of radius 0.1, 0.5 and $0.8 \mu\text{m}$) in air for (a) TM and (b) TE polarizations. The shaded areas correspond to the frequency region where the dielectric function of SiC is negative.

that their resonance frequency is (and remains) relatively close to the resonance frequency ω_T where the material losses are quite high. Indicative plots of LiF and SiC absorption and scattering efficiencies for different cylinder radii are presented in Appendix 5.5.2.

Calculating the quality factor, Q , of the different modes dominating the long wavelength extinction response of LiF and SiC cylinders, with $Q = -\text{Re}[\omega_{\text{res}}]/(2\text{Im}[\omega_{\text{res}}])$, we obtain the result shown in Figs. 5.5(c) for LiF and 5.5(d) for SiC. We observe that for small cylinder radii the quality factor of the TE₁ mode, which is sensitive to the environment and thus suitable for sensing applications, gets values higher than 20 for LiF and higher than 100 for SiC cylinders. Such values are higher than the corresponding ones of plasmonic antennas (of the same size parameter, $k_h R$) in the visible [126]–[128], indicating the suitability of polaritonic rods in sensing applications in the THz and IR part of the EM spectrum. Regarding the "magnetic" modes TE₀/TM₁, for LiF their quality factor changes very slowly with increasing radius and retains values close to 18 (17.59 for $R = 0.5 \mu\text{m}$ to 17.12 for $R = 1.6 \mu\text{m}$). For SiC their quality factor decrease with increasing radius occurs much more quickly due to the much lower Γ/ω_T and the quicker departure of the resonance frequency from the highly lossy region around ω_T .

5.3.2 Effective Medium

We can now turn our attention to the calculation of effective medium material parameters ε_{eff} and μ_{eff} for systems comprised of polaritonic cylinders in a host. In Fig. 5.6 we plot all the components of the relative effective permittivity and permeability tensors, both real and imaginary parts, for LiF cylinders in air for the same set of radii discussed in Section 5.2.1 for single scattering, i.e. 0.3 , 1 and $1.5 \mu\text{m}$, and LiF filling ratio 30%. We also plot the effective

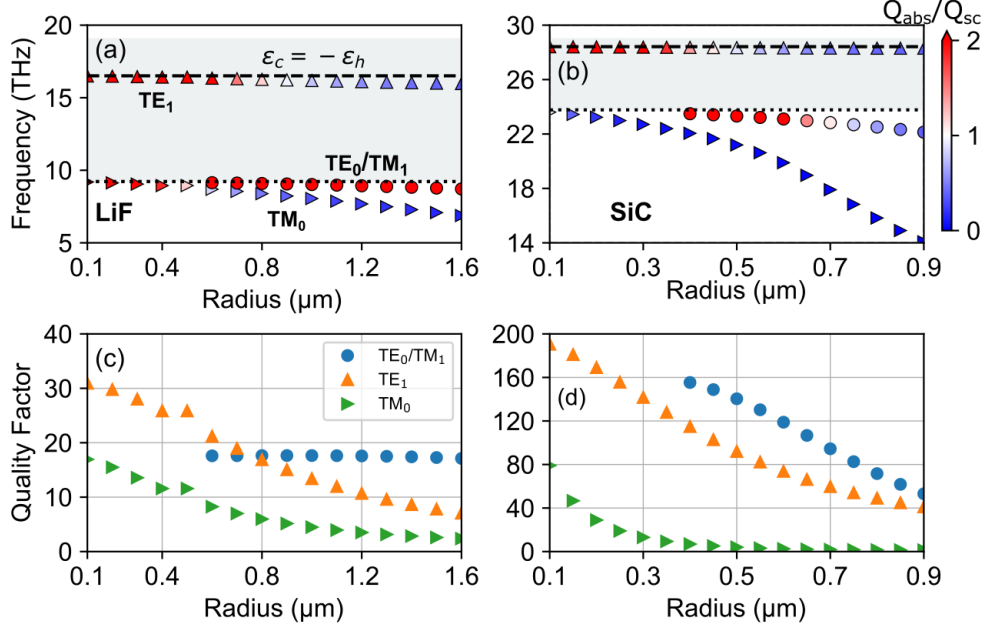


Figure 5.5: Top panels: Resonance frequencies and absorption over scattering efficiency $Q_{\text{abs}}/Q_{\text{sc}}$ (color) at the resonance frequency of the TM_0 (rotated triangles), TE_0/TM_1 (circles) and the TE_1 (upright triangles) modes as function of the radius for a (a) LiF and a (b) SiC cylinder in air ($\epsilon_h = 1$). The dashed line shows the quasi-static resonance condition for the TE_1 $\epsilon_c(\omega) = -\epsilon_h$, and the shaded area corresponds to the frequency region where the dielectric functions of LiF and SiC are negative. Bottom panels: Quality factor $-\text{Re}(\omega_{\text{res}})/(2\text{Im}(\omega_{\text{res}}))$ for the modes of a (c) LiF and (d) SiC cylinder in air.

permittivities in the quasistatic limit ($k_h R \ll 1$ and $k_c R \ll 1$) using the Maxwell-Garnett approximation (see Eq. (5.24)) [96]. Since $\mu_h = \mu_c = 1$ the effective magnetic permeabilities in the quasistatic limit are both equal to unity. As one can see in Fig. 5.6, the effective permittivities and permeabilities exhibit Lorentzian-type resonances at frequencies close to their associated mode eigenfrequencies of a single cylinder, shown in Fig. 5.5. In a similar fashion to the single-cylinder eigenmodes, the resonances in the effective parameters move to lower frequencies and the maximum values of ϵ_{eff} and μ_{eff} increase for larger radii.

In particular, the so called electric modes, TM_0 , TE_1 , lead to effective permittivity resonances, while the magnetic modes, TM_1 , TE_0 , to effective permeability resonances. Since the magnetic modes do not appear/resonate in the quasistatic regime (i.e. for small cylinder radii) the permeability resonances are not present in that regime, in agreement also with the MG formulation. In fact the accurate description and reproduction of magnetic effects in non-magnetic composites is one of the great merits of CPA regarding metamaterial effects and capabilities.

Regarding the effective permittivity of Fig. 5.6, while for small cylinder radius the CPA results coincide with the (size independent) Maxwell-Garnett results, as we increase the cylinder radius, exciting more resonances and thus more rich electromagnetic response, the Maxwell-Garnett is not able to describe the response of the inhomogeneous medium and thus to reproduce the achievable metamaterial properties.

A demonstration of this inability and the accuracy and success of our CPA approach is given in Fig. 5.7, where we compare the Maxwell-Garnett and the CPA results with full wave simulations for a polaritonic system that has been realized also experimentally [105]; that is a system of LiF cylinders (of radius $1.3\mu\text{m}$ and filling ratio 6.95%) in a KCl host. The results of Fig. 5.8, as well as analogous results for systems with smaller or larger cylinder radii, clearly

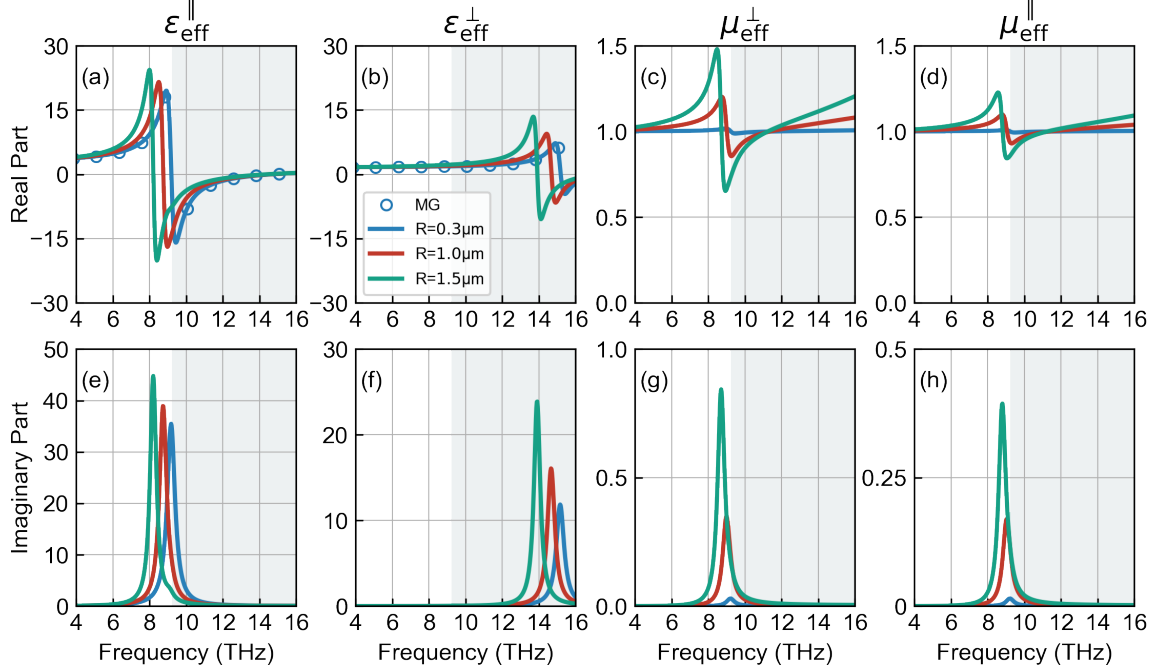


Figure 5.6: Real (upper row) and imaginary (lower row) parts of the parallel and perpendicular components of the relative effective permittivity, ϵ_{eff} (first and second columns), and permeability, μ_{eff} (third and fourth columns), for LiF cylinders with filling ratio 30% in air, for different radii, R , (mentioned in the legends) using the CPA (lines) and the Maxwell-Garnett approximation (circles). The shaded areas correspond to the frequency region where the dielectric function of LiF is negative.

demonstrate that CPA can describe with satisfactory accuracy the electromagnetic response of structures with larger-size cylinders (i.e. of $k_c R \approx 1$), polaritonic or high-index-dielectric.

We have to add here that the observed in Fig. 5.7 slight discrepancy between CPA and full-wave simulation results at around 8 THz is due to the fact that in this region $k_{\text{eff}}^{\text{TM}} R_2 \approx 3$, which is beyond the regime of validity of CPA - note that the semi-analytical CPA formulas have been obtained under the condition $k_{\text{eff}} R_2 < 1$. Besides that condition, which is specific to the current implementation of the CPA, in general, for higher frequencies, such as $k_h R_2 > 1$, where the structures are not sub-wavelength anymore and higher order modes (not considered here) along with lattice effects start to become important, the CPA (such as almost all the homogeneous medium descriptions) becomes less and less accurate.

Coming back to our model systems, in Fig. 5.8 we plot the components of the relative effective permittivity and permeability tensors for SiC cylinders in air for radii 0.1, 0.5 and $0.8 \mu\text{m}$ (the same ones discussed in connection with Fig. 5.4). The filling fraction also here is chosen to be equal to 30%. As in the case of LiF in air, we observe also here resonant permittivity and permeability, closely connected with single cylinder resonances, as discussed in the case of Fig. 5.6. A significant difference here is the stronger magnetic response leading to even negative permeability values; this is a result of the higher permittivity values of SiC compared to LiF (compare the permittivity values of Fig. 5.1(a) and 5.1(b)), and thus of the stronger displacement current.

A closer examination of Figs. 5.6 and 5.8 indicates that there is a variety of interesting and useful metamaterial properties achievable by our polaritonic rod systems. These include (a) engineerable permittivity response comprising of both high positive values, negative values, and near-zero values; (b) engineerable permeability, including negative permeability values; (c) double-negative response, i.e. permittivity and permeability both negative, resulting to negative refractive index response; (d) hyperbolic response. Below we comment in more detail

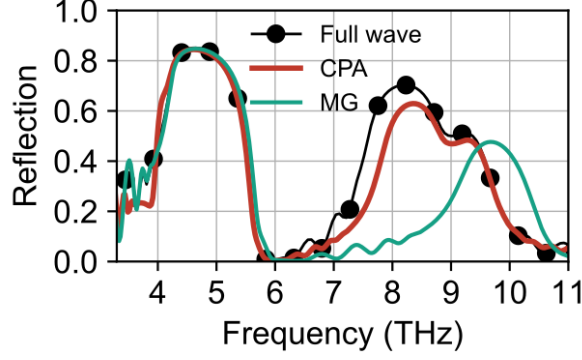


Figure 5.7: Normal incidence, TM reflection spectra for a slab of LiF cylinders with radius $R = 1.3\mu\text{m}$ and filling ratio $f = 6.95\%$ in KCl host in a square arrangement. The reflection is calculated by the commercial finite element method electromagnetic solver Comsol Multiphysics, considering a computational system of 7 unit cell thickness (along propagation direction). The full wave reflection results (black line and dots) are compared with results for a homogeneous effective medium of the same thickness as the actual system and effective parameters obtained through CPA (red line) and Maxwell-Garnett approximation (green line). KCl was modelled using Eq. (5.1) with parameters $\varepsilon_\infty = 2.045$, $\omega_T/2\pi = 4.21\text{THz}$, $\omega_L/2\pi = 6.196\text{THz}$ and $\Gamma/2\pi = 0.156\text{THz}$ [105].

on the above properties and response, generalizing to any polaritonic-rod-based composite. Moreover in Appendix 5.5.3 we present also plots of the effective permittivity and permeability components shown in Figs. 5.6 and 5.8 in a smaller vertical-axis range, to reveal and highlight the values of the effective components away from the resonances.

A. Engineerable permittivity response: Although in the bulk polaritonic materials we already have a rich permittivity response, including both positive, negative and near-zero values, structuring the polaritonic material in the form of cylinders we have the potential to engineer the permittivity values, reaching negative values even below the resonance of the corresponding bulk material (compare, e.g., Fig. 5.1(a) and Fig. 5.6(a) or Fig. 5.1(b) and Fig. 5.8(a)), reaching *desired* negative (or positive) values different than those of the bulk material as, e.g., to, adjust the impedance of the system with that of its surrounding medium, combining properly the real and imaginary parts of the effective ε as, e.g., to reduce losses in the region of operation, moving the epsilon-near-zero response in the desired frequency range, etc. The effective permittivity values can be engineered by changing either the cylinders radii or the cylinders filling ratio. *B. Engineerable permeability response:* As Fig. 5.8 shows, in properly designed systems of polaritonic rods, owing to the large permittivity values of the polaritonic materials, we have the ability to achieve resonant permeability associated with negative values for both TE and TM polarization if the underlying single-cylinder resonance is strong enough. The negative permeability response is favored by polaritonic materials of high ε (compare the LiF with the SiC case), by cylinders of larger radii (as $k_c R \approx 1$) and by large cylinder filling ratio. As in the permittivity case, the effective permeability values can be engineered by changing either the cylinders radii or the cylinders filling ratio.

C. Double negative response: Regarding the double negative response resulting to negative refractive index, in the SiC system shown in Fig. 5.8 we see that such a response is achievable (for TM polarization and normal incidence) for both $R = 0.5\mu\text{m}$ and $R = 0.8\mu\text{m}$. (For $R = 0.8\mu\text{m}$ $\varepsilon_{\text{eff}}^{\parallel}$ and μ_{eff}^{\perp} are both negative between 22.2THz and 22.8THz). Adjusting the cylinder radii or the filling ratio, one can engineer this response, engineering thus the effective impedance of the system and the effective refractive index. Having the potential to engineer separately refractive index and impedance offers a valuable tool for wave propagation manipulation, as it allows

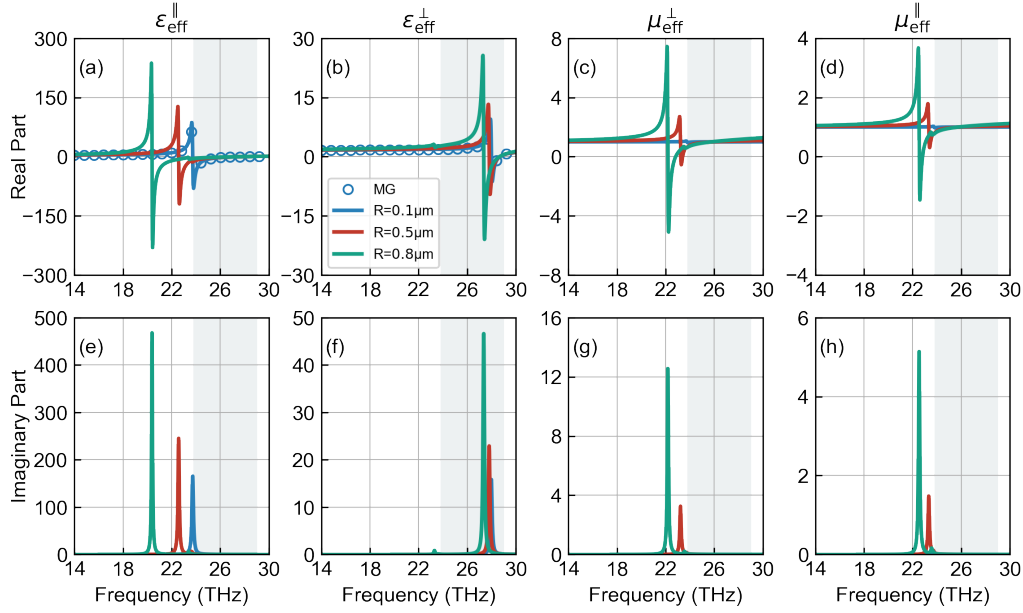


Figure 5.8: Real (upper row) and imaginary (lower row) parts of the parallel and perpendicular components of the relative effective permittivity ε (first and second columns), and permeability, μ (third and fourth columns), for SiC cylinders with filling ratio 30% in air, for different radii, R (mentioned in the legends), using the CPA (lines) and the Maxwell-Garnett approximation (circles). The shaded areas correspond to the frequency region where the dielectric function of SiC is negative.

perfect coupling to the surrounding medium or perfect transmission combined with desired phase propagation features.

D. *Hyperbolic response*: Taking into account the dispersion relations for TM and TE modes [129], i.e.

$$\text{TM} : \frac{k_{\perp}^2}{\mu_{\text{eff}}^{\perp} \varepsilon_{\text{eff}}^{\parallel}} + \frac{k_{\parallel}^2}{\mu_{\text{eff}}^{\perp} \varepsilon_{\text{eff}}^{\perp}} = \left(\frac{\omega}{c}\right)^2 \quad (5.28)$$

$$\text{TE} : \frac{k_{\perp}^2}{\varepsilon_{\text{eff}}^{\perp} \mu_{\text{eff}}^{\parallel}} + \frac{k_{\parallel}^2}{\varepsilon_{\text{eff}}^{\perp} \mu_{\text{eff}}^{\perp}} = \left(\frac{\omega}{c}\right)^2 \quad (5.29)$$

(where k_{\perp} and k_{\parallel} refer to the perpendicular and parallel to the cylinders axes wavevector components), along with the results of Figs. 5.6 and 5.8, one can see that the condition for hyperbolic response for the TM modes for $\mu_{\text{eff}}^{\perp} > 0$, i.e. $\varepsilon_{\text{eff}}^{\parallel} \cdot \varepsilon_{\text{eff}}^{\perp} < 0$, can be easily achieved for both the LiF and SiC systems in two different frequency regions even in the quasistatic limit. In the first region, around ω_T and near the TM_0 resonance frequency, the out-of-plane components $\varepsilon_{\text{eff}}^{\parallel}$ are negative for all radii (at least for $R > 0.1 \mu\text{m}$) while the in-plane components $\varepsilon_{\text{eff}}^{\perp}$ are positive; the medium in this case is called *Hyperbolic Metamaterial Type I (HMM I)*. The second region where hyperbolic response due to different signs of the ε_{eff} components is feasible is close to the TE_1 resonance, where $\varepsilon_{\text{eff}}^{\perp}$ are negative and $\varepsilon_{\text{eff}}^{\parallel}$ positive. The medium in this case is called *Hyperbolic Metamaterial Type II (HMM II)* and it is considered more suitable (than HMM I) for the so-called dark field superlensing [84] (requiring filtering out of the small wavenumbers) and for the achievement of high Purcell factors [107].

The hyperbolic-response-related merit of our systems (and of many polaritonic systems) is not restricted though only to TM polarization and the above mentioned features. There additional and important features stemming from the possibility of also negative μ_{eff} besides negative ε_{eff} , which exists in our SiC systems.

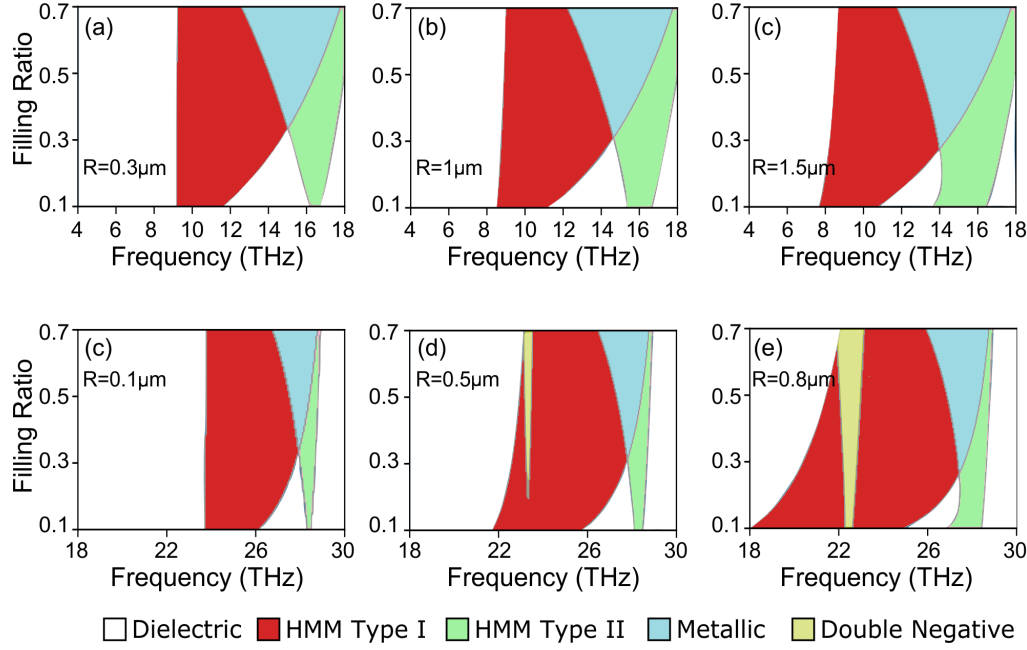


Figure 5.9: Optical phase diagrams for the TM modes for LiF (top row) and SiC (bottom row) cylinders in air for different radii, R , of the cylinders. The color marks the different attainable metamaterial-related responses of the systems: Dielectric (White color): Both $\varepsilon_{\text{eff}}^{\parallel} > 0$, $\varepsilon_{\text{eff}}^{\perp} > 0$, $\mu_{\text{eff}}^{\parallel} > 0$, $\mu_{\text{eff}}^{\perp} > 0$, HMM Type I (red): $\varepsilon_{\text{eff}}^{\parallel} < 0$, $\varepsilon_{\text{eff}}^{\perp} > 0$, HMM Type II (green): $\varepsilon_{\text{eff}}^{\parallel} > 0$, $\varepsilon_{\text{eff}}^{\perp} < 0$, Metallic (blue): $\varepsilon_{\text{eff}}^{\parallel} < 0$, $\varepsilon_{\text{eff}}^{\perp} < 0$, DNG (yellow): $\varepsilon_{\text{eff}}^{\parallel} < 0$, $\mu_{\text{eff}}^{\perp} < 0$.

As can be observed in Figs. 5.8 and 5.13 (in Appendix 5.5.3), for $R = 0.8 \mu\text{m}$, μ_{eff}^{\perp} is negative in the region 22.2-22.8 THz and $\mu_{\text{eff}}^{\parallel}$ is negative at 22.55-22.8 THz; since in these regions $\varepsilon_{\text{eff}}^{\parallel}$ is also negative while $\varepsilon_{\text{eff}}^{\perp}$ positive, taking into account the relations (5.28) and (5.29), one can see that in the region 22.2-22.54 THz there is hyperbolic response (HMM II) also for the TE polarization, own to the opposite sign of the two μ_{eff} components ($\mu_{\text{eff}}^{\perp} < 0$, $\mu_{\text{eff}}^{\parallel} > 0$). Moreover, in the region, 22.2-22.8 THz in which for TM polarization and normal incidence we achieve double negative response, one can see that for off-normal incidence the dispersion of the system is hyperbolic ($\varepsilon_{\text{eff}}^{\parallel} < 0$, $\mu_{\text{eff}}^{\perp} < 0$, $\varepsilon_{\text{eff}}^{\perp} > 0$) but with negative phase advance in the plane perpendicular to the cylinders. Such a peculiar feature may be associated with uncommon and still unexplored propagation characteristics and wave control possibilities. Moreover, the possibility for hyperbolic response own also to negative permeability components gives a great flexibility for dispersion engineering for arbitrary polarization (and for unpolarized light), and, besides, it gives the ability to highly control also the system impedance, issues crucial for both superlensing applications and applications related to thermal emission and radiation control [130].

Optical Phase Diagrams - Filling Ratio Influence

To illustrate further and more clearly the different attainable properties and capabilities of systems of polaritonic rods, we investigate for our two systems the frequency regions where the above mentioned interesting MM responses occur as we change the rods filling ratio, for the TM modes, based on Eq. (5.28). In Fig. 5.9 we plot for both systems (i.e. LiF and SiC) the optical phase diagrams, showing the different interesting optical response regions as a function of filling ratio and frequency, for various radii. There the different regions are marked with

different colors: With red the HMM I region, with green the HMM II, with yellow the DNG region (achievable for TM polarization - normal incident) and with blue the fully metallic region ($\varepsilon_{\text{eff}}^{\perp} < 0$ and $\varepsilon_{\text{eff}}^{\parallel} < 0$) for both polarizations. Regarding the hyperbolic response, for simplicity in the plots we mark only the regions of hyperbolic dispersion originating from the electric response. The magnetic-response-originated hyperbolic dispersion region is always embedded in the DNG region, in the same way as discussed in the last paragraph of the previous subsection, in connection with the data of Figs. 5.8 and 5.13.

As one can see in Fig. 5.9, there is a pattern on the achievable response: high- ε region at low frequencies is followed by a HMM I region starting near the optical phonon frequency ω_T and extending into the reststrahlen band ($\omega_T < \omega < \omega_L$). Moreover, for high frequencies ($\omega > \omega_T$) and high filling ratios there is a region (green areas in Fig. 5.9) where the material exhibits a purely metallic response (both $\varepsilon_{\text{eff}}^{\parallel} < 0$ and $\varepsilon_{\text{eff}}^{\perp} < 0$). In addition, the boundaries between the different optical phases correspond to frequencies where epsilon-near-zero is achievable since one or more of the components of the effective permittivity changes sign. Finally, the DNG region is always inside the HMM I region and requires polaritonic materials of high permittivity values (i.e. of strong phonon-polariton resonance) and not extremely subwavelength in size cylinders; moreover it is favored from larger cylinder filling ratios.

5.4 Conclusions

Prompted by the constantly growing interest on polaritonic and dielectric metamaterials, we presented here a detailed study of the electromagnetic response of metamaterial systems formed by polaritonic rods in a dielectric host, in the THz region of the electromagnetic spectrum. Employing as model systems systems of LiF and SiC rods, we initially studied the response of single rod and we calculated the extinction efficiency for different radii of the rod, in order to identify the nature and behavior of the major resonances for each polarization. Subsequently, using the single-rod scattering formulation and data and employing the Coherent Phase Approximation effective medium approach, which can accurately describe an inhomogeneous medium even beyond the quasistatic regime, we obtained closed formulas for the effective parameters of systems made of polaritonic rods in a host and we applied them in the cases of LiF and SiC rods. We found that by proper selection of the radius and the filling ratio of the rods one can achieve a variety of interesting and useful metamaterial properties in polaritonic rod systems. These properties include engineerable permittivity (having high positive, negative and near-zero values), engineerable permeability (of both positive and negative values), hyperbolic response, double negative response and others. The possibility to achieve this rich variety of physical properties in the THz region, which is of high technological interest, combined with the ease of fabrication of many of those systems, makes polaritonic rod metamaterials ideal candidates for any device aiming THz wave propagation and scattering control.

5.5 Appendices

5.5.1 Effective Medium Derivation

In this appendix we give a brief derivation of the relations for the effective medium. We consider a coated cylinder (along \hat{z} direction) with core radius R_1 and shell thickness $R_2 - R_1$ embedded in an infinite medium with material parameters $\varepsilon_{\text{eff}}, \mu_{\text{eff}}$. The system is shown in Fig. 5.2(c). The core cylinder is made of a material with material parameters ε_c, μ_c and the shell of a material with material parameters ε_h, μ_h .

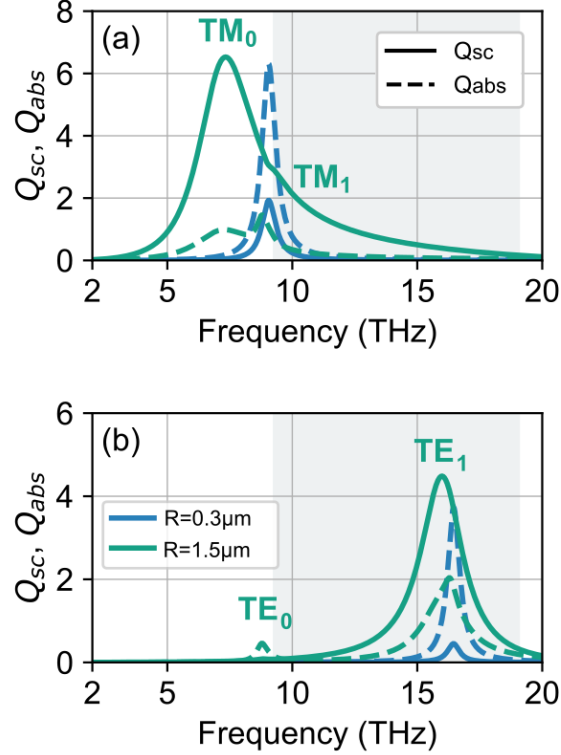


Figure 5.10: Scattering (solid lines) and absorption (dashed lines) efficiencies of a LiF cylinder (of radius 0.3 and 1.5 μm) in air for (a) TM and (b) TE polarization. The shaded areas correspond to the frequency region where the dielectric function of LiF is negative.

Depending on the incident wave polarization the fields (in G-CGS system of units) in each region can be expanded on the appropriate cylindrical harmonics $\mathbf{N}_{emk} = kZ_m(k\rho) \cos(m\varphi) \hat{z}$ and $\mathbf{M}_{emk} = -\frac{m}{\rho} Z_m(k\rho) \sin(m\varphi) \hat{\rho} - kZ'_m(k\rho) \cos(m\varphi) \hat{\varphi}$, with k the wavenumber, $Z_m(k\rho) = H_m(k\rho)$ for outward-going waves and $Z_m(k\rho) = J_m(k\rho)$ for inward-going waves [120]. For TE polarization (electric field perpendicular to the cylinder axis) the fields outside the coated cylinder are a sum of the incident (inward) and scattered (outward) fields, and can be expressed as

$$\mathbf{E}_{\text{out}} = i \sum_{m=0}^{\infty} A_{mk_{\text{eff}}} \left[D_m^{\text{TE}} \mathbf{M}_{emk_{\text{eff}}}^{(\text{outward})} + \mathbf{M}_{emk_{\text{eff}}}^{(\text{inward})} \right] \quad (5.30)$$

$$\mathbf{H}_{\text{out}} = \frac{ck_{\text{eff}}}{\omega\mu_{\text{eff}}} \sum_{m=0}^{\infty} A_{mk_{\text{eff}}} \left[D_m^{\text{TE}} \mathbf{N}_{emk_{\text{eff}}}^{(\text{outward})} + \mathbf{N}_{emk_{\text{eff}}}^{(\text{inward})} \right] \quad (5.31)$$

where D_m^{TE} are the scattering coefficients and $A_{mk} = \frac{1}{k} \frac{2}{1+\delta_{m0}} i^m$. In an analogous way one can express the fields in all the regions of the scattering system, i.e. in the core cylinder and the coating. The scattering coefficients and all the coefficients appearing in the expansion of the fields in cylindrical harmonics can be obtained by imposing the appropriate boundary conditions at the different system interfaces. Applying those conditions one can find that the scattering coefficient D_m^{TE} take the form

$$D_m^{\text{TE}} = \frac{n_h \mu_{\text{eff}} \mathcal{T}_m J'_m(k_{\text{eff}} R_2) - n_{\text{eff}} \mu_h \mathcal{K}_m J_m(k_{\text{eff}} R_2)}{n_{\text{eff}} \mu_h \mathcal{K}_m H_m(k_{\text{eff}} R_2) - n_h \mu_{\text{eff}} \mathcal{T}_m H'_m(k_{\text{eff}} R_2)} \quad (5.32)$$

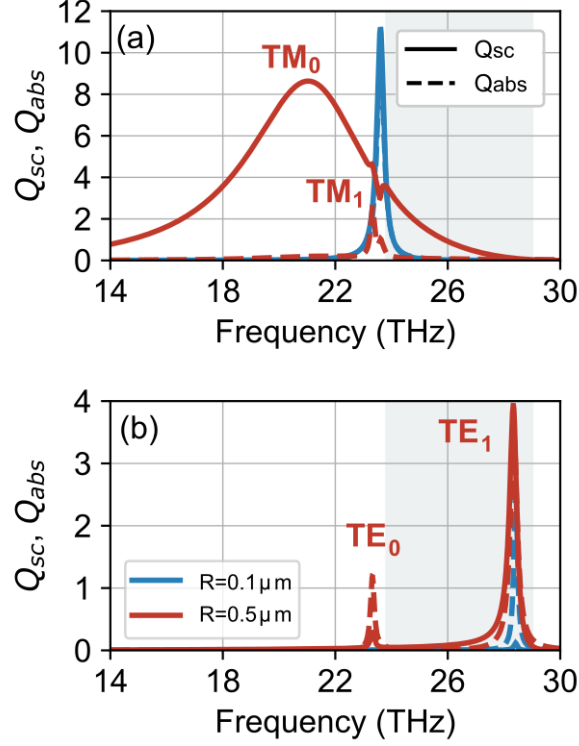


Figure 5.11: Scattering (solid lines) and absorption (dashed lines) efficiencies of a SiC cylinder (of radius 0.1 and 0.5 μm) in air for (a) TM and (b) TE polarization. The shaded areas correspond to the frequency region where the dielectric function of SiC is negative.

where

$$\mathcal{K}_m = \Theta_m H'_m(k_h R_2) + \Phi_m J'_m(k_h R_2) \quad (5.33)$$

$$\mathcal{T}_m = \Theta_m H_m(k_h R_2) + \Phi_m J_m(k_h R_2) \quad (5.34)$$

with

$$\Theta_m = n_c \mu_h J'_m(k_h R_1) J_m(k_c R_1) - n_h \mu_c J_m(k_h R_1) J'_m(k_c R_1) \quad (5.35)$$

$$\Phi_m = n_h \mu_c H_m(k_h R_1) J'_m(k_c R_1) - n_c \mu_h H'_m(k_h R_1) J_m(k_c R_1) \quad (5.36)$$

and $\Theta_m/\Phi_m = a_m^{\text{TE}}(R_1; c, h)$ are the scattering coefficients of a single cylinder of radius R_1 with material parameters ε_c and μ_c embedded in a host material of parameters ε_h and μ_h , i.e. a cylinder of the original system to be homogenized.

For TM polarization the fields outside the coated cylinder can be expressed as

$$\mathbf{E}_{\text{out}} = \sum_{m=0}^{\infty} A_m k_{\text{eff}} \left[D_m^{\text{TE}} \mathbf{N}_{emk_{\text{eff}}}^{(\text{outward})} + \mathbf{N}_{emk_{\text{eff}}}^{(\text{inward})} \right] \quad (5.37)$$

$$\mathbf{H}_{\text{out}} = i \frac{ck_{\text{eff}}}{\omega \mu_{\text{eff}}} \sum_{m=0}^{\infty} A_m k_{\text{eff}} \left[D_m^{\text{TM}} \mathbf{M}_{emk_{\text{eff}}}^{(\text{outward})} + \mathbf{M}_{emk_{\text{eff}}}^{(\text{inward})} \right] \quad (5.38)$$

with the m th-order scattering coefficient given by

$$D_m^{\text{TM}} = \frac{n_h \mu_{\text{eff}} \mathcal{U}_m J_m(k_{\text{eff}} R_2) - n_{\text{eff}} \mu_h \mathcal{Y}_m J'_m(k_{\text{eff}} R_2)}{n_{\text{eff}} \mu_h \mathcal{Y}_m H'_m(k_{\text{eff}} R_2) - n_h \mu_{\text{eff}} \mathcal{U}_m H_m(k_{\text{eff}} R_2)} \quad (5.39)$$

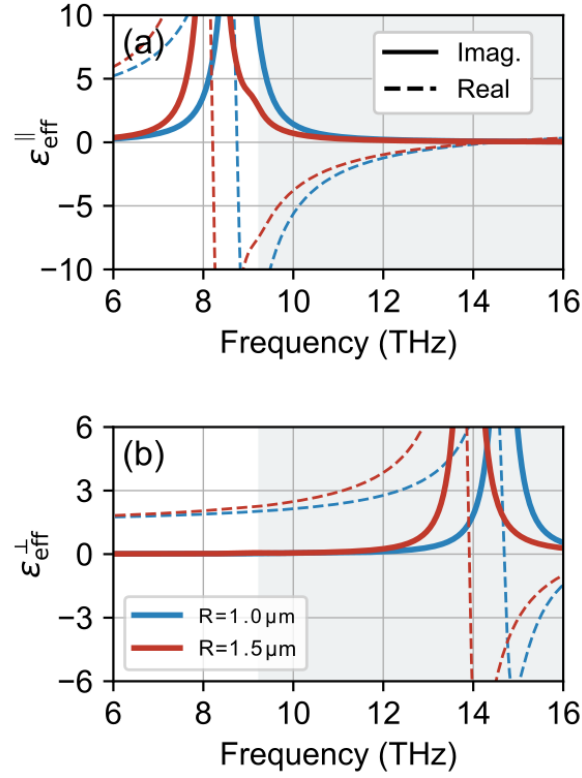


Figure 5.12: Imaginary (solid lines) and real (dashed lines) parts of the parallel (a) and the perpendicular (b) components of the relative effective permittivity for LiF cylinders with filling ratio 30% in air, for different radii, R (mentioned in the legends), using the CPA. The shaded areas correspond to the frequency region where the dielectric function of LiF is negative.

where

$$\mathcal{Y}_m = \Pi_m H_m(k_h R_2) + \Lambda_m J_m(k_h R_2) \quad (5.40)$$

$$\mathcal{U}_m = \Pi_m H'_m(k_h R_2) + \Lambda_m J'_m(k_h R_2) \quad (5.41)$$

and

$$\Lambda_m = n_h \mu_c H'_m(k_h R_1) J_m(k_c R_1) - n_c \mu_h H_m(k_h R_1) J'_m(k_c R_1) \quad (5.42)$$

$$\Pi_m = n_c \mu_h J_m(k_h R_1) J'_m(k_c R_1) - n_h \mu_c J'_m(k_h R_1) J_m(k_c R_1) \quad (5.43)$$

where $\Pi_m/\Lambda_m = a_m^{\text{TM}}(R_1; c, h)$. Following the CPA main concept, for the medium hosting the coated inclusion to be the valid effective medium (i.e. the medium approximating the original system of cylinders of ε_c and μ_c in the host of ε_h and μ_h), we must require the scattering cross section from the coated inclusion to be identically zero. Hence, all the scattering coefficients must be set equal to zero. That is,

$$D_m^{\text{P}} = 0 \quad (5.44)$$

where $\text{P} = \{\text{TM}, \text{TE}\}$. This equation reduces to the much simpler one, that is

$$a_m^{\text{P}}(R_1; c, h) = a_m^{\text{P}}(R_2; \text{eff}, h) \quad (5.45)$$

In Eq. (5.45) we have only the coefficients of simple (non-coated) cylinders (given by Eqs. (5.2) and (5.3)), since the scattering coefficient $a_m^{\text{P}}(R; A, B)$ denotes the m -th order coefficient for a cylinder of radius R and material parameters ε_A, μ_A embedded in a medium with ε_B, μ_B .

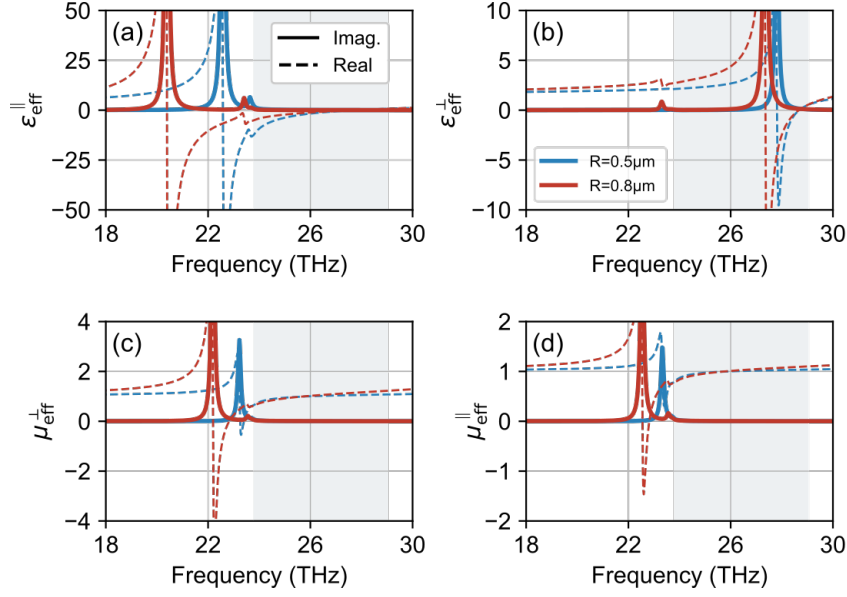


Figure 5.13: Imaginary (solid lines) and real (dashed lines) parts of parallel ((a),(d)) and perpendicular ((b), (c)) components of the relative effective permittivity (upper row) and permeability (lower row) for SiC cylinders with filling ratio 30% in air, for different radii, R (mentioned in the legends) using the CPA. The shaded areas correspond to the frequency region where the dielectric function of SiC is negative.

If we consider only the $m = 0$ and $m = 1$ terms in Eq. (5.45), which are the dominant terms in the long-wavelength limit, we can find explicit relations for all components of the permittivity and permeability tensors in the region $k_{\text{eff}}R_2 < 1$. To do so we replace the Bessel functions with argument $k_{\text{eff}}R_2$ (of order 0 and 1 and their derivatives) by their limiting expressions for small argument, employing the series expansions

$$J_0(x) \approx 1 - \frac{x^2}{4} \quad (5.46)$$

$$-J_1(x) = J'_0(x) \approx -\frac{x}{2} + \frac{x^3}{16} \quad (5.47)$$

$$J'_1(x) \approx \frac{1}{2} - \frac{3}{16}x^2 \quad (5.48)$$

$$H_0(x) \approx \frac{2i}{\pi} [\ln(x/2) + \gamma] + 1 \quad (5.49)$$

$$-H_1(x) = H'_0(x) \approx \frac{2i}{\pi x} - \frac{x}{2} + i\alpha x \quad (5.50)$$

$$H'_1(x) \approx \frac{2i}{\pi x^2} + \frac{1}{2} + \frac{i}{\pi} - i\alpha \quad (5.51)$$

where $\gamma = 0.577215$ is the Euler-Mascheroni constant and $\alpha = -\frac{1}{\pi} [\ln(x/2) + \gamma - \frac{1}{2}]$.

Employing Eqs. (5.45) and (5.46)-(5.51) (keeping in most of the cases only their lowest order term) we result to the effective medium formulas (5.16)-(5.19) of the main text. In particular,

$$a_0^{\text{TM}}(R_1; c, h) = a_0^{\text{TM}}(R_2; \text{eff}, h) \rightarrow \varepsilon_{\text{eff}}^{\parallel} \quad (5.52)$$

$$a_1^{\text{TM}}(R_1; c, h) = a_1^{\text{TM}}(R_2; \text{eff}, h) \rightarrow \mu_{\text{eff}}^{\perp} \quad (5.53)$$

$$a_0^{\text{TE}}(R_1; c, h) = a_0^{\text{TE}}(R_2; \text{eff}, h) \rightarrow \mu_{\text{eff}}^{\parallel} \quad (5.54)$$

$$a_1^{\text{TE}}(R_1; c, h) = a_1^{\text{TE}}(R_2; \text{eff}, h) \rightarrow \varepsilon_{\text{eff}}^{\perp} \quad (5.55)$$

5.5.2 Scattering/absorption

To illustrate more clearly the dependence of the single-cylinder absorption and scattering efficiencies on the cylinder radius, which was discussed in connection with Fig. 6.4, we present here the scattering and absorption efficiencies for different indicative radii. Fig. 5.10 shows the scattering and absorption efficiencies for a LiF cylinder in air, while Fig. 5.11 shows corresponding results for a SiC cylinder. As can be seen in Figs. 5.10 and Fig. 5.11, the results support the discussion of Section 5.3.1 regarding the tendencies of the scattering and absorption efficiencies as the cylinder radius increases.

5.5.3 Effective parameters

In Figs. 5.12 and 5.13 we plot the imaginary part of the effective permittivity and permeability components for the systems of LiF and SiC cylinders discussed in Section 5.3.2 (for the LiF case only the effective permittivity components are plotted). We also plot there the real part of those components, copied from Figs. 5.6 and 5.8, for an easy comparison and assessment of the functionality of the composites. As can be seen from Figs. 5.12 and 5.13, apart of a very narrow frequency region around the resonance frequencies of the components where the losses are significant, in all other frequency regions the losses are quite negligible. This shows that, unlike many plasmonic systems, in polaritonic rod systems resistive losses are not a major problem hindering their applicability.

Closing, we should note that the results presented for both LiF and SiC systems concern frequency regions where $k_h R_2 < 1$, where the contribution of higher order modes and of lattice (or multiple scattering) effects is still not important, and thus the CPA results are expected to be highly accurate. Beyond this regime (which for LiF systems of $R = 1.5 \mu\text{m}$, $f = 30\%$, is up to 16 THz and for SiC of $R = 0.8 \mu\text{m}$, $f = 30\%$, is up to 30 THz) the CPA results are expected to become less and less accurate. Moreover the peak values of the calculated effective permittivity and permeability (i.e. the values exactly and very close to the position of the resonance) may be not very accurate, as at those frequencies the CPA restriction $k_{\text{eff}} R_2$ might be violated (these regions though, due to the high associated losses, are not considered suitable in applications involving polaritonic metamaterials).

CHAPTER 6

SINGLE SCATTERING AND EFFECTIVE MEDIUM DESCRIPTION FOR GRAPHENE- AND FOR METASURFACE-COATED AND MULTICOATED CYLINDERS

6.1 Introduction

As mentioned in the previous chapters, electromagnetic metamaterials are artificial, structured materials comprised from subwavelength resonant building blocks, the meta-atoms. Due to their versatile nature, metamaterials offer the possibility of novel and unconventional electromagnetic wave control, and thus advancements in a large variety of applications, including imaging, sensing, communications, energy harvesting, etc. [41], [131]–[134]. Metamaterials' exceptional electromagnetic properties stem to a larger degree from the architecture of the meta-atoms; through this architecture, the distribution of the local currents excited by an impinging electromagnetic wave is engineered, providing the desired response. Meta-atoms may consist of properly aligned metallic cut wires, behaving as macroscopic resonant electric dipoles and producing a resonant electric response (resonant permittivity), and/or metallic split ring resonators, leading to resonant circulating currents and the emergence of a resonant magnetic response [135]. Another approach to create resonant electric and/or magnetic response is by exploiting the Mie-based resonances in high index dielectric (or semiconducting) meta-atoms; this approach is typically proposed for applications in high (IR and optical) frequencies [45], [79], where metals experience detrimentally high losses. Through resonant magnetic and/or electric response one can engineer a plethora of different and peculiar metamaterial properties, such as negative, near zero permittivity and/or permeability, negative refractive index, giant chirality, peculiar anisotropy, asymmetric effects and many more [136]–[139]. (Note that because of the subwavelength meta-atom size metamaterials provide homogeneous-medium-like (effective) properties and response.)

Besides bulk (three-dimensional) metamaterials, many additional exciting functionalities stem from the electromagnetic wave interaction with thin meta-atom layers, known as metasurfaces, which attract a constantly growing research attention. Metasurfaces, by allowing modulation of the meta-atoms along them, allow the engineering of both phase and amplitude of the electromagnetic fields impinging on them, acquiring thus the ability to replace bulk, heavy and difficult to use conventional optical elements (mirrors, lenses, etc.). Due to their ultrathin nature and the subwavelength meta-atom size, metasurfaces can be conveniently described as effective electromagnetic sheets [34]. Metasurfaces comprising of a thin layer sustaining orthogonal electric and magnetic dipoles, have been utilized for applications as reflect-arrays, transmit-arrays, holographic surfaces and others [140]. Moreover, metasurfaces' fine electromagnetic features have been shown to enable enhanced detection and sensing, thin film polarizers, multiband shielding and other functionalities [141]–[143].

As mentioned, metamaterials and metasurfaces can be made of metallic, dielectric or semiconducting components. They can be also made of a combination of dielectric, semiconducting

and metallic parts in a properly designed meta-atom architecture and cluster arrangement. A scheme that has gained significant popularity is structures composed of coated (or even multi-coated) cylinders or spheres. Such structures are characterized by a relative straightforward design and have been proposed for a variety of applications due to the increased degree of design freedom related to the thicknesses and constituent materials in each layer. With proper selection of geometry and materials, coated cylinders or spheres can lead to overlapping of different resonances, which is crucial in metasurfaces since it can offer full transmission or reflection and 2π phase modulation (allowing in principle arbitrary wavefront control), or resonances with engineered quality factors. Applications of such structures include super-scattering [144]–[148] and electromagnetic cloaking [47], [147], [149]–[155], lenses and many others [156]. Moreover, metamaterials made of cylindrical meta-atoms, which are the systems of our interest here, are inherently anisotropic, allowing the possibility of hyperbolic dispersion relation and negative index [157]. Such structures can be experimentally realized following the progress of micro and nanotechnology, especially of emerging technologies focused on the implementation of carbon nanotubes, where there are already metamaterial and photonic crystal orientated developments [158]–[161]. Even more interesting electromagnetic features can occur in cylindrical meta-atoms coated with tunable sheets bearing individual electric and/or magnetic resonances to be combined with the response of the coated atom. Such coatings may involve, for example, a 2D material like uniform graphene or a structured (patterned) graphene sheet or an electromagnetically thin cluster of cut wires or split ring resonators [149], [154], [162]–[164], e.g. in a flexible metasurface implementation [165], [166]. It should be mentioned here that graphene in particular, either in a patterned metasurface form or as a uniform sheet is very appealing as a coating material due to the ultrathin geometry and the exceptional tunable properties, especially in the THz wavelengths where we find its Drude-like response [56], [57], [167].

It is clear that an analytical assessment of the electromagnetic response of coated and multicoated cylinders-based metamaterial structures is important, as it gives the possibility for the in-depth understanding of the physical mechanisms that lead to the resonant features and response, and, subsequently, for engineering of this response through structure optimization, targeting advanced electromagnetic functionalities and applications. Assemblies of resonant cylinders can be treated as an effective homogeneous material in the limit of small characteristic lengths (radius, unit cell size) compared to the wavelength of interest. Homogenization approaches applied in systems of coated spheres and cylinders have shown that coatings provide many interesting effects, as for example an increased bandwidth of negative permittivity and permeability in comparison with their non-coated counterparts [168]. However, to our knowledge, an analytic homogenization approach that can incorporate a random number (larger than one) of coatings for each cylinder has not been reported in the literature yet. Additionally, although the scattering properties of cylinders and spheres coated with graphene metasurfaces have been quite extensively studied, coatings/sheets showing arbitrary resonant electric and/or resonant magnetic response (representing more complex metasurface-coatings and allowing delicate interplay of electric and magnetic dipoles, resulting to additional advanced functionalities) [16], [17], [36], [169]–[173] are much less explored.

The aim of this chapter is to analyze in detail the resonant behaviour and wave propagation in systems of multilayer cylinders coated with uniform graphene sheets and/or with arbitrary metasurfaces of both electric and magnetic response; also to provide a homogenization method for analytically calculating the effective electromagnetic properties in such systems. Towards this direction, we derive an homogeneous effective medium approach for infinitely-long cylindrical nanotube clusters with a random number of layers and with the incorporation of both electric and magnetic sheet conductivities at each interface. Our homogenization approach is based on the well known in the solid state physics community Coherent Potential Approximation, CPA [11], [51], [104], [118], [119], introduced and discussed also in the previous chapter.

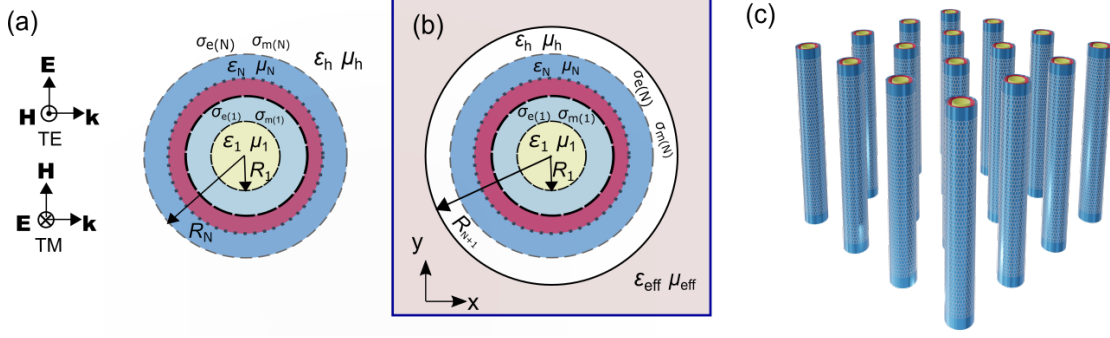


Figure 6.1: (a) Top view schematic of N co-centric cylinders and polarization definition. We assume normal incidence. Each cylinder layer is characterized by electric permittivity ϵ_ℓ and magnetic permeability μ_ℓ . The interface between the ℓ -th and the $(\ell + 1)$ -th layer is coated, in the most general case, with a metasurface with arbitrary electric conductivity $\sigma_{e(\ell)}$ and magnetic conductivity $\sigma_{m(\ell)}$. The coated cylinder is embedded in a host with electric permittivity ϵ_h and magnetic permeability μ_h . (b) Schematic of the setup for the effective medium derivation for a system of infinite parallel cylinders as the one of (a) -see panel (c). In the effective medium setup the original coated cylinder is coated with an additional cylindrical layer made of the host material of the original system, with radius $R_{N+1} = R_N/\sqrt{f}$, where f is the cylinders filling ratio in the original system; the augmented cylinder is embedded in the homogeneous effective medium to be evaluated, with permittivity ϵ_{eff} and permeability μ_{eff} . (c) Three-dimensional view of a metamaterial formed as an array of coated cylinders as the one of (a).

We apply the method in two different systems: (i) uniform graphene-coated cylinders with tunable response and (ii) cylinders coated with metasurfaces of arbitrary electric and magnetic resonance. In both systems we study the single meta-atom scattering and the effective medium response which unveils the existence of rich electromagnetic features, i.e., hyperbolic response of both type I and type II and for both polarizations, double negative response, and epsilon-near-zero and mu-near-zero response. The chapter is organized as follows: In Sec. 6.2 we present our method, i.e., starting from the single meta-atom scattering we derive the relations for the effective medium electric permittivity and magnetic permeability tensor components, aiming to analyze the response of the multilayer nanotube systems and to understand the effect of the interplay of material, metasurfaces and structure resonances (note that the method is developed for cylindrical meta-atoms with arbitrary number of coatings and with metasurface at each interface). In Sections 6.3.1 and 6.3.2 we apply the method in tunable graphene-coated multilayer cylindrical nanotubes and in multilayer cylindrical nanotubes with each layer coated with a metasurface with both electric and magnetic surface response and we show the engineerable effective electric permittivity and magnetic permeability response leading to the emergence of the alternating optical phases. Finally we present the conclusions on our work.

6.2 Methods

We begin our analysis from the methods derived and/or employed in this work for the system shown in Fig. 6.1. In the first part we present the THz electric and magnetic sheet conductivities employed. In the second part we present first the derivation of a Transfer Matrix Method, which allows us to calculate the scattering properties of a cylinder composed of N co-centered layers of different materials, with metasurfaces at the interfaces of these layers. Next, we derive the CPA-based effective medium model for arrays of such multilayered cylinders, based on the single scattering calculations.

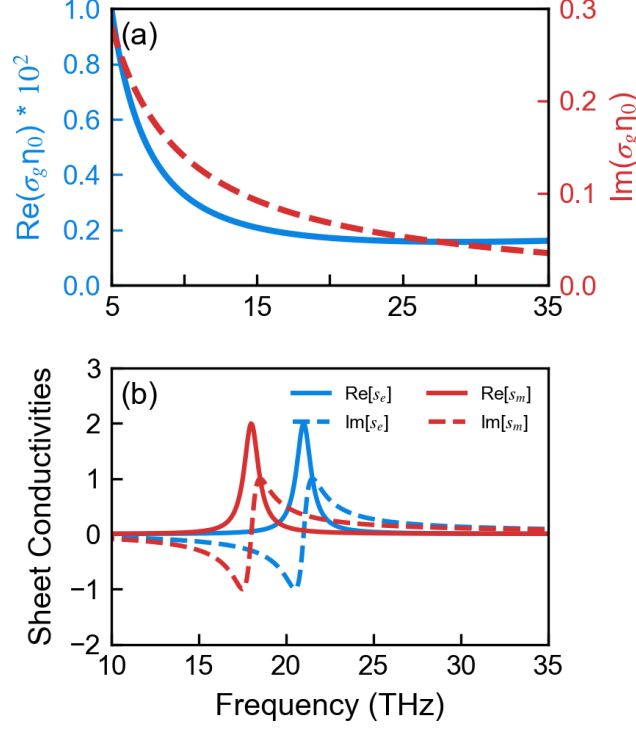


Figure 6.2: (a) Real part (times 100) (left axis, blue line) and imaginary part (right axis, red line) of the sheet conductivity of a uniform graphene sheet modelled by RPA and Eq. (6.1), assuming Fermi level $E_F = 0.2$ eV and relaxation time $\tau = 1$ ps. (b) Normalized real (solid lines) and imaginary (dashed lines) parts of electric (s_e) and magnetic (s_m) sheet conductivities calculated using Eqs. (6.4)-(6.5), assuming parameters $\omega_e/2\pi = 21$ THz, $\Gamma_e/2\pi = \Gamma_m/2\pi = 2$ THz, $\kappa_e/2\pi = \kappa_m/2\pi = 1$ THz and $\omega_m/2\pi = 18$ THz; for the definition of those parameters see main text.

6.2.1 2D Conductivities

In this section we present the electromagnetic properties of the 2D sheets/coatings considered in this work, i.e., the uniform graphene sheet and the metasurface exhibiting both electric and magnetic resonance. Although these sheets/coatings are the same discussed in Chapter 4, in connection with the perfect absorber investigations, we add a short discussion also here for the sake of completeness.

For the graphene case the conductivity as a function of the Fermi energy, E_F , and the temperature, T , was obtained by Kubo formula, derived in the context of Rapid Phase Approximation (RPA) [74]; it reads as

$$\sigma_g(\omega) = \sigma_{\text{intra}} + \sigma_{\text{inter}} \quad (6.1)$$

where the intraband contribution is

$$\sigma_{\text{intra}}(\omega) = \frac{2e^2 k_B T}{\pi \hbar^2} \frac{i}{\omega + i\tau^{-1}} \ln \left[2 \cosh \left(\frac{E_F}{2k_B T} \right) \right] \quad (6.2)$$

and the interband contribution is

$$\begin{aligned} \sigma_{\text{inter}}(\omega) = & \frac{e^2}{4\hbar} \left(\frac{1}{2} + \frac{1}{\pi} \arctan \left(\frac{\hbar\omega - 2E_F}{2k_B T} \right) \right) \\ & - \frac{i}{2\pi} \ln \left[\frac{(\hbar\omega + 2E_F)^2}{(\hbar\omega - 2E_F)^2 + (2k_B T)^2} \right]. \end{aligned} \quad (6.3)$$

Here ω is the angular frequency, $\hbar = 1.055 \times 10^{-34}$ Js the reduced Planck constant, $k_B = 1.38 \times 10^{-23}$ J \cdot K $^{-1}$ the Boltzmann constant, $e = 1.602 \times 10^{-19}$ C the electron charge and τ the electrons' relaxation time. Unless otherwise stated, for the majority of this chapter we use a Fermi level $E_F = 0.2$ eV and a typical relaxation time $\tau = 1$ ps. The real and imaginary part of the graphene conductivity for these values are shown in Fig. 6.2(a).

Regarding the metasurface sheets (coatings here), usually in the literature, their response is approximated by a sheet material with effective electric and magnetic 2D conductivities consisting of a summation of Lorentzian resonances [16], [17], [37], [173], [174]. To simplify our analysis we consider here a metasurface with isotropic surface conductivities and a single electric and magnetic resonance:

$$s_e = \sigma_e \eta_0 = \frac{i\kappa_e \omega}{\omega^2 - \omega_e^2 + i\omega\Gamma_e} \quad (6.4)$$

$$s_m = \frac{\sigma_m}{\eta_0} = \frac{i\kappa_m \omega}{\omega^2 - \omega_m^2 + i\omega\Gamma_m} \quad (6.5)$$

where $\omega_{e/m}$ are the resonance frequencies, and $\kappa_{e/m}$, $\Gamma_{e/m}$ are parameters of the lorentzians (see Chapter 4). For the purpose of the present analysis we have chosen the values of the parameters involved in the conductivities as $f_e = \omega_e/2\pi = 21$ THz, $\Gamma_e/2\pi = \Gamma_m/2\pi = 1$ THz, $\kappa_e/2\pi = \kappa_m/2\pi = 2$ THz and $f_m = \omega_m/2\pi = 18$ THz. The real and imaginary part of the corresponding electric and magnetic conductivities are shown in Fig. 6.2(b).

6.2.2 Single Scattering

Having defined the sheet conductivities of the graphene and metasurface coatings we move to the investigation of a single cylinder system. We consider an infinitely-long cylinder consisting of N co-centered layers. The system is shown in Fig. 6.1(a). The ℓ -th layer is characterized by its thickness $\Delta_\ell = R_\ell - R_{\ell-1}$ ($R_0 = 0$), where R_ℓ is the distance from the center to the perimeter of the ℓ -th layer; its relative electric permittivity is ε_ℓ , the relative magnetic permeability is μ_ℓ , the electric surface conductivity is $\sigma_{e(\ell)}$ and the magnetic surface conductivity is $\sigma_{m(\ell)}$. The cylinder is embedded in a host material with relative electric permittivity ε_h and magnetic permeability μ_h . We consider wave propagation perpendicular to the cylinder axis. Since the cylinder is infinitely-long and there is no propagation component parallel to its axis, the problem here, as in the case of Chapter 5, is two dimensional and can be decoupled into two separate polarizations, the transverse electric (TE), with the electric field normal to the cylinder axis, and the transverse magnetic (TM) polarization, with the magnetic field normal to the cylinder axis. In each layer the fields can be expanded on the basis of cylindrical vector harmonics. In the ℓ -th layer the field $\mathbf{F} = \{\mathbf{E}, \mathbf{H}\}$ (electric or magnetic) parallel to the cylinder axis (z direction) will be

$$\mathbf{F}_\ell \sim \sum_\nu \left[c_{\ell\nu} \mathbf{N}_{e\nu k_\ell}^{(\text{outward})} + d_{\ell\nu} \mathbf{N}_{e\nu k_\ell}^{(\text{inward})} \right], \quad (6.6)$$

with $\mathbf{N}_{e\nu k_\ell}^{(\text{outward})} \sim H_\nu(k_\ell r)$ and $\mathbf{N}_{e\nu k_\ell}^{(\text{inward})} \sim J_\nu(k_\ell r)$ standing for the outgoing and ingoing cylindrical harmonics respectively [120]. The functions $J_\nu(\cdot)$ and $H_\nu(\cdot)$ are the Bessel and Hankel function of order ν and $k_\ell = \sqrt{\varepsilon_\ell \mu_\ell} \omega / c$. The expansion coefficients $c_{\ell\nu}$ and $d_{\ell\nu}$ can be calculated by imposing the appropriate boundary conditions at each interface [13], [14], [175]:

$$\hat{\rho} \times [\mathbf{E}_{\ell+1} - \mathbf{E}_\ell] = -\mathbf{j}_{m(\ell)} = -\sigma_{m(\ell)} \frac{\mathbf{H}_\ell + \mathbf{H}_{\ell+1}}{2} \quad (6.7)$$

$$\hat{\rho} \times [\mathbf{H}_{\ell+1} - \mathbf{H}_\ell] = \mathbf{j}_{e(\ell)} = \sigma_{e(\ell)} \frac{\mathbf{E}_\ell + \mathbf{E}_{\ell+1}}{2} \quad (6.8)$$

where $\hat{\rho}$ is the unit vector along the radial direction. Here we have chosen a set of Bessel functions for our descriptions that is not linearly independent, i.e. $J_\nu(x)$ and $H_\nu(x)$ instead of $J_\nu(x)$ and $Y_\nu(x)$ that are commonly used in the literature, because it is more convenient for the effective medium description in Section 6.2.3.

By applying the boundary conditions, Eq. (6.7) and Eq. (6.8), at each of the interfaces of the N layers of the cylinder, we construct a matrix equation which connects the fields in the innermost layer with the fields outside the cylinder (incident + scattered field), for each cylindrical wave/harmonic excited. This Transfer Matrix equation reads:

$$\mathbb{M}_{(N),\nu}^P \begin{pmatrix} b_\nu \\ 0 \end{pmatrix} = \begin{pmatrix} 1 \\ a_\nu \end{pmatrix} \quad (6.9)$$

where $\mathbb{M}_{(N),\nu}^P$ is the total transfer matrix for polarization P. With a_ν we denote the scattering coefficient of the scattered wave (for coefficient 1 of the incident wave) and with b_ν the coefficient for the core layer while ν stands for the excited mode (cylindrical harmonic). For polarization $P = \{\text{TE}, \text{TM}\}$ we can write the transfer matrix $\mathbb{T}_{\ell\nu}^P$ which transfers the fields from the (ℓ) -th layer to the fields in the $(\ell + 1)$ -th layer as

$$\mathbb{T}_{\ell\nu}^P \begin{pmatrix} d_{\ell\nu} \\ c_{\ell\nu} \end{pmatrix} = \begin{pmatrix} d_{(\ell+1),\nu} \\ c_{(\ell+1),\nu} \end{pmatrix} \quad (6.10)$$

For TE polarization the matrix $\mathbb{T}_{\ell\nu}^{\text{TE}}$ has the form

$$\mathbb{T}_{\ell\nu}^{\text{TE}} = [\mathbb{D}_{(\ell+1)\nu}^{\text{TE}}(R_\ell)]^{-1} \cdot [\mathbb{X}_\ell^+]^{-1} \cdot \mathbb{X}_\ell^- \cdot \mathbb{D}_{\ell\nu}^{\text{TE}}(R_\ell) \quad (6.11)$$

where

$$\mathbb{D}_{\ell\nu}^{\text{TE}}(R_\ell) = \begin{pmatrix} J'_\nu(k_\ell R_\ell) & H'_\nu(k_\ell R_\ell) \\ \frac{1}{\eta_\ell} J_\nu(k_\ell R_\ell) & \frac{1}{\eta_\ell} H_\nu(k_\ell R_\ell) \end{pmatrix}. \quad (6.12)$$

and the surface conductivity matrices (\mathbb{X}) are

$$\mathbb{X}_\ell^\pm = \begin{pmatrix} 1 & \pm i\sigma_{m(\ell)}/2\eta_0 \\ \mp i\sigma_{e(\ell)}\eta_0/2 & 1 \end{pmatrix} \quad (6.13)$$

where $\eta_\ell = \sqrt{\mu_\ell/\varepsilon_\ell}$ is the impedance of the ℓ -th layer and $\eta_0 = \sqrt{\mu_0/\varepsilon_0}$ is the vacuum impedance.

For TM polarization we get

$$\mathbb{T}_{\ell\nu}^{\text{TM}} = [\mathbb{D}_{(\ell+1)\nu}^{\text{TM}}(R_\ell)]^{-1} \cdot [\mathbb{X}_\ell^-]^{-1} \cdot \mathbb{X}_\ell^+ \cdot \mathbb{D}_{\ell\nu}^{\text{TM}}(R_\ell) \quad (6.14)$$

$$\mathbb{D}_{\ell\nu}^{\text{TM}}(R_\ell) = \begin{pmatrix} J_\nu(k_\ell R_\ell) & H_\nu(k_\ell R_\ell) \\ \frac{1}{\eta_\ell} J'_\nu(k_\ell R_\ell) & \frac{1}{\eta_\ell} H'_\nu(k_\ell R_\ell) \end{pmatrix} \quad (6.15)$$

The details of the calculations are presented in the Appendix.

The total transfer matrix reads as

$$\mathbb{M}_{(N),\nu}^P = \prod_{\ell=N}^1 \mathbb{T}_{\ell\nu}^P \quad (6.16)$$

From Eq. (6.9), we can define the coefficients b_ν (field in the core layer) and a_ν (scattered field coefficient) as

$$b_\nu = \frac{1}{\mathbb{M}_{(N),\nu}^{(11)}}, \quad (6.17)$$

$$a_\nu = \mathbb{M}_{(N),\nu}^{(21)} b_\nu = \frac{\mathbb{M}_{(N),\nu}^{(21)}}{\mathbb{M}_{(N),\nu}^{(11)}}. \quad (6.18)$$

The scattering and extinction efficiencies of the whole structure can all be written in terms of a_ν as

$$Q_{\text{ext}}^{\text{P}} = -\frac{2}{|k_h R_N|} \text{Re} \left[a_0^{\text{P}} + 2 \sum_{\nu=1}^{\infty} a_\nu^{\text{P}} \right], \quad (6.19)$$

$$Q_{\text{sc}}^{\text{P}} = \frac{2}{|k_h R_N|} \left[|a_0^{\text{P}}|^2 + 2 \sum_{\nu=1}^{\infty} |a_\nu^{\text{P}}|^2 \right]. \quad (6.20)$$

Metasurface-covered cylinder: Having the above equations, one can derive limiting expressions for different systems of practical or theoretical interest. Here we derive expressions for the resonance frequencies (poles) of the $\nu = 1$ mode of a single-layer cylinder coated with a metasurface. For a single cylindrical layer ($N = 1$) with radius $R_1 = R$ coated with a surface with conductivities σ_e and σ_m in a host material with electric permittivity ε_h and magnetic permeability μ_h , the scattering coefficients will be given based on Eq. (6.18). In the limit $k_h R \ll 1$ and ignoring terms containing the interaction term $\sigma_e \sigma_m$, the poles of the TE₁ mode can be found from the expression

$$\frac{1}{\eta_1} \frac{J_1(k_1 R)}{J_1'(k_1 R)} = \frac{\sigma_e \eta_0 \eta_h - i k_h R}{i \eta_h + k_h R \sigma_m \eta_0^{-1}} \quad (6.21)$$

Further, if we take the quasistatic limit of $k_h R \ll 1$ and $k_1 R \ll 1$, we find

$$\varepsilon_1 \frac{\omega}{c} R = \frac{i \sigma_e \eta_0 + \varepsilon_h \frac{\omega}{c} R}{\varepsilon_h i \sigma_m \eta_0^{-1} \frac{\omega}{c} R - 1} \quad (6.22)$$

or

$$\varepsilon_1 \varepsilon_h i \sigma_m \eta_0^{-1} \left(\frac{\omega}{c} R \right)^2 - (\varepsilon_1 + \varepsilon_h) \frac{\omega}{c} R = i \sigma_e \eta_0 \quad (6.23)$$

For the sake of our analysis we ignore the damping term in the conductivities (see Eqs. (6.4)-(6.5)), i.e. we consider

$$s_{e/m} = \frac{i \kappa_{e/m} \omega}{\omega^2 - \omega_{e/m}^2} \quad (6.24)$$

For $x = k_0 R = \omega R/c \ll 1$ we can write the magnetic sheet conductivity as $s_m = \sigma_m \eta_0^{-1} \simeq i \kappa_m (-(c/R) \cdot x/\omega_m^2 - (c/R)^3 \cdot x^3/\omega_m^4) + \mathcal{O}(x^4)$, and hence, can ignore the first term of Eq. (6.23). In this case, we can use Eqs. (6.23) and (6.24) to get:

$$-(\varepsilon_1 + \varepsilon_h) \frac{\omega}{c} R = i \frac{\kappa_e \omega}{\omega^2 - \omega_e^2} \quad (6.25)$$

or

$$-(\varepsilon_1 + \varepsilon_h) \frac{\omega}{c} R (\omega^2 - \omega_e^2) = -\kappa_e \omega \quad (6.26)$$

or

$$(\varepsilon_1 + \varepsilon_h) \frac{R}{c} (\omega^2 - \omega_e^2) = \kappa_e. \quad (6.27)$$

Finally we find that the frequency of the TE₁ resonance of the structure is at

$$\omega_{\text{TE}_1}^2 \simeq \omega_e^2 + \frac{c \kappa_e}{(\varepsilon_1 + \varepsilon_h) R}. \quad (6.28)$$

An equivalent expression can be obtained for the TM₁ resonance:

$$\omega_{\text{TM}_1}^2 \simeq \omega_m^2 + \frac{c \kappa_m}{(\mu_1 + \mu_h) R}. \quad (6.29)$$

For graphene, if we ignore the interband conductivity term in Eq. (6.1), the sheet conductivity takes the form $\sigma_g(\omega) \simeq i \kappa_g / \omega$, where $\kappa_g = \frac{2e^2 k_B T}{\pi \hbar^2} \ln \left[2 \cosh \left(\frac{E_F}{2k_B T} \right) \right]$; we again get a $1/\sqrt{R}$ dependence of the TE₁ mode resonance frequency.

6.2.3 Effective Medium Theory

In this section we derive the components of the effective permittivity and permeability tensors for a uniaxial anisotropic system of infinitely-long parallel circular multicoated cylinders of N layers each and surface electric and magnetic conductivities at each interface.

We follow the same approach as the one of Chapter 5, where we calculated the effective medium parameters for a cluster of cylinders without coating and surface conductivities [51], [104]. To derive the effective medium equations in the case of N -coated cylinders we consider a cylinder of $N+1$ layers embedded in the effective medium, as depicted in Fig. 6.1(b), and we require the vanishing of the scattering amplitudes. The $(N+1)$ -th layer of that cylinder is the host of the original system (with $\varepsilon_{N+1} = \varepsilon_h$ and $\mu_{N+1} = \mu_h$) with thickness $R_{N+1} - R_N$. The radius R_{N+1} of the outer layer is determined by the filling ratio, f , of the cylinders in the original system, as $f = R_N^2/R_{N+1}^2$. The host material in the configuration of Fig. 6.1(b) has permittivity $\varepsilon_{\text{eff}} = \varepsilon_{\text{eff}}^{\perp}(\hat{x}\hat{x} + \hat{y}\hat{y}) + \varepsilon_{\text{eff}}^{\parallel}\hat{z}\hat{z}$ and permeability $\mu_{\text{eff}} = \mu_{\text{eff}}^{\perp}(\hat{x}\hat{x} + \hat{y}\hat{y}) + \mu_{\text{eff}}^{\parallel}\hat{z}\hat{z}$. In order to derive the expressions for the tensor components of effective permittivity and permeability we require that the scattering coefficients of the scattered field in the effective medium, $a_{\nu}^{(\text{eff})}$ vanish. After algebraic manipulations (see details in Appendix 6.5.2), this requirement leads to expressions for the coefficients of the original system, which read as

$$a_{\nu}^{\text{P}}(R_{N+1}; \text{eff}, h) = a_{\nu}^{\text{P}}(\{R_1, \dots, R_N\}; \{A_1, \dots, A_N\}, h) \quad (6.30)$$

where $a_{\nu}^{\text{P}}(R_{N+1}; \text{eff}, h)$ are the scattering coefficients of a single-layered cylinder with electric permittivity ε_{eff} , magnetic permeability μ_{eff} and radius R_{N+1} , embedded in a host with electric permittivity ε_h and magnetic permeability μ_h . In the right-hand-side of Eq. (6.30), $a_{\nu}^{\text{P}}(\{R_1, \dots, R_N\}; \{A_1, \dots, A_N\}, h)$ are the scattering coefficient of the original system, consisting of N co-centered cylinders with radii $\{R_1, R_2, \dots, R_N\}$ and materials (including surface conductivities at each interface) $\{A_1, A_2, \dots, A_N\}$ in the host material (of the original system). In the metamaterial frequency range, $k_h R_{N+1} < 1$, however, there are only two dominant modes per polarization, the lower order ones, i.e. the $\nu = 0$ and the $\nu = 1$ mode. In the limit $k_{\text{eff}} R_{N+1} \ll 1$, we can replace the Bessel functions in Eq. (6.30) with their limiting expressions assuming small arguments [121] - see Chapter 5. Considering only the $\nu = 0$ and $\nu = 1$ modes per polarization, we can obtain analytical expressions for all the components of the effective electric permittivity and magnetic permeability tensors, which read as

$$\varepsilon_{\text{eff}}^{\parallel} = -\frac{2\varepsilon_h}{k_h R_{N+1}} \left[\frac{J'_0(k_h R_{N+1}) + H'_0(k_h R_{N+1})a_0^{\text{TM}}}{J_0(k_h R_{N+1}) + H_0(k_h R_{N+1})a_0^{\text{TM}}} \right] \quad (6.31)$$

$$\mu_{\text{eff}}^{\perp} = \frac{\mu_h}{k_h R_{N+1}} \left[\frac{J_1(k_h R_{N+1}) + H_1(k_h R_{N+1})a_1^{\text{TM}}}{J'_1(k_h R_{N+1}) + H'_1(k_h R_{N+1})a_1^{\text{TM}}} \right] \quad (6.32)$$

$$\mu_{\text{eff}}^{\parallel} = -\frac{2\mu_h}{k_h R_{N+1}} \left[\frac{J'_0(k_h R_{N+1}) + H'_0(k_h R_{N+1})a_0^{\text{TE}}}{J_0(k_h R_{N+1}) + H_0(k_h R_{N+1})a_0^{\text{TE}}} \right] \quad (6.33)$$

$$\varepsilon_{\text{eff}}^{\perp} = \frac{\varepsilon_h}{k_h R_{N+1}} \left[\frac{J_1(k_h R_{N+1}) + H_1(k_h R_{N+1})a_1^{\text{TE}}}{J'_1(k_h R_{N+1}) + H'_1(k_h R_{N+1})a_1^{\text{TE}}} \right] \quad (6.34)$$

Equations (6.31)-(6.34) have the same form as the relations obtained in Chapter 5. Finally, if we further take the limit $k_h R_{N+1} \ll 1$, we get

$$\varepsilon_{\text{eff}}^{\parallel} = \varepsilon_h \left[1 - \frac{f}{(k_h R_N)^2} \frac{4i}{\pi} a_0^{\text{TM}} \right] \quad (6.35)$$

$$\mu_{\text{eff}}^{\perp} = \mu_h \left[\frac{(k_h R_N)^2 - f \frac{4i}{\pi} a_1^{\text{TM}}}{(k_h R_N)^2 + f \frac{4i}{\pi} a_1^{\text{TM}}} \right] \quad (6.36)$$

$$\mu_{\text{eff}}^{\parallel} = \mu_h \left[1 - \frac{f}{(k_h R_N)^2} \frac{4i}{\pi} a_0^{\text{TE}} \right] \quad (6.37)$$

$$\varepsilon_{\text{eff}}^{\perp} = \varepsilon_h \left[\frac{(k_h R_N)^2 - f \frac{4i}{\pi} a_1^{\text{TE}}}{(k_h R_N)^2 + f \frac{4i}{\pi} a_1^{\text{TE}}} \right] \quad (6.38)$$

where $f = R_N^2/R_{N+1}^2$ is the filling ratio. Note here that for cylinder without any coating ($N = 1, \sigma_e = 0, \sigma_m = 0$) in the quasistatic limit (i.e. $k_h R_{N+1} \ll 1, k_1 R \ll 1$), Eqs. (6.31)-(6.34) reduce to the well-known Maxwell-Garnett expressions.

6.3 Results and Discussion

6.3.1 Single scattering

Graphene cylinders

We begin our analysis by calculating the extinction efficiencies of (i) a single-layered and (ii) a multi-layered cylinder, coated by homogeneous graphene layers. We assume that all the cylinder layers are air, i.e. $\varepsilon_\ell = 1$ and $\mu_\ell = 1$, and the same for the host material. The geometry is comprised, in fact, of co-centered cylindrical cells/sheets with electric surface conductivity $\sigma_e = \sigma_g$ calculated using Eq. (6.1) and plotted in Fig. 6.2(a). (Such a geometry can be considered as a good approximation of a family of single and double-wall carbon nanotubes.) The extinction efficiencies for a single graphene cylindrical layer of variable radius, $R = 35$ nm, $R = 45$ nm and $R = 55$ nm, are shown in Fig. 6.3(a), while the extinction efficiencies for a double-layered cylinder with variable outer-layer radius R_2 are shown in Fig. 6.3(b). For the single graphene layer [Fig. 6.3(a)] there is only one dominant peak in the extinction spectrum, originated from the dipolar $\nu = 1$ mode for TE polarization. We denote this mode as TE_1 . Since, in this frequency region the imaginary part of the surface conductivity of graphene [Fig. 6.2(a)] is positive, the mode is similar in nature to the Localized Surface Plasmon Resonance (LSPR) sustained in metallic rods [125].

For the double-layered case ($N = 2$) shown in Fig. 6.3(b) we consider a core of constant radius $R_1 = 45$ nm and the variable outer layer radius: $R_2 = 70$ nm, $R_2 = 80$ nm and $R_2 = 90$ nm. In this case, the TE_1 mode manifests as two distinct resonances at frequencies below and above the TE_1 resonance for the single layer case. Here, we denote these resonances in order of increasing frequency as $\text{TE}_1^{(1)}$ and $\text{TE}_1^{(2)}$. From the frequency of the modes, one can conclude that the mode $\text{TE}_1^{(1)}$ comes predominately from the contribution of the outer layer (probably shifted due to the presence and interaction with the inner one), while $\text{TE}_1^{(2)}$ from the contribution of the core-layer, slightly shifted due to the interaction with the outer layer. A worth-mentioning feature of Fig. 6.3(b) is the small frequency shift of the $\text{TE}_1^{(1)}$ peak with the change of the radius R_2 , compared, e.g., with the corresponding shift observed in Fig. 6.3(a). Possible cause of this difference might be the presence of the inner layer. We should note

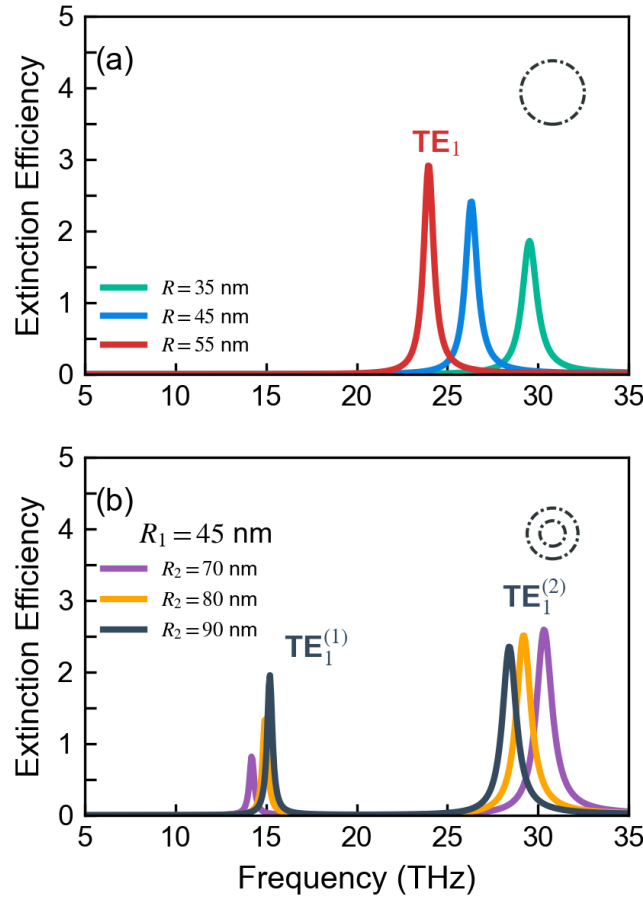


Figure 6.3: Extinction efficiencies, Q_{ext} , in (a) a single-layer graphene cylindrical tube in air with varying radius, R , and (b) a double-layered graphene cylinder in air with inner radius $R_1 = 45$ nm, and variable outer layer radii R_2 for TE polarization. All layers exhibit surface conductivity σ_g with Fermi level $E_F = 0.2$ eV and relaxation time $\tau = 1$ ps. All cylinder bulk (inter-surface) layers are made of air.

here that for this case the extinction efficiency for TM polarization is below 10^{-2} , with no resonances for both cases, and it is not shown here.

The dependence of the resonance frequencies on the radii of the graphene cylindrical layers, which are calculated by finding the poles of the scattering coefficients a_ν [Eq. (6.18)], are shown in Figs. 6.4(a)-(b). We observe that the resonance frequency in the single-layered cylinder scales with the radius of the cylinder with a $1/\sqrt{R}$ dependence as we derived in Eq. (6.28) (see Sec. 6.2.2). The tendency of TE_1 modes for the double-layered case ($N = 2$) can be explained in terms of mode hybridization, where the modes coupling leads to a lower-frequency "bonding" mode and a higher-frequency *anti-bonding* mode [147], [176]–[178].

Metasurface cylinders

Next, we turn our attention to cylinders formed by metasurfaces having both electric and magnetic response. We consider two cases: (i) a single-layered cylinder of variable radius and (ii) a double-layered cylinder of the same metasurface at each layer with fixed inner-layer radius. The metasurfaces have conductivities, $\sigma_{e(1)} = \sigma_{e(2)}$ and $\sigma_{m(1)} = \sigma_{m(2)}$, presenting a resonance, as it is shown in Fig. 6.2(b), and $\varepsilon_1 = \varepsilon_2 = \varepsilon_h = 1$. The extinction efficiencies for both TE and TM polarizations and for the single- and the double-layered cylinders are shown in Fig. 6.5.

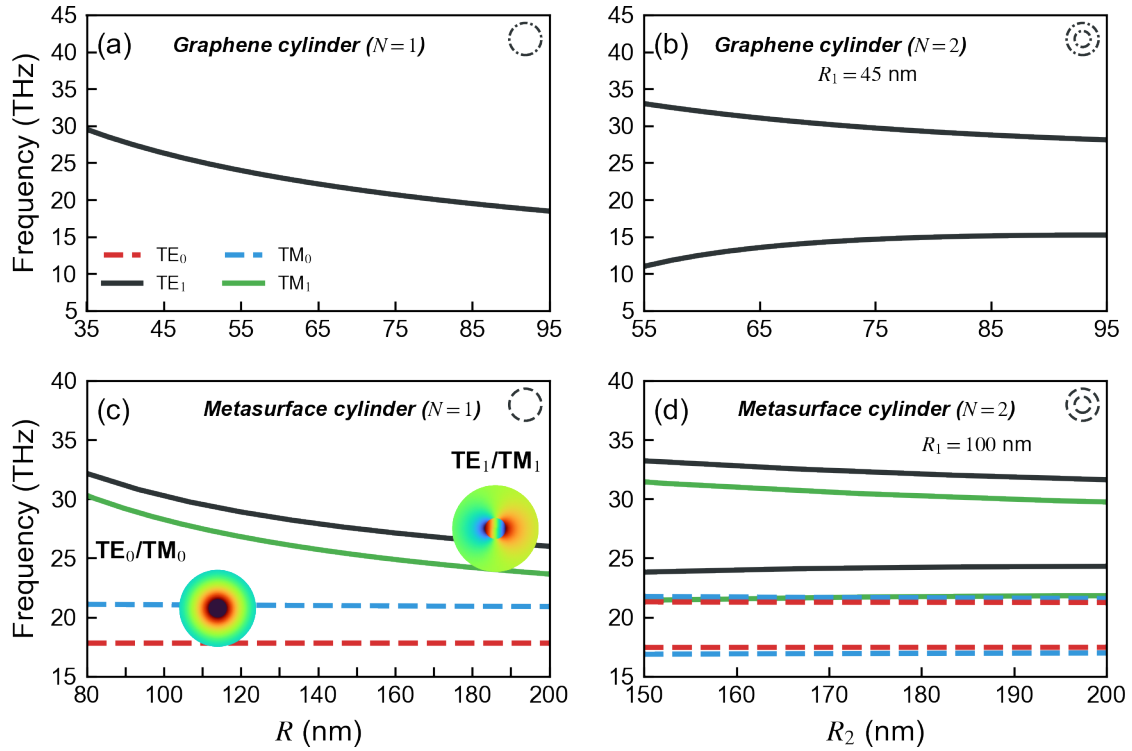


Figure 6.4: Resonance frequencies of first two modes, $\nu = 0$ and $\nu = 1$, per polarization, TE and TM, for: (a) a single-layered graphene cylinder versus its radius, R ; (b) a double-layered graphene cylinder for different outer-layer radii, R_2 and constant core radius $R_1 = 45$ nm; (c) a single-layered metasurface-formed cylinder of different radii, R ; (d) a double-layered metasurface cylinder with core radius $R_1 = 100$ nm and variable interlayer radii R_2 . The characteristic field distributions of the z component of the electric (magnetic) field for TM (TE) polarization for the $\nu = 0$ and $\nu = 1$ modes are shown in the insets of (c).

In the single-layered cylinders we investigate cases of various radii: $R = 50$ nm, $R = 100$ nm and $R = 150$ nm. There are two resonances for both TE and TM polarizations. The electric in nature TM₀ and the magnetic in nature TE₀ modes appear just below the resonance frequencies of the electric sheet conductivity, $f_e = \omega_e/2\pi = 21$ THz, and the magnetic sheet conductivity, $f_m = \omega_m/2\pi = 18$ THz, respectively. Just below f_e (f_m) the imaginary part of the electric (magnetic) sheet conductivity of the metasurface is negative [see Fig. 6.2(b)] leading to positive equivalent electrical permittivity (magnetic permeability); this case is similar to the polaritonic cylinders for small radii we have discussed in Chapter 5. On the other hand, the dipole-like modes, TE₁ and TM₁, fall in the regions of positive imaginary part of electric and magnetic conductivity respectively.

Next we study the case of the double-layered cylinder formed of the same metasurface, at inner layer radius $R_1 = 100$ nm and different outer layer radii R_2 . We observe two dipolar ($\nu = 1$) electric and magnetic modes, TE₁⁽¹⁾ and TE₁⁽²⁾, TM₁⁽¹⁾ and TM₁⁽²⁾, one of lower and one of higher frequency than the corresponding modes of a single-layered cylinder, similar to the graphene case we discussed in the previous paragraph. Note here that the TM₁⁽¹⁾ mode [see Fig. 6.4(d)] is very close in frequency with the TM₀⁽²⁾ mode.

The dependence of the resonance frequencies of the dominant modes on the radius of the single-layered cylinder and on the radius R_2 for the double-layered case, for constant $R_1 = 100$ nm, is shown in Figs. 6.4(c)-(d). It is interesting to observe in Fig. 6.4(c) and Fig. 6.4(d) that the TE₀ and TM₀ modes for the double-layered case also split into two resonances, although

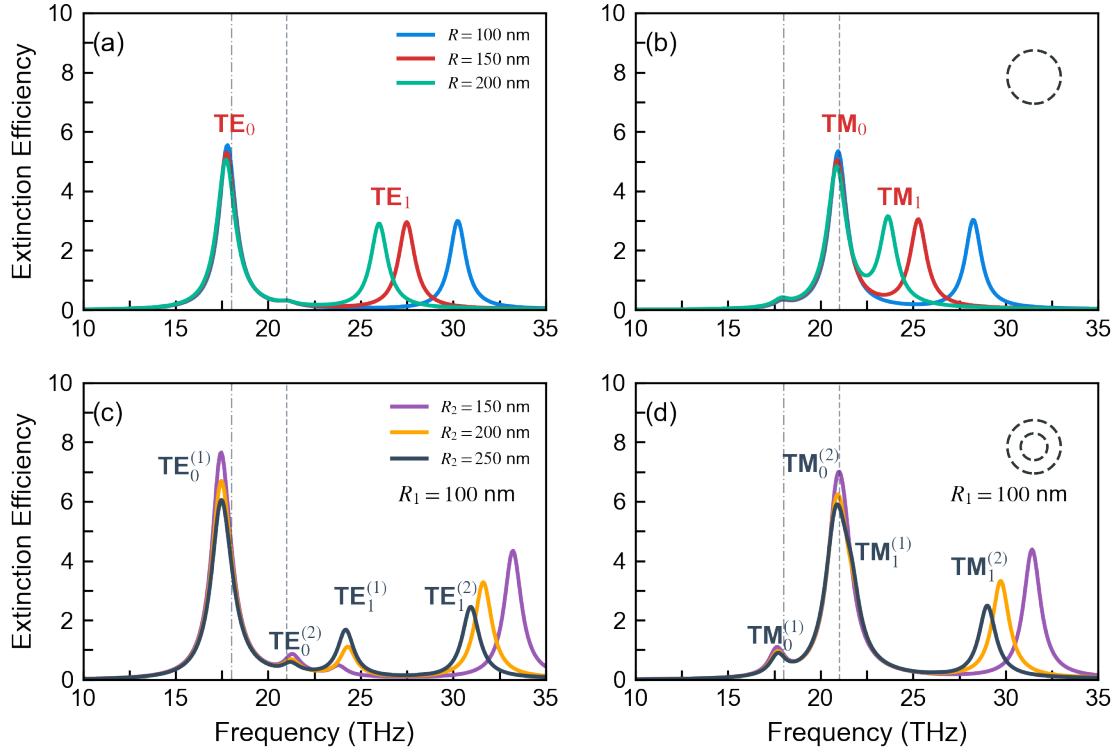


Figure 6.5: Extinction efficiencies, Q_{ext} , for: (a) and (b), a single-layered ($N = 1$) metasurface-formed cylinder of variable radius, R , for TE (a) and TM (b) polarization; (c) and (d), a double-layered ($N = 2$) metasurface cylinder with constant core radius $R_1 = 100$ nm and variable outer-layer radius, R_2 , for TE (c) and TM (d) polarization. The vertical dashed grey lines in the panels indicate the resonant frequencies of the metasurface magnetic and the electric conductivities at $f_m = 18$ THz and $f_e = 21$ THz, respectively. The symbols associated with each resonance are explained in the main text.

the splitting is less pronounced than the one of the TE_1 (black lines) and TM_1 (green lines) modes. To further elucidate this effect we plot the zeroth-th order scattering coefficients a_0 , in Fig. 6.6, for a double-layered cylinder with $R_1 = 100$ nm and $R_2 = 150$ nm as a function of the magnetic sheet conductivity resonance frequency, f_m , with constant $f_e = 21$ THz. For instance, for the TE polarization, we can observe that the strength of the weaker $\text{TE}_0^{(2)}$ resonance becomes more prominent and approaches in frequency the $\text{TE}_0^{(1)}$ as the resonance frequency f_m approaches f_e . Interestingly, even in the case of $f_e = f_m$, the two resonances remain distinct as a result of the interaction of the layers about the electric and magnetic conductivity resonance. However, the splitting of the TE_0 modes is absent when the electric conductivity is zero (see Fig. 6.12 in Appendix 6.5.3). Similar behaviour is observed in the case of the TM_0 mode.

6.3.2 Effective medium theory and alternating optical phases

Graphene cylinders

We turn our attention now to the effective medium parameters ε_{eff} and μ_{eff} for clusters of graphene and metasurface cylinders in air, aligned in a square lattice, as presented in Fig. 6.1(c). The cylinders considered are the ones discussed in the previous section. We examine initially the uniform graphene cases. In Fig. 6.7 we plot the real and imaginary parts of the tensor

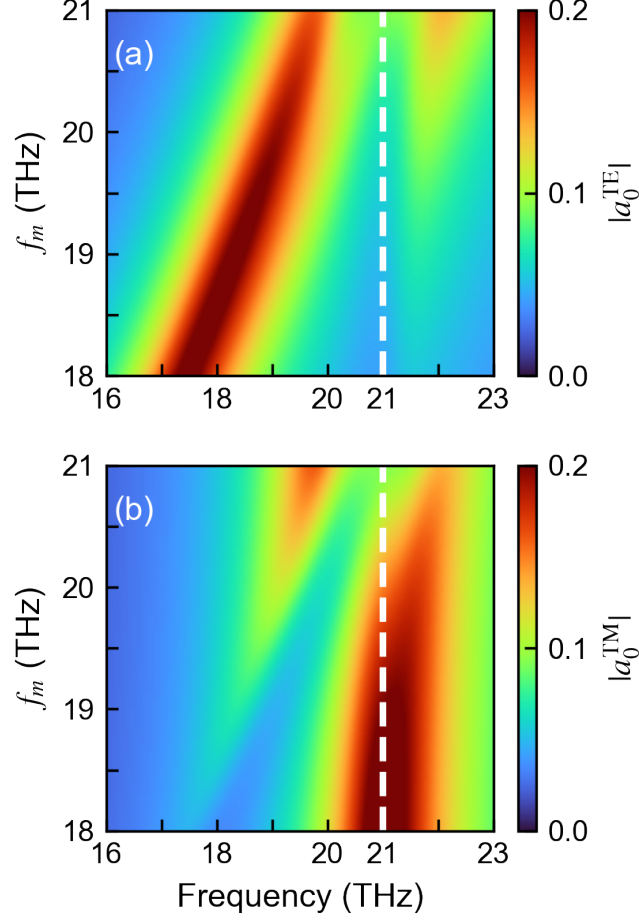


Figure 6.6: Zeroth-order scattering coefficients, a_0 , as a function of the magnetic surface conductivity resonance frequency f_m for (a) TE and (b) TM polarizations for a double-layered metasurface cylinder ($N = 2$) with core radius $R_1 = 100$ nm, interlayer distance $R_2 = 150$ nm and constant electric surface conductivity resonance frequency $f_e = 21$ THz (dashed vertical line).

components of effective electric permittivity $\varepsilon_{\text{eff}} = \varepsilon_{\text{eff}}^{\perp}(\hat{x}\hat{x} + \hat{y}\hat{y}) + \varepsilon_{\text{eff}}^{\parallel}\hat{z}\hat{z}$ for single-layered graphene cylinders [Fig. 6.7(a) and Fig. 6.7(c)] and double-layered cylinders [Fig. 6.7(b) and Fig. 6.7(d)] for constant filling ratio, $f = 20\%$, and different radii. As one can see, for both the single- and the double-layered cases there are lorentzian-shaped resonances for the in-plane component of the effective electric permittivity, $\varepsilon_{\text{eff}}^{\perp}$, close in frequency to the corresponding TE_1 resonances [see Figs. 6.3 and 6.4(a)-(b)]. Also we can observe a Drude-like response for the parallel component of effective electric permittivity $\varepsilon_{\text{eff}}^{\parallel}$ for both arrays of single- and double-layered graphene cylinders. All the components of the effective magnetic permeability μ_{eff} are equal to unity and are not shown here. As the radius of the cylinders increases the resonance of the $\varepsilon_{\text{eff}}^{\perp}$ moves to lower frequencies. Interestingly, for single-layered cylinders all the components of the effective electric permittivity vanish at the same frequency, close to the TE_1 mode resonance frequency. For instance, for $R = 45$ nm the Epsilon-Near-Zero (ENZ) is achieved at 23.7 THz and moves to lower frequencies as the radius of the cylinder increases. This result along with Eqs. (6.31) and (6.34) suggests that $a_0^{\text{TM}} = a_1^{\text{TE}}$ at that frequency for the single-layered graphene cylinder. Further examinations showed that the monochromatic vanishing of both components of effective permittivity tensor holds only for the symmetric case, where the material inside the graphene layer and the host are the same (air here). On the

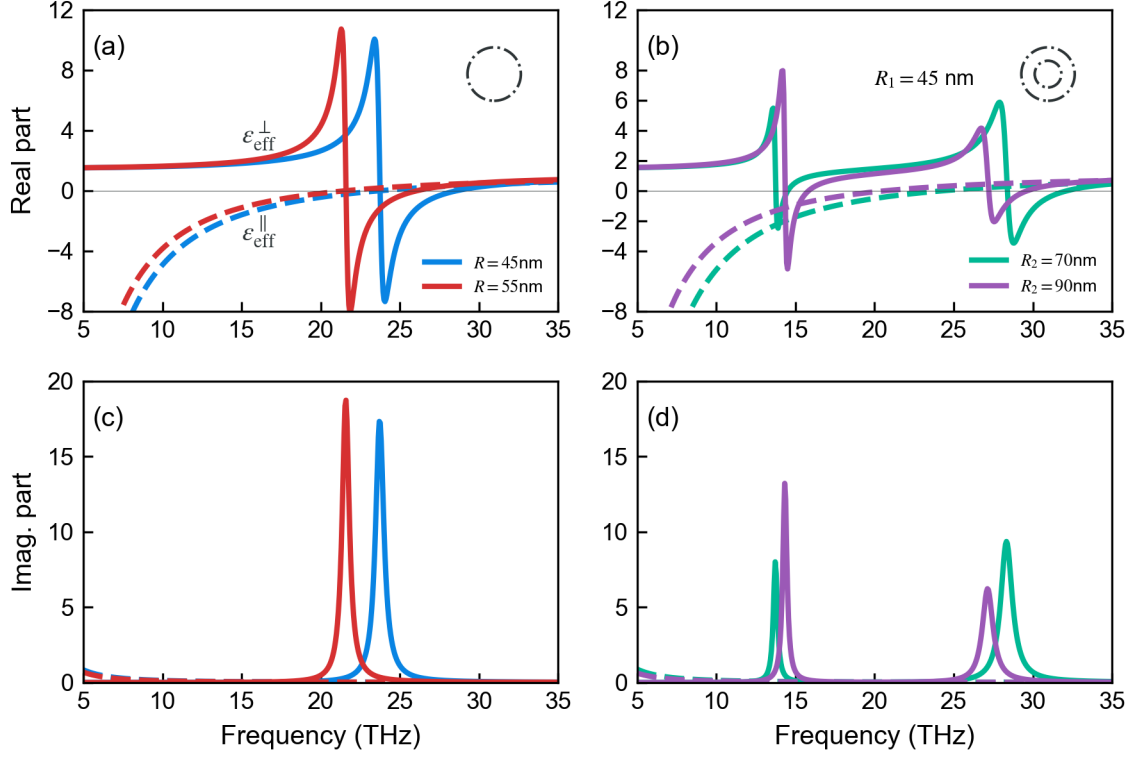


Figure 6.7: Real (top row) and imaginary (bottom row) parts of the parallel $\epsilon_{\text{eff}}^{\parallel}$ (dashed curves) and perpendicular $\epsilon_{\text{eff}}^{\perp}$ (solid curves) components of the relative effective permittivity ϵ_{eff} for: (a) and (c) a system made of single-layered ($N = 1$) graphene cylinders of variable radius, $R = 45$ nm (blue curves) and $R = 55$ nm (red curves) in air; (b) and (d) a system of double-layered ($N = 2$) graphene cylinders in air, with constant core radius $R_1 = 45$ nm, and for outer layer radii $R_2 = 70$ nm (green curves) and $R_2 = 90$ nm (purple curves); the cylinders filling ratio is in all cases equal to $f = 20\%$.

other hand, for the double-layered cylinders, due to the presence of multiple resonances, there are several frequencies where the $\epsilon_{\text{eff}}^{\perp}$ vanishes.

Moreover, as one can notice, there are frequency regions where the in-plane and out-of-plane components of the effective electric permittivity have different signs, i.e. $\epsilon_{\text{eff}}^{\perp} \cdot \epsilon_{\text{eff}}^{\parallel} < 0$. This is the condition for hyperbolic response (i.e. dispersion relation of the shape of hyperbola - see also previous chapter) for TM-polarized waves, as can be seen by taking into account the the dispersion relations for an anisotropic homogeneous material [129],

$$\text{TM: } \frac{k_{\perp}^2}{\mu_{\text{eff}}^{\perp} \epsilon_{\text{eff}}^{\parallel}} + \frac{k_{\parallel}^2}{\mu_{\text{eff}}^{\parallel} \epsilon_{\text{eff}}^{\perp}} = \left(\frac{\omega}{c}\right)^2, \quad (6.39)$$

$$\text{TE: } \frac{k_{\perp}^2}{\mu_{\text{eff}}^{\parallel} \epsilon_{\text{eff}}^{\perp}} + \frac{k_{\parallel}^2}{\mu_{\text{eff}}^{\perp} \epsilon_{\text{eff}}^{\parallel}} = \left(\frac{\omega}{c}\right)^2, \quad (6.40)$$

where k_{\parallel} and k_{\perp} stand for the wave-vector components parallel and perpendicular to the cylinder axis respectively. For example, for the single-layered graphene cylinders with radius $R = 45$ nm [blue curve in Fig. 6.7(a)] the condition for hyperbolic response is achieved up to 28.6 THz, where both $\epsilon_{\text{eff}}^{\perp}$ and $\epsilon_{\text{eff}}^{\parallel}$ become positive. We can further distinguish the hyperbolic metamaterial response of our systems into two different frequency regions by considering the different signs of $\epsilon_{\text{eff}}^{\perp}$ and $\epsilon_{\text{eff}}^{\parallel}$. For frequencies below the TE₁ resonance the in-plane components

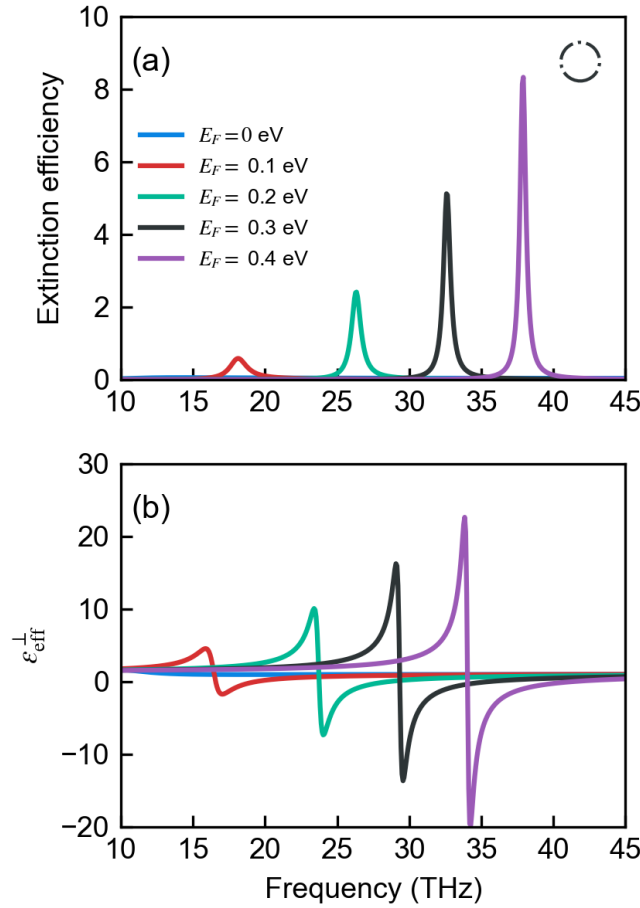


Figure 6.8: (a) Extinction efficiency for TE polarization for a single-layered graphene cylinder with radius $R = 45$ nm in air, for different Fermi energies, E_F . (b) Real part of the in-plane component of effective electric permittivity $\epsilon_{\text{eff}}^{\perp}$ for a system of single-layered graphene cylinders as the one of panel (a), in air, with cylinder filling ratio $f = 20\%$.

$\epsilon_{\text{eff}}^{\perp}$ are positive, while the out-of-plane component $\epsilon_{\text{eff}}^{\parallel}$ is negative; thus we have *type I hyperbolic metamaterial (HMM I)*. For radius $R = 45$ nm (blue curve in Fig. 6.7) we have $\epsilon_{\text{eff}}^{\perp} > 0$ and $\epsilon_{\text{eff}}^{\parallel} < 0$ up to frequency 26.7 THz. On the other hand, in the frequency region 26.7 THz-28.6 THz and radius $R = 45$ nm we have $\epsilon_{\text{eff}}^{\perp} < 0$ and $\epsilon_{\text{eff}}^{\parallel} > 0$, thus *hyperbolic metamaterial type II (HMM II)* response. The response is more rich for the metamaterial comprised of double-layered graphene cylinders shown in Fig. 6.7(b) and Fig. 6.7(d). Considering the case with constant core radius, $R_1 = 45$ nm, and variable outer layer radii, $R_2 = 70$ nm [green curve in Fig. 6.7(b) and Fig. 6.7(d)] and $R_2 = 90$ nm [purple curve in Fig. 6.7(b) and Fig. 6.7(d)], we see that there are alternating optical phases (HMM I, metallic, HMM II and dielectric) at frequencies close to the two TE_1 resonances. For instance, for $R_2 = 70$ nm we find HMM I response in the frequency region up to 13.7 THz and 14.6-24.3 THz and HMM II response in the frequency region 28.5 - 32. THz.

We should mention also here that the response of graphene-shells and graphene-coated rods is highly tunable by changing the Fermi level of graphene. This, as mentioned, can be accomplished by various methods, including chemical doping, voltage tuning and photoexcitation. The dependence of the extinction efficiency for a single-layered graphene cylinder is presented in Fig. 6.8(a). Here we modify the Fermi energy of the graphene, $E_F = 0, 0.1, 0.2, 0.3, 0.4$ eV. As observed the extinction efficiency is very small (maximum of $Q_{\text{ext}} = 0.05$) for the

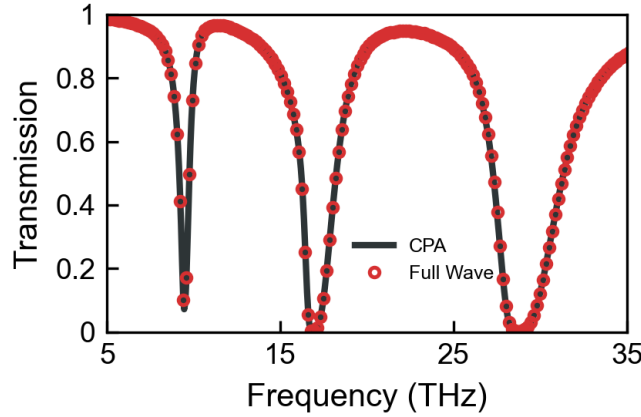


Figure 6.9: Normal incidence, TE transmission spectra for a slab of triple-layered graphene cylinders with radii $R_1 = 45$ nm, $R_2 = 90$ nm and $R_3 = 135$ nm and filling ratio $f = 20\%$ in air, in a square arrangement. The transmission is calculated by the commercial finite element method electromagnetic solver Comsol Multiphysics, considering a computational system of 7 unit cell thickness (along the propagation direction). The full wave transmission results (red circles) are compared with results for a homogeneous effective medium of the same thickness as the actual system and effective parameters obtained through our CPA-based effective medium approach (black line).

case of zero Fermi level; as the Fermi energy increases the extinction efficiency becomes larger and the resonance shifts to higher frequencies.

Fig. 6.8(b); shows the in-plane component of the effective electric permittivity $\epsilon_{\text{eff}}^{\perp}$ for cylinders with radius $R = 45$ nm and filling ratio $f = 20\%$, for different Fermi energies $E_F = 0, 0.1, 0.2, 0.3, 0.4$ eV. The effective permittivity results are presented in parallel with single-scattering data (Fig. 6.8(a)), to facilitate the understanding of the observed response. We see that the TE_1 resonance of the single scattering setup [Fig. 6.8(a)] is moving towards higher frequencies as the Fermi level grows, and the resonance becomes stronger in both extinction efficiency and effective electric permittivity spectra.

Formulation validation

In order to verify the validity and accuracy of the developed effective medium approach we compare its results with equivalent full-wave simulations data. Specifically we calculate the transmission and reflection spectra through a slab consisting of seven unit cells (along propagation direction) of a triple-layered ($N = 3$) graphene cylinder arranged in a square lattice using the full wave numerical analysis software COMSOL MULTIPHYSICS, and we compare the results with the response (obtained by transfer matrix calculations) of a slab with electric permittivity ϵ_{eff} and magnetic permeability μ_{eff} and same thickness as the actual system. The transmission comparison for TE polarization is shown in Fig. 6.9. We find excellent agreement between full wave simulations and the effective medium model. As expected, we observe that there are three frequency regions where the transmission through the structure tends to zero, in agreement with the frequency regions where $\epsilon_{\text{eff}}^{\perp}$ becomes negative.

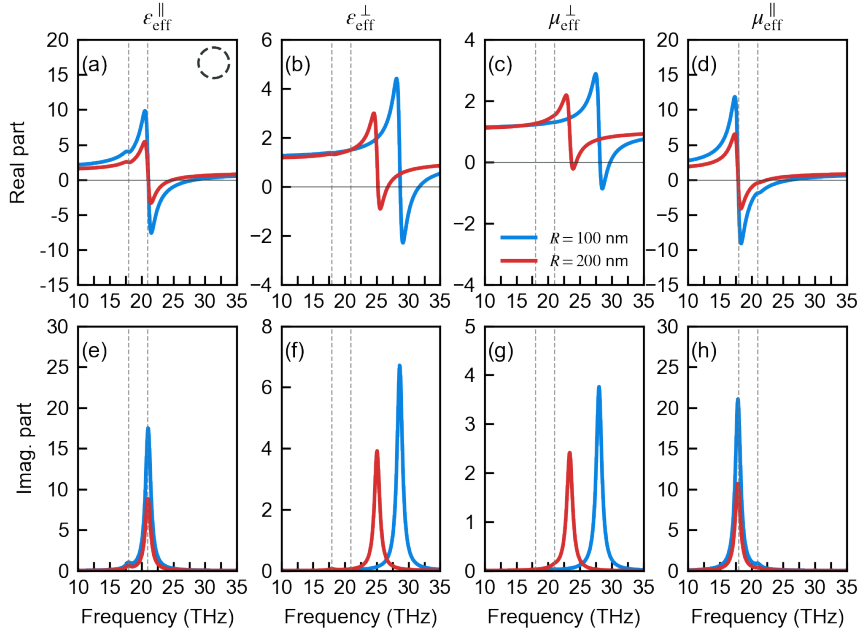


Figure 6.10: Real (top row) and imaginary (bottom) parts of the tensor components of effective permittivity ε_{eff} (first column $\varepsilon_{\text{eff}}^{\parallel}$ and second column $\varepsilon_{\text{eff}}^{\perp}$) and effective permeability μ_{eff} (third column $\mu_{\text{eff}}^{\parallel}$ and fourth column μ_{eff}^{\perp}) for a system/metamaterial of single-layered ($N = 1$) metasurface-formed cylinders in air, for different radii, $R = 100$ nm (blue lines) and $R = 200$ nm (red lines), and filling ratio $f = 20\%$. The vertical dashed lines indicate the resonance frequencies of the magnetic ($f_m = 18$ THz) and electric sheet conductivity ($f_e = 21$ THz).

Metasurface-based cylinders

Next, we turn our attention to the effective response of arrays of metasurface-based cylinders, investigating the single-layered and double-layered cylinder systems as previously; the results are presented in Fig. 6.10 and Fig. 6.11, respectively. The effective medium parameters in a single-layered cylinder metasurface for both TE and TM polarizations are shown in Fig. 6.10 for two cylinders radii, $R = 100$ nm (blue curves) and $R = 200$ nm (red curves). As one can notice there are frequency regions where the medium becomes *double negative* (DNG) resulting in negative refractive index, i.e. both $\varepsilon_{\text{eff}} < 0$ and $\mu_{\text{eff}} < 0$. For $R = 100$ nm and TM polarization both $\varepsilon_{\text{eff}}^{\parallel}$ and μ_{eff}^{\perp} are negative between frequencies 28.19 THz and 28.64 THz, with the magnetic response originating from the metasurface magnetic sheet conductivity resonance. For the larger cylinder-radius system DNG is achieved for TM polarization, at lower frequencies. In particular, for $R = 200$ nm the medium exhibits DNG response in the frequency region 23.73-24.38 THz. On the other hand, for TE polarization there is no DNG response ($\varepsilon_{\text{eff}}^{\perp} < 0$ and $\mu_{\text{eff}}^{\parallel} < 0$) for the parameters studied here. It is interesting to observe that the metasurface-cylinders system exhibits HMM response for both TM and TE polarizations. By considering the anisotropic material dispersion relations of Eqs. (6.39)-(6.40) and the results shown in Fig. 6.10 one can see that there are both HMM I and HMM II responses for both TM and TE polarizations. In particular, the arrays of metasurface-coated cylinders with $R = 100$ nm (blue curves in Fig. 6.10) and filling ratio $f = 20\%$ exhibit HMM I response ($\mu_{\text{eff}}^{\perp}\varepsilon_{\text{eff}}^{\parallel} < 0$ and $\mu_{\text{eff}}^{\parallel}\varepsilon_{\text{eff}}^{\perp} > 0$) in the frequency range 21.1-28.15 THz and 28.7-29.75 THz and HMM II ($\mu_{\text{eff}}^{\perp}\varepsilon_{\text{eff}}^{\parallel} > 0$ and $\mu_{\text{eff}}^{\parallel}\varepsilon_{\text{eff}}^{\perp} < 0$) response in the frequency range 28.2-28.6 THz and in the frequency range 29.8-31.7 THz for TM polarization. Also, for TE polarization there is HMM I response ($\varepsilon_{\text{eff}}^{\perp}\mu_{\text{eff}}^{\parallel} < 0$ and $\varepsilon_{\text{eff}}^{\parallel}\mu_{\text{eff}}^{\perp} > 0$) in

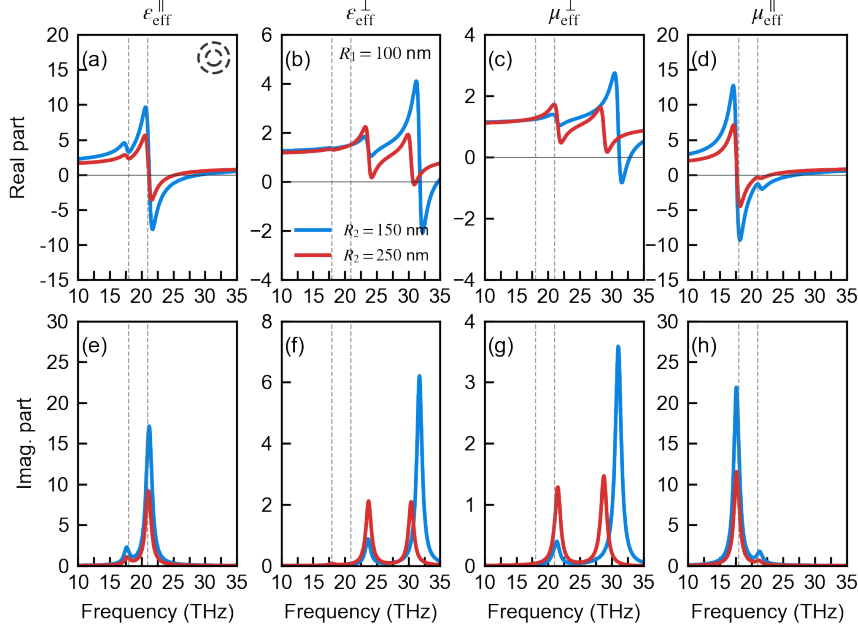


Figure 6.11: Real (top row) and imaginary (bottom) parts of the tensor components of effective permittivity ε_{eff} (first column $\varepsilon_{\text{eff}}^{\parallel}$, second column $\varepsilon_{\text{eff}}^{\perp}$) and effective permeability μ_{eff} (third column $\mu_{\text{eff}}^{\parallel}$, fourth column μ_{eff}^{\perp}) for a system/metamaterial of double-layered ($N = 2$) metasurface-formed cylinders in air, with core radius $R_1 = 100$ nm and for different outer-layer radii, $R_2 = 150$ nm (blue lines) and $R_2 = 250$ nm (red lines), and filling ratio $f = 20\%$. The vertical dashed lines indicate the resonance frequencies of the magnetic ($f_m = 18$ THz) and electric sheet conductivity ($f_e = 21$ THz).

the frequency regions 17.97-26.53 THz and 28.75-29.75 THz, and HMM II response ($\varepsilon_{\text{eff}}^{\perp}\mu_{\text{eff}}^{\parallel} > 0$ and $\varepsilon_{\text{eff}}^{\perp}\mu_{\text{eff}}^{\perp} < 0$) in the frequency range 28.19-28.7 THz.

We close our analysis by investigating the effective medium parameters for the double-layered metasurface cylinders systems which are shown Fig. 6.11. Similar to the single-layered cylinder case, we find a rich electromagnetic response. The main difference compared to the single-layered cylinders is the number of resonances associated with the TE_1 and TM_1 modes (affecting the magnetic permeability $\mu_{\text{eff}}^{\parallel}$ and electric permittivity $\varepsilon_{\text{eff}}^{\perp}$ components respectively). There are again regions of alternating optical phase (between HMM I and HMM II) for both TE and TM polarizations. For instance, for $R_1 = 100$ nm and $R_2 = 150$ nm there is a HMM I response in the frequency regions 21.17-29.34 THz and in 31.84-32.9 THz and a HMM II response in the frequency region 32.95-34.64 THz for TM polarization. For TE polarization there is HMM I response in the frequency regions 17.72-27.33 THz, 31.84-32.9 THz and HMM II response in the frequency region 31.24-31.79 THz. We should note here that we didn't find any frequency region of DNG response for the double-layered metasurface cylinders system. However, our results suggest that DNG response can be achieved also for this case by properly tuning the structure parameters (radii, filling ratio, materials).

6.4 Conclusions

We derived analytically the single scattering cross-sections for multilayer co-centric cylinders where every layer can be coated with metasurfaces of arbitrary sheet-conductivities, both

electric and magnetic. Using this formalism we further derived effective medium parameters for metamaterials composed of the above-mentioned co-centric cylinders.

Next we applied the formalism developed, performing a detailed study of metamaterial systems composed of (a) graphene nanotubes of one and two concentric layers, and (b) nanotubes formed from a metasurface having both electric and magnetic response, in the THz region of the electromagnetic spectrum, and we derived semi-analytical formulas for the effective medium parameters for those systems.

Initially, we calculated the single meta-atom extinction efficiency for both systems, for single-layered and double-layered co-center cylindrical configurations, assuming variable geometrical parameters, and We identified the nature of the dominant modes, i.e., the fundamental ($\nu = 0$) and dipolar ($\nu = 1$) modes, that contribute to the extinction spectrum. Next, we calculated the effective medium parameters of the systems. We found that by properly choosing the number of layers and radii, the resulting metamaterial systems can exhibit a rich electromagnetic response, own to the engineerable permittivity and permeability; this rich response includes a variety of alternating optical phases, i.e., hyperbolic response of both type I and type II for both TE and TM polarizations, double negative response and regions of epsilon-near-zero and mu-near-zero response. Our results suggest that the response of the metasurface-coated cylinders can be exploited for the design of multifunctional materials and devices for the control of THz electromagnetic radiation. The approach can be employed to every frequency regime with proper adjustments.

6.5 Appendices

6.5.1 Transfer Matrix Method

In this appendix we derive the transfer matrices used in our analysis. For TE polarization the magnetic field is parallel to the cylinder axis, $\mathbf{H} = H_z \hat{z}$. The electric and magnetic fields in the ℓ -th layer can be expanded on the basis of the cylindrical vector harmonics as:

$$\mathbf{E}_\ell = i \sum_{\nu=-\infty}^{\infty} \frac{i^\nu}{k_\ell} \left[c_{\ell\nu} \mathbf{M}_{e\nu k_\ell}^{(\text{outward})} + d_{\ell\nu} \mathbf{M}_{e\nu k_\ell}^{(\text{inward})} \right] \quad (6.41)$$

$$\mathbf{H}_\ell = \frac{1}{\eta_\ell} \sum_{\nu=-\infty}^{\infty} \frac{i^\nu}{k_\ell} \left[c_{\ell\nu} \mathbf{N}_{e\nu k_\ell}^{(\text{outward})} + d_{\ell\nu} \mathbf{N}_{e\nu k_\ell}^{(\text{inward})} \right] \quad (6.42)$$

where c is the speed of light in vacuum, $k_\ell = \sqrt{\varepsilon_\ell \mu_\ell} \frac{\omega}{c}$ and $\eta_\ell = \sqrt{\mu_\ell / \varepsilon_\ell}$. The coefficients $c_{\ell\nu}$ and $d_{\ell\nu}$ can be determined from the boundary conditions at the surface of the cylinder.

The boundary conditions at the interface between the ℓ -th and the $(\ell + 1)$ -th layer can be written as:

$$E_{\ell+1}^\varphi - E_\ell^\varphi = -\sigma_m(\ell) \frac{H_\ell^z + H_{\ell+1}^z}{2} \quad (6.43)$$

$$H_{\ell+1}^z - H_\ell^z = -\sigma_e(\ell) \frac{E_\ell^\varphi + E_{\ell+1}^\varphi}{2} \quad (6.44)$$

Now, we can connect the fields with the transfer matrix as:

$$\mathbb{T}_{\ell\nu}^P \begin{pmatrix} d_{\ell\nu} \\ c_{\ell\nu} \end{pmatrix} = \begin{pmatrix} d_{(\ell+1),\nu} \\ c_{(\ell+1),\nu} \end{pmatrix} \quad (6.45)$$

Where $\mathbb{T}_{\ell\nu}^P$ is the transfer matrix that connects the fields in the ℓ -th and $(\ell + 1)$ -th layer of the multi-layer cylinder for polarization $P = \{\text{TE}, \text{TM}\}$. For TM polarization (the electric field is

parallel to the cylinder axis, $\mathbf{E}=E_z\hat{z}$) the electric and magnetic fields in the ℓ -th layer can be expanded as:

$$\mathbf{H}_\ell = -\frac{i}{\eta_\ell} \sum_{\nu=-\infty}^{\infty} \frac{i^\nu}{k_\ell} \left[c_{\ell\nu} \mathbf{M}_{e\nu k_\ell}^{(\text{outward})} + d_{\ell\nu} \mathbf{M}_{e\nu k_\ell}^{(\text{inward})} \right] \quad (6.46)$$

$$\mathbf{E}_\ell = \sum_{\nu=-\infty}^{\infty} \frac{i^\nu}{k_\ell} \left[c_{\ell\nu} \mathbf{N}_{e\nu k_\ell}^{(\text{outward})} + d_{\ell\nu} \mathbf{N}_{e\nu k_\ell}^{(\text{inward})} \right] \quad (6.47)$$

The boundary conditions between the ℓ -th and the $(\ell + 1)$ -th layer can be written as:

$$E_{\ell+1}^z - E_\ell^z = \sigma_{m(\ell)} \frac{H_\ell^\varphi + H_{\ell+1}^\varphi}{2} \quad (6.48)$$

$$H_{\ell+1}^\varphi - H_\ell^\varphi = \sigma_{e(\ell)} \frac{E_\ell^z + E_{\ell+1}^z}{2} \quad (6.49)$$

6.5.2 Effective Medium Theory

In this appendix we derive the the total transfer matrix formulation which reads:

$$\mathbb{M}_{(N+1),\nu} \begin{pmatrix} b_\nu \\ 0 \end{pmatrix} = \begin{pmatrix} 1 \\ a_\nu^{(N+2)} \end{pmatrix} \quad (6.50)$$

with $\mathbb{M}_{(N+1),\nu}$ being the total transfer matrix of the layered infinitely-long cylinder with $N + 1$ layers.

$$\mathbb{M}_{(N+1),\nu} \begin{pmatrix} b_\nu \\ 0 \end{pmatrix} = \begin{pmatrix} 1 \\ a_\nu^{(N+2)} \end{pmatrix} \quad (6.51)$$

Therefore, the scattering coefficient $a_\nu^{(N+2)}$ will be:

$$b_\nu = \frac{1}{\mathbb{M}_{(N+1),\nu}^{(11)}} \quad (6.52)$$

$$a_\nu^{(N+2)} = \mathbb{M}_{(N+1),\nu}^{(21)} b_\nu = \frac{\mathbb{M}_{(N+1),\nu}^{(21)}}{\mathbb{M}_{(N+1),\nu}^{(11)}} \quad (6.53)$$

In order for an incoming wave to see a truly homogeneous medium, this coefficient has to vanish:

$$a_\nu^{(N+2)} = \mathbb{M}_{(N+1),\nu}^{(21)} b_\nu = \frac{\mathbb{M}_{(N+1),\nu}^{(21)}}{\mathbb{M}_{(N+1),\nu}^{(11)}} = 0 \quad (6.54)$$

which leads to:

$$\mathbb{M}_{(N+1),\nu}^{(21)} = 0. \quad (6.55)$$

For a system of N layers the total transfer matrix for the effective medium system can be written as:

$$\mathbb{M}_{(N+1),\nu} = \prod_{\ell=N+1}^1 \mathbb{T}_{\ell\nu} = \mathbb{T}_{(N+1),\nu} \prod_{\ell=N}^1 \mathbb{T}_{\ell\nu} \quad (6.56)$$

For simplicity we will denote $\mathbb{B}_{(N),\nu} = \prod_{\ell=N}^1 \mathbb{T}_{\ell\nu}$. This matrix contains information only about the original system. Using index notation for matrix multiplication $C^{ik} = \sum_j A^{ij} B^{jk}$ the generalized-CPA equation will be

$$\mathbb{M}_{(N+1),\nu}^{(21)} = 0 = \mathbb{T}_{(N+1),\nu}^{(21)} \mathbb{B}_{(N),\nu}^{(11)} + \mathbb{T}_{(N+1),\nu}^{(22)} \mathbb{B}_{(N),\nu}^{(21)} \quad (6.57)$$

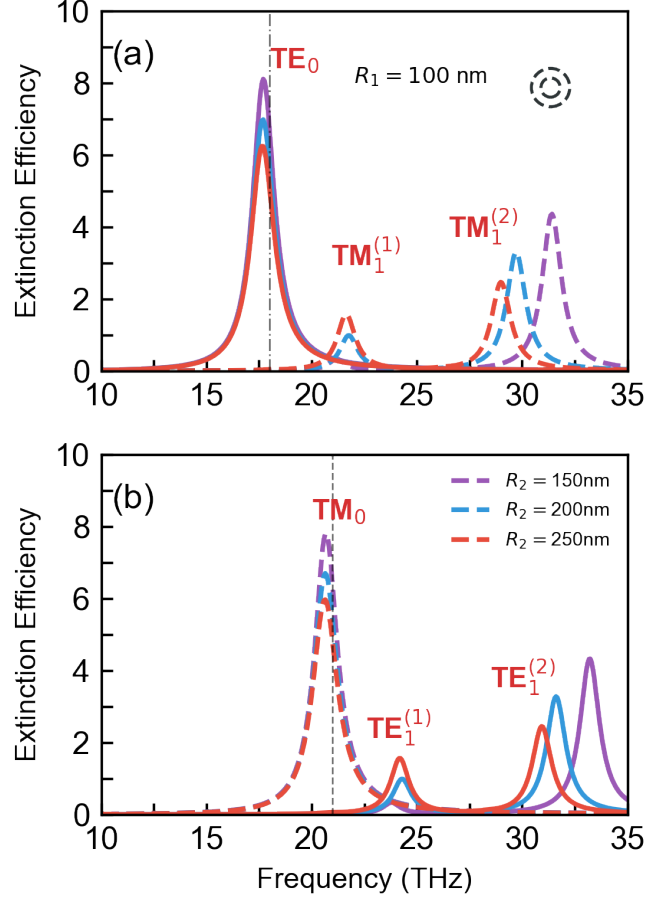


Figure 6.12: TE (solid lines) and TM (dashed lines) extinction efficiencies for a double-layered metasurface-coated cylinder ($N=2$) with core radius $R_1 = 100$ nm and variable outer layer radii R_2 for metasurfaces with (a) magnetic surface conductivity σ_m with $f_m = 18$ THz and $\sigma_e = 0$, and (b) electric surface conductivity σ_e with $f_e = 21$ THz and $\sigma_m = 0$. The vertical dashed grey lines indicate the resonances of the sheet conductivities.

or

$$-\frac{\mathbb{T}_{(N+1),\nu}^{(21)}}{\mathbb{T}_{(N+1),\nu}^{(22)}} = \frac{\mathbb{B}_{(N),\nu}^{(21)}}{\mathbb{B}_{(N),\nu}^{(11)}} \quad (6.58)$$

For the term appearing in the left-hand-side we have, $a_\nu(R_{N+1}; \text{eff}, h) = -\mathbb{T}_{(N+1),\nu}^{21}/\mathbb{T}_{(N+1),\nu}^{22}$, which is equal to the scattering coefficient of a single cylinder with electric permittivity ε_{eff} , magnetic permeability μ_{eff} and radius R_{N+1} embedded in a host with electric permittivity ε_h and magnetic permeability μ_{eff} . The right-hand-side is equal to $a_\nu^{(N)} = \mathbb{B}_{(N),\nu}^{21}/\mathbb{B}_{(N),\nu}^{11}$ (scattering coefficient of N -layer cylinder).

6.5.3 Extinction efficiencies for $N = 2$ and $\sigma_e = 0$ or $\sigma_m = 0$

Here we briefly discuss the case of a double-layered cylinder coated with a metasurface for the case of either $\sigma_e = 0$ or $\sigma_m = 0$. We keep $R_1 = 100$ nm, $f_e = 21$ THz and $f_m = 18$ THz. The extinction efficiencies are shown in Fig. 6.12. Comparing these results with Fig. 6.5(c)-(d) of the main text one can see several differences. Starting from the case with $\sigma_e = 0$ [Fig. 6.12(a)], we can see that the electric modes are absent from the extinction spectrum with only the

magnetic modes TE_0 and TM_1 being present. Interestingly, while the splitting in the dipolar TM_1 mode occurs, there is no splitting for the TE_0 mode in contrast to the metasurface with non-zero σ_e and σ_m . Similar conclusions can be reached for the case of $\sigma_m = 0$ where only the electric TM_0 and TE_1 modes appear in the extinction spectrum.

CHAPTER 7

LOCAL DENSITY OF STATES FOR INVERSE WOODPILE STRUCTURES

7.1 Introduction

¹ Controlling the properties of matter by means of quantum light lies at the heart of quantum optics and cavity quantum electrodynamics (cQED). A prime example is the control of the radiative rate of elementary emitters such as atoms, ions, molecules, or quantum dots. Such control is essential for myriad applications ranging from miniature lasers and light-emitting diodes [7], [179], via single-photon sources for quantum information processing [180], to solar energy harvesting [181]. To explore such new applications, a suitably tailored dielectric environment is required wherein the vacuum fluctuations, that play a central role in spontaneous emission [182], [183], are controlled. Much after the early realization by Purcell [184] that an emitter's environment such as a cavity controls the emission rate, spontaneous emission control has become one of the main drivers of the burgeoning field of nanophotonics [185]–[189]. Following the seminal predictions by Bykov and by Yablonovitch, emission control was first studied on photonic crystals [6], [7]. Emission control has also successfully been pursued with many different nanophotonic systems and many different quantum emitters, for instance, atoms and dye molecules in Fabry–Pérot microcavities [190], [191], quantum dots in pillar microcavities [192], [193], ions in whispering gallery-mode microspheres [194]–[196], dye molecules in plasmonic nanocavities and on nanoantennae [197]–[201], or dye in metamaterials [202], [203].

In the weak-coupling approximation in cQED, that is also known as the Wigner–Weisskopf approximation [204], spontaneous emission of an excited quantum emitter is precisely described by Fermi's golden rule [205] wherein the radiative decay rate is linearly proportional to the local density of optical states (LDOS). The LDOS counts the available number of electromagnetic modes each weighted by its strength, at each point \mathbf{r}_0 , and the projection of their electric field along the axes x, y, z [206]–[208]. The LDOS depends sensitively on the close environment of the emitter. Interestingly, the LDOS not only controls spontaneous emission and blackbody radiation, but also plays a role in van der Waals and Casimir dispersion forces and in Förster resonant energy transfer between different emitters [209]. Since the LDOS represents the density of vacuum fluctuations, it controls the amount of vacuum noise experienced by a qubit [210].

From theory, it is well-known that the LDOS is radically inhibited at frequencies within the 3D band gap in an infinite three-dimensional (3D) photonic crystal [4], [207], [211]–[216]. The LDOS vanishes at any position in the unit cell, and thus throughout the whole crystal, as well as for all dipole orientations. Concerning photonic crystal experiments, the first studies were reported on 3D crystals without 3D band gap [217]–[229], or on band gap crystals with low-efficiency emitters [230], [231], and in parallel there was a theoretical study on the anomalous

¹This work was conducted in collaboration with University of Twente, Complex Photonic Systems group (Prof. W. L. Vos)

Lamb shift [232]. Leistikow *et al.* studied efficient quantum dots in inverse woodpile photonic band gap crystals and observed exponential time-resolved decay, typical of weak coupling [233]. A $10\times$ inhibited spontaneous emission rate was observed inside the band gap. Since the emission was averaged over many emitters, it was inferred that a single quantum dot at the center of the crystal would be up to $160\times$ inhibited. To date, however, these results have not been interpreted by theory or numerical calculations.

It is obvious that experimental studies and devices employ finite photonic band gap crystals, where energy can radiate from the boundaries of the finite crystal. Consequently, states from the infinite surrounding vacuum tunnel into the crystal², leading to a non-zero LDOS and DOS inside the band gap [234], [235]. Therefore, it is natural to wonder how the LDOS in the gap depends on the position and orientation of the emitter inside the finite crystal? For two-dimensional (2D) photonic crystals, Asatryan *et al.* found in numerical calculations that the LDOS decreases exponentially from the surface into the crystal [236]. Hermann and Hess found a strong position and orientation dependence of spontaneous emission within the unit cell of an inverse opal, and saw that the inhibition in the band gap is of the two order of magnitudes, even for relatively small crystals [237]. Kole reported an exponentially growing inhibition towards the center of a spherical inverse opal photonic band gap crystal [238]. Leistikow *et al.* proposed that the LDOS averaged over a unit cell decreases exponentially with position for frequencies inside the 3D band gap, with a characteristic length scale, the so-called LDOS decay length; no prediction was offered though for the dependence within the unit cell [233].

Thus, it appears that calculations of the 3D LDOS in a 3D photonic band gap crystal are scarce in literature, due to their extensive computational cost and complexity. In this work, we systematically investigate the position- and orientation-dependent inhibition of the LDOS in the band gap of 3D inverse woodpile crystals with finite support. Despite recent progress on analytical approaches in nanophotonics [239], [240], there are to date no known analytic solutions for realistic 3D crystals, hence we have embarked on a numerical study to address the questions above. We study the role of the emitter position and interpret the computational results by an analytical expression for the expected behavior of the LDOS. We also study the role of the dipole orientation, and compare it to theoretically known behavior [241]. Since we decided to investigate the experimental results of Leistikow *et al.* [233], we have chosen to study the inverse woodpile crystal structure that was originally proposed by Ho *et al.* [242]. In our study, we find remarkable physical features, namely, (1) that the LDOS decreases exponentially as the emitter position goes from the surface towards the center of the crystal, (2) the magnitude of the exponential length scale, the LDOS decay length ℓ_ρ , is mostly determined by far-field radiation effects, whereas the amplitude prefactor is mostly determined by near-field effects, and (3) the magnitude of the LDOS decay length ℓ_ρ is remarkably close to the Bragg length - that typifies directional transport [243]–[245] - which implies that the LDOS is strikingly directional.

7.2 Methods

7.2.1 The structure of the finite crystal

The inverse woodpile photonic crystal has a primitive unit cell that is illustrated in Figure 7.1. The crystal structure consists of two orthogonal 2D arrays of identical cylindrical pores with radius $r_p = 0.24a$ running parallel to the x and z axes [242].³ The lattice constants are a

²A finite physical system, such as a photonic band gap crystal, that is surrounded by an infinite vacuum, or a bath, has in a strict mathematical sense a so-called finite support.

³For 2D arrays of pores only, the 2D LDOS has been studied by several interesting papers, notably Refs. [246]–[248]

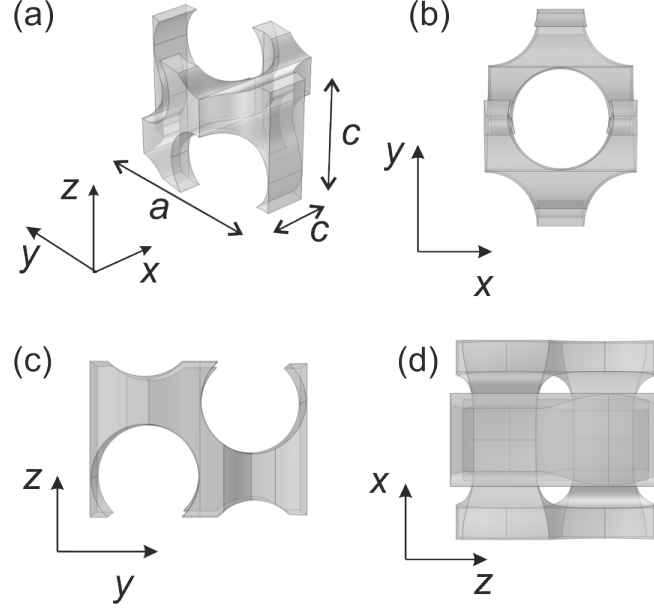


Figure 7.1: Unit cell of the inverse woodpile structure. (a) Bird's eye view of the tetragonal unit cell with two cylinders per lattice point, with lattice parameters c in the x -direction, a in the y -direction, and c in the z -direction. (b) View of the xy face of the unit cell, (c) of the yz face, and (d) of the xz face.

(in the y -direction) and c (in the x and z directions) in a ratio $a/c = \sqrt{2}$ for the crystal structure to be cuboid with a diamond-like symmetry. We discuss the LDOS as a function of the reduced frequency $\tilde{\omega}$ that is defined as $\tilde{\omega} \equiv \omega a / (2\pi c_0)$ with c_0 the speed of light in vacuum. The backbone of the crystal has the dielectric constant $\epsilon_b = 12.1$, typical of silicon in the near infrared and telecom spectral ranges. The cylindrical pores are considered to be either empty ($\epsilon_p = 1$) or filled with a dielectric with $\epsilon_p = 2.25$, that is typical for liquids, such as toluene, which are used to suspend quantum dot emitters in experiments; see Ref. [233]. In the experimentally relevant spectral range, silicon and toluene are essentially lossless. The finite crystals have an extent of N unit cells along each of the x , y , and z axes with a total volume of $V = N^3$ unit cells.

Figure 7.2(a) shows the band structure of the infinite crystal with empty pores calculated using the plane wave expansion method [249]. The shaded area in Figure 7.2(a) indicates the 3D photonic band gap with a broad relative bandwidth $\Delta\tilde{\omega}/\tilde{\omega}_{\text{mid}} = 25.0\%$, centered at $\tilde{\omega}_{\text{mid}} = 0.585$, in good agreement with earlier work [250]–[252]. Figure 7.2(b) shows the band structure for the crystal filled with toluene. Due to the decreased dielectric contrast the 3D photonic band gap has a reduced relative width, $\Delta\tilde{\omega}/\tilde{\omega}_{\text{mid}} = 6.4\%$. The band gap is centered at a lower frequency, near $\tilde{\omega}_{\text{mid}} = 0.49$, due to the increased effective average dielectric constant [253]. It is seen that in both air- and toluene-crystal cases the ΓY stop-band is larger than the ΓX and the ΓZ . This is sensible since in the y -direction one encounters dielectric contrast for two sets of pores whereas along the x - and z -direction one encounters dielectric contrast for only one set of pores.

7.2.2 Computation of the local density of states

It is well-known that the LDOS $\rho^{(i)}(\omega, \mathbf{r}_0)$ at a point \mathbf{r}_0 projected along the i -axis ($i = \{x, y, z\}$) is proportional to the total power $P^{(i)}(\omega, \mathbf{r}_0)$ radiated by an electric point dipole current source $\mathbf{J}(\omega, \mathbf{r}_0) = -i\omega \mathbf{p}(\omega) \delta(\mathbf{r} - \mathbf{r}_0)$ with dipole moment $\mathbf{p}(\omega)$ that points along the

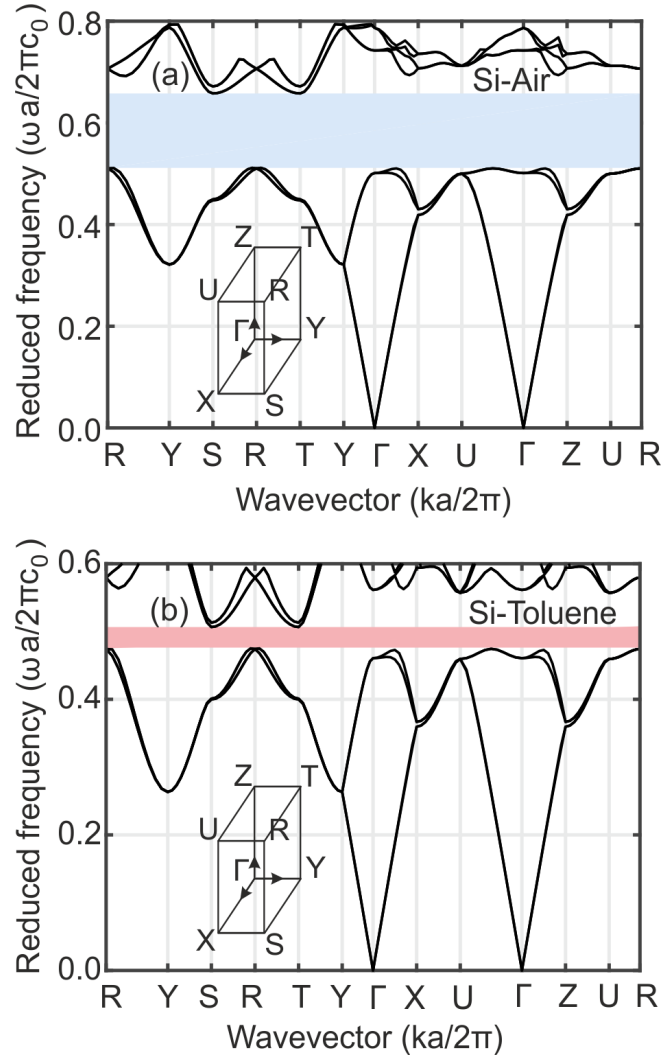


Figure 7.2: Band structures for an infinite inverse woodpile crystal made of silicon ($\varepsilon_b = 12.1$) with cylindrical pores filled with (a) air ($\varepsilon_p = 1.0$) and (b) toluene ($\varepsilon_p = 2.25$). The letters on the x -axes stand for the high symmetry points of the Brillouin zone shown in the inset. The blue and pink shaded bars indicate the 3D photonic band gap, from 0.511 to 0.658 in (a) and from 0.475 to 0.507 in (b).

unit vector \hat{e}_i of the i -axis.⁴ It is therefore convenient to normalize the total power emitted inside a nanostructured medium to the power $P_0^{(i)}(\omega, \mathbf{r}_0)$ emitted by a same dipole in a homogeneous isotropic medium with the same dielectric constant ε as where the dipole sits in the nanostructure. The normalized power is equal to the ratio of the LDOS in the nanostructured medium and the LDOS in a homogeneous medium with dielectric constant ε , and reads [254], [255]:

$$\frac{\rho^{(i)}(\omega, \mathbf{r}_0)}{\rho_0^{(i)}(\omega, \mathbf{r}_0)} = \frac{P^{(i)}(\omega, \mathbf{r}_0)}{P_0^{(i)}(\omega, \mathbf{r}_0)}. \quad (7.1)$$

Using Poynting's theorem [15], the power $P^{(i)}(\omega, \mathbf{r}_0)$ radiated by the dipole at position \mathbf{r}_0 is equal to inner product of the dipole moment and the local electric field $\mathbf{E}(\omega, \mathbf{r}_0)$ at the position of the dipole,

$$P^{(i)}(\omega, \mathbf{r}_0) = \frac{1}{2} \omega \text{Im} [\mathbf{E}(\omega, \mathbf{r}_0) \cdot \mathbf{p}^*(\omega)], \quad (7.2)$$

⁴In MEEP the current source is defined as $\mathbf{J}(\omega, \mathbf{r}_0) = \mathbf{p}(\omega) \delta(\mathbf{r} - \mathbf{r}_0)$ and hence, the power is: $P^{(i)}(\omega, \mathbf{r}_0) = -(1/2) \text{Re} [\mathbf{E} \cdot \mathbf{p}^*(\omega)]$

where we use complex notation and consider steady-state (time-average).

To calculate the power radiated by the dipole inside the finite-size photonic crystals we used the open-source implementation MEEP [256] of the finite-difference time domain (FDTD) method [257]. The finite-size crystal is surrounded by a uniform dielectric buffer with the same dielectric constant as that of the low- ε material in the pores. The computational volume is bounded on all sides by perfectly matched layers of thickness a to emulate infinite space. A dipolar point source is placed at the position of interest, \mathbf{r}_0 , with a Gaussian spectrum of central frequency equal to the mid-gap frequencies, $\tilde{\omega}_{\text{mid}} = 0.58$ and $\tilde{\omega}_{\text{mid}} = 0.49$ for empty and toluene-filled crystals, respectively. The full width at half maximum (FWHM) of the source spectrum was chosen to be equal to $\Delta\tilde{\omega} = 0.8$ to cover all the spectral features of interest.

To assess possible numerical artifacts of our method, we have compared the computed LDOS at the center of a dielectric Mie-sphere with analytical results [258], where the details are presented in the Appendix 7.5.1. For the best resolution (smallest grid size) and for a frequency range around the central frequency of the Gaussian pulse, we find deviation up to 3% outside Mie resonances, and about 10% near Mie-resonances, as shown in Figure 7.8. The spatial grid size of $\Delta = a/30$ was used in the photonic crystal calculations, since this gave a good match with the analytic test results for a Mie sphere (see Appendix 7.5.1), while keeping the computation time within reasonable bounds. The calculations were performed on a workstation with an Intel Core i7 processor with 8 CPU cores at 3.4 GHz clock speed and with 32GB RAM. To keep the simulations tractable, we studied 3D finite crystals with a volume $V = N^3 = 3^3$ unit cells. The simulation times were equal to $600(a/c_0)$; the real computation time was around 5000 s in order to achieve sufficient convergence of our calculations.

7.3 Results and discussion

7.3.1 Local density of states versus emitter position

We turn to the dependence of the LDOS $\rho^{(i)}(\omega, \mathbf{r}_0)$ on the position \mathbf{r}_0 inside the crystal at frequencies ω inside the 3D photonic band gap. We study the LDOS along trajectories in three different high-symmetry crystal directions. First, we consider the LDOS along the axis of the central pore pointing in the z -direction, as shown in Figure 7.3. Figure 7.3(a) illustrates the $(x = 0, y = 0, z)$ positions where the LDOS is probed. This set of probe positions are all in the same embedding medium (either air or toluene), which facilitates the interpretation. Figure 7.3(b) presents the calculated LDOS for the silicon-air crystal at the mid gap frequency ($\tilde{\omega}_{\text{mid}} = 0.58$) and Figure 7.3(c) shows the LDOS for the toluene-filled crystal at the mid gap frequency ($\tilde{\omega}_{\text{mid}} = 0.49$). The silicon-air data strongly decrease from the crystal surface to the center of the crystal. For x - and z -oriented dipoles, the normalized LDOS tends from about 1 to $5 \cdot 10^{-2}$, corresponding to a relative inhibition of $20\times$ at the center. For the y -oriented dipole, the normalized LDOS tends from about 0.4 to $5 \cdot 10^{-2}$, corresponding to a relative inhibition of $8\times$ at the center. In the toluene-filled crystal, see Fig. 7.3(c), similar trends appear, although with smaller inhibitions, of about $2\times$ to $3\times$, since the refractive-index contrast and thus the photonic strength is less than in the air-filled crystal. Aside, we note that the LDOS near the crystal surface is slightly enhanced (for x - and z -oriented dipoles) or slightly decreased (for y dipoles), which we tentatively attribute to surface modes [5] or to the fact that the vacuum modes are reflected by the crystal surface thus leading to interference just outside the surface, similar to the well-known Fresnel interference just outside a mirror [15].

Let us briefly compare to the experiments by Leistikow *et al.* [233], who studied the emission of quantum dots suspended in toluene that were embedded in silicon inverse woodpile structures. In the corresponding Fig. 7.3(c), we observe a substantial inhibition of the LDOS, in agreement

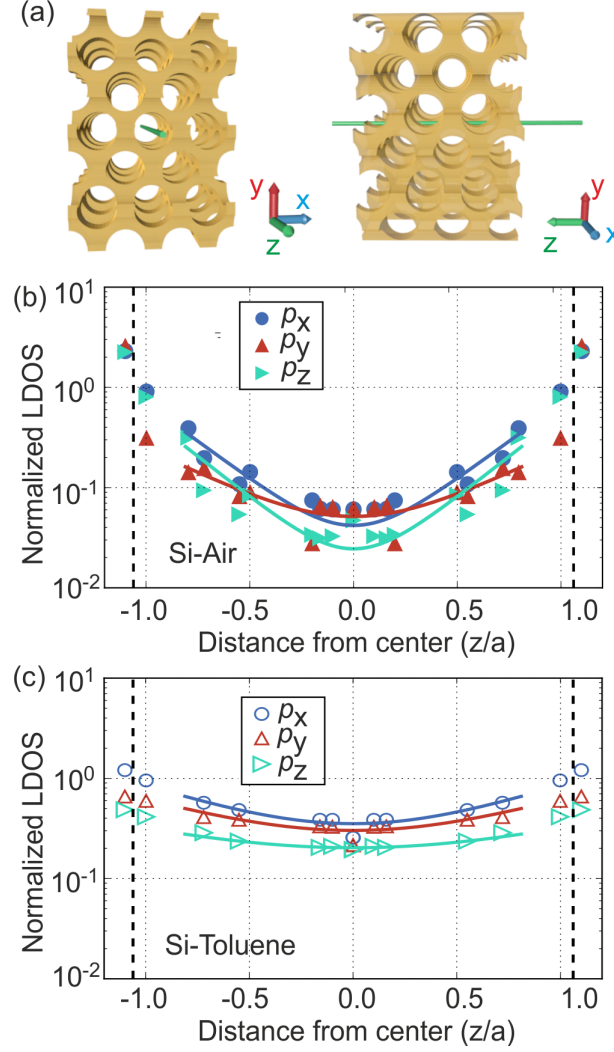


Figure 7.3: (a) Schematic of the $V = N^3 = 3^3$ crystal (N : unit cells number per direction) from two different perspectives; left: (001) view, right: (100) view. The green line ($x = 0, y = 0, z$) connects the positions where the LDOS is probed. (b, c) Normalized LDOS as a function of position along the z -axis at the mid-gap frequency for a (b) silicon-air crystal ($\tilde{\omega}_{\text{mid}} = 0.58$) and (c) a toluene-air crystal ($\tilde{\omega}_{\text{mid}} = 0.49$) with size $N^3 = 3^3$. Blue circles are for x -dipoles, p_x , red up-pointing triangles for y -dipoles, p_y , and green right-pointing triangles for z -dipoles, p_z . The drawn curves are exponential models of the data [Eq. (7.3)], with colors matching the relevant dipole orientation. The extent of the crystal is indicated by vertical dashed lines.

with the experimental observations. In the current situation, the inhibition at the center of the crystal is less (2 to 8 times) than in the experiments (more than 10 times), which is sensible since in the present case the crystal is smaller ($N^3 = 3^3$) than the ones in the experiments ($N^3 = 12^3$). There are aspects where no definite statements can be made, for instance, since the current results pertain to a single dipole that has a definite orientation, whereas in the experiment an ensemble of quantum dots was studied that sampled many positions throughout the whole crystal (80% of the whole volume) and whose dipole orientations were random.

Since the trend of the LDOS versus z -position in Figure 7.3(b) is exponential within the domain that is computationally tractable here, we interpret the data with a model consisting of two exponentials:

$$\frac{\rho^{(i)}(z)}{\rho_0} = A_i(e^{z/\ell_\rho^{(i)}} + e^{-z/\ell_\rho^{(i)}}). \quad (7.3)$$

	Air	Air	Toluene	Toluene
Orientation	$\ell_\rho^{(i)}/a$	A_i	$\ell_\rho^{(i)}/a$	A_i
$\hat{\mathbf{e}}_x$	0.286	0.021	0.653	0.176
$\hat{\mathbf{e}}_y$	0.449	0.026	0.743	0.151
$\hat{\mathbf{e}}_z$	0.267	0.012	0.973	0.101

Table 7.1: Parameters of Eq. (7.3) to model the normalized LDOS versus position along the z -direction shown in Fig. 7.3(b) and (c) for crystals with $N = 3$. Here, $\ell_\rho^{(i)}$ is the LDOS decay length and A_i is the amplitude prefactor. Parameters are given for silicon-air and for silicon-toluene crystals, and the rows are for dipoles oriented in the x , y , and z directions.

The main characteristic is the LDOS decay length $\ell_\rho^{(i)}$ that pertains to dipole orientation $\hat{\mathbf{e}}_i$. In case of a strong inhibition of the LDOS, as is the case in a broad 3D photonic band gap, $\ell_\rho^{(i)}$ will be small, and $\ell_\rho^{(i)}$ increases for less inhibition.⁵ As discussed below, the LDOS length $\ell_\rho^{(i)}$ is connected to far-field radiation effects of the dipole.

In Eq. (7.3) each exponential originates from one of the two opposite (x, y) -surfaces of the crystal (at $z/a = \pm 1.5/\sqrt{2} = \pm 1.06$), hence the plus and minus signs with twice the same characteristic LDOS decay length $\ell_\rho^{(i)}$. And A_i is a prefactor that equals half the LDOS at the center of the crystal (since $\rho^{(i)}(z=0)/\rho_0 = 2A_i$). As discussed below, A_i appears to be connected to near field effects of the dipole. In the modeling of the computed LDOS data with Eq. (7.3), we exclude the two data points near the surface to avoid complications due to surface and edge states and Fresnel interference. The solid curves in Fig. 7.3(b) and Fig. 7.3(c) are the fitted curves according to Eq. (7.3) for both silicon-air and silicon-toluene crystals and each of the three dipole orientations. The exponential model tracks the calculated LDOS data better in the toluene-filled crystal than the air-filled crystal, likely since in the former case the LDOS shows a weaker spatial dependence due to the reduced dielectric contrast, hence deviations are expected to be smaller. The resulting LDOS decay lengths and the prefactors are listed in Table 7.1 for both air-filled and toluene-filled crystals.

7.3.2 Model parameters and far-field and near-field

Table 7.1 shows that for the air-filled crystal the LDOS decay lengths are consistently smaller than for the toluene-filled crystals for all dipole orientations, $\hat{\mathbf{e}}_x$, $\hat{\mathbf{e}}_y$, and $\hat{\mathbf{e}}_z$. The shorter LDOS decay lengths are a direct consequence of the higher dielectric contrast in the air-filled crystal, which results in a broader gap (see Fig. 7.2) and thus stronger inhibitions. In their study on silicon-toluene crystals, Leistikow et al. [233] inferred the LDOS decay length to be equal to about $\ell_\rho^{(i)}/a = 1$. This is in fair agreement (between 3 and 35% greater) with the results in Table 7.1, which is a gratifying consistency between the experimental and computed results.

When considering all parameters in Table 7.1, it is instructive to discuss the role of the dipole orientation $\hat{\mathbf{e}}_i$ on both the characteristic LDOS length $\ell_\rho^{(i)}$ and the amplitude prefactor A_i . Starting with the air-filled crystal, we observe that the $\hat{\mathbf{e}}_x$ and $\hat{\mathbf{e}}_z$ oriented dipoles have smaller LDOS decay lengths ($\ell_\rho^{(x)}/a = 0.286$, $\ell_\rho^{(z)}/a = 0.267$) than the $\hat{\mathbf{e}}_y$ oriented dipole ($\ell_\rho^{(y)}/a = 0.449$). This result can be rationalized by a simple model wherein we consider a dipole to have a far-field radiation pattern typical of a homogeneous medium, namely predominantly in its equatorial plane [15] - see Fig. 7.4(a). Hence, the $\hat{\mathbf{e}}_x$ dipole radiates predominantly in the yz -plane in the crystal. The light that would propagate in this plane notably encounters the ΓY and

⁵Conversely, the inverse LDOS decay length may be considered to be a qualitative measure for the strength of a band gap.

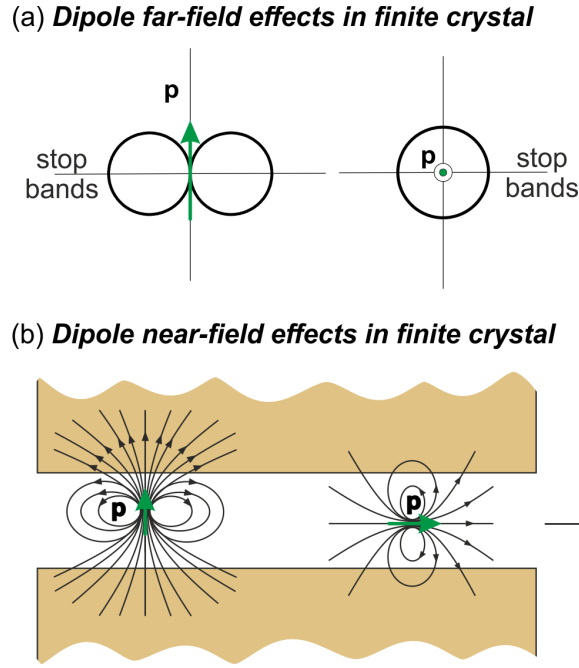


Figure 7.4: Schematic of a dipole (green) and its radiation pattern inside a finite photonic crystal. (a) The far-field components are maximal in the equatorial plane, where stop bands affect the local density of states. (b) For a dipole at the center of a pore, the near-field component is enhanced by the nearby high-index medium when the dipole is orientated toward this medium. The near-field component is hardly enhanced when the dipole is oriented along the pore axis (x or z).

the ΓZ high symmetry directions where the gap is wider (and intermediate directions) as seen in section 7.2.1. Hence, we naturally expect a strong inhibition in the yz -plane, which agrees qualitatively with the small LDOS decay length for the \hat{e}_x orientation. A similar reasoning holds for the \hat{e}_z dipole, whose equatorial plane is the xy -plane in the crystal that again includes the ΓY gap, and thus the LDOS decay length is also small. Conversely, in case of the \hat{e}_y dipole, the equatorial plane is the xz -plane in the crystal. This plane contains the relatively narrower ΓX and ΓZ gaps (but not the broad ΓY gap). Hence, less inhibition is expected than for the other orientations, which agrees well with the observed longer LDOS decay length. Thus, we conclude that arguments based solely on the far-field radiation pattern of the dipole located within the photonic crystal serve to explain the relative strength of the characteristic LDOS length observed for different dipole orientations.

We now turn to the role of the dipole orientation on the prefactor A_i . Here, we observe that the \hat{e}_z dipole exhibits the smallest prefactor ($A_z = 0.012$), whereas the \hat{e}_x and the \hat{e}_y dipoles have almost twice greater and closely similar prefactors ($A_x = 0.021$ and $A_y = 0.026$). To understand this behavior, we recall that in the near-field regime a dipole has the strongest field component $\mathbf{E}(\omega, \mathbf{r}_0)_i$ in the same direction i as its orientation \hat{e}_i [15], as illustrated in Fig. 7.4(b). Let us first consider the \hat{e}_y dipole orientation that has the maximum field in the y -direction $\mathbf{E}(\omega, \mathbf{r}_0)_y$. In the y -direction the $\mathbf{E}(\omega, \mathbf{r}_0)_y$ field crosses the air-silicon interface within a short distance, equal to $\Delta y = 0.12a = 0.12 \times 0.585\lambda = \lambda/14$. Therefore, this near-field experiences a polarization in the high-index material that enhances the near field. The enhanced near-field is apparently scattered to far-field radiation (by the interface), which leads to an enhanced LDOS and thus a larger prefactor A_y . Conversely, the \hat{e}_x and \hat{e}_z dipoles exhibit near fields in the x and z -directions where the field is completely inside the uniform air-filled pore. Thus the concomitant near fields experience no polarization enhancement by the silicon, hence

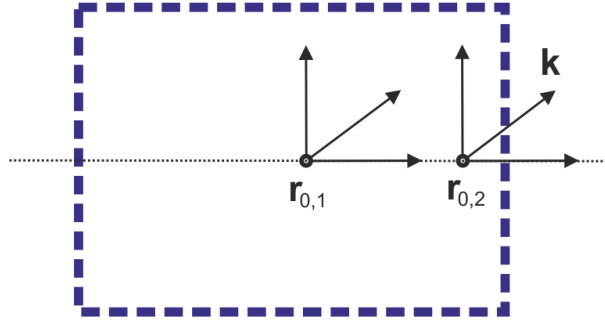


Figure 7.5: Schematic representation of the position vector $\mathbf{r}=(r_x, r_y, r_z)$ and the complex wavevector $\mathbf{k} = (k'_x + ik''_x, k'_y + ik''_y, k'_z + ik''_z)$ in the crystal under study, comprising of $N = 3$ unit cells. Inside the band gap where we calculate the LDOS the imaginary part of \mathbf{k} is nonzero. The position vector lies along the axis defined in each of the position dependence case studies in Fig. 7.3, Fig. 7.6 and Fig. 7.7.

the smaller values of A_x and A_z prefactors. Based of this reasoning we conclude that the A_i prefactors are mainly associated with the near-field distributions of the $\hat{\mathbf{e}}_i$ oriented dipoles. For convenience, the results of our discussion are summarized in Table 7.2.

	Far field	Near field
p_x	More inhib. (ΓY gap)	Strong field (\perp diel.)
p_y	Less inhib. only $\Gamma X, \Gamma Z$ gaps	Strong field (\perp diel.)
p_z	More inhib. (ΓY gap)	Weaker field (\parallel diel.)
	Concl.: affects $\ell_\rho^{(i)}$	Concl.: affects A_i

Table 7.2: Table summarizing the discussion of the near and far field effects on the LDOS decay lengths $\ell_\rho^{(i)}$ and the prefactor A_i . The LDOS decay lengths are mainly affected by the far field and the band gaps in the directions of the radiation. The prefactors A_i are mainly affected by near field effects and by polarization effects due to presence of nearby high-index material.

In the case of toluene-filled crystal, the behavior of the LDOS amplitude A_i is similar as in the silicon-air crystal. As seen in Table 7.1, the dipole with polarization $\hat{\mathbf{e}}_z$ exhibits the smallest amplitude ($A_z = 0.101$), followed by the dipoles polarized along $\hat{\mathbf{e}}_y$ and $\hat{\mathbf{e}}_x$ that have similar amplitudes (0.151 versus 0.176). We thus conclude that the near field has the same impact in this case. The characteristic LDOS length $\ell_\rho^{(i)}$, however, does not exhibit the same pattern as in the silicon-air case. As shown in Table 7.1 the strongest inhibition in this case, that is the smaller LDOS length, is found for the $\hat{\mathbf{e}}_x$ oriented dipole, followed by the $\hat{\mathbf{e}}_y$ dipole, and the $\hat{\mathbf{e}}_z$ dipole. The mismatch between the air and toluene cases is possibly caused by the fact that in the silicon-toluene crystal, the reduced refractive index contrast probably leads to an increase of the directional Bragg length, which becomes larger than the crystal size of $3 \times 3 \times 3$ unit cells considered here. In the toluene case, it is probably not meaningful to interpret the LDOS inside the crystal with band structure features, since the infinite crystal is not reached in the computations. In the silicon-air crystal, the Bragg length is sufficiently small compared to the crystal size, thus the infinite crystal limit is effectively reached; hence a reasoning invoking the interference associated with the band gaps in the band structure is meaningful.

7.3.3 Comparison between LDOS decay length and Bragg length

To put the LDOS decay length in perspective, we compare it to the well-known Bragg length L_B [243]–[245] that describes the exponential decay of a directional incident light beam with a frequency inside a photonic gap. This directional decay is described by a nonzero imaginary part of the wavevector, \mathbf{k}'' , due to Bragg diffraction. The imaginary part of the wavevector is inversely equal to the Bragg length L_B .

For silicon-air inverse woodpile crystals with the same pore radii as here, the Bragg length L_B was computed by Devashish *et al.* [252] by the finite-element method. For x -polarized incident plane waves, they found $L_B^{(x)} = 0.262a$, and $L_B^{(y)} = 0.428a$ for y -polarized illumination. These values are similar to the LDOS decay lengths, $\ell_\rho^{(x)} = 0.286a$ and $\ell_\rho^{(y)} = 0.449a$, in Table 7.1 for x - and y -oriented dipoles, respectively. Considering the difference in the underlying physics of these two lengths, namely the LDOS versus directional propagation, in other words, the real part of the Green function [259] versus the imaginary part of the Green function, it is remarkable for the two different length scales to match so closely.

To further support our interpretation, we consider in the schematic in Fig. 7.5 a dipole at two different positions inside a finite crystal, where we assume the positions to be on the z -axis as in Fig. 7.3. The dipole emits in many different directions in wave vector space (in wave vector space, a crystal as in Fig. 7.3 is more extended in the horizontal wave vector direction). Let us first consider an $\hat{\mathbf{e}}_x$ -oriented dipole that radiates mostly in the (y, z) -plane. Since the dipole has a frequency within the band gap, the radiation in any direction will be exponentially damped, since the wave vector is in every direction complex. Thus, the radiation in the z -direction is less damped close to the crystal surface (at position $\mathbf{r}_{0,2}$) than deeper inside, at position $\mathbf{r}_{0,1}$. Radiation in the perpendicular y -direction is equally damped at the different positions, since in this direction the dipole is everywhere at the same distance from the crystal-vacuum interface (similar considerations pertain to the x -direction). Radiation in an oblique direction with wave vector \mathbf{k} will also be increasingly damped when the dipole is located at increasing depth in the crystal. The behavior seen in Fig. 7.3 suggests that apparently the behavior of the LDOS with z -position is mostly determined by the z -directed radiation (that is in its purest sense described by the Bragg length), and hardly by the y -directed or other oblique radiation with wave vector \mathbf{k} . Thus, whereas the LDOS usually integrates over a broad spectrum of field modes with wave vectors corresponding to *all* directions, apparently the radiation tending in the closest vacuum-crystal interface dominates the spectrum. On the other hand, the fact that the LDOS integrates over a broad spectrum, instead of a single wave vector as in the Bragg length, explains perhaps why the LDOS decay length is somewhat larger than the corresponding Bragg length.

7.3.4 LDOS along different trajectories

We show in Figures 7.6 and 7.7 the normalized LDOS on the trajectories along x -axis and the diagonal path on the xz -plane, respectively. In both of these cases the calculations refer only to the silicon-air crystal. Once again, the position of the emitters are shown in the schematics of the upper panels of Fig. 7.6 and Fig. 7.7 respectively while the LDOS values are plotted in the bottom panel. Along these paths, the emitter goes through both the silicon and air regions inside the crystal. Since in the experiments by Leistikow *et al.* the LDOS was only probed for emitters placed in the low-index region, we have not considered the LDOS inside the high-index silicon. While moving across the air-Si interface, the normalized LDOS does not reveal a smooth and continuous behavior, which makes it impossible to use a simple exponential model such as Eq. (7.3). Indeed, similar strongly varying behavior across the low and high-index regions within a unit cell has already been noted in Ref. [234] for the much simpler case of a finite-size Bragg stack (i.e. an "one-dimensional photonic crystal").

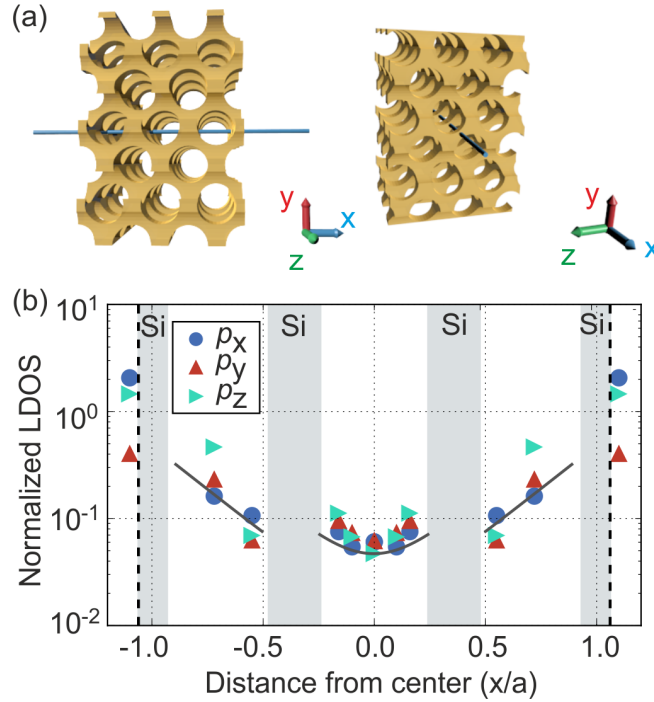


Figure 7.6: (a) Schematic of the $V = N^3 = 3^3$ crystal (N : unit cells number per direction) from two different perspectives; left: (001) view, right: (100) view. The blue line ($x, y = 0, z = 0$) connecting the positions where the LDOS is probed seen from two different perspectives. (b) Normalized LDOS as a function of position along the x -axis at the mid-gap frequency ($\tilde{\omega}_{\text{mid}} = 0.58$) for a silicon-air crystal with size $N^3 = 3^3$. Blue circles are for x -dipoles, p_x , red triangles are for y -dipoles, p_y , blue-green right-pointing triangles are for z -dipoles, p_z . The lines passing through the data points are guides to the eye. The shaded areas are the silicon backbone.

To highlight this behavior in our 3D crystal, we only draw guides to the eye that mark the trend of the LDOS in each direction. They are marked as black solid curves in Fig. 7.6(b) and Fig. 7.7(b). In both cases it appears that LDOS reveal abrupt variations while tending across the Si regions, which are highlighted in gray. Interestingly, for the x -polarization, when moving towards the vacuum-crystal interface from the center, LDOS shifts down across the silicon region when calculated on x -axis (Fig. 7.6(b)) whereas it shifts up when calculated on the diagonal of the xz -plane (in Fig. 7.7(b)).

7.3.5 Practical consequences

Let us briefly discuss a number of practical implications of our work, namely how to apply 3D photonic band gaps to emission control, quantum information processing, and photovoltaics.

In the field of spontaneous emission control, since the radiative rate is proportional to the LDOS, controlling the LDOS is a key step [189]. Hence it is clear that a 3D photonic band gap offers an extreme spontaneous emission control. In the field of photovoltaics, it is well known that an efficient absorber is equivalent to an efficient emitter [260]. Hence, a 3D photonic band gap could offer a control means to photovoltaics. In the field of quantum information science, it is relevant to shield qubits from ubiquitous vacuum fluctuations that lead to decoherence of the quantum states [210], [261]. One solution to this challenge is to place the qubits (assuming they are dipolar) in a 3D photonic band gap that covers the relevant frequency range of the qubits. Our work provides a design rule, namely where to place a dipolar emitter inside a

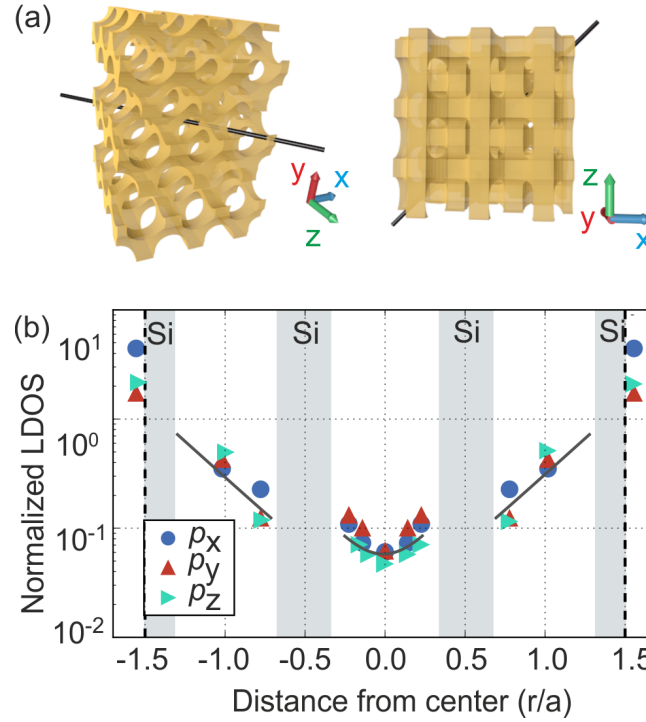


Figure 7.7: (a) Schematic of the $V = N^3 = 3^3$ crystal (N : unit cells number per direction) from two different perspectives, left: (001) view, right: (010) view. The black line ($x, y = 0, z = x$) connecting the positions where the LDOS is probed. (b) Normalized LDOS as a function of position along the xz -diagonal ($y = 0$) at the mid-gap frequency ($\tilde{\omega}_{\text{mid}} = 0.58$) for a silicon-air crystal with size $N^3 = 3^3$. Blue circles are for x -dipoles p_x , red triangles are for y -dipoles p_y , blue-green right-pointing triangles are for z -dipoles p_z . The lines passing through the data points are guides to the eye and the shaded areas are the silicon backbone.

photonic band gap crystal for a certain emission control, and, equivalently, where to place a dipole for a certain absorption control, and again equivalently, where to place a qubit for a certain decoherence control.

For instance, if one requires the density of vacuum fluctuations - hence the LDOS - to be shielded by a factor $10\times$, Fig. 7.3 shows that this is feasible for dipoles placed anywhere between $-0.5a \leq z \leq +0.5a$ about the center. For dipoles operating at optical frequencies corresponding to 1500 nm in the telecom range, this position freedom corresponds to a relatively large range, of about 700 nm. A slight limitation to our study is that we only consider positions in the low-index medium of the photonic crystal nanostructure, although these positions occupy no less than 80 vol% of the whole crystal volume [262]. The results in Fig. 7.3 also show that a tenfold shielding of the vacuum fluctuations is robust with respect to the orientation of the transition dipole moment of the dipole.

It is exhilarating that a silicon-air crystal has a significant inhibition of the LDOS, in view of the relatively small crystal size of only $V = 3 \times 3 \times 3$ unit cells. For dipolar emitters (qubits) operating at optical frequencies corresponding to 1500 nm, this would correspond to a small 3D silicon nanophotonic device, with a volume as small as $V = 4.2 \mu\text{m}^3$. Such a robustness with respect to the crystal size is due to the small LDOS decay length that is much less than one lattice spacing. In parallel to this work, an experimental study of the directional stop bands of (necessarily finite) 3D photonic band gap crystals [263] is also reaching the conclusion that relatively small micron-sized crystals are powerful tools to control directional transport.

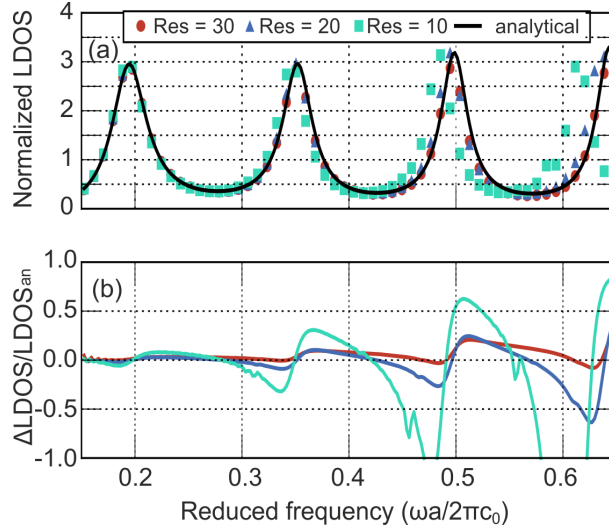


Figure 7.8: (a) LDOS at the center of a sphere for three different resolutions (10 (blue-green squares), 20 (blue triangles), and 30 points per radius (red circles)) of the FDTD grid versus the analytical solution (black curve). (b) Difference between the FDTD calculated results and the analytical solution for three different resolutions: 10 grid points per radius (blue-green squares), 20 grid points per radius (blue triangles), and 30 grid points per radius (red circles)).

7.4 Conclusions

We have presented a computational study of the inhibition of the LDOS in the 3D photonic band gap of a finite-size 3D photonic crystal. In particular, we focused on crystals with the silicon inverse woodpile structure that were recently studied experimentally. To this end, we considered the LDOS dependence on emitter's position and orientation inside the crystal. Our calculations showed that except for special cases, it is generally not possible to model the LDOS decrease away from the vacuum-crystal interface with a simple exponential model. However, in the cases where the exponential model did work, the LDOS decay length turned out to be surprisingly similar to the Bragg length. As for the impact of crystal size on the LDOS suppression, we found that a crystal comprising of only $3 \times 3 \times 3$ unit cells, if it is of high dielectric contrast (silicon-air), already provided more than ten times inhibition of the LDOS around its center. Therefore, for experiments designed to shield quantum systems from vacuum fluctuations, very small volume devices may well be sufficient to fulfill the design requirements on LDOS suppression.

7.5 Appendices

7.5.1 Numerical calculation of the LDOS

We numerically calculate the LDOS by relating the electric field at the location of the electric point dipole to the power radiated by the dipole - see Eq. (7.2). The electric field is obtained by placing a point dipole source at point \mathbf{r}_0 with a dipole moment parallel to x , y , or z axes. The transient amplitude of the dipole moment is described by a short Gaussian pulse to generate sufficient band width to cover the entire frequency spectrum of interest. After the initial excitation has vanished, we obtain the electric field component parallel to the dipole moment at \mathbf{r}_0 versus time t at every time step and take the Fourier transform to obtain the frequency-resolved field $\mathbf{E}(\omega, \mathbf{r}_0)$. This approach has also been used in earlier studies; see for instance Refs. [237], [264]–[266].

To validate the calculation of the LDOS with MEEP FDTD-code, we compare the results of FDTD method with analytical results, namely the modification of LDOS at the center of a dielectric sphere [258], [267]. We consider a sphere of radius $a = 1$ (reduced units) made of a dielectric material with real dielectric constant $\varepsilon_b = 12.1$. Fig. 7.8(a) shows the LDOS predicted by exact calculations (solid line) which exhibits resonances at reduced frequencies 0.2, 0.35, 0.50, associated with the Mie-resonances of the sphere. The numerical results were obtained with a Gaussian pulse centered at $\tilde{\omega} = 0.4$ and width $\Delta\tilde{\omega} = 0.9$. The numerically computed LDOS using the FDTD method is shown in the same figure as discrete points for various grid resolutions, defined as the number of sampling points over a radial distance. Good agreement is found between the analytical and numerically computed LDOS specially at higher resolution (30 grid points).

In Fig. 7.8(b), we quantify the convergence between analytical and numerical results by showing the relative difference (in percentage) between the numerical and analytical results. We observe that the convergence is better at frequencies outside the resonances - up to 3% near the central frequency 0.4 of the spectrum - than for the frequencies around the resonances, typically up to 10% near the central frequency 0.4. The most extreme differences appear at the upper edge of the spectrum where the precision is limited by the low intensity of the excitation pulse in the computation. This is expected due to the fact that the lifetime of the modes on-resonance is much greater and hence, more computational time is required for these frequencies. The numerical calculations are in an excellent agreement with the analytical results, to within 10% near resonances and 3% for off-resonance frequencies. Therefore, we conclude that the simulated results provide a faithful representation of the physics under study.

BIBLIOGRAPHY

- [1] M. S. Zubairy, *A Very Brief History of Light*. Cham: Springer International Publishing, 2016, pp. 3–24. DOI: [10.1007/978-3-319-31903-2_1](#) (cit. on p. 1).
- [2] M. Faraday, “X. The Bakerian Lecture. —Experimental relations of gold (and other metals) to light,” *Philos. Trans. R. Soc. London*, vol. 147, pp. 145–181, Dec. 1857, ISSN: 0261-0523. DOI: [10.1098/rstl.1857.0011](#) (cit. on p. 1).
- [3] J. C. Maxwell, “VIII. A dynamical theory of the electromagnetic field,” *Philos. Trans. R. Soc. London*, vol. 155, pp. 459–512, Dec. 1865, ISSN: 0261-0523. DOI: [10.1098/rstl.1865.0008](#) (cit. on p. 1).
- [4] E. N. Economou, *The Physics of Solids*. Berlin, Heidelberg: Springer Berlin Heidelberg, 2010, ISBN: 978-3-642-02068-1. DOI: [10.1007/978-3-642-02069-8](#) (cit. on pp. 2, 75).
- [5] Joannopoulos, John D. and Johnson, Steven G., Winn, J. N. and Meade, R. D., *Photonic Crystals: Molding the Flow of Light*, 2nd. Princeton Univ. Press, 2008 (cit. on pp. 2, 79).
- [6] V. P. Bykov, “Spontaneous Emission in a Periodic Structure,” *Sov. Phys. – JETP (Journal Theor. Exp. Physics)*, vol. 62, p. 269, 1972 (cit. on pp. 2, 75).
- [7] E. Yablonovitch, “Inhibited Spontaneous Emission in Solid-State Physics and Electronics,” *Phys. Rev. Lett.*, vol. 58, no. 20, pp. 2059–2062, May 1987, ISSN: 0031-9007. DOI: [10.1103/PhysRevLett.58.2059](#) (cit. on pp. 2, 75).
- [8] G. Mie, “Beiträge zur Optik trüber Medien, speziell kolloidaler Metallösungen,” *Ann. Phys.*, vol. 330, no. 3, pp. 377–445, 1908, ISSN: 00033804. DOI: [10.1002/andp.19083300302](#) (cit. on pp. 2, 3, 36).
- [9] C. F. Bohren and D. R. Huffman, *Absorption and Scattering of Light by Small Particles*. Wiley, Apr. 1998, ISBN: 9780471293408. DOI: [10.1002/9783527618156](#) (cit. on pp. 2, 3, 34–36).
- [10] P. Markos and C. M. Soukoulis, *Wave Propagation*. Princeton, NJ: Princeton University Press, Dec. 2008, ISBN: 9781400835676. DOI: [10.1515/9781400835676](#) (cit. on pp. 2, 5, 22).
- [11] P. Sheng, *Introduction to Wave Scattering, Localization and Mesoscopic Phenomena*. Berlin, Heidelberg: Springer Berlin Heidelberg, 2006, vol. 88, ISBN: 978-3-540-29155-8. DOI: [10.1007/3-540-29156-3](#) (cit. on pp. 3, 33, 54).
- [12] T. Zhan, X. Shi, Y. Dai, X. Liu, and J. Zi, “Transfer matrix method for optics in graphene layers,” *J. Phys. Condens. Matter*, vol. 25, no. 21, p. 215 301, May 2013, ISSN: 0953-8984. DOI: [10.1088/0953-8984/25/21/215301](#) (cit. on pp. 5, 22).
- [13] E. Kuester, M. Mohamed, M. Piket-May, and C. Holloway, “Averaged transition conditions for electromagnetic fields at a metafilm,” *IEEE Trans. Antennas Propag.*, vol. 51, no. 10, pp. 2641–2651, Oct. 2003, ISSN: 0018-926X. DOI: [10.1109/TAP.2003.817560](#) (cit. on pp. 5, 57).
- [14] C. L. Holloway, E. F. Kuester, and A. Dienstfrey, “Characterizing Metasurfaces/Metafilms: The Connection Between Surface Susceptibilities and Effective Material Properties,”

- IEEE Antennas Wirel. Propag. Lett.*, vol. 10, pp. 1507–1511, 2011, ISSN: 1536-1225. DOI: [10.1109/LAWP.2011.2182591](https://doi.org/10.1109/LAWP.2011.2182591) (cit. on pp. 5, 12, 27, 57).
- [15] J. D. Jackson, *Classical electrodynamics*, 3rd ed. New York, NY: Wiley, 1999, ISBN: 9780471309321 (cit. on pp. 9, 35, 78, 79, 81, 82).
- [16] P. Tassin, T. Koschny, and C. M. Soukoulis, “Effective material parameter retrieval for thin sheets: Theory and application to graphene, thin silver films, and single-layer metamaterials,” *Phys. B Condens. Matter*, vol. 407, no. 20, pp. 4062–4065, Oct. 2012, ISSN: 09214526. DOI: [10.1016/j.physb.2012.01.119](https://doi.org/10.1016/j.physb.2012.01.119) (cit. on pp. 12, 27, 54, 57).
- [17] O. Tsilipakos, T. Koschny, and C. M. Soukoulis, “Antimatched Electromagnetic Metasurfaces for Broadband Arbitrary Phase Manipulation in Reflection,” *ACS Photonics*, vol. 5, no. 3, pp. 1101–1107, Mar. 2018, ISSN: 2330-4022. DOI: [10.1021/acsp Photonics.7b01415](https://doi.org/10.1021/acsp Photonics.7b01415) (cit. on pp. 12, 27, 54, 57).
- [18] J. D. Joannopoulos, S. G. Johnson, W. J. N., and R. D. Meade, *Photonic Crystals: Molding the Flow of Light*, 2nd. Princeton Univ. Press, 2008 (cit. on p. 13).
- [19] D. G. Baranov, A. Krasnok, T. Shegai, A. Alù, and Y. Chong, “Coherent perfect absorbers: linear control of light with light,” *Nat. Rev. Mater.*, vol. 2, no. 12, p. 17 064, Dec. 2017, ISSN: 2058-8437. DOI: [10.1038/natrevmats.2017.64](https://doi.org/10.1038/natrevmats.2017.64) (cit. on pp. 15, 21).
- [20] Y. Rádi, C. R. Simovski, and S. A. Tretyakov, “Thin Perfect Absorbers for Electromagnetic Waves: Theory, Design, and Realizations,” *Phys. Rev. Appl.*, vol. 3, no. 3, p. 037 001, Mar. 2015, ISSN: 2331-7019. DOI: [10.1103/PhysRevApplied.3.037001](https://doi.org/10.1103/PhysRevApplied.3.037001) (cit. on p. 15).
- [21] Y. Cui, Y. He, Y. Jin, F. Ding, L. Yang, Y. Ye, S. Zhong, Y. Lin, and S. He, “Plasmonic and metamaterial structures as electromagnetic absorbers,” *Laser Photon. Rev.*, vol. 8, no. 4, pp. 495–520, Jul. 2014, ISSN: 18638880. DOI: [10.1002/lpor.201400026](https://doi.org/10.1002/lpor.201400026) (cit. on p. 15).
- [22] T. V. Teperik, F. J. García de Abajo, A. G. Borisov, M. Abdelsalam, P. N. Bartlett, Y. Sugawara, and J. J. Baumberg, “Omnidirectional absorption in nanostructured metal surfaces,” *Nat. Photonics*, vol. 2, no. 5, pp. 299–301, May 2008, ISSN: 1749-4885. DOI: [10.1038/nphoton.2008.76](https://doi.org/10.1038/nphoton.2008.76) (cit. on p. 15).
- [23] C. Wu, B. Neuner, J. John, A. Milder, B. Zollars, S. Savoy, and G. Shvets, “Metamaterial-based integrated plasmonic absorber/emitter for solar thermo-photovoltaic systems,” *J. Opt.*, vol. 14, no. 2, p. 024 005, Feb. 2012, ISSN: 20408986. DOI: [10.1088/2040-8978/14/2/024005](https://doi.org/10.1088/2040-8978/14/2/024005) (cit. on p. 15).
- [24] N. I. Landy, C. M. Bingham, T. Tyler, N. Jokerst, D. R. Smith, and W. J. Padilla, “Design, theory, and measurement of a polarization-insensitive absorber for terahertz imaging,” *Phys. Rev. B*, vol. 79, no. 12, p. 125 104, Mar. 2009, ISSN: 1098-0121. DOI: [10.1103/PhysRevB.79.125104](https://doi.org/10.1103/PhysRevB.79.125104) (cit. on p. 15).
- [25] M. A. Kats and F. Capasso, “Optical absorbers based on strong interference in ultra-thin films,” *Laser Photon. Rev.*, vol. 10, no. 5, pp. 735–749, Sep. 2016, ISSN: 1863-8880. DOI: [10.1002/lpor.201600098](https://doi.org/10.1002/lpor.201600098) (cit. on p. 15).
- [26] G. Kajtár, M. Kafesaki, E. N. Economou, and C. M. Soukoulis, “Theoretical model of homogeneous metal–insulator–metal perfect multi-band absorbers for the visible spectrum,” *J. Phys. D: Appl. Phys.*, vol. 49, no. 5, p. 055 104, Feb. 2016, ISSN: 0022-3727. DOI: [10.1088/0022-3727/49/5/055104](https://doi.org/10.1088/0022-3727/49/5/055104) (cit. on pp. 15–17, 19).
- [27] I. S. Nefedov, C. A. Valagiannopoulos, S. M. Hashemi, and E. I. Nefedov, “Total absorption in asymmetric hyperbolic media,” *Sci. Rep.*, vol. 3, no. 1, p. 2662, Dec. 2013, ISSN: 2045-2322. DOI: [10.1038/srep02662](https://doi.org/10.1038/srep02662) (cit. on p. 15).

- [28] D. G. Baranov, J. H. Edgar, T. Hoffman, N. Bassim, and J. D. Caldwell, “Perfect interferenceless absorption at infrared frequencies by a van der Waals crystal,” *Phys. Rev. B*, vol. 92, no. 20, p. 201 405, Nov. 2015, ISSN: 1098-0121. DOI: [10.1103/PhysRevB.92.201405](#) (cit. on p. 15).
- [29] M. Yan, “Metal–insulator–metal light absorber: a continuous structure,” *J. Opt.*, vol. 15, no. 2, p. 025 006, Feb. 2013, ISSN: 2040-8978. DOI: [10.1088/2040-8978/15/2/025006](#) (cit. on pp. 15, 19).
- [30] S. Foteinopoulou, G. C. R. Devarapu, G. S. Subramania, S. Krishna, and D. Wasserman, “Phonon-polaritonics: enabling powerful capabilities for infrared photonics,” *Nanophotonics*, vol. 8, no. 12, pp. 2129–2175, Dec. 2019, ISSN: 2192-8614. DOI: [10.1515/nanoph-2019-0232](#) (cit. on pp. 16, 31, 33).
- [31] P. B. Johnson and R. W. Christy, “Optical Constants of the Noble Metals,” *Phys. Rev. B*, vol. 6, no. 12, pp. 4370–4379, Dec. 1972, ISSN: 0556-2805. DOI: [10.1103/PhysRevB.6.4370](#) (cit. on p. 16).
- [32] E. D. Palik, *Handbook of Optical Constants of Solids*. Cambridge: Elsevier, 1985, ISBN: 9780080547213. DOI: [10.1016/C2009-0-20920-2](#) (cit. on p. 17).
- [33] G. Kenanakis, D. Vernardou, A. Dalamagkas, and N. Katsarakis, “Photocatalytic and electrooxidation properties of TiO₂ thin films deposited by sol–gel,” *Catal. Today*, vol. 240, pp. 146–152, Feb. 2015, ISSN: 09205861. DOI: [10.1016/j.cattod.2014.05.007](#) (cit. on p. 17).
- [34] S. B. Glybovski, S. A. Tretyakov, P. A. Belov, Y. S. Kivshar, and C. R. Simovski, “Metasurfaces: From microwaves to visible,” *Phys. Rep.*, vol. 634, pp. 1–72, 2016 (cit. on pp. 21, 53).
- [35] M. Chen, M. Kim, A. M. Wong, and G. V. Eleftheriades, “Huygens’ metasurfaces from microwaves to optics: a review,” *Nanophotonics*, vol. 7, no. 6, pp. 1207–1231, Jun. 2018, ISSN: 2192-8614. DOI: [10.1515/nanoph-2017-0117](#) (cit. on p. 21).
- [36] A. Alù, “Mantle cloak: Invisibility induced by a surface,” *Phys. Rev. B*, vol. 80, no. 24, p. 245 115, Dec. 2009, ISSN: 1098-0121. DOI: [10.1103/PhysRevB.80.245115](#) (cit. on pp. 21, 54).
- [37] N. Mohammadi Estakhri and A. Alù, “Wave-front Transformation with Gradient Metasurfaces,” *Phys. Rev. X*, vol. 6, no. 4, p. 041 008, Oct. 2016, ISSN: 2160-3308. DOI: [10.1103/PhysRevX.6.041008](#) (cit. on pp. 21, 57).
- [38] M. Beruete and I. Jáuregui-López, “Terahertz sensing based on metasurfaces,” *Adv. Opt. Mater.*, vol. 8, no. 3, 2020. DOI: [10.1002/adom.201900721](#) (cit. on p. 21).
- [39] E. Skoulas, A. C. Tasolamprou, G. Kenanakis, and E. Stratakis, “Laser induced periodic surface structures as polarizing optical elements,” *Appl Surf Sci*, vol. 541, 2021 (cit. on p. 21).
- [40] X. Zhang and Z. Liu, “Superlenses to overcome the diffraction limit,” *Nat. Mater.*, vol. 7, no. 6, pp. 435–441, 2008 (cit. on p. 21).
- [41] G. Perrakis, A. C. Tasolamprou, G. Kenanakis, E. Economou, S. Tzortzakis, and M. Kafesaki, “Combined nano and micro structuring for enhanced radiative cooling and efficiency of photovoltaic cells,” *Sci. Rep.*, vol. 11, no. 1, p. 11 552, 2021 (cit. on pp. 21, 53).
- [42] J. Zhou, L. Zhang, G. Tuttle, T. Koschny, and C. Soukoulis, “Negative index materials using simple short wire pairs,” *Physical Review B - Condensed Matter and Materials Physics*, vol. 73, no. 4, 2006. DOI: [10.1103/PhysRevB.73.041101](#) (cit. on p. 21).

- [43] M. Arif Hussain Ansari, A. Jha, Z. Akhter, and M. Jaleel Akhtar, “Multi-band rf planar sensor using complementary split ring resonator for testing of dielectric materials,” *IEEE Sensors Journal*, vol. 18, no. 16, pp. 6596–6606, 2018. DOI: [10.1109/JSEN.2018.2822877](https://doi.org/10.1109/JSEN.2018.2822877) (cit. on p. 21).
- [44] A. C. Tasolamprou, D. Mentzaki, Z. Viskadourakis, E. N. Economou, M. Kafesaki, and G. Kenanakis, “Flexible 3d printed conductive metamaterial units for electromagnetic applications in microwaves,” *Materials*, vol. 13, no. 17, 2020. DOI: [10.3390/ma13173879](https://doi.org/10.3390/ma13173879) (cit. on p. 21).
- [45] A. Kuznetsov, A. Miroshnichenko, M. Brongersma, Y. Kivshar, and B. Luk’yanchuk, “Optically resonant dielectric nanostructures,” *Science*, vol. 354, no. 6314, 2016. DOI: [10.1126/science.aag2472](https://doi.org/10.1126/science.aag2472) (cit. on pp. 21, 53).
- [46] V. I. Shcherbinin, V. I. Fesenko, T. I. Tkachova, and V. R. Tuz, “Superscattering from subwavelength corrugated cylinders,” *Phys. Rev. Applied*, vol. 13, p. 024 081, 2 Feb. 2020 (cit. on p. 21).
- [47] S. Batool, M. Nisar, F. Frezza, and F. Mangini, “Cloaking Using the Anisotropic Multilayer Sphere,” *Photonics*, vol. 7, no. 3, p. 52, Jul. 2020, ISSN: 2304-6732. DOI: [10.3390/photonics7030052](https://doi.org/10.3390/photonics7030052) (cit. on pp. 21, 54).
- [48] T. Tsiftsis, C. Valagiannopoulos, H. Liu, A.-A. Boulogeorgos, and N. Miridakis, “Metasurface-coated devices: A new paradigm for energy-efficient and secure 6g communications,” *IEEE Vehicular Technology Magazine*, Nov. 2021 (cit. on p. 21).
- [49] C. Liaskos, A. Tsioliariidou, S. Ioannidis, A. Pitsillides, and I. F. Akyildiz, “Realizing ambient backscatter communications with intelligent surfaces in 6g wireless systems,” *IEEE Wireless Communications*, pp. 1–8, 2021. DOI: [10.1109/MWC.101.2100233](https://doi.org/10.1109/MWC.101.2100233) (cit. on p. 21).
- [50] E. Takou, A. C. Tasolamprou, O. Tsilipakos, and E. N. Economou, “Dynamic anapole in metasurfaces made of sculptured cylinders,” *Phys. Rev. B*, vol. 100, p. 085 431, 8 Aug. 2019. DOI: [10.1103/PhysRevB.100.085431](https://doi.org/10.1103/PhysRevB.100.085431) (cit. on p. 21).
- [51] C. P. Mavdis, A. C. Tasolamprou, E. N. Economou, C. M. Soukoulis, and M. Kafesaki, “Polaritonic cylinders as multifunctional metamaterials: Single scattering and effective medium description,” *Phys. Rev. B*, vol. 102, no. 15, p. 155 310, Oct. 2020, ISSN: 2469-9950. DOI: [10.1103/PhysRevB.102.155310](https://doi.org/10.1103/PhysRevB.102.155310) (cit. on pp. 21, 54, 60).
- [52] J. R. Piper and S. Fan, “Total Absorption in a Graphene Monolayer in the Optical Regime by Critical Coupling with a Photonic Crystal Guided Resonance,” *ACS Photonics*, vol. 1, no. 4, pp. 347–353, Apr. 2014, ISSN: 2330-4022. DOI: [10.1021/ph400090p](https://doi.org/10.1021/ph400090p) (cit. on p. 21).
- [53] N. Kakenov, O. Balci, T. Takan, V. A. Ozkan, H. Altan, and C. Kocabas, “Observation of gate-tunable coherent perfect absorption of terahertz radiation in graphene,” *ACS Photonics*, vol. 3, no. 9, pp. 1531–1535, 2016. DOI: [10.1021/acsphotonics.6b00240](https://doi.org/10.1021/acsphotonics.6b00240). eprint: <https://doi.org/10.1021/acsphotonics.6b00240> (cit. on p. 21).
- [54] E. Galiffi, J. Pendry, and P. Huidobro, “Broadband tunable thz absorption with singular graphene metasurfaces,” *ACS Nano*, vol. 12, no. 2, pp. 1006–1013, 2018. DOI: [10.1021/acsnano.7b07951](https://doi.org/10.1021/acsnano.7b07951) (cit. on p. 21).
- [55] S. Doukas, A. Chatzilari, A. Dagkli, A. Papagiannopoulos, and E. Lidorikis, “Deep and fast free-space electro-absorption modulation in a mobility-independent graphene-loaded Bragg resonator,” *Appl. Phys. Lett.*, vol. 113, no. 1, p. 011 102, Jul. 2018, ISSN: 0003-6951. DOI: [10.1063/1.5030699](https://doi.org/10.1063/1.5030699) (cit. on p. 21).

- [56] A. C. Tasolamprou, A. . Koulouklidis, C. Daskalaki, C. P. Mavidis, G. Kenanakis, G. Deligeorgis, Z. Viskadourakis, P. Kuzhir, S. Tzortzakis, M. Kafesaki, E. N. Economou, and C. M. Soukoulis, “Experimental demonstration of ultrafast thz modulation in a graphene-based thin film absorber through negative photoinduced conductivity,” *ACS Photonics*, vol. 6, no. 3, pp. 720–727, 2019 (cit. on pp. 21, 54).
- [57] A. Ahmadivand, B. Gerislioglu, and Z. Ramezani, “Gated graphene island-enabled tunable charge transfer plasmon terahertz metamodulator,” *Nanoscale*, vol. 11, no. 17, pp. 8091–8095, 2019 (cit. on pp. 21, 54).
- [58] B. Zeng, Z. Huang, A. Singh, Y. Yao, A. Azad, A. Mohite, A. Taylor, D. Smith, and H.-T. Chen, “Hybrid graphene metasurfaces for high-speed mid-infrared light modulation and single-pixel imaging,” *Light: Science and Applications*, vol. 7, no. 1, 2018. DOI: [10.1038/s41377-018-0055-4](https://doi.org/10.1038/s41377-018-0055-4) (cit. on p. 21).
- [59] Y. Fan, N.-H. Shen, F. Zhang, Q. Zhao, H. Wu, Q. Fu, Z. Wei, H. Li, and C. Soukoulis, “Graphene plasmonics: A platform for 2d optics,” *Advanced Optical Materials*, vol. 7, no. 3, 2019. DOI: [10.1002/adom.201800537](https://doi.org/10.1002/adom.201800537) (cit. on p. 21).
- [60] E. Galiffi, P. Huidobro, P. Gonçalves, N. Mortensen, and J. Pendry, “Probing graphene’s nonlocality with singular metasurfaces,” *Nanophotonics*, vol. 9, no. 2, pp. 309–316, 2020. DOI: [10.1515/nanoph-2019-0323](https://doi.org/10.1515/nanoph-2019-0323) (cit. on p. 21).
- [61] A. D. Koulouklidis, E. Kyriakou, C. Daskalaki, M. S. Ergoktas, A. C. Tasolamprou, M. Kafesaki, C. Kocabas, and S. Tzortzakis, “Observation of ultrafast thz self-actions in graphene based modulators,” in *2021 Conference on Lasers and Electro-Optics Europe European Quantum Electronics Conference (CLEO/Europe-EQEC)*, 2021, pp. 1–1. DOI: [10.1109/CLEO/Europe-EQEC52157.2021.9542561](https://doi.org/10.1109/CLEO/Europe-EQEC52157.2021.9542561) (cit. on p. 21).
- [62] N. I. Landy, S. Sajuyigbe, J. J. Mock, D. R. Smith, and W. J. Padilla, “Perfect metamaterial absorber,” *Phys. Rev. Lett.*, vol. 100, p. 207 402, 20 May 2008. DOI: [10.1103/PhysRevLett.100.207402](https://doi.org/10.1103/PhysRevLett.100.207402) (cit. on p. 21).
- [63] A. N. Papadimopoulos, N. V. Kantartzis, N. L. Tsitsas, and C. A. Valagiannopoulos, “Wide-angle absorption of visible light from simple bilayers,” *Appl. Opt.*, vol. 56, no. 35, pp. 9779–9786, Dec. 2017. DOI: [10.1364/AO.56.009779](https://doi.org/10.1364/AO.56.009779) (cit. on p. 21).
- [64] G. Kenanakis, C. Mavidis, E. Vasilaki, N. Katsarakis, M. Kafesaki, E. Economou, and C. Soukoulis, “Perfect absorbers based on metal–insulator–metal structures in the visible region: A simple approach for practical applications,” *Applied Physics A: Materials Science and Processing*, vol. 123, no. 1, 2017. DOI: [10.1007/s00339-016-0711-6](https://doi.org/10.1007/s00339-016-0711-6) (cit. on p. 21).
- [65] Y. Ra’di, C. R. Simovski, and S. A. Tretyakov, “Thin perfect absorbers for electromagnetic waves: Theory, design, and realizations,” *Phys. Rev. Applied*, vol. 3, p. 037 001, 3 Mar. 2015. DOI: [10.1103/PhysRevApplied.3.037001](https://doi.org/10.1103/PhysRevApplied.3.037001) (cit. on p. 21).
- [66] I. S. Nefedov, C. A. Valagiannopoulos, and L. A. Melnikov, “Perfect absorption in graphene multilayers,” *Journal of Optics*, vol. 15, no. 11, p. 114 003, Oct. 2013. DOI: [10.1088/2040-8978/15/11/114003](https://doi.org/10.1088/2040-8978/15/11/114003) (cit. on p. 21).
- [67] R. Fante and M. McCormack, “Reflection properties of the salisbury screen,” *IEEE Transactions on Antennas and Propagation*, vol. 36, no. 10, pp. 1443–1454, 1988. DOI: [10.1109/8.8632](https://doi.org/10.1109/8.8632) (cit. on pp. 21, 26).
- [68] F. Ding, J. Dai, Y. Chen, J. Zhu, Y. Jin, and S. Bozhevolnyi, “Broadband near-infrared metamaterial absorbers utilizing highly lossy metals,” *Scientific Reports*, vol. 6, 2016. DOI: [10.1038/srep39445](https://doi.org/10.1038/srep39445) (cit. on p. 22).

- [69] N. Mou, S. Sun, H. Dong, S. Dong, Q. He, L. Zhou, and L. Zhang, "Hybridization-induced broadband terahertz wave absorption with graphene metasurfaces," *Opt. Express*, vol. 26, no. 9, pp. 11 728–11 736, Apr. 2018. doi: [10.1364/OE.26.011728](#) (cit. on p. 22).
- [70] X. Wang and S. A. Tretyakov, "Toward ultimate control of terahertz wave absorption in graphene," *IEEE Transactions on Antennas and Propagation*, vol. 67, no. 4, pp. 2452–2461, 2019. doi: [10.1109/TAP.2018.2889144](#) (cit. on p. 22).
- [71] P. Yu, L. Besteiro, Y. Huang, J. Wu, L. Fu, H. Tan, C. Jagadish, G. Wiederrecht, A. Govorov, and Z. Wang, "Broadband metamaterial absorbers," *Advanced Optical Materials*, vol. 7, no. 3, 2019. doi: [10.1002/adom.201800995](#) (cit. on p. 22).
- [72] R. Alaee, M. Albooyeh, and C. Rockstuhl, "Theory of metasurface based perfect absorbers," *Journal of Physics D: Applied Physics*, vol. 50, no. 50, 2017. doi: [10.1088/1361-6463/aa94a8](#) (cit. on p. 22).
- [73] X. Huang, X. Zhang, Z. Hu, M. Aqeeli, and A. Alburaikan, "Design of broadband and tunable terahertz absorbers based on graphene metasurface: Equivalent circuit model approach," *IET Microwaves, Antennas and Propagation*, vol. 9, no. 4, pp. 307–312, 2015. doi: [10.1049/iet-map.2014.0152](#) (cit. on p. 22).
- [74] L. A. Falkovsky and A. A. Varlamov, "Space-time dispersion of graphene conductivity," *The European Physical Journal B*, vol. 56, no. 4, pp. 281–284, Apr. 2007, ISSN: 1434-6028. doi: [10.1140/epjb/e2007-00142-3](#) (cit. on pp. 24, 56).
- [75] M. Kerker, D.-S. Wang, and C. L. Giles, "Electromagnetic scattering by magnetic spheres," *J. Opt. Soc. Am.*, vol. 73, no. 6, p. 765, Jun. 1983, ISSN: 0030-3941. doi: [10.1364/JOSA.73.000765](#) (cit. on p. 29).
- [76] V. G. Veselago, "THE ELECTRODYNAMICS OF SUBSTANCES WITH SIMULTANEOUSLY NEGATIVE VALUES OF ϵ AND μ ," *Sov. Phys. Uspekhi*, vol. 10, no. 4, pp. 509–514, Apr. 1968, ISSN: 0038-5670. doi: [10.1070/PU1968v010n04ABEH003699](#) (cit. on p. 31).
- [77] J. Pendry, A. Holden, D. Robbins, and W. Stewart, "Magnetism from conductors and enhanced nonlinear phenomena," *IEEE Trans. Microw. Theory Tech.*, vol. 47, no. 11, pp. 2075–2084, 1999, ISSN: 00189480. doi: [10.1109/22.798002](#) (cit. on p. 31).
- [78] R. A. Shelby, "Experimental Verification of a Negative Index of Refraction," *Science*, vol. 292, no. 5514, pp. 77–79, Apr. 2001, ISSN: 00368075. doi: [10.1126/science.1058847](#) (cit. on p. 31).
- [79] L. Peng, L. Ran, H. Chen, H. Zhang, J. A. Kong, and T. M. Grzegorczyk, "Experimental Observation of Left-Handed Behavior in an Array of Standard Dielectric Resonators," *Phys. Rev. Lett.*, vol. 98, no. 15, p. 157 403, Apr. 2007, ISSN: 0031-9007. doi: [10.1103/PhysRevLett.98.157403](#) (cit. on pp. 31, 53).
- [80] K. Vynck, D. Felbacq, E. Centeno, A. I. Căbuz, D. Cassagne, and B. Guizal, "All-dielectric rod-type metamaterials at optical frequencies," *Phys. Rev. Lett.*, vol. 102, p. 133 901, 13 Mar. 2009. doi: [10.1103/PhysRevLett.102.133901](#) (cit. on p. 31).
- [81] Y. Liu, G. Bartal, and X. Zhang, "All-angle negative refraction and imaging in a bulk medium made of metallic nanowires in the visible region," *Opt. Express*, vol. 16, no. 20, p. 15 439, Sep. 2008, ISSN: 1094-4087. doi: [10.1364/OE.16.015439](#) (cit. on p. 31).
- [82] A. Poddubny, I. Iorsh, P. Belov, and Y. Kivshar, "Hyperbolic metamaterials," *Nat. Photonics*, vol. 7, no. 12, pp. 948–957, Dec. 2013, ISSN: 1749-4885. doi: [10.1038/nphoton.2013.243](#) (cit. on p. 31).

- [83] W. Yan, L. Shen, L. Ran, and J. A. Kong, "Surface modes at the interfaces between isotropic media and indefinite media," *J. Opt. Soc. Am. A*, vol. 24, no. 2, p. 530, Feb. 2007, ISSN: 1084-7529. DOI: [10.1364/JOSAA.24.000530](#) (cit. on p. 31).
- [84] T. Rep  n, A. Novitsky, M. Willatzen, and A. V. Lavrinenko, "Pseudocanalization regime for magnetic dark-field hyperlenses," *Phys. Rev. B*, vol. 96, no. 19, p. 195 166, Nov. 2017, ISSN: 2469-9950. DOI: [10.1103/PhysRevB.96.195166](#) (cit. on pp. 31, 45).
- [85] M. Kim, S. So, K. Yao, Y. Liu, and J. Rho, "Deep sub-wavelength nanofocusing of UV-visible light by hyperbolic metamaterials," *Sci. Rep.*, vol. 6, no. 1, p. 38 645, Dec. 2016, ISSN: 2045-2322. DOI: [10.1038/srep38645](#) (cit. on p. 31).
- [86] M. S. Habib, A. Stefani, S. Atakaramians, S. C. Fleming, and B. T. Kuhlmey, "Analysis of a hyperprism for exciting high- k modes and subdiffraction imaging," *Phys. Rev. B*, vol. 100, no. 11, p. 115 146, Sep. 2019, ISSN: 2469-9950. DOI: [10.1103/PhysRevB.100.115146](#) (cit. on p. 31).
- [87] Z. Jacob, I. I. Smolyaninov, and E. E. Narimanov, "Broadband Purcell effect: Radiative decay engineering with metamaterials," *Appl. Phys. Lett.*, vol. 100, no. 18, p. 181 105, Apr. 2012, ISSN: 0003-6951. DOI: [10.1063/1.4710548](#) (cit. on p. 31).
- [88] D. Lu, H. Qian, K. Wang, H. Shen, F. Wei, Y. Jiang, E. E. Fullerton, P. K. L. Yu, and Z. Liu, "Nanostructuring Multilayer Hyperbolic Metamaterials for Ultrafast and Bright Green InGaN Quantum Wells," *Adv. Mater.*, vol. 30, no. 15, p. 1 706 411, Apr. 2018, ISSN: 09359648. DOI: [10.1002/adma.201706411](#) (cit. on p. 31).
- [89] M. Silveirinha and N. Engheta, "Tunneling of Electromagnetic Energy through Sub-wavelength Channels and Bends using ϵ -Near-Zero Materials," *Phys. Rev. Lett.*, vol. 97, no. 15, p. 157 403, Oct. 2006, ISSN: 0031-9007. DOI: [10.1103/PhysRevLett.97.157403](#) (cit. on p. 31).
- [90] R. Maas, J. Parsons, N. Engheta, and A. Polman, "Experimental realization of an epsilon-near-zero metamaterial at visible wavelengths," *Nat. Photonics*, vol. 7, no. 11, pp. 907–912, Nov. 2013, ISSN: 1749-4885. DOI: [10.1038/nphoton.2013.256](#) (cit. on p. 31).
- [91] G. Briere, B. Cluzel, and O. Demichel, "Improving the transmittance of an epsilon-near-zero-based wavefront shaper," *Opt. Lett.*, vol. 41, no. 19, p. 4542, Oct. 2016, ISSN: 0146-9592. DOI: [10.1364/OL.41.004542](#) (cit. on p. 31).
- [92] K. C. Huang, M. L. Povinelli, and J. D. Joannopoulos, "Negative effective permeability in polaritonic photonic crystals," *Appl. Phys. Lett.*, vol. 85, no. 4, pp. 543–545, Jul. 2004, ISSN: 0003-6951. DOI: [10.1063/1.1775291](#) (cit. on p. 31).
- [93] S. Foteinopoulou, M. Kafesaki, E. N. Economou, and C. M. Soukoulis, "Two-dimensional polaritonic photonic crystals as terahertz uniaxial metamaterials," *Phys. Rev. B*, vol. 84, no. 3, p. 035 128, Jul. 2011, ISSN: 1098-0121. DOI: [10.1103/PhysRevB.84.035128](#) (cit. on pp. 31, 34).
- [94] S. Jahani and Z. Jacob, "All-dielectric metamaterials," *Nat. Nanotechnol.*, vol. 11, no. 1, pp. 23–36, Jan. 2016, ISSN: 1748-3387. DOI: [10.1038/nnano.2015.304](#) (cit. on p. 32).
- [95] I. Liberal, Y. Li, and N. Engheta, "Magnetic field concentration assisted by epsilon-near-zero media," *Philos. Trans. R. Soc. A Math. Phys. Eng. Sci.*, vol. 375, no. 2090, p. 20 160 059, Mar. 2017, ISSN: 1364-503X. DOI: [10.1098/rsta.2016.0059](#) (cit. on p. 33).
- [96] M. J. C. Garnett, "Colours in metal glasses and in metallic films," *Philos. Trans. R. Soc. London. Ser. A*, vol. 203, no. 359-371, pp. 385–420, Jan. 1904, ISSN: 0264-3952. DOI: [10.1098/rsta.1904.0024](#) (cit. on pp. 33, 37, 42).

- [97] J. A. Schuller and M. L. Brongersma, “General properties of dielectric optical antennas,” *Opt. Express*, vol. 17, no. 26, p. 24 084, Dec. 2009, ISSN: 1094-4087. DOI: [10.1364/OE.17.024084](#) (cit. on pp. 33, 36).
- [98] N. A. Butakov and J. A. Schuller, “Designing Multipolar Resonances in Dielectric Metamaterials,” *Sci. Rep.*, vol. 6, no. 1, p. 38 487, Dec. 2016, ISSN: 2045-2322. DOI: [10.1038/srep38487](#) (cit. on p. 33).
- [99] V. Yannopapas and A. Moroz, “Negative refractive index metamaterials from inherently non-magnetic materials for deep infrared to terahertz frequency ranges,” *J. Phys. Condens. Matter*, vol. 17, no. 25, pp. 3717–3734, Jun. 2005, ISSN: 0953-8984. DOI: [10.1088/0953-8984/17/25/002](#) (cit. on p. 33).
- [100] V. Yannopapas, “Artificial magnetism and negative refractive index in three-dimensional metamaterials of spherical particles at near-infrared and visible frequencies,” *Appl. Phys. A*, vol. 87, no. 2, pp. 259–264, Mar. 2007, ISSN: 0947-8396. DOI: [10.1007/s00339-006-3815-6](#) (cit. on p. 33).
- [101] S. O’Brien and J. B. Pendry, “Magnetic activity at infrared frequencies in structured metallic photonic crystals,” *J. Phys. Condens. Matter*, vol. 14, no. 25, p. 307, Jul. 2002, ISSN: 09538984. DOI: [10.1088/0953-8984/14/25/307](#) (cit. on pp. 33, 37).
- [102] J. A. Schuller, R. Zia, T. Taubner, and M. L. Brongersma, “Dielectric Metamaterials Based on Electric and Magnetic Resonances of Silicon Carbide Particles,” *Phys. Rev. Lett.*, vol. 99, no. 10, p. 107 401, Sep. 2007, ISSN: 0031-9007. DOI: [10.1103/PhysRevLett.99.107401](#) (cit. on pp. 33, 34).
- [103] X. Zhang and Y. Wu, “Effective medium theory for anisotropic metamaterials,” *Sci. Rep.*, vol. 5, no. 1, p. 7892, Jul. 2015, ISSN: 2045-2322. DOI: [10.1038/srep07892](#) (cit. on p. 33).
- [104] Y. Wu, J. Li, Z.-Q. Zhang, and C. T. Chan, “Effective medium theory for magnetodielectric composites: Beyond the long-wavelength limit,” *Phys. Rev. B*, vol. 74, p. 085 111, 8 Aug. 2006. DOI: [10.1103/PhysRevB.74.085111](#) (cit. on pp. 33, 34, 37, 54, 60).
- [105] A. Reyes-Coronado, M. F. Acosta, R. I. Merino, V. M. Orera, G. Kenanakis, N. Katsarakis, M. Kafesaki, C. Mavdis, J. G. de Abajo, E. N. Economou, and C. M. Soukoulis, “Self-organization approach for THz polaritonic metamaterials,” *Opt. Express*, vol. 20, no. 13, p. 14 663, Jun. 2012, ISSN: 1094-4087. DOI: [10.1364/OE.20.014663](#) (cit. on pp. 33, 34, 42, 44).
- [106] R. Hillenbrand, “Towards phonon photonics: scattering-type near-field optical microscopy reveals phonon-enhanced near-field interaction,” *Ultramicroscopy*, vol. 100, no. 3-4, pp. 421–427, Aug. 2004, ISSN: 03043991. DOI: [10.1016/j.ultramic.2003.11.017](#) (cit. on p. 33).
- [107] M. S. Mirmoosa, S. Y. Kosulnikov, and C. R. Simovski, “Magnetic hyperbolic metamaterial of high-index nanowires,” *Phys. Rev. B*, vol. 94, no. 7, p. 075 138, Aug. 2016, ISSN: 2469-9950. DOI: [10.1103/PhysRevB.94.075138](#) (cit. on pp. 34, 37, 45).
- [108] A. C. Tasolamprou, O. Tsilipakos, M. Kafesaki, C. M. Soukoulis, and E. N. Economou, “Toroidal eigenmodes in all-dielectric metamolecules,” *Phys. Rev. B*, vol. 94, no. 20, p. 205 433, Nov. 2016, ISSN: 2469-9950. DOI: [10.1103/PhysRevB.94.205433](#) (cit. on p. 34).
- [109] E. Takou, A. C. Tasolamprou, O. Tsilipakos, and E. N. Economou, “Dynamic anapole in metasurfaces made of sculptured cylinders,” *Phys. Rev. B*, vol. 100, p. 085 431, 8 2019 (cit. on p. 34).

- [110] M. Massaouti, A. A. Basharin, M. Kafesaki, M. F. Acosta, R. I. Merino, V. M. Orera, E. N. Economou, C. M. Soukoulis, and S. Tzortzakis, “Eutectic epsilon-near-zero metamaterial terahertz waveguides,” *Opt. Lett.*, vol. 38, no. 7, p. 1140, Apr. 2013, ISSN: 0146-9592. DOI: [10.1364/OL.38.001140](#) (cit. on p. 34).
- [111] D. A. Pawlak, S. Turczynski, M. Gajc, K. Kolodziejek, R. Diduszko, K. Rozniatowski, J. Smalc, and I. Vendik, “How Far Are We from Making Metamaterials by Self-Organization? The Microstructure of Highly Anisotropic Particles with an SRR-Like Geometry,” *Adv. Funct. Mater.*, vol. 20, no. 7, pp. 1116–1124, Mar. 2010, ISSN: 1616301X. DOI: [10.1002/adfm.200901875](#) (cit. on p. 34).
- [112] D. Ward, E. Statz, and K. Nelson, “Fabrication of polaritonic structures in LiNbO₃ and LiTaO₃ using femtosecond laser machining,” *Appl. Phys. A*, vol. 86, no. 1, pp. 49–54, Nov. 2006, ISSN: 0947-8396. DOI: [10.1007/s00339-006-3721-y](#) (cit. on p. 34).
- [113] Y. H. Fu, A. I. Kuznetsov, A. E. Miroshnichenko, Y. F. Yu, and B. Luk’yanchuk, “Directional visible light scattering by silicon nanoparticles,” *Nat. Commun.*, vol. 4, no. 1, p. 1527, Jun. 2013, ISSN: 2041-1723. DOI: [10.1038/ncomms2538](#) (cit. on p. 34).
- [114] A. C. Tasolamprou, L. Zhang, M. Kafesaki, T. Koschny, and C. M. Soukoulis, “Experimentally excellent beaming in a two-layer dielectric structure,” *Opt. Express*, vol. 22, no. 19, pp. 23 147–23 152, 2014 (cit. on p. 34).
- [115] I. Staude and J. Schilling, “Metamaterial-inspired silicon nanophotonics,” *Nat. Photonics*, vol. 11, no. 5, pp. 274–284, May 2017, ISSN: 1749-4885. DOI: [10.1038/nphoton.2017.39](#) (cit. on p. 34).
- [116] C. P. Mavidis, A. C. Tasolamprou, S. B. Hasan, T. Koschny, E. N. Economou, M. Kafesaki, C. M. Soukoulis, and W. L. Vos, “Local density of optical states in the three-dimensional band gap of a finite photonic crystal,” *Phys. Rev. B*, vol. 101, no. 23, p. 235 309, Jun. 2020, ISSN: 2469-9950. DOI: [10.1103/PhysRevB.101.235309](#) (cit. on p. 34).
- [117] A. C. Tasolamprou, L. Zhang, E. N. Economou, C. M. Soukoulis, and T. Koschny, “Surface states on photonic crystals as hybrid dielectric metasurface bound states of the termination layer,” *ACS Photonics*, vol. 0, no. ja, null, 2020. DOI: [10.1021/acsp Photonics.0c01083](#) (cit. on p. 34).
- [118] M. Kafesaki and E. N. Economou, “Acoustic waves in random media,” *Europhys. Lett.*, vol. 37, no. 1, pp. 7–12, 1997 (cit. on pp. 34, 54).
- [119] —, “Acoustic and elastic waves in random media - cpa,” *Ann Phys Leipzig*, vol. 7, no. 5-6, pp. 383–388, 1998 (cit. on pp. 34, 54).
- [120] J. A. Stratton, *Electromagnetic Theory*. Hoboken, NJ, USA: John Wiley & Sons, Inc., Oct. 2015, ISBN: 9781119134640. DOI: [10.1002/9781119134640](#) (cit. on pp. 34, 35, 48, 57).
- [121] M. Abramowitz, I. A. Stegun, and D. Miller, *Handbook of Mathematical Functions With Formulas, Graphs and Mathematical Tables*. Washington D.C.: United States Department of Commerce, National Institute of Standards and Technology (NBS), 1964 (cit. on pp. 36, 60).
- [122] S. A. Maier, *Plasmonics: fundamentals and applications*. Springer Science & Business Media, 2007 (cit. on p. 37).
- [123] R. Ruppin, “Evaluation of extended Maxwell-Garnett theories,” *Opt. Commun.*, vol. 182, no. 4-6, pp. 273–279, Aug. 2000, ISSN: 00304018. DOI: [10.1016/S0030-4018\(00\)00825-7](#) (cit. on p. 37).

- [124] L. Dell’Anna and M. Merano, “Clausius-Mossotti Lorentz-Lorenz relations and retardation effects for two-dimensional crystals,” *Phys. Rev. A*, vol. 93, no. 5, p. 053 808, May 2016, ISSN: 2469-9926. DOI: [10.1103/PhysRevA.93.053808](https://doi.org/10.1103/PhysRevA.93.053808) (cit. on p. 37).
- [125] C. A. Pfeiffer, E. N. Economou, and K. L. Ngai, “Surface polaritons in a circularly cylindrical interface: Surface plasmons,” *Phys. Rev. B*, vol. 10, no. 8, pp. 3038–3051, Oct. 1974, ISSN: 0556-2805. DOI: [10.1103/PhysRevB.10.3038](https://doi.org/10.1103/PhysRevB.10.3038) (cit. on pp. 39, 61).
- [126] F. Wang and Y. R. Shen, “General Properties of Local Plasmons in Metal Nanostructures,” *Phys. Rev. Lett.*, vol. 97, no. 20, p. 206 806, Nov. 2006, ISSN: 0031-9007. DOI: [10.1103/PhysRevLett.97.206806](https://doi.org/10.1103/PhysRevLett.97.206806) (cit. on p. 41).
- [127] X. Zheng, V. Volskiy, V. K. Valev, G. A. E. Vandenbosch, and V. V. Moshchalkov, “Line position and quality factor of plasmonic resonances beyond the quasi-static limit: A full-wave eigenmode analysis route,” *IEEE Journal of Selected Topics in Quantum Electronics*, vol. 19, no. 3, pp. 4 600 908–4 600 908, 2013 (cit. on p. 41).
- [128] M. Hrto ņ, A. Kone čná, M. Horák, T. š. Šíkola, and V. K řápek, “Plasmonic antennas with electric, magnetic, and electromagnetic hot spots based on babinet’s principle,” *Phys. Rev. Applied*, vol. 13, p. 054 045, 5 May 2020. DOI: [10.1103/PhysRevApplied.13.054045](https://doi.org/10.1103/PhysRevApplied.13.054045) (cit. on p. 41).
- [129] R. A. Depine, M. E. Inchaussandague, and A. Lakhtakia, “Classification of dispersion equations for homogeneous, dielectric-magnetic, uniaxial materials,” *J. Opt. Soc. Am. A*, vol. 23, no. 4, p. 949, Apr. 2006, ISSN: 1084-7529. DOI: [10.1364/JOSAA.23.000949](https://doi.org/10.1364/JOSAA.23.000949) (cit. on pp. 45, 66).
- [130] S. S. Kruk, Z. J. Wong, E. Pshenay-Severin, K. O’Brien, D. N. Neshev, Y. S. Kivshar, and X. Zhang, “Magnetic hyperbolic optical metamaterials,” *Nat. Commun.*, vol. 7, no. 1, p. 11 329, Sep. 2016, ISSN: 2041-1723. DOI: [10.1038/ncomms11329](https://doi.org/10.1038/ncomms11329) (cit. on p. 46).
- [131] X. Zhang and Z. Liu, “Superlenses to overcome the diffraction limit,” *Nat. Mater.*, vol. 7, no. 6, pp. 435–441, 2008 (cit. on p. 53).
- [132] C. M. Soukoulis and M. Wegener, “Past achievements and future challenges in the development of three-dimensional photonic metamaterials,” *Nat. Photon.*, vol. 5, no. 9, pp. 523–530, 2011 (cit. on p. 53).
- [133] Y. Lee, S.-J. Kim, H. Park, and B. Lee, “Metamaterials and metasurfaces for sensor applications,” *Sensors*, vol. 17, no. 8, 2017 (cit. on p. 53).
- [134] C. Liaskos, S. Nie, A. Tsioliaridou, A. Pitsillides, S. Ioannidis, and I. Akyildiz, “A new wireless communication paradigm through software-controlled metasurfaces,” *IEEE Commun Mag*, vol. 56, no. 9, pp. 162–169, 2018 (cit. on p. 53).
- [135] C. M. Soukoulis, J. Zhou, T. Koschny, M. Kafesaki, and E. N. Economou, “The science of negative index materials,” *J. Phys Condens Matter*, vol. 20, no. 30, p. 304 217, 2008 (cit. on p. 53).
- [136] L. Ferrari, C. Wu, D. Lepage, X. Zhang, and Z. Liu, “Hyperbolic metamaterials and their applications,” *Prog. Quantum Electron*, vol. 40, pp. 1–40, 2015. DOI: [10.1016/j.pquantelec.2014.10.001](https://doi.org/10.1016/j.pquantelec.2014.10.001) (cit. on p. 53).
- [137] S. Liu, T. Cui, Q. Xu, D. Bao, L. Du, X. Wan, W. Tang, C. Ouyang, X. Zhou, H. Yuan, H. Ma, W. Jiang, J. Han, W. Zhang, and Q. Cheng, “Anisotropic coding metamaterials and their powerful manipulation of differently polarized terahertz waves,” *Light Sci. Appl.*, vol. 5, 2016. DOI: [10.1038/lsa.2016.76](https://doi.org/10.1038/lsa.2016.76) (cit. on p. 53).
- [138] A. Basharin, C. Mavridis, M. Kafesaki, E. Economou, and C. Soukoulis, “Epsilon near zero based phenomena in metamaterials,” *Phys. Rev. B Condens. Matter Mater. Phys.*, vol. 87, no. 15, 2013. DOI: [10.1103/PhysRevB.87.155130](https://doi.org/10.1103/PhysRevB.87.155130) (cit. on p. 53).

- [139] I. Katsantonis, S. Droulias, C. M. Soukoulis, E. N. Economou, and M. Kafesaki, “Pt-symmetric chiral metamaterials: Asymmetric effects and pt-phase control,” *Phys. Rev. B*, vol. 101, p. 214 109, 21 Jun. 2020. DOI: [10.1103/PhysRevB.101.214109](https://doi.org/10.1103/PhysRevB.101.214109) (cit. on p. 53).
- [140] M. Chen, M. Kim, A. M. Wong, and G. V. Eleftheriades, “Huygens’ metasurfaces from microwaves to optics: A review,” *Nanophotonics*, vol. 7, no. 6, pp. 1207–1231, 2018. DOI: [doi:10.1515/nanoph-2017-0117](https://doi.org/10.1515/nanoph-2017-0117) (cit. on p. 53).
- [141] M. Beruete and I. Jáuregui-López, “Terahertz sensing based on metasurfaces,” *Adv. Opt. Mater.*, vol. 8, no. 3, 2020. DOI: [10.1002/adom.201900721](https://doi.org/10.1002/adom.201900721) (cit. on p. 53).
- [142] E. Skoulas, A. C. Tasolamprou, G. Kenanakis, and E. Stratakis, “Laser induced periodic surface structures as polarizing optical elements,” *Applied Surface Science*, vol. 541, 2021. DOI: [10.1016/j.apsusc.2020.148470](https://doi.org/10.1016/j.apsusc.2020.148470) (cit. on p. 53).
- [143] H. Zhu, Q. Li, C. Tao, Y. Hong, Z. Xu, W. Shen, S. Kaur, P. Ghosh, and M. Qiu, “Multispectral camouflage for infrared, visible, lasers and microwave with radiative cooling,” *Nature Communications*, vol. 12, no. 1, 2021. DOI: [10.1038/s41467-021-22051-0](https://doi.org/10.1038/s41467-021-22051-0) (cit. on p. 53).
- [144] Z. Ruan and S. Fan, “Superscattering of Light from Subwavelength Nanostructures,” *Phys. Rev. Lett.*, vol. 105, no. 1, p. 013 901, Jun. 2010, ISSN: 0031-9007. DOI: [10.1103/PhysRevLett.105.013901](https://doi.org/10.1103/PhysRevLett.105.013901) (cit. on p. 54).
- [145] S. Lepeshov, A. Krasnok, and A. Alù, “Nonscattering-to-Superscattering Switch with Phase-Change Materials,” *ACS Photonics*, vol. 6, no. 8, pp. 2126–2132, Aug. 2019, ISSN: 2330-4022. DOI: [10.1021/acsp Photonics.9b00674](https://doi.org/10.1021/acsp Photonics.9b00674) (cit. on p. 54).
- [146] H.-W. Wu, Y. Fang, J.-Q. Quan, Y.-Z. Han, Y.-Q. Yin, Y. Li, and Z.-Q. Sheng, “Multi-frequency superscattering with high Q factors from a deep-subwavelength spoof plasmonic structure,” *Phys. Rev. B*, vol. 100, no. 23, p. 235 443, Dec. 2019, ISSN: 2469-9950. DOI: [10.1103/PhysRevB.100.235443](https://doi.org/10.1103/PhysRevB.100.235443) (cit. on p. 54).
- [147] S. H. Raad, C. J. Zapata-Rodríguez, and Z. Atlasbaf, “Graphene-coated resonators with frequency-selective super-scattering and super-cloaking,” *J. Phys. D: Appl. Phys.*, vol. 52, no. 49, p. 495 101, Dec. 2019, ISSN: 0022-3727. DOI: [10.1088/1361-6463/ab3fbc](https://doi.org/10.1088/1361-6463/ab3fbc) (cit. on pp. 54, 62).
- [148] S. H. Raad, C. J. Zapata-Rodríguez, and Z. Atlasbaf, “Multi-frequency super-scattering from sub-wavelength graphene-coated nanotubes,” *J. Opt. Soc. Am. B*, vol. 36, no. 8, pp. 2292–2298, 2019 (cit. on p. 54).
- [149] A. Alù and N. Engheta, “Achieving transparency with plasmonic and metamaterial coatings,” *Phys. Rev. E*, vol. 72, no. 1, p. 016 623, Jul. 2005, ISSN: 1539-3755. DOI: [10.1103/PhysRevE.72.016623](https://doi.org/10.1103/PhysRevE.72.016623) (cit. on p. 54).
- [150] H. M. Bernety and A. B. Yakovlev, “Cloaking of single and multiple elliptical cylinders and strips with confocal elliptical nanostructured graphene metasurface,” *J. Phys. Condens. Matter*, vol. 27, no. 18, p. 185 304, May 2015, ISSN: 0953-8984. DOI: [10.1088/0953-8984/27/18/185304](https://doi.org/10.1088/0953-8984/27/18/185304) (cit. on p. 54).
- [151] L. Zhang, Y. Shi, and C.-H. Liang, “Optimal illusion and invisibility of multilayered anisotropic cylinders and spheres,” *Opt. Express*, vol. 24, no. 20, p. 23 333, Oct. 2016, ISSN: 1094-4087. DOI: [10.1364/OE.24.023333](https://doi.org/10.1364/OE.24.023333) (cit. on p. 54).
- [152] M. Naserpour, C. J. Zapata-Rodríguez, S. M. Vuković, H. Pashaeiadi, and M. R. Belić, “Tunable invisibility cloaking by using isolated graphene-coated nanowires and dimers,”

- Sci. Rep.*, vol. 7, no. 1, p. 12 186, Dec. 2017, ISSN: 2045-2322. DOI: [10.1038/s41598-017-12413-4](https://doi.org/10.1038/s41598-017-12413-4) (cit. on p. 54).
- [153] G. Labate, A. Alù, and L. Matekovits, “Surface-admittance equivalence principle for nonradiating and cloaking problems,” *Phys. Rev. A*, vol. 95, no. 6, p. 063 841, Jun. 2017, ISSN: 2469-9926. DOI: [10.1103/PhysRevA.95.063841](https://doi.org/10.1103/PhysRevA.95.063841) (cit. on p. 54).
 - [154] V. I. Shcherbinin, V. I. Fesenko, T. I. Tkachova, and V. R. Tuz, “Superscattering from subwavelength corrugated cylinders,” *Phys. Rev. Applied*, vol. 13, p. 024 081, 2 Feb. 2020. DOI: [10.1103/PhysRevApplied.13.024081](https://doi.org/10.1103/PhysRevApplied.13.024081) (cit. on p. 54).
 - [155] K. Zheng, Z. Zhang, F. Qin, and Y. Xu, “Invisible Mie scatterer,” *Opt. Lett.*, vol. 46, no. 20, p. 5248, Oct. 2021, ISSN: 0146-9592. DOI: [10.1364/OL.443021](https://doi.org/10.1364/OL.443021) (cit. on p. 54).
 - [156] J. A. Lock, “Scattering of an electromagnetic plane wave by a Luneburg lens III Finely stratified sphere model,” *J. Opt. Soc. Am. A*, vol. 25, no. 12, p. 2991, Dec. 2008, ISSN: 1084-7529. DOI: [10.1364/JOSAA.25.002991](https://doi.org/10.1364/JOSAA.25.002991) (cit. on p. 54).
 - [157] R. Kumar and K. Kajikawa, “Superscattering from cylindrical hyperbolic metamaterials in the visible region,” *Opt. Express*, vol. 28, no. 2, pp. 1507–1517, Jan. 2020. DOI: [10.1364/OE.379547](https://doi.org/10.1364/OE.379547) (cit. on p. 54).
 - [158] T. Kaplas and P. Kuzhir, “Ultra-thin pyrocarbon films as a versatile coating material,” *Nanoscale Res. Lett.*, vol. 12, no. 1, p. 121, 2017 (cit. on p. 54).
 - [159] P. Kuzhir, A. Paddubskaya, D. Bychanok, A. Liubimau, A. Ortona, V. Fierro, and A. Celzard, “3d-printed, carbon-based, lossy photonic crystals: Is high electrical conductivity the must?” *Carbon*, vol. 171, pp. 484–492, 2021. DOI: [10.1016/j.carbon.2020.09.020](https://doi.org/10.1016/j.carbon.2020.09.020) (cit. on p. 54).
 - [160] M. Shuba, D. Yuko, P. Kuzhir, S. Maksimenko, V. Ksenevich, S.-H. Lim, T.-H. Kim, and S.-M. Choi, “Electromagnetic and optical responses of a composite material comprising individual single-walled carbon-nanotubes with a polymer coating,” *Scientific Reports*, vol. 10, no. 1, 2020. DOI: [10.1038/s41598-020-66247-8](https://doi.org/10.1038/s41598-020-66247-8) (cit. on p. 54).
 - [161] O. Sedelnikova, D. Gorodetskiy, A. Kurennya, K. Baskakova, E. Shlyakhova, A. Makarova, G. Gorokhov, D. Bychanok, P. Kuzhir, S. Maksimenko, L. Bulusheva, and A. Okotrub, “Laser patterning of aligned carbon nanotubes arrays: Morphology, surface structure, and interaction with terahertz radiation,” *Mater.*, vol. 14, no. 12, p. 3275, 2021 (cit. on p. 54).
 - [162] P.-Y. Chen, J. Soric, Y. R. Padooru, H. M. Bernety, A. B. Yakovlev, and A. Alù, “Nanostructured graphene metasurface for tunable terahertz cloaking,” *New Journal of Physics*, vol. 15, 2013. DOI: [10.1088/1367-2630/15/12/123029](https://doi.org/10.1088/1367-2630/15/12/123029) (cit. on p. 54).
 - [163] T. Christensen, A.-P. Jauho, M. Wubs, and N. A. Mortensen, “Localized plasmons in graphene-coated nanospheres,” *Physical Review B - Condensed Matter and Materials Physics*, vol. 91, no. 12, 2015. DOI: [10.1103/PhysRevB.91.125414](https://doi.org/10.1103/PhysRevB.91.125414) (cit. on p. 54).
 - [164] T. I. Tkachova, V. I. Shcherbinin, and V. I. Tkachenko, “Selectivity properties of cylindrical waveguides with longitudinal wall corrugations for second-harmonic gyrotrons,” *Journal of Infrared, Millimeter, and Terahertz Waves*, vol. 40, no. 10, pp. 1021–1034, 2019. DOI: [10.1007/s10762-019-00623-y](https://doi.org/10.1007/s10762-019-00623-y) (cit. on p. 54).
 - [165] Q. Qian, Y. Yan, and C. Wang, “Flexible metasurface black nickel with stepped nanopillars,” *Optics Letters*, vol. 43, no. 6, pp. 1231–1234, 2018. DOI: [10.1364/OL.43.001231](https://doi.org/10.1364/OL.43.001231) (cit. on p. 54).
 - [166] A. C. Tasolamprou, D. Mentzaki, Z. Viskadourakis, E. Economou, M. Kafesaki, and G. Kenanakis, “Flexible 3d printed conductive metamaterial units for electromagnetic appli-

- cations in microwaves,” *Materials*, vol. 13, no. 17, 2020. doi: [10.3390/ma13173879](https://doi.org/10.3390/ma13173879) (cit. on p. 54).
- [167] G. Yao, F. Ling, J. Yue, C. Luo, J. Ji, and J. Yao, “Dual-band tunable perfect metamaterial absorber in the thz range,” *Optics Express*, vol. 24, no. 2, pp. 1518–1527, 2016. doi: [10.1364/OE.24.001518](https://doi.org/10.1364/OE.24.001518) (cit. on p. 54).
- [168] S. Yan and G. A. E. Vandenbosch, “INCREASING THE NRI BANDWIDTH OF DIELECTRIC SPHERE-BASED METAMATERIALS BY COATING,” *Prog. Electromagn. Res.*, vol. 132, pp. 1–23, 2012, issn: 1559-8985. doi: [10.2528/PIER12070612](https://doi.org/10.2528/PIER12070612) (cit. on p. 54).
- [169] H.-Y. She, L.-W. Li, O. J. F. Martin, and J. R. Mosig, “Surface polaritons of small coated cylinders illuminated by normal incident TM and TE plane waves,” *Opt. Express*, vol. 16, no. 2, p. 1007, 2008, issn: 1094-4087. doi: [10.1364/OE.16.001007](https://doi.org/10.1364/OE.16.001007) (cit. on p. 54).
- [170] M. Danaeifar and N. Granpayeh, “Wideband invisibility by using inhomogeneous metasurfaces of graphene nanodisks in the infrared regime,” *J. Opt. Soc. Am. B*, vol. 33, no. 8, p. 1764, Aug. 2016, issn: 0740-3224. doi: [10.1364/JOSAB.33.001764](https://doi.org/10.1364/JOSAB.33.001764) (cit. on p. 54).
- [171] E. Shokati, N. Granpayeh, and M. Danaeifar, “Wideband and multi-frequency infrared cloaking of spherical objects by using the graphene-based metasurface,” *Appl. Opt.*, vol. 56, no. 11, p. 3053, Apr. 2017, issn: 0003-6935. doi: [10.1364/AO.56.003053](https://doi.org/10.1364/AO.56.003053) (cit. on p. 54).
- [172] Z. Hamzavi-Zarghani, A. Yahaghi, L. Matekovits, and A. Farmani, “Tunable mantle cloaking utilizing graphene metasurface for terahertz sensing applications,” *Opt. Express*, vol. 27, no. 24, p. 34 824, Nov. 2019, issn: 1094-4087. doi: [10.1364/OE.27.034824](https://doi.org/10.1364/OE.27.034824) (cit. on p. 54).
- [173] S. Droulias, “Chiral sensing with achiral isotropic metasurfaces,” *Phys. Rev. B*, vol. 102, no. 7, p. 075 119, Aug. 2020, issn: 2469-9950. doi: [10.1103/PhysRevB.102.075119](https://doi.org/10.1103/PhysRevB.102.075119) (cit. on pp. 54, 57).
- [174] Y. Ra’di, V. S. Asadchy, and S. A. Tretyakov, “Tailoring Reflections From Thin Composite Metamirrors,” *IEEE Trans. Antennas Propag.*, vol. 62, no. 7, pp. 3749–3760, Jul. 2014, issn: 0018-926X. doi: [10.1109/TAP.2014.2319851](https://doi.org/10.1109/TAP.2014.2319851) (cit. on p. 57).
- [175] M. Dehmollaian, N. Chamanara, and C. Caloz, “Wave Scattering by a Cylindrical Metasurface Cavity of Arbitrary Cross Section: Theory and Applications,” *IEEE Trans. Antennas Propag.*, vol. 67, no. 6, pp. 4059–4072, Jun. 2019, issn: 0018-926X. doi: [10.1109/TAP.2019.2905711](https://doi.org/10.1109/TAP.2019.2905711) (cit. on p. 57).
- [176] E. Prodan, C. Radloff, N. J. Halas, and P. Nordlander, “A hybridization model for the plasmon response of complex nanostructures,” *Science*, vol. 302, no. 5644, pp. 419–422, 2003. doi: [10.1126/science.1089171](https://doi.org/10.1126/science.1089171). eprint: <https://science.sciencemag.org/content/302/5644/419.full.pdf> (cit. on p. 62).
- [177] W. Liu, R. F. Oulton, and Y. S. Kivshar, “Geometric interpretations for resonances of plasmonic nanoparticles,” *Sci. Rep.*, vol. 5, no. 1, p. 12 148, Dec. 2015, issn: 2045-2322. doi: [10.1038/srep12148](https://doi.org/10.1038/srep12148) (cit. on p. 62).
- [178] R. Li, B. Zheng, X. Lin, R. Hao, S. Lin, W. Yin, E. Li, and H. Chen, “Design of Ultracompact Graphene-Based Superscatterers,” *IEEE J. Sel. Top. Quantum Electron.*, vol. 23, no. 1, pp. 130–137, Jan. 2017, issn: 1077-260X. doi: [10.1109/JSTQE.2016.2537267](https://doi.org/10.1109/JSTQE.2016.2537267) (cit. on p. 62).

- [179] A. Tandraechanurat, S. Ishida, D. Guimard, M. Nomura, S. Iwamoto, and Y. Arakawa, “Lasing oscillation in a three-dimensional photonic crystal nanocavity with a complete bandgap,” *Nature Photonics*, vol. 5, pp. 91–94, 2011 (cit. on p. 75).
- [180] W. L. Barnes, G. Björk, J.-M. Gérard, P. Jonsson, J. Wasey, P. Worthing, and V. Zwiller, “Solid-state single photon sources: Light collection strategies,” *Eur. Phys. J. D*, vol. 18, pp. 197–210, 2000 (cit. on p. 75).
- [181] J. G. Fleming, S. Y. Lin, I. El-Kady, R. Biswas, and K.-M. Ho, “All-metallic three-dimensional photonic crystals with a large infrared bandgap,” *Nature (London)*, vol. 471, pp. 52–55, 2002 (cit. on p. 75).
- [182] S. Haroche, “Cavity quantum electrodynamics,” in *Fundamental systems in quantum optics*, J. Dalibard, J. M. Raimond, and J. Zinn-Justin, Eds., North Holland, Amsterdam, 1992, pp. 767–940 (cit. on p. 75).
- [183] P. Milonni, *The Quantum Vacuum: An Introduction to Quantum Electrodynamics*, 1st. Boston: Academic Press, 1994 (cit. on p. 75).
- [184] E. M. Purcell, “Spontaneous emission probabilities at radio frequencies,” *Phys. Rev.*, vol. 69, no. 11-12, p. 681, Jun. 1946, ISSN: 0031-899X. DOI: [10.1103/PhysRev.69.674](https://doi.org/10.1103/PhysRev.69.674) (cit. on p. 75).
- [185] C. M. Soukoulis, Ed., *Photonic Crystals and Light Localization in the 21st Century*. Dordrecht: Springer Netherlands, 2001, ISBN: 978-0-7923-6948-6. DOI: [10.1007/978-94-010-0738-2](https://doi.org/10.1007/978-94-010-0738-2) (cit. on p. 75).
- [186] L. Novotny and B. Hecht, *Principles of Nano-Optics*. Cambridge: Cambridge University Press, 2006, ISBN: 9780511813535. DOI: [10.1017/CBO9780511813535](https://doi.org/10.1017/CBO9780511813535) (cit. on p. 75).
- [187] J.-M. Lourtioz, H. Benisty, V. Berger, J.-M. Gérard, D. Maystre, A. Tchebnokov, and D. Pagnoux, *Photonic Crystals*. Berlin, Heidelberg: Springer Berlin Heidelberg, 2008, ISBN: 978-3-540-78346-6. DOI: [10.1007/978-3-540-78347-3](https://doi.org/10.1007/978-3-540-78347-3) (cit. on p. 75).
- [188] M. Ghulinyan and L. Pavesi, Eds., *Light Localisation and Lasing*. Cambridge: Cambridge University Press, 2015, ISBN: 9781139839501. DOI: [10.1017/CBO9781139839501](https://doi.org/10.1017/CBO9781139839501) (cit. on p. 75).
- [189] W. L. Barnes, S. A. R. Horsley, and W. L. Vos, “Classical antennae, quantum emitters, and densities of optical states,” *J. Opt.*, vol. 22, 2020. eprint: [arXiv:1909.05619](https://arxiv.org/abs/1909.05619) (physics.optics) (cit. on pp. 75, 85).
- [190] P. Goy, J. M. Raimond, M. Gross, and S. Haroche, “Observation of Cavity-Enhanced Single-Atom Spontaneous Emission,” *Phys. Rev. Lett.*, vol. 50, no. 24, pp. 1903–1906, Jun. 1983, ISSN: 0031-9007. DOI: [10.1103/PhysRevLett.50.1903](https://doi.org/10.1103/PhysRevLett.50.1903) (cit. on p. 75).
- [191] F. D. Martini, G. Innocenti, G. R. Jacobovitz, and P. Mataloni, “Anomalous Spontaneous Emission Time in a Microscopic Optical Cavity,” *Phys. Rev. Lett.*, vol. 59, no. 26, pp. 2955–2958, Dec. 1987, ISSN: 0031-9007. DOI: [10.1103/PhysRevLett.59.2955](https://doi.org/10.1103/PhysRevLett.59.2955) (cit. on p. 75).
- [192] J. Gérard, B. Sermage, B. Gayral, B. Legrand, E. Costard, and V. Thierry-Mieg, “Enhanced Spontaneous Emission by Quantum Boxes in a Monolithic Optical Microcavity,” *Phys. Rev. Lett.*, vol. 81, no. 5, pp. 1110–1113, Aug. 1998, ISSN: 0031-9007. DOI: [10.1103/PhysRevLett.81.1110](https://doi.org/10.1103/PhysRevLett.81.1110) (cit. on p. 75).
- [193] M. Pelton, C. Santori, J. Vučković, B. Zhang, G. S. Solomon, J. Plant, and Y. Yamamoto, “Efficient Source of Single Photons: A Single Quantum Dot in a Micropost Microcavity,” *Phys. Rev. Lett.*, vol. 89, no. 23, p. 233 602, Nov. 2002, ISSN: 0031-9007. DOI: [10.1103/PhysRevLett.89.233602](https://doi.org/10.1103/PhysRevLett.89.233602) (cit. on p. 75).

- [194] F. Treussart, J. Hare, L. Collot, V. Lefèvre, D. S. Weiss, V. Sandoghdar, J. M. Raimond, and S. Haroche, “Quantized atom-field force at the surface of a microsphere,” *Opt. Lett.*, vol. 19, no. 20, p. 1651, Oct. 1994, ISSN: 0146-9592. DOI: [10.1364/OL.19.001651](#) (cit. on p. 75).
- [195] H. Mabuchi and H. J. Kimble, “Atom galleries for whispering atoms: binding atoms in stable orbits around an optical resonator,” *Opt. Lett.*, vol. 19, no. 10, p. 749, May 1994, ISSN: 0146-9592. DOI: [10.1364/OL.19.000749](#) (cit. on p. 75).
- [196] V. Sandoghdar, F. Treussart, J. Hare, V. Lefèvre-Seguin, J. -M. Raimond, and S. Haroche, “Very low threshold whispering-gallery-mode microsphere laser,” *Phys. Rev. A*, vol. 54, no. 3, R1777–R1780, Sep. 1996, ISSN: 1050-2947. DOI: [10.1103/PhysRevA.54.R1777](#) (cit. on p. 75).
- [197] P. Anger, P. Bharadwaj, and L. Novotny, “Enhancement and Quenching of Single-Molecule Fluorescence,” *Phys. Rev. Lett.*, vol. 96, no. 11, p. 113 002, Mar. 2006, ISSN: 0031-9007. DOI: [10.1103/PhysRevLett.96.113002](#) (cit. on p. 75).
- [198] O. L. Muskens, V. Giannini, J. A. Sánchez-Gil, and J. Gómez Rivas, “Strong Enhancement of the Radiative Decay Rate of Emitters by Single Plasmonic Nanoantennas,” *Nano Lett.*, vol. 7, no. 9, pp. 2871–2875, Sep. 2007, ISSN: 1530-6984. DOI: [10.1021/nl0715847](#) (cit. on p. 75).
- [199] A. Rose, T. B. Hoang, F. McGuire, J. J. Mock, C. Ciraci, D. R. Smith, and M. H. Mikkelsen, “Control of Radiative Processes Using Tunable Plasmonic Nanopatch Antennas,” *Nano Lett.*, vol. 14, no. 8, pp. 4797–4802, Aug. 2014, ISSN: 1530-6984. DOI: [10.1021/nl501976f](#) (cit. on p. 75).
- [200] T. B. Hoang, G. M. Akselrod, C. Argyropoulos, J. Huang, D. R. Smith, and M. H. Mikkelsen, “Ultrafast spontaneous emission source using plasmonic nanoantennas,” *Nat. Commun.*, vol. 6, no. 1, p. 7788, Nov. 2015, ISSN: 2041-1723. DOI: [10.1038/ncomms8788](#) (cit. on p. 75).
- [201] R. Chikkaraddy, B. de Nijs, F. Benz, S. J. Barrow, O. A. Scherman, E. Rosta, A. Demetriadou, P. Fox, O. Hess, and J. J. Baumberg, “Single-molecule strong coupling at room temperature in plasmonic nanocavities,” *Nature*, vol. 535, no. 7610, pp. 127–130, Jul. 2016, ISSN: 0028-0836. DOI: [10.1038/nature17974](#) (cit. on p. 75).
- [202] M. A. Noginov, H. Li, Y. A. Barnakov, D. Dryden, G. Nataraj, G. Zhu, C. E. Bonner, M. Mayy, Z. Jacob, and E. E. Narimanov, “Controlling spontaneous emission with metamaterials,” *Opt. Lett.*, vol. 35, no. 11, p. 1863, Jun. 2010, ISSN: 0146-9592. DOI: [10.1364/OL.35.001863](#) (cit. on p. 75).
- [203] D. Lu, J. J. Kan, E. E. Fullerton, and Z. Liu, “Enhancing spontaneous emission rates of molecules using nanopatterned multilayer hyperbolic metamaterials,” *Nat. Nanotechnol.*, vol. 9, no. 1, pp. 48–53, Jan. 2014, ISSN: 1748-3387. DOI: [10.1038/nnano.2013.276](#) (cit. on p. 75).
- [204] V. Weisskopf and E. Wigner, “Berechnung der natürlichen Linienbreite auf Grund der Diracschen Lichttheorie,” *Zeitschrift für Phys.*, vol. 63, no. 1-2, pp. 54–73, Jan. 1930, ISSN: 1434-6001. DOI: [10.1007/BF01336768](#) (cit. on p. 75).
- [205] E. Fermi, “Quantum Theory of Radiation,” *Rev. Mod. Phys.*, vol. 4, no. 1, pp. 87–132, Jan. 1932, ISSN: 0034-6861. DOI: [10.1103/RevModPhys.4.87](#) (cit. on p. 75).
- [206] E. Snoeks, A. Lagendijk, and A. Polman, “Measuring and Modifying the Spontaneous Emission Rate of Erbium near an Interface,” *Phys. Rev. Lett.*, vol. 74, no. 13, pp. 2459–2462, Mar. 1995, ISSN: 0031-9007. DOI: [10.1103/PhysRevLett.74.2459](#) (cit. on p. 75).

- [207] R. Sprik, B. A. van Tiggelen, and A. Lagendijk, “Optical emission in periodic dielectrics,” *Europhysics Lett.*, vol. 35, pp. 265–270, 1996 (cit. on p. 75).
- [208] W. L. Barnes, “Fluorescence near interfaces: The role of photonic mode density,” *J. Mod. Optics*, vol. 45, pp. 661–699, 1998 (cit. on p. 75).
- [209] M. Wubs and W. L. Vos, “Förster resonance energy transfer rate in any dielectric nanophotonic medium with weak dispersion,” *New J. Phys.*, vol. 18, no. 5, p. 053 037, May 2016, ISSN: 1367-2630. DOI: [10.1088/1367-2630/18/5/053037](https://doi.org/10.1088/1367-2630/18/5/053037) (cit. on p. 75).
- [210] A. A. Clerk, M. H. Devoret, S. M. Girvin, F. Marquardt, and R. J. Schoelkopf, “Introduction to quantum noise, measurement, and amplification,” *Rev. Mod. Phys.*, vol. 82, no. 2, pp. 1155–1208, Apr. 2010, ISSN: 0034-6861. DOI: [10.1103/RevModPhys.82.1155](https://doi.org/10.1103/RevModPhys.82.1155) (cit. on pp. 75, 85).
- [211] S. John and J. Wang, “Quantum electrodynamics near a photonic band gap: Photon bound states and dressed atoms,” *Phys. Rev. Lett.*, vol. 64, no. 20, pp. 2418–2421, May 1990, ISSN: 0031-9007. DOI: [10.1103/PhysRevLett.64.2418](https://doi.org/10.1103/PhysRevLett.64.2418) (cit. on p. 75).
- [212] K. Busch and S. John, “Photonic band gap formation in certain self-organizing systems,” *Phys. Rev. E*, vol. 58, no. 3, pp. 3896–3908, Sep. 1998, ISSN: 1063-651X. DOI: [10.1103/PhysRevE.58.3896](https://doi.org/10.1103/PhysRevE.58.3896) (cit. on p. 75).
- [213] Z.-Y. Li and Y. Xia, “Full vectorial model for quantum optics in three-dimensional photonic crystals,” *Phys. Rev. A*, vol. 63, no. 4, p. 043 817, Mar. 2001, ISSN: 1050-2947. DOI: [10.1103/PhysRevA.63.043817](https://doi.org/10.1103/PhysRevA.63.043817) (cit. on p. 75).
- [214] N. Vats, S. John, and K. Busch, “Theory of fluorescence in photonic crystals,” *Phys. Rev. A*, vol. 65, no. 4, p. 043 808, Mar. 2002, ISSN: 1050-2947. DOI: [10.1103/PhysRevA.65.043808](https://doi.org/10.1103/PhysRevA.65.043808) (cit. on p. 75).
- [215] X.-H. Wang, B.-Y. Gu, R. Wang, and H.-Q. Xu, “Decay Kinetic Properties of Atoms in Photonic Crystals with Absolute Gaps,” *Phys. Rev. Lett.*, vol. 91, no. 11, p. 113 904, Sep. 2003, ISSN: 0031-9007. DOI: [10.1103/PhysRevLett.91.113904](https://doi.org/10.1103/PhysRevLett.91.113904) (cit. on p. 75).
- [216] I. S. Nikolaev, W. L. Vos, and A. F. Koenderink, “Accurate calculation of the local density of optical states in inverse-opal photonic crystals,” *J. Opt. Soc. Am. B*, vol. 26, pp. 987–997, 2009, ISSN: 1098-0121. DOI: [10.1364/JOSAB.26.000987](https://doi.org/10.1364/JOSAB.26.000987) (cit. on p. 75).
- [217] T. Yamasaki and T. Tsutsui, “Spontaneous emission from fluorescent molecules embedded in photonic crystals consisting of polystyrene microspheres,” *Appl. Phys. Lett.*, vol. 72, no. 16, pp. 1957–1959, Apr. 1998, ISSN: 0003-6951. DOI: [10.1063/1.121234](https://doi.org/10.1063/1.121234) (cit. on p. 75).
- [218] K. Yoshino, S. B. Lee, S. Tatsuhara, Y. Kawagishi, M. Ozaki, and A. A. Zakhidov, “Observation of inhibited spontaneous emission and stimulated emission of rhodamine 6G in polymer replica of synthetic opal,” *Appl. Phys. Lett.*, vol. 73, no. 24, pp. 3506–3508, Dec. 1998, ISSN: 0003-6951. DOI: [10.1063/1.122819](https://doi.org/10.1063/1.122819) (cit. on p. 75).
- [219] A. Blanco, C. López, R. Mayoral, H. Míguez, F. Meseguer, A. Mifsud, and J. Herrero, “CdS photoluminescence inhibition by a photonic structure,” *Appl. Phys. Lett.*, vol. 73, no. 13, pp. 1781–1783, Sep. 1998, ISSN: 0003-6951. DOI: [10.1063/1.122280](https://doi.org/10.1063/1.122280) (cit. on p. 75).
- [220] M. Megens, J. E. G. J. Wijnhoven, A. Lagendijk, and W. L. Vos, “Fluorescence lifetimes and linewidths of dye in photonic crystals,” *Phys. Rev. A*, vol. 59, no. 6, pp. 4727–4731, Jun. 1999, ISSN: 1050-2947. DOI: [10.1103/PhysRevA.59.4727](https://doi.org/10.1103/PhysRevA.59.4727) (cit. on p. 75).
- [221] P. Lodahl, A. Floris van Driel, I. S. Nikolaev, A. Irman, K. Overgaag, D. Vanmaekelbergh, and W. L. Vos, “Controlling the dynamics of spontaneous emission from quantum dots

- by photonic crystals,” *Nature*, vol. 430, no. 7000, pp. 654–657, Aug. 2004, issn: 0028-0836. doi: [10.1038/nature02772](https://doi.org/10.1038/nature02772) (cit. on p. 75).
- [222] I. S. Nikolaev, P. Lodahl, A. F. van Driel, A. F. Koenderink, and W. L. Vos, “Strongly non-exponential time-resolved fluorescence of quantum-dot ensembles in three-dimensional photonic crystals,” *Phys. Rev. B*, vol. 75, no. 11, p. 115 302, Mar. 2007, issn: 1098-0121. doi: [10.1103/PhysRevB.75.115302](https://doi.org/10.1103/PhysRevB.75.115302) (cit. on p. 75).
- [223] I. S. Nikolaev, P. Lodahl, and W. L. Vos, “Fluorescence Lifetime of Emitters with Broad Homogeneous Linewidths Modified in Opal Photonic Crystals,” *J. Phys. Chem. C*, vol. 112, no. 18, pp. 7250–7254, May 2008, issn: 1932-7447. doi: [10.1021/jp7111439](https://doi.org/10.1021/jp7111439) (cit. on p. 75).
- [224] R. A. L. Vallée, K. Baert, B. Kolaric, M. Van der Auweraer, and K. Clays, “Nonexponential decay of spontaneous emission from an ensemble of molecules in photonic crystals,” *Phys. Rev. B*, vol. 76, no. 4, p. 045 113, Jul. 2007, issn: 1098-0121. doi: [10.1103/PhysRevB.76.045113](https://doi.org/10.1103/PhysRevB.76.045113) (cit. on p. 75).
- [225] M. J. Ventura and M. Gu, “Engineering Spontaneous Emission in a Quantum-Dot-Doped Polymer Nanocomposite with Three-Dimensional Photonic Crystals,” *Adv. Mater.*, vol. 20, no. 7, pp. 1329–1332, Apr. 2008, issn: 09359648. doi: [10.1002/adma.200701703](https://doi.org/10.1002/adma.200701703) (cit. on p. 75).
- [226] C. Vion, C. Barthou, P. Bénalloul, C. Schwob, L. Coolen, A. Gruzintev, G. Emel’chenko, V. Masalov, J.-M. Frigerio, and A. Maître, “Manipulating emission of CdTeSe nanocrystals embedded in three-dimensional photonic crystals,” *J. Appl. Phys.*, vol. 105, no. 11, p. 113 120, Jun. 2009, issn: 0021-8979. doi: [10.1063/1.3129311](https://doi.org/10.1063/1.3129311) (cit. on p. 75).
- [227] G. Subramania, Y.-J. Lee, A. J. Fischer, T. S. Luk, C. J. Brinker, and D. Dunphy, “Emission modification of CdSe quantum dots by titanium dioxide visible logpile photonic crystal,” *Appl. Phys. Lett.*, vol. 95, no. 15, p. 151 101, Oct. 2009, issn: 0003-6951. doi: [10.1063/1.3245309](https://doi.org/10.1063/1.3245309) (cit. on p. 75).
- [228] M. R. Jorgensen, J. W. Galusha, and M. H. Bartl, “Strongly Modified Spontaneous Emission Rates in Diamond-Structured Photonic Crystals,” *Phys. Rev. Lett.*, vol. 107, no. 14, p. 143 902, Sep. 2011, issn: 0031-9007. doi: [10.1103/PhysRevLett.107.143902](https://doi.org/10.1103/PhysRevLett.107.143902) (cit. on p. 75).
- [229] Z. Ning, Y. Ren, S. Hoogland, O. Voznyy, L. Levina, P. Stadler, X. Lan, D. Zhitomirsky, and E. H. Sargent, “All-Inorganic Colloidal Quantum Dot Photovoltaics Employing Solution-Phase Halide Passivation,” *Adv. Mater.*, vol. 24, no. 47, pp. 6295–6299, Dec. 2012, issn: 09359648. doi: [10.1002/adma.201202942](https://doi.org/10.1002/adma.201202942) (cit. on p. 75).
- [230] A. F. Koenderink, L. Bechger, H. P. Schriemer, A. Lagendijk, and W. L. Vos, “Broadband Fivefold Reduction of Vacuum Fluctuations Probed by Dyes in Photonic Crystals,” *Phys. Rev. Lett.*, vol. 88, no. 14, p. 143 903, Mar. 2002, issn: 0031-9007. doi: [10.1103/PhysRevLett.88.143903](https://doi.org/10.1103/PhysRevLett.88.143903) (cit. on p. 75).
- [231] S. Ogawa, M. Imada, S. Yoshimoto, M. Okano, and S. Noda, “Control of Light Emission by 3D Photonic Crystals,” *Science*, vol. 305, pp. 227–229, 2004, issn: 0036-8075. doi: [10.1126/science.1097968](https://doi.org/10.1126/science.1097968) (cit. on p. 75).
- [232] A. A. Asatryan, L. C. Botten, N. A. Nicorovici, R. C. McPhedran, and C. M. de Sterke, “Frequency shift of sources embedded in finite two-dimensional photonic clusters,” *Waves in Random and Complex Media*, vol. 16, no. 2, pp. 151–165, May 2006, issn: 1745-5030. doi: [10.1080/17455030500455853](https://doi.org/10.1080/17455030500455853) (cit. on p. 76).
- [233] M. D. Leistikow, A. P. Mosk, E. Yeganegi, S. R. Huisman, A. Lagendijk, and W. L. Vos, “Inhibited Spontaneous Emission of Quantum Dots Observed in a 3D Photonic Band

- Gap,” *Phys. Rev. Lett.*, vol. 107, no. 19, p. 193 903, Nov. 2011, ISSN: 0031-9007. DOI: [10.1103/PhysRevLett.107.193903](https://doi.org/10.1103/PhysRevLett.107.193903) (cit. on pp. 76, 77, 79, 81).
- [234] E. Yeganegi, A. Lagendijk, A. P. Mosk, and W. L. Vos, “Local density of optical states in the band gap of a finite one-dimensional photonic crystal,” *Phys. Rev. B*, vol. 89, no. 4, p. 045 123, Jan. 2014, ISSN: 1098-0121. DOI: [10.1103/PhysRevB.89.045123](https://doi.org/10.1103/PhysRevB.89.045123) (cit. on pp. 76, 84).
- [235] C. Hermann and O. Hess, “Modified spontaneous-emission rate in an inverted-opal structure with complete photonic bandgap,” *J. Opt. Soc. Am. B*, vol. 19, no. 12, p. 3013, Dec. 2002, ISSN: 0740-3224. DOI: [10.1364/JOSAB.19.003013](https://doi.org/10.1364/JOSAB.19.003013) (cit. on p. 76).
- [236] L. Botten, N. Nicorovici, R. McPhedran, C. Sterke, and A. Asatryan, “Photonic band structure calculations using scattering matrices,” *Phys. Rev. E*, vol. 64, no. 4, p. 046 603, Sep. 2001, ISSN: 1063-651X. DOI: [10.1103/PhysRevE.64.046603](https://doi.org/10.1103/PhysRevE.64.046603) (cit. on p. 76).
- [237] C. Hermann and O. Hess, “Modified spontaneous-emission rate in an inverted-opal structure with complete photonic bandgap,” *J. Opt. Soc. Am. B*, vol. 19, no. 12, p. 3013, Dec. 2002, ISSN: 0740-3224. DOI: [10.1364/JOSAB.19.003013](https://doi.org/10.1364/JOSAB.19.003013) (cit. on pp. 76, 87).
- [238] J. S. Kole, “New methods for the numerical solution of Maxwell’s Equations,” Ph.D. dissertation, University of Groningen, 2003 (cit. on p. 76).
- [239] J. R. de Lasson, J. Mørk, and P. T. Kristensen, “Three-dimensional integral equation approach to light scattering, extinction cross sections, local density of states, and quasi-normal modes,” *J. Opt. Soc. Am. B*, vol. 30, no. 7, p. 1996, Jul. 2013, ISSN: 0740-3224. DOI: [10.1364/JOSAB.30.001996](https://doi.org/10.1364/JOSAB.30.001996) (cit. on p. 76).
- [240] S. E. Skipetrov, *Finite-size scaling of the density of states inside band gaps of ideal and disordered photonic crystals*, 2019. arXiv: [arXiv:1909.13661](https://arxiv.org/abs/1909.13661) [[cond-mat.dis-nn](https://arxiv.org/abs/1909.13661)] (cit. on p. 76).
- [241] W. L. Vos, A. F. Koenderink, and I. S. Nikolaev, “Orientation-dependent spontaneous emission rates of a two-level quantum emitter in any nanophotonic environment,” *Phys. Rev. A*, vol. 80, no. 5, p. 053 802, Nov. 2009, ISSN: 1050-2947. DOI: [10.1103/PhysRevA.80.053802](https://doi.org/10.1103/PhysRevA.80.053802) (cit. on p. 76).
- [242] K. Ho, C. Chan, C. Soukoulis, R. Biswas, and M. Sigalas, “Photonic band gaps in three dimensions: New layer-by-layer periodic structures,” *Solid State Commun.*, vol. 89, no. 5, pp. 413–416, Feb. 1994, ISSN: 00381098. DOI: [10.1016/0038-1098\(94\)90202-X](https://doi.org/10.1016/0038-1098(94)90202-X) (cit. on p. 76).
- [243] S. Y. Lin and G. Arjavalingam, “Tunneling of electromagnetic waves in two-dimensional photonic crystals,” *Opt. Lett.*, vol. 18, no. 19, p. 1666, Oct. 1993, ISSN: 0146-9592. DOI: [10.1364/OL.18.001666](https://doi.org/10.1364/OL.18.001666) (cit. on pp. 76, 84).
- [244] Y. A. Vlasov, V. N. Astratov, O. Z. Karimov, A. A. Kaplyanskii, V. N. Bogomolov, and A. V. Prokofiev, “Existence of a photonic pseudogap for visible light in synthetic opals,” *Phys. Rev. B*, vol. 55, no. 20, R13357–R13360, May 1997, ISSN: 0163-1829. DOI: [10.1103/PhysRevB.55.R13357](https://doi.org/10.1103/PhysRevB.55.R13357) (cit. on pp. 76, 84).
- [245] Y. Neve-Oz, M. Golosovsky, D. Davidov, and A. Frenkel, “Bragg attenuation length in metallo-dielectric photonic band gap materials,” *J. Appl. Phys.*, vol. 95, no. 11, pp. 5989–5993, Jun. 2004, ISSN: 0021-8979. DOI: [10.1063/1.1713028](https://doi.org/10.1063/1.1713028) (cit. on pp. 76, 84).
- [246] A. A. Asatryan, S. Fabre, K. Busch, R. C. McPhedran, L. C. Botten, C. M. de Sterke, and N.-A. P. Nicorovici, “Two-dimensional local density of states in two-dimensional

- photonic crystals,” *Opt. Express*, vol. 8, no. 3, p. 191, Jan. 2001, ISSN: 1094-4087. DOI: [10.1364/OE.8.000191](https://doi.org/10.1364/OE.8.000191) (cit. on p. 76).
- [247] A. A. Asatryan, K. Busch, R. C. McPhedran, L. C. Botten, C. M. de Sterke, and N. A. Nicorovici, “Two-dimensional Green tensor and local density of states in finite-sized two-dimensional photonic crystals,” *Waves in Random Media*, vol. 13, no. 1, pp. 9–25, Jan. 2003, ISSN: 0959-7174. DOI: [10.1088/0959-7174/13/1/302](https://doi.org/10.1088/0959-7174/13/1/302) (cit. on p. 76).
- [248] D. J. Kan, L. C. Botten, C. G. Poulton, A. A. Asatryan, and K. B. Dossou, “Semianalytical formulations for the surface modes of photonic woodpiles,” *Phys. Rev. A*, vol. 84, no. 4, p. 043 805, Oct. 2011, ISSN: 1050-2947. DOI: [10.1103/PhysRevA.84.043805](https://doi.org/10.1103/PhysRevA.84.043805) (cit. on p. 76).
- [249] S. G. Johnson and J. D. Joannopoulos, “Block-iterative frequency-domain methods for Maxwell’s equations in a planewave basis,” *Opt. Express*, vol. 8, no. 3, p. 173, Jan. 2001, ISSN: 1094-4087. DOI: [10.1364/OE.8.000173](https://doi.org/10.1364/OE.8.000173) (cit. on p. 77).
- [250] R. Hillebrand, S. Senz, W. Hergert, and U. Gösele, “Macroporous-silicon-based three-dimensional photonic crystal with a large complete band gap,” *J. Appl. Phys.*, vol. 94, no. 4, pp. 2758–2760, Aug. 2003, ISSN: 0021-8979. DOI: [10.1063/1.1593796](https://doi.org/10.1063/1.1593796) (cit. on p. 77).
- [251] L. A. Woldering, A. P. Mosk, R. W. Tjerkstra, and W. L. Vos, “The influence of fabrication deviations on the photonic band gap of three-dimensional inverse woodpile nanostructures,” *J. Appl. Phys.*, vol. 105, no. 9, p. 093 108, May 2009, ISSN: 0021-8979. DOI: [10.1063/1.3103777](https://doi.org/10.1063/1.3103777) (cit. on p. 77).
- [252] D. Devashish, S. B. Hasan, J. J. W. van der Vegt, and W. L. Vos, “Reflectivity calculated for a three-dimensional silicon photonic band gap crystal with finite support,” *Phys. Rev. B*, vol. 95, no. 15, p. 155 141, Apr. 2017, ISSN: 2469-9950. DOI: [10.1103/PhysRevB.95.155141](https://doi.org/10.1103/PhysRevB.95.155141) (cit. on pp. 77, 84).
- [253] S. Datta, C. T. Chan, K. M. Ho, and C. M. Soukoulis, “Effective dielectric constant of periodic composite structures,” *Phys. Rev. B*, vol. 48, no. 20, pp. 14 936–14 943, Nov. 1993, ISSN: 0163-1829. DOI: [10.1103/PhysRevB.48.14936](https://doi.org/10.1103/PhysRevB.48.14936) (cit. on p. 77).
- [254] A. F. Oskooi and S. G. Johnson, “Electromagnetic wave source conditions,” in *Advances in FDTD Computational Electrodynamics, Photonics and Nanotechnology*, A. Taflov, A. F. Oskooi, and S. G. Johnson, Eds., Boston: Artech, 2013, ch. 4, pp. 65–100 (cit. on p. 78).
- [255] G. D’Aguanno, N. Mattiucci, M. Centini, M. Scalora, and M. J. Bloemer, “Electromagnetic density of modes for a finite-size three-dimensional structure,” *Phys. Rev. E*, vol. 69, no. 5, p. 057 601, May 2004, ISSN: 1539-3755. DOI: [10.1103/PhysRevE.69.057601](https://doi.org/10.1103/PhysRevE.69.057601) (cit. on p. 78).
- [256] A. F. Oskooi, D. Roundy, M. Ibanescu, P. Bermel, J. D. Joannopoulos, and S. G. Johnson, “MEEP: A flexible free-software package for electromagnetic simulations by the FDTD method,” *Computer Physics Communications*, vol. 181, pp. 687–702, 2010 (cit. on p. 79).
- [257] K. Yee, “Numerical solution of initial boundary value problems involving maxwell’s equations in isotropic media,” *IEEE Transactions on Antennas and Propagation*, vol. 14, pp. 302–307, 1966 (cit. on p. 79).
- [258] H. Chew, “Transition rates of atoms near spherical surfaces,” *J. Chem. Phys.*, vol. 87, no. 2, pp. 1355–1360, Jul. 1987, ISSN: 0021-9606. DOI: [10.1063/1.453317](https://doi.org/10.1063/1.453317) (cit. on pp. 79, 88).

- [259] E. N. Economou, *Green's Functions in Quantum Physics*. Berlin, Heidelberg: Springer Berlin Heidelberg, 2006, vol. 7, ISBN: 978-3-540-28838-1. DOI: [10.1007/3-540-28841-4](#) (cit. on p. 84).
- [260] A. Polman and H. A. Atwater, "Photonic design principles for ultrahigh-efficiency photovoltaics," *Nat. Mater.*, vol. 11, no. 3, pp. 174–177, Mar. 2012, ISSN: 1476-1122. DOI: [10.1038/nmat3263](#) (cit. on p. 85).
- [261] W. L. Vos and L. A. Woldering, "Cavity quantum electrodynamics with three-dimensional photonic bandgap crystals," in *Light Localisation and Lasing*, M. Ghulinyan and L. Pavesi, Eds., Cambridge Univ. Press, Cambridge, 2015, pp. 180–216 (cit. on p. 85).
- [262] D. Devashish, "3D periodic photonic nanostructures with disrupted symmetries," Ph.D. dissertation, University of Twente, 2017 (cit. on p. 86).
- [263] T. Tajiri, S. Takahashi, C. A. M. Harteveld, Y. Arakawa, S. Iwamoto, and W. L. Vos, *Reflectivity of Finite 3D GaAs Photonic Band Gap Crystals*, 2020. arXiv: [arXiv:2001.06226 \[physics.optics\]](#) (cit. on p. 86).
- [264] Y. Xu, J. S. Vučković, R. K. Lee, O. J. Painter, A. Scherer, and A. Yariv, "Finite-difference time-domain calculation of spontaneous emission lifetime in a microcavity," *J. Opt. Soc. Am. B*, vol. 16, no. 3, p. 465, Mar. 1999, ISSN: 0740-3224. DOI: [10.1364/JOSAB.16.000465](#) (cit. on p. 87).
- [265] A. F. Koenderink, M. Kafesaki, C. M. Soukoulis, and V. Sandoghdar, "Spontaneous emission rates of dipoles in photonic crystal membranes," *J. Opt. Soc. Am. B*, vol. 23, no. 6, p. 1196, Jun. 2006, ISSN: 0740-3224. DOI: [10.1364/JOSAB.23.001196](#) (cit. on p. 87).
- [266] K. Ishizaki, M. Okano, and S. Noda, "Numerical investigation of emission in finite-sized, three-dimensional photonic crystals with structural fluctuations," *J. Opt. Soc. Am. B*, vol. 26, no. 6, p. 1157, Jun. 2009, ISSN: 0740-3224. DOI: [10.1364/JOSAB.26.001157](#) (cit. on p. 87).
- [267] W. A. Saunders, K. J. Vahala, H. A. Atwater, and R. C. Flagan, "Resonance-enhanced spontaneous emission from quantum dots," *J. Appl. Phys.*, vol. 72, no. 2, pp. 806–808, Jul. 1992, ISSN: 0021-8979. DOI: [10.1063/1.351818](#) (cit. on p. 88).